REFERENCE COPY

JPL
SPS 37-35, VOL. 1
Cy 473

UNCLASSIFIED

NATIONAL AERONAUTICS AND SPACE ADMINISTRATION

Space Programs Summary No. 37-35, Volume I

for the period July 1, 1965 to August 31, 1965

The Lunar Program

(Title Unclassified)

LAB B04232

JET PROPULSION LABORATORY
LIBRARY

NOV 16 1965

CALIFORNIA INSTITUTE OF TECHNOLOGY

JET PROPULSION LABORATORY
CALIFORNIA INSTITUTE OF TECHNOLOGY
PASADENA, CALIFORNIA

September 30, 1965

Classification Changed
UNCLASSIFIED
JPL-Letter from NASA-Langley
on Nov. 4, 1970, signed by W. E. Hanson
Date: Jan. 4, 1971 By: A. Castain

GROUP 4 — 3 year — Downgraded

This document contains information affecting the national [redacted] of the United States within the meaning of the Espionage Laws, Title 18, U.S.C., Sections 793 and 794, the transmission or revelation of which in any manner to an unauthorized person is prohibited by law.

[redacted]

UNCLASSIFIED

Preface

The *Space Programs Summary* is a six-volume, bimonthly publication that documents the current project activities and supporting research and advanced development efforts conducted or managed by JPL for the NASA space exploration programs. The titles of all volumes of the *Space Programs Summary* are:

Vol. I. The Lunar Program (Confidential)

Vol. II. The Planetary–Interplanetary Program (Confidential)

Vol. III. The Deep Space Network (Unclassified)

Vol. IV. Supporting Research and Advanced Development (Unclassified)

Vol. V. Supporting Research and Advanced Development (Confidential)

Vol. VI. Space Exploration Programs and Space Sciences (Unclassified)

The *Space Programs Summary,* Vol. VI consists of an unclassified digest of appropriate material from Vols. I, II, and III; an original presentation of technical supporting activities, including engineering development of environmental-test facilities, and quality assurance and reliability; and a reprint of the space science instrumentation studies of Vols. I and II.

W. H. Pickering

W. H. Pickering, *Director*
Jet Propulsion Laboratory

Space Programs Summary No. 37-35, Volume I

Copyright © 1965, Jet Propulsion Laboratory, California Institute of Technology

Prepared under Contract No. NAS 7-100, National Aeronautics & Space Administration

This [redacted] information affecting the national defense of the United States, within the meaning of [redacted] Title 18, U.S.C., Sections 793 and 794, the transmission or revelation of which in any manner to an unauthorized person is prohibited by [redacted]

UNCLASSIFIED

UNCLASSIFIED

Contents

I. *Ranger* Project 1
A. Introduction 1
B. Systems 2
II. *Surveyor* Project 6
A. Introduction 6
B. System Engineering and Reliability 7
C. System Analysis 9
D. System Testing 32
E. Launch Operations 38
F. Space Flight Operations 47
G. Aerospace Ground Equipment 47
H. Flight Control 49
I. Electronics 59
J. Electrical Power Supply 64
K. Propulsion 68
L. Spacecraft Vehicle and Mechanisms for Basic Bus 80
M. Scientific Payload 84
N. Thermal Control 100
O. Engineering Mechanics 111
References 123

UNCLASSIFIED

CONFIDENTIAL

I. *Ranger* Project

A. Introduction

The *Ranger* Project was established to develop a space flight technology for transporting engineering and scientific instruments to the Moon and planets. Nine *Ranger* launchings, using *Atlas D–Agena B* vehicles, were planned; all of these flights have now been made.

Rangers I and *II* (Block I) were not lunar-oriented, but were engineering evaluation flights to test the basic systems to be employed in later lunar and planetary missions. Several scientific experiments were carried on a non-interference basis. Both spacecraft performed satisfactorily within the constraints of the obtained satellite orbit. *Rangers III, IV,* and *V* (Block II) carried a gamma-ray instrument, a TV camera, and a rough-landing seismometer capsule; each of these flights experienced failures.

The objective of the *Ranger* Block III *(Rangers VI, VII, VIII,* and *IX)* flights was to obtain pictures of the lunar surface, at least an order of magnitude better than those obtainable with Earth-based photography, which will be of benefit to both the scientific program and the U.S. manned lunar flight program. The *Ranger VI* spacecraft, which was launched from the Eastern Test Range (ETR) on January 30, 1964, and impacted the Moon essentially on target on February 2, 1964, did not accomplish the flight objective due to a failure of the TV subsystem to transmit pictures. An extensive analysis of the TV subsystem failure was conducted, new and reworked hardware was assembled as the *Ranger VII* TV subsystem, and extensive testing of the reassembled TV subsystem was performed.

The *Ranger VII* spacecraft was launched from the ETR on July 28, 1964, and impacted the Moon on target on July 31, 1964. The mission flight objective was accomplished. The outstanding events of the mission were the precision of the trajectory correction and the transmission of 4304 video pictures of the lunar surface.

The *Ranger VIII* spacecraft was launched from the ETR on February 17, 1965, and impacted the Moon on target on February 20, 1965. The mission flight objective was again accomplished, and approximately 7000 high-quality video pictures of the lunar surface were transmitted from the spacecraft. The final calculated impact point represented a miss of only 15 miles from the originally selected aiming point.

The *Ranger IX* spacecraft was launched from the ETR on March 21, 1965, and impacted the Moon on target on March 24, 1965. Again, the mission flight objective was accomplished; following a successful terminal maneuver, 5814 excellent-quality video pictures of the lunar surface

UNCLASSIFIED

were transmitted from the spacecraft. The resolution of the final pictures is the best resolution obtained during any of the Block III flights. For the first time, the video signals, as relayed from the Goldstone Space Communications Station to JPL by microwave link, were scan-converted for live commercial TV transmission. The final calculated impact point of *Ranger IX* represented a miss of only 4 miles from the originally selected aiming point.

B. Systems

1. Ranger VIII and IX Video Data Processing

a. Task Number One: to determine the time of impact on the Moon of Ranger VIII and IX[1]. The method of determining the impact time with reference to the NASA Time Code is shown in Fig. 1. Three channels of data from the Ampex FR1400 tape-recorder–reproducer were utilized in determining the time of impact, viz, (1) analog video track, (2) 1-Mc track, and (3) the time code track.

For the *Ranger VIII* mission the 1-pps pulse occurring at 051:09:57:37 GMT was selected as the initiating pulse. The following events then occur. The 1-pps pulse enables both counters to start counting. One counter counts the 1-Mc signal and the other counter counts the number of full lines of data in the last picture. When the pre-set counter has counted the number of full lines of data, it initiates a stop pulse to the counter which is counting the 1-Mc signal. Time is now known to the beginning of the last line of video data. The increment of time during which real data were transmitted during the last line is determined from the photograph shown in Fig. 2.

For the *Ranger IX* mission the 1-pps pulse occurring at 083:14:08:21 GMT was selected as the initiating pulse.

The following data were obtained from the *Ranger VIII* mission by counting the 1-Mc signal from 051:09:57:37 GMT to the start of the last line of data of the P-4 camera.

X_i	X_i	X_i	X_i
1019132	1019132	1019097	1019084
117	096	114	106
111	110	125	109
104	097	110	112
112	107	119	107
108	117	114	121
116	063	117	
130	085	131	

The mean of this data is 1.019110 sec.
The standard deviation of this data is 15.1 μsec.
The data are shown in a form convenient for computation in Table 1 of the Appendix.

[1] Does not include propagation time between Earth and Moon or delay within the spacecraft.

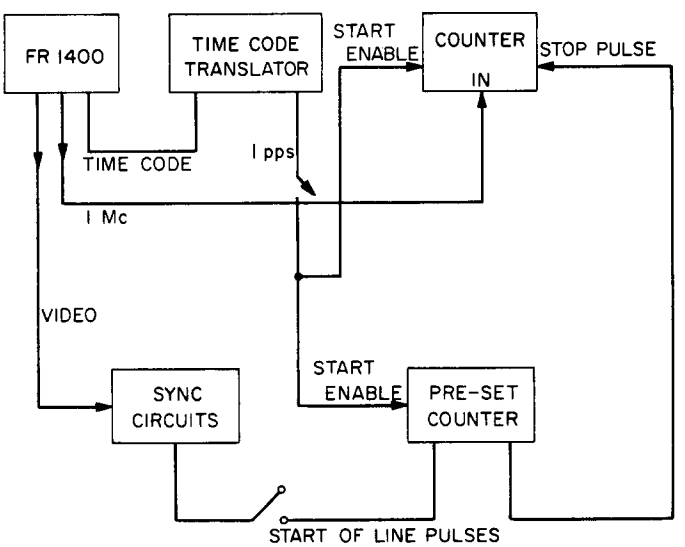

Fig. 1. Method of determining the impact time with reference to the NASA Time Code

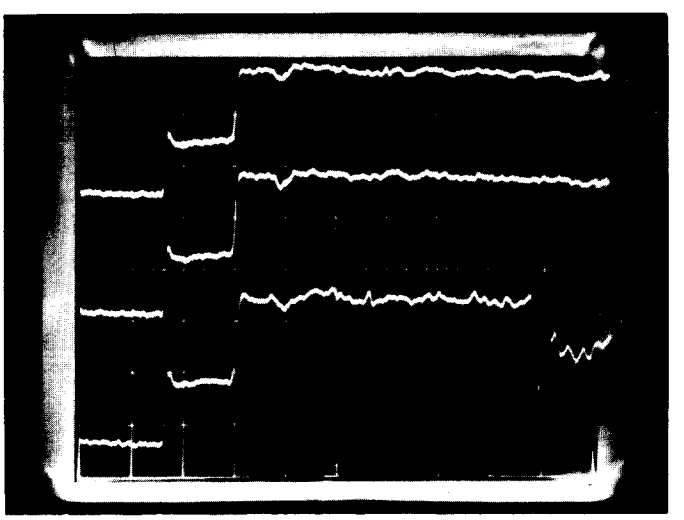

Fig. 2. *Ranger VIII* mission: beginning of the last 3 lines of data from the P-4 camera

UNCLASSIFIED

The following data were obtained from the *Ranger IX* mission by counting the 1-Mc signal from 083:14:08:21 GMT to the start of the last line of data of the P-3 camera.

X_i	X_i	X_i	X_i	X_i
325326	325325	325341	325345	325339
324	324	326	323	332
338	328	327	304	336
319	326	311	321	307
336	324	360	349	333
345	352	317	329	319
330	329	309	332	341
321	312	317	343	333

The mean of this data is 325329 μsec.
The standard deviation of this data is 12.7 μsec.
The data are shown in a form convenient for computation in Table 2 of the Appendix.

Reference time for the Ranger VIII mission: 051:09:57:37 GMT. Time from 051:09:57:37 to the beginning of the last line of data was 1.019110 sec. Time from beginning of the last line of data to impact was 401 μsec. Addition of the above times yields an impact time of 051:09:57:38.019511. The time of impact is believed correct to within $\pm$25 μsec (15 μsec due to electronic measurement error and approximately 10 μsec due to interpreting the time of impact from the last line of data; see photograph, Fig. 2). The photograph shows the beginning of each of the last three lines of data from the P-4 camera. Impact is indicated on the third line of the photo, which is the 37th line of the picture. The time scale on the photo is 45 μsec/cm.

Reference time for the Ranger IX mission: 083:14:08:21 GMT. Time from 083:14:08:21 to the beginning of the last line of data was 0.325329 sec. Time from beginning of last line of data to impact was 162 μsec. Addition of the above times yields an impact time of 083:14:08:21.325491. The time of impact is believed correct to within $\pm$25 μsec. Fig. 3 shows the beginning of each of the last three lines of data from the P-3 camera. Impact is indicated on the third line of the photograph, which is the 273rd line of the picture. The time scale on the photograph is 45 μsec/cm.

b. Task Number Two: to determine the variation in time required to transmit one picture at two separated times during the Ranger VIII and IX missions.

Ranger VIII Mission. The following data were obtained (Fig. 4) from counting the 1-Mc signal during 40 frames of P-camera data starting at 051:09:46:43 GMT and continuing for approximately 34 sec. This was approximately 11 min before impact.

Run number	1-Mc count
1	8400124
2	123
3	123

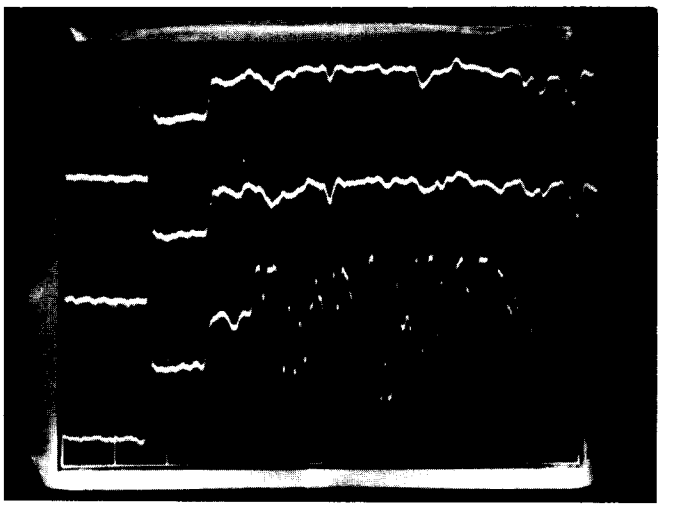

Fig. 3. *Ranger IX* mission: beginning of the last 3 lines of data from the P-3 camera

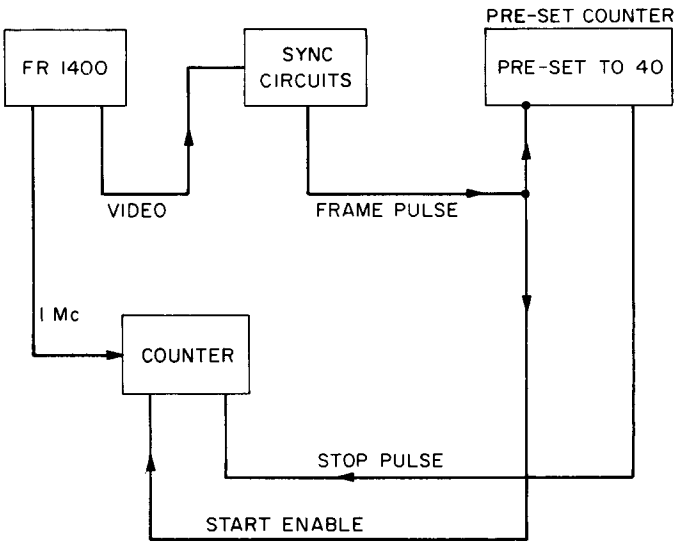

Fig. 4. Equipment setup used for determining X_i

UNCLASSIFIED

The following data were obtained from counting the 1-Mc signal during 40 frames of P-camera data starting at 051:09:55:12 and continuing for approximately 34 sec. This was approximately 2 min before impact.

Run number	1-Mc count
1	8400149
2	148
3	148

The data indicate that approximately 26 μsec more time is required to complete 40 P-camera frames near the end of the mission than was required 11 min earlier in the mission.

Ranger IX Mission. The following data were obtained (Fig. 4) from counting the 1-Mc signal during 40 frames of P-camera data starting at 083:13:59:23 and continuing for approximately 34 sec. This was approximately 9 min before impact.

Run number	1-Mc count
1	8399848
2	849
3	849

The following data were obtained from counting the 1-Mc signal during 40 frames of the P-camera data starting at 083:14:07:41 and continuing for approximately 34 sec. This was approximately 40 sec before impact.

Run number	1-Mc count
1	8399884
2	889
3	896
4	900
5	885
6	891
	Average: 8399889

The data indicate that approximately 40 μsec more time is required to complete 40 P-camera frames near the end of the mission than was required 8 min before impact.

c. Appendix.

Table 1. P-camera data from *Ranger VIII* mission

i	X_i	Frequency f_i	Coded score x_i	f_ix_i	$f_ix_i^2$
1	132	2	22	44	968
2	131	1	21	21	441
3	130	1	20	20	400
4	125	1	15	15	225
5	121	1	11	11	121
6	119	1	9	9	81
7	117	3	7	21	147
8	116	1	6	6	36
9	114	2	4	8	32
10	112	2	2	4	8
11	111	1	1	1	1
12	110	2	0	0	0
13	109	1	−1	−1	1
14	108	1	−2	−2	4
15	107	2	−3	−6	18
16	106	1	−4	−4	16
17	104	1	−6	−6	36
18	97	2	−13	−26	338
19	96	1	−14	−14	196
20	85	1	−25	−25	625
21	84	1	−26	−26	676
22	63	1	−47	−47	2209
		$\Sigma f_i = 30$		$\Sigma f_ix_i = +3$	$\Sigma f_ix_i^2 = 6578$

$$X_o = 110$$

$$\overline{X} = X_0 + i\overline{x} \qquad \text{where } i = 1$$

$$\overline{x} = \frac{\Sigma f_i x_i}{N} \qquad \text{where } N = 30$$

$$\overline{x} = \frac{+3}{30} = \frac{1}{10}$$

$$\overline{X} = 110 + (1)(0.1) \doteq 110$$

$$S^2 = \frac{\Sigma f_i x_i^2 - (\Sigma f_i x_i)^2/N}{N-1}$$

$$= \frac{6578 - 9/30}{30 - 1} = \frac{6578}{29}$$

$$= 227$$

$$S = 15.1$$

$$S = is = (1)(15.1) = 15.1 \text{ μsec}$$

UNCLASSIFIED

UNCLASSIFIED

Table 2. P-camera data from *Ranger IX* mission

i	X_i	Frequency f_i	Coded score x_i	$f_i x_i$	$f_i x_i^2$
1	60	1	34	34	1036
2	52	1	26	26	676
3	49	1	23	23	529
4	45	2	19	38	722
5	43	1	17	34	578
6	41	2	15	30	450
7	39	1	13	13	169
8	38	1	12	12	144
9	36	2	10	20	200
10	33	2	7	14	98
11	32	2	6	12	72
12	30	1	4	4	16
13	29	2	3	6	18
14	28	1	2	2	4
15	27	1	1	1	1
16	26	3	0	0	0
17	25	1	−1	−1	1
18	24	3	−2	−6	12
19	23	1	−3	−3	9
20	21	2	−5	−10	50
21	19	2	−7	−14	98
22	17	2	−9	−18	162
23	12	1	−14	−14	196
24	11	1	−15	−15	225
25	9	1	−17	−17	289
26	7	1	−19	−19	461
27	4	1	−22	−22	484

$$\overline{X} = X_0 + \overline{x} \qquad \text{where } X_0 = 325326$$

$$\overline{x} = \frac{269 - 139}{40} = \frac{130}{40} = 3$$

$$\overline{X} = 325326 + 3 = 325329\ \mu\text{sec}$$

$$S^2 = \frac{6700 - (130)^2/40}{39}$$

$$= \frac{6700 - 1690/4}{39}$$

$$= \frac{6700 - 422.5}{39}$$

$$= \frac{6278}{39}$$

$$= 161$$

$$S = 12.7\ \mu\text{sec (standard)}$$

UNCLASSIFIED

UNCLASSIFIED

II. *Surveyor* Project

A. Introduction

Calculated to span the gap between the *Ranger* flights and Project *Apollo*, the *Surveyor* spacecraft is designed to take the next step in lunar technology by attempting soft landings on the Moon. The first launches will be engineering test missions to demonstrate system capability up to soft landing, and limited post-landing operations. The engineering payload includes elements of redundancy, diagnostic telemetry, touchdown instrumentation, and survey TV.

Following the engineering test missions, *Surveyor's* objectives are to extend our knowledge of lunar conditions and to verify suitability of *Apollo* landing sites. The science payload is planned to consist of two-camera TV, micrometeorite ejecta, single-axis seismometer, alpha particle scattering, soil sampler, and touchdown dynamics experiments.

Hughes Aircraft Company, Space Systems Division, is under contract to develop and fabricate the first seven spacecraft. The launch vehicle is a combination *Atlas/Centaur*. The JPL Space Flight Operations and Deep Space Network (Mission Operations System) will be utilized for flight control and tracking. The first flight is scheduled for late 1965.

The major portion of the following material relating to the *Surveyor* spacecraft system was derived from material prepared by the Hughes Aircraft Company; articles prepared by the JPL Technical Sections are identified by footnotes to the article titles. The principal model designations and vehicles discussed are defined in Table 1.

Table 1. Model and vehicle designations

Designation	Description
SC-1–4	Flight spacecraft with engineering payload
SC-6–8	Flight spacecraft with scientific payload
A-21	Model designation for spacecraft with engineering payload (SC-1–4)
A-21A	Model designation for spacecraft with scientific payload (SC-6–8)
T-21	Model A-21 prototype system test spacecraft
SC-5	Model A-21A proof test model spacecraft
T-2	Simplified spacecraft for evaluation of terminal descent propulsion and flight control
S-2	Test spaceframe for vibration, shock, and static structural tests
S-6, -7	Test spaceframe for vernier propulsion system tests
S-9	Structural test model
S-10	Temperature control model

UNCLASSIFIED

B. System Engineering and Reliability

1. A-21 Spacecraft Configuration

The first four flight spacecraft (Model A-21) are designed to carry an engineering instrument payload to evaluate spacecraft performance and lunar soft-landing characteristics. The current A-21 weight summary is shown in Table 2. The A-21 balance summary showing the center-of-gravity location is given in Table 3.

Table 2. A-21 spacecraft weight summary

Item	Current design weight, lb
Total separated weight	2175.63
Basic bus	695.35
Usable propellant	1417.31
Engineering payload	62.97

Table 3. A-21 spacecraft weight and balance summary

Condition	Weight, lb	Vertical center of gravity Z[a], in.	Lateral center of gravity X, in.	Lateral center of gravity Y, in.
Spacecraft after *Centaur* separation	2175.63	12.02	0.07	−0.22
Maximum touchdown weight	645.54	16.80	0.08	−0.25
Minimum touchdown weight	599.13	17.59	0.09	−0.23

[a]Inches above landing gear hinge line (Spacecraft Station 48.48).

2. A-21A Spacecraft Configuration

Three flight spacecraft, designated A-21A, are designed to carry the scientific instrument payload to evaluate the lunar environment and lunar surface visual characteristics. This payload, which is in addition to the basic bus engineering instrumentation, includes two survey TV cameras, the alpha particle scattering instrument, the single-axis seismometer, the micrometeorite ejecta detector, the soil mechanics surface sampler, and the touchdown dynamics experiment.

The previous A-21A/114 design study incorporated provisions for simultaneous transmission of approach television and engineering data during the terminal descent phase. This mode was provided to simplify the command sequence during terminal descent and to enable a larger number of approach television pictures to be obtained. Design work on the provisions for this operating mode performed since the end of the study has also permitted further simplification of interconnections and testing. The low data-rate auxiliary, the signal processing auxiliary, and the new 250-kc subcarrier oscillator required for the new mode are planned for incorporation into the central signal processor. This consolidation will reduce the number of unit interconnections in the compartment. Reliability is expected to be improved and testing simplified. Also, the 250-kc subcarrier oscillator required for engineering data transmittal simultaneously with television will be located in a more functional position.

The current A-21A weight summary is shown in Table 4. The A-21A balance summary showing the center-of-gravity location is given in Table 5.

Table 4. A-21A spacecraft weight summary

Item	Current design weight, lb
Total separated weight	2450.00
Basic bus	726.27
Usable propellant	1606.56
Scientific payload	117.17

Table 5. A-21A spacecraft weight and balance summary

Condition	Weight, lb	Vertical center of gravity z[a], in.	Lateral center of gravity x, in.	Lateral center of gravity y, in.
Spacecraft after *Centaur* separation	2450.00	11.86	0.31	−0.52
Maximum touchdown weight	751.22	16.67	0.38	−0.61
Minimum touchdown weight	698.56	17.44	0.42	−0.61

[a]Inches above landing gear hinge line (Spacecraft Station 48.48).

3. A-21 A Priori Reliability

For the flight and landing phase, the *a priori* reliability for the A-21 spacecraft is 0.815. Table 6 shows the current *a priori* reliabilities by subsystem.

Table 6. A-21 subsystem *a priori* reliability for flight and landing phase

Subsystem	Reliability
Telecommunications	0.975
Vehicle mechanisms	0.987
Propulsion[a]	0.922
Electrical power	0.960
Flight controls	0.956
System	0.815

[a]Excludes vernier engine thrust chamber assemblies.

4. SC-1 A Priori Reliability

Based on test data the reliability estimate for SC-1 is 0.51 for the flight and landing mission. The data is provided by system test experience on SC-1 units. When system test experience is not available on a unit, flight acceptance test data is used. Table 7 shows the current data-based reliability estimate for SC-1 by subsystem.

Table 7. SC-1 subsystem *a priori* reliability estimates for flight and landing phase (based on test data)

Subsystem	Reliability
Telecommunications	0.802
Vehicle mechanisms	0.829
Propulsion[a]	0.924
Electrical power	0.873
Flight controls	0.944
System	0.51

[a]Excludes vernier engine thrust chamber assemblies.

5. Trouble and Failure Report (TFR) Status

Increased emphasis has been placed upon the TFR task in terms of documentation and technical adequacy. The Control Center at Hughes Aircraft Company (HAC) has been reorganized, departmentalized, and streamlined. TFR's receive more control and individual attention than before. Project management is supporting a more qualified technical description, verification, and corrective action. A weekly series of TFR technical reviews is now underway wherein TFR's are discussed individually by JPL and HAC cognizant engineers.

6. SC-1 Special Tests

A series of special tests was run on the SC-1 vehicle to supply additional confidence in the functional performance of the vehicle. Description of the tests and available results follow.

Optimum charge regulator logic checkout. This test was designed to provide additional confidence in the logic which determines the function of the optimum charge regulator in the *Surveyor* power system. The test was completed satisfactorily with no problems.

Power system noise investigation. This test monitored the noise on all of the spacecraft power busses. The test has been completed but, as of this time, the data has not been evaluated. However, during the test, no problems were noted.

Overload trip circuit bypass mode. This test was run to determine whether the overload trip circuit in the boost regulator was operating properly after incorporation of necessary changes. Operation was satisfactory; no new problems were noted.

Gyro heater threshold test. This test evaluated the performance of the flight control gyro heater control circuitry under low battery voltage. It was determined that the gyro heater control circuitry cycled erratically. An investigation to determine the cause and effect of the cycling is underway.

Voltage drop on 29-v flight control return with electronic control unit (ECU) operating. These tests were conducted to determine whether the squib gate circuitry in the flight control electronics is susceptible to transients that may occur during midcourse or terminal descent and to ascertain if these transients can cause premature firing of the explosive bolts and retro igniter. Noise measurements were made between the squib return and 29-vdc return as the spacecraft was exercised in the midcourse and terminal descent modes of operation. A Tektronix 564 scope was set up to measure the output of the flight control sensor squib gate signal (set to trigger at 29 peak to peak). At no time did the scope trigger, or any of the squib simulators fire inadvertently. The measured noise had a positive amplitude between 0.6 and 0.8 vdc, 6 μsec, with a repetition rate of 5 kc (dc value $\approx$ 0.480 vdc). Tests were run at the unit level to determine the marginality of the system. This test data indicated that it takes $\approx$4.0 vdc, at $\approx$10 μsec and at a repetition rate of 5 kc to obtain a flight control sensor squib gate output (27.5 vdc, 4 μsec).

Roll actuator open loop gain. This special test was to check that the roll actuator can position Vernier Engine 1 to oppose any spacecraft roll rotations and that it has a scale factor of 1.7 $\pm$0.4 deg of engine rotation per degree of spacecraft roll rotation. The data obtained showed

that for rotations of 1, 2, and 3 deg about the roll axis the scale factor was 1.79, 1.695, and 1.49 deg of engine rotation per degree of roll rotation, respectively.

Qualitative squib circuit test. A test was run in which squib simulators were substituted for the actual spacecraft squibs and were fired using low battery terminal voltage. The simulators were supplied enough current to fire an actual squib.

RF group noise test. This test, scheduled for the first week in August, will be performed to determine the susceptibility of the RF equipment aboard the spacecraft to conducted noise.

Transient on command lines. Command lines were monitored using a recorder and an oscilloscope to indicate the presence of transients on these lines which may inadvertently give false commands. The data has not been evaluated but there were no visual indications of any transients existing which could cause a problem.

Telemetry current channel noise. A check of the spacecraft current channel measurements will be run to determine the noise content. This test will be performed after the current measurement amplifiers in the engineering signal processor and auxiliary engineering signal processor are reworked to provide proper frequency rolloff.

Telemetry system calibration/verification. A test will be run to provide one-point verification for all telemetry channels on the spacecraft. Where possible, the verification data will be obtained from previous test runs. This test should be completed the second week in August.

Ground integrity tests. A continuity check of the isolation of the various grounding systems was performed on the SC-1 spacecraft. This test indicated a short in one of the harness shields to the spacecraft frame. This short was repaired and no further problems occurred.

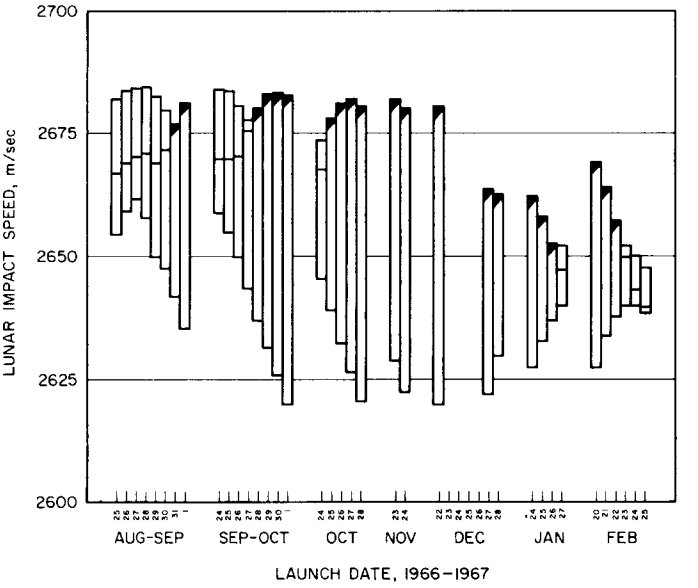

Fig. 1. Variation of parking orbit lunar impact speed (August 1966 to February 1967)

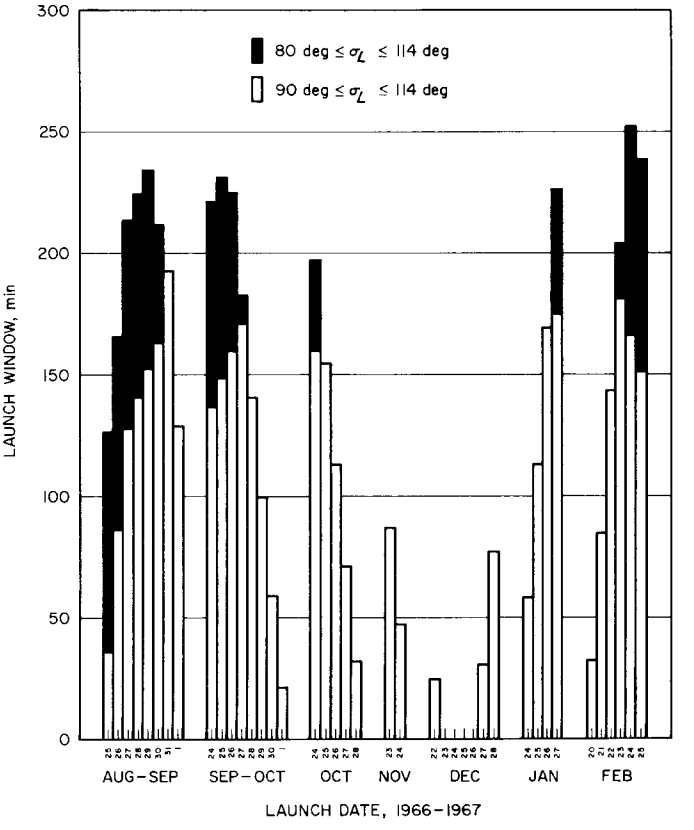

Fig. 2. Parking orbit launch windows (August 1966 to February 1967)

C. System Analysis

1. Variation of Parking Orbit Lunar Impact Speed and Launch Windows for August–September 1966 Through February 1967

Figs. 1 and 2 present parking orbit trajectory data for the Goldstone Deep Space Instrumentation Facility

UNCLASSIFIED

(DSIF) station for the period August–September 1966 through February 1967. One change in the ground rules (*SPS 37-33*, Vol. I) was made to generate these data: The coast time is constrained to lie between 2 and 20 min instead of 2 and 25 min in order to conform to the requirements of Mission D as specified in Ref. 1.

Fig. 1 shows the daily variation of lunar impact speed. The top of a bar indicates impact speed expected for earliest arrival and minimum launch azimuth. The bottom of a bar represents expected impact speed for latest arrival and maximum launch azimuth. A line falling between these two extremes represents the impact speed expected for early arrival and minimum launch azimuth when the lower azimuth limit is relaxed from 90 to 80 deg. The days shaded at the top and not showing a line intersecting the bar are those days when the coast-time constraints limit the launch azimuth. On all shaded days shown, the 20-min coast time has limited the maximum launch azimuth to lie between 90 and 114 deg for early arrival.

Fig. 2 presents the launch window for the same period, for launch azimuth constraints of 80 deg $\leq \sigma_L \leq$ 114 deg and 90 deg $\leq \sigma_L \leq$ 114 deg.

2. Intensity, Magnitude, and Spacecraft Coordinates of Earth and Moon for Mission A

Several selected *Surveyor* Mission A trajectories (Table 8) have been examined to determine intensity (total brightness), magnitude, and spacecraft coordinates of the Earth and the Moon as a function of time from injection. The data were generated for a study of the effect of Earth and Moon intensity on a search for the star Canopus.

Table 8. Selected Mission A trajectories

Launch date, 1965	Launch azimuth, deg
Oct. 1	91.5, 115
Oct. 2	97.5
Oct. 3	106.5
Oct. 25	93.4
Oct. 30	102.0
Nov. 26	98.4

The first two trajectories bound the range of launch azimuths for the first launch period in the fourth quarter of 1965. The next two represent two other days in that launch period, at the opening or lowest possible launch azimuth. The trajectories for October 25, 30, and November 26 are samples from the following two launch periods. The spacecraft coordinate system used is shown in Fig. 3.

In the cruise mode the Sun is located in the direction of the spacecraft $-$ z-axis, the y-axis is perpendicular to the z-axis and to a line from the spacecraft to the star Canopus (as shown in Fig. 3), and the x-axis completes a right-handed coordinate system. The angle ϕ is measured in the x-y plane positive from x toward y and ranges from -180 to $+180$ deg. Angle θ is measured from the x-y plane positive toward the $+$ z-axis and ranges from -90 to $+90$ deg.

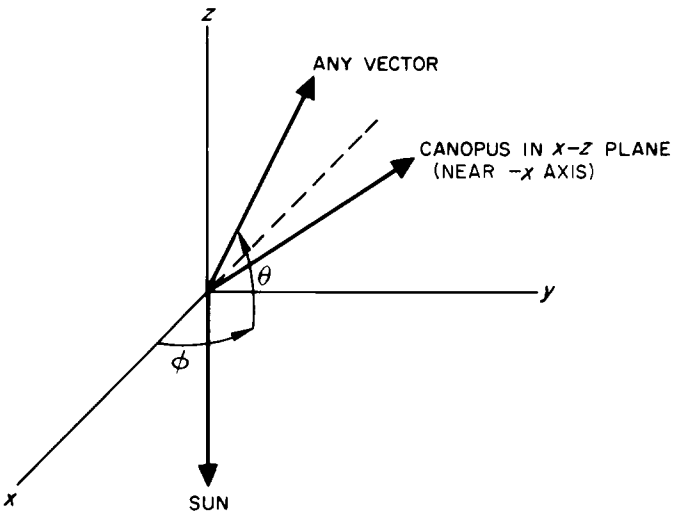

Fig. 3. Spacecraft coordinate system during cruise mode

A sample set of figures is presented for a launch on October 30, 1965, at a launch azimuth of 102 deg. Fig. 4 shows ϕ and θ as functions of time for the Earth and Moon mass centers, and for three DSIF stations: Goldstone, Canberra, and Johannesburg. (Please note the two different scales for the angle ϕ.) Fig. 5 illustrates how the intensity and magnitude of the Earth and Moon vary through the same trajectories. The equations were obtained from Ref. 2.

[1]These cruise-mode coordinates are valid only when the spacecraft is locked on both the Sun and the star Canopus. Before Sun acquisition, or for about 30 min after injection, this coordinate system is not established, and therefore the coordinates shown in Fig. 3 should not be used. After Sun acquisition but before Canopus lock (between 2 and 8 hr after injection), the roll coordinate ϕ is not established. The value shown for angle θ is, however, correct. Also, during the midcourse and terminal maneuvers the cruise-mode coordinates cannot be used.

UNCLASSIFIED

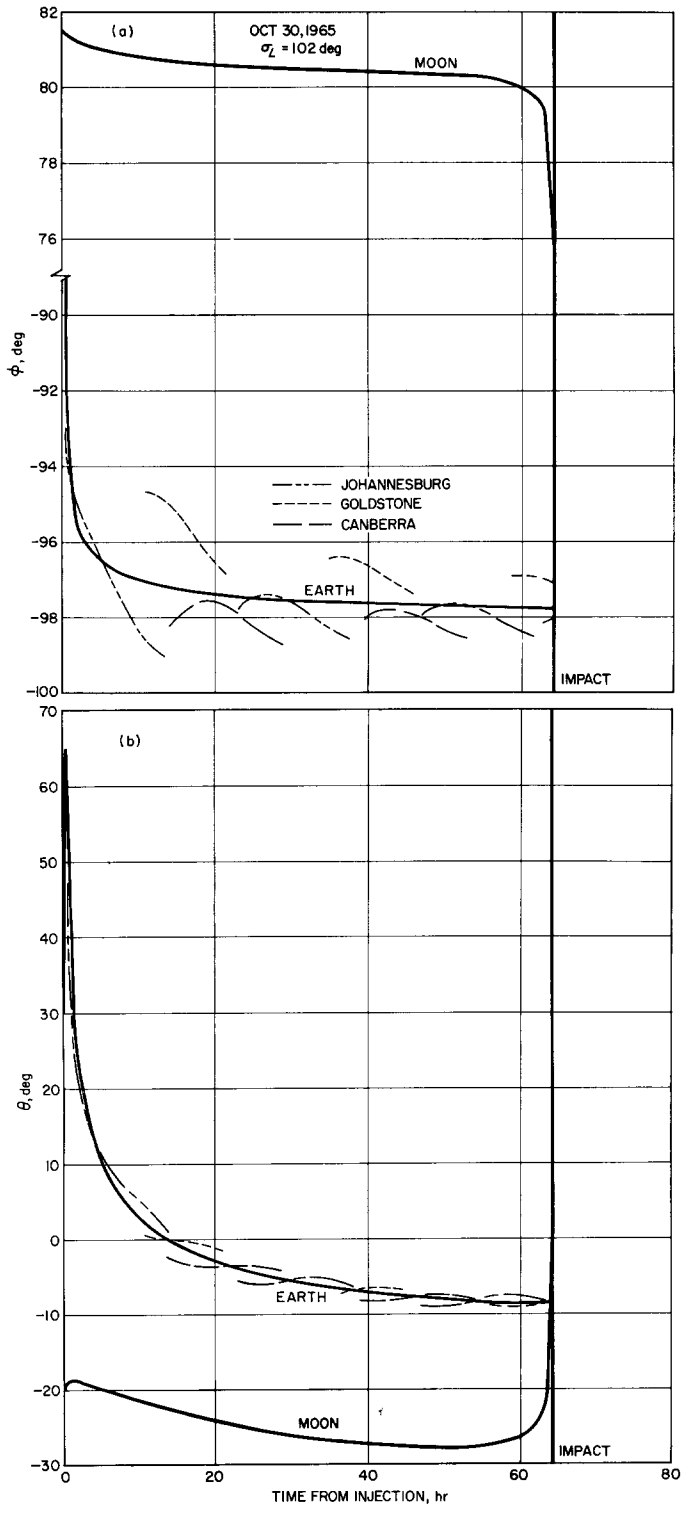

Fig. 4. Function of time from injection: (a) angle ϕ; (b) angle θ

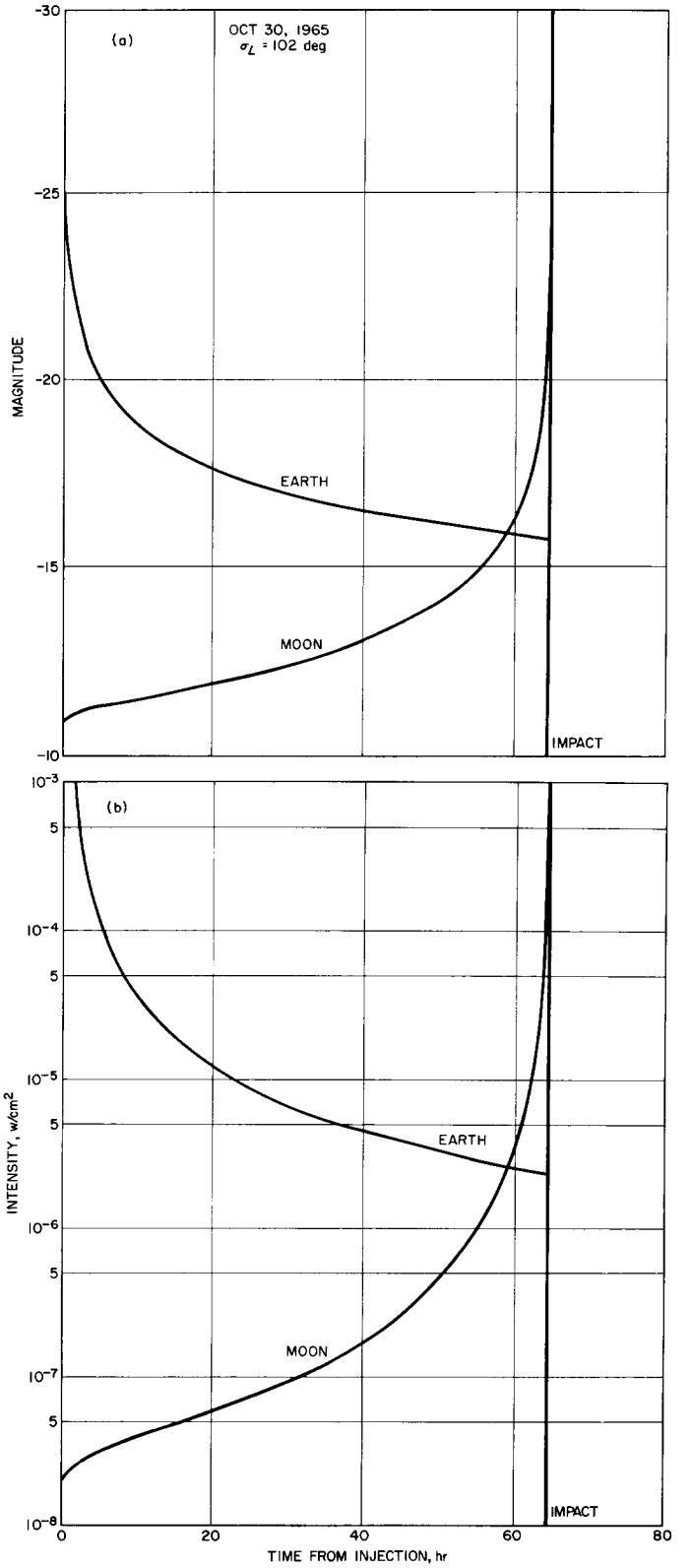

Fig. 5. Function of time from injection: (a) magnitude; (b) intensity

3. *Centaur* Interference with Sun Acquisition

An investigation has been performed to determine the region of interference of reflected sunlight from the *Centaur* stage with the *Surveyor* acquisition Sun sensor. The results indicate that the interference region extends over a very short range from the spacecraft and the probability of interference is very low.

Initial Sun acquisition is begun 51 sec after the spacecraft separates from the *Centaur* when the spacecraft begins a roll maneuver to have the acquisition Sun sensor acquire the Sun. A ground command backup capability has been incorporated to permit initiation of Sun acquisition if the automatic mode has not been completed properly.

The *Centaur* was assumed to be a 52% specular reflecting cylinder 10 ft in diameter and 25 ft in length. Specular rather than diffuse reflection was assumed in order to set up a "worst case" for analysis. The relationship between light energy gathered by the Sun sensor and distance between the *Centaur* and spacecraft is

$$H = \rho \frac{a}{2R} s^* \cos\left(\frac{\theta}{2}\right)$$

where a = cylinder radius = 5.25 ft, R = *Centaur*–spacecraft separation distance, ft, θ = incidence angle of Sun's rays = 0 deg (maximum effect), ρ = albedo or percentage of incidence light reflected = 52%, and H is in Suns for $s^* = 1.0$.

The curved line in Fig. 6 is a plot of this relationship. The dashed line is the level or threshold at which the acquisition Sun sensor logic outputs a detection signal. The vertical lines indicate the limits on the separation distance for separaton rates of 0.7 and 1.0 ft/sec; at the beginning of Sun acquisition the spacecraft is expected to be within these limits. Fig. 7 gives the *Centaur*–spacecraft relative geometry for the first 51 sec after separation.

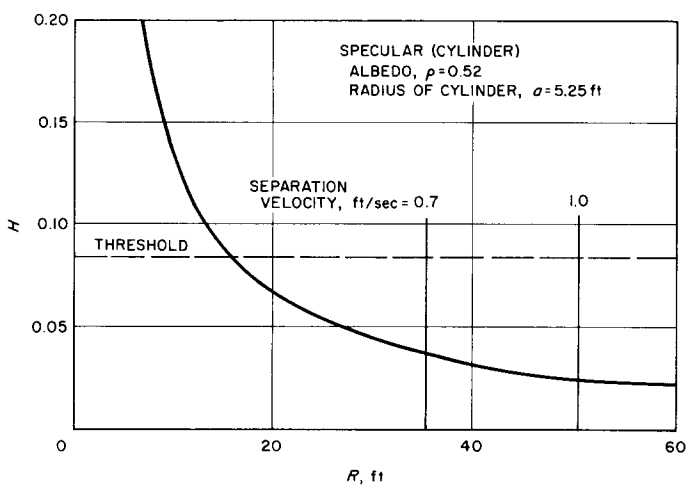

Fig. 6. *Centaur* reflected light received by secondary Sun sensor H vs separation distribution R

It is apparent from Fig. 6 that within the separation limits shown the sunlight reflected from the *Centaur* does not have sufficient energy content to be detected by the acquisition Sun sensor.

Although assumption that the *Centaur* is a reflecting cylinder is valid for the major portion of the vehicle, there is a possibility that reflections may emanate from the ends of the vehicle. Considering the small cross-sectional area presented by such surfaces, the separation distances that would exist at the time they might present a problem (near the end of the *Centaur* attitude maneuver), and the probability of a reflecting surface lying within the acquisition Sun sensor field of view during the acquisition period, the probability of interference is extremely low.

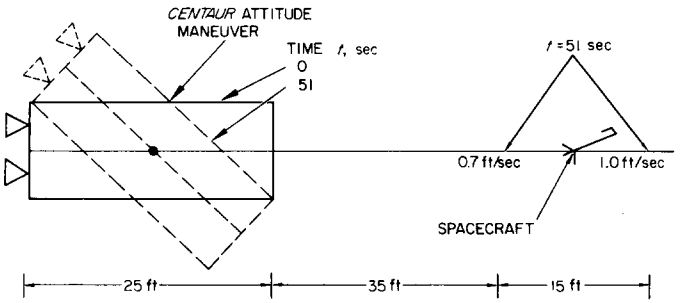

Fig. 7. *Centaur*–spacecraft relationship 51 sec after separation

4. Analysis of Vernier Propellant Reserve for Nonmanifolded Feed System

During the *Surveyor* retro phase the three vernier engines provide the control moments necessary to hold the spacecraft in an inertially fixed attitude. In the event of main retro misalignment, the thrusts of the three verniers during retro are unequal and they therefore consume propellant at unequal rates. The unequal propellant consumption rates cause a displacement of the spacecraft center of mass, and this displacement in turn interacts through the flight control system to affect the thrust magnitudes of the three verniers.

When the vernier propellant tanks were connected by manifolding, the total vernier propellant necessary for

the retro phase was rather easily determined, since the total thrust of the verniers is assumed constant. With the manifolding removed, however, it is necessary to find the maximum mass of propellant which a single vernier might consume. Assuming an initial 1800-in.-lb retro misalignment, the maximum mass consumed by a vernier engine during the retro phase until burnout is found to be $\overline{m}_A = 10.08 - 3.46 \sin i$, where i is the vernier plane angle between the main retro moment and the vernier engine, and $\overline{m}_A$ is in pounds. This implies that a single vernier's maximum consumption is $10.08 + 3.46 = 13.55$ lb of propellant and that 13.54 lb will cover 99% of all cases.

In the manifolded case, a total of $3 \times 10.08 = 30.24$ lb of vernier propellant would be consumed during retro. With the removal of manifolding, $3 \times (13.54) = 40.62$ lb must be loaded, since any engine might be the "bad" one. Hence unmanifolding the verniers increases the vernier propellant loading by a total of 10.38 lb.[2] Plots of propellant consumption, cg location, and thrust levels are shown in Figs. 8 through 12.

Fig. 13 shows the location of the *Surveyor* vernier engines and their propellant tanks (for simplicity, both fuel and oxidizer are shown coalesced). The basic planform is the equilateral triangle, and triangular symmetry prevails. The main retro engine fits into position as shown in Fig. 14. Its mass center does not coincide with the centroid, but has y coordinate b_0, as does the initial total mass center (Fig. 15).

The two-dimensional analysis assumes zero moments about the y-axis and equal thrust on Verniers B and C.

[2]This analysis is valid for consideration of only the removal of the manifolding. When all the mechanization and guidance errors which require extra propellant are combined statistically, the increase in propellant weight required to maintain the probability of success unchanged is only about 5 lb.

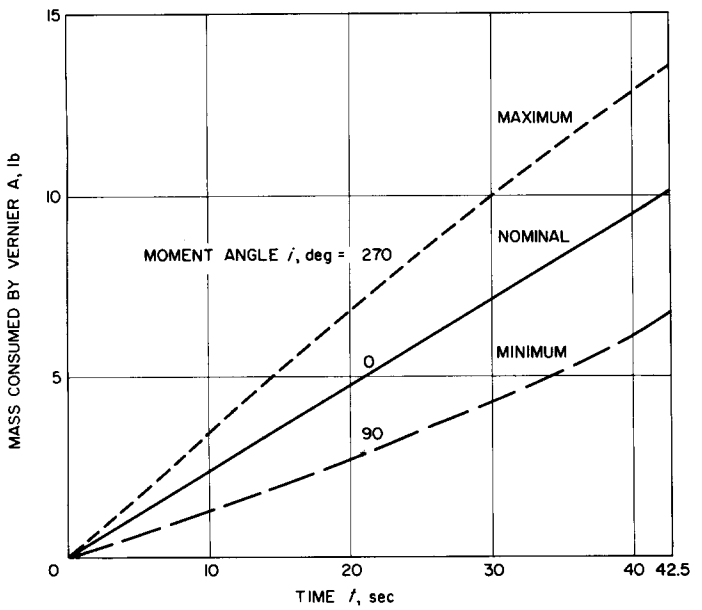

Fig. 8. Propellant consumption (Vernier A engine) vs time

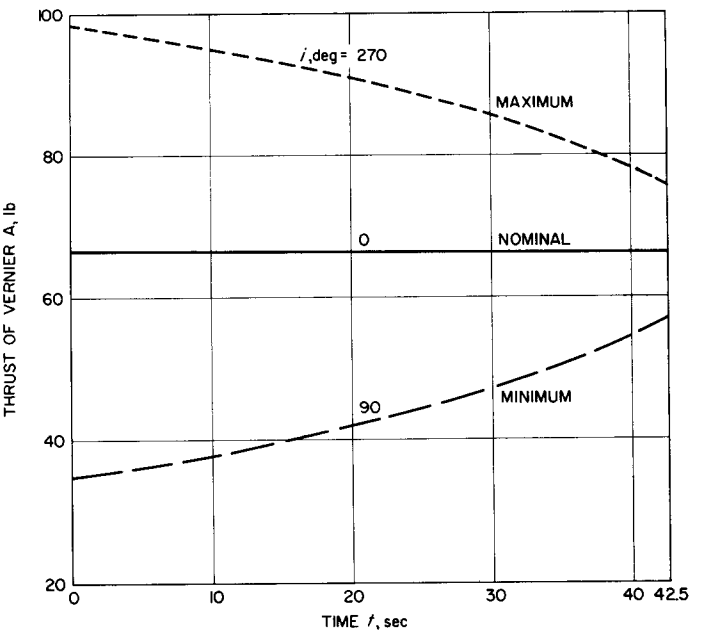

Fig. 9. Thrust of Vernier A engine vs time

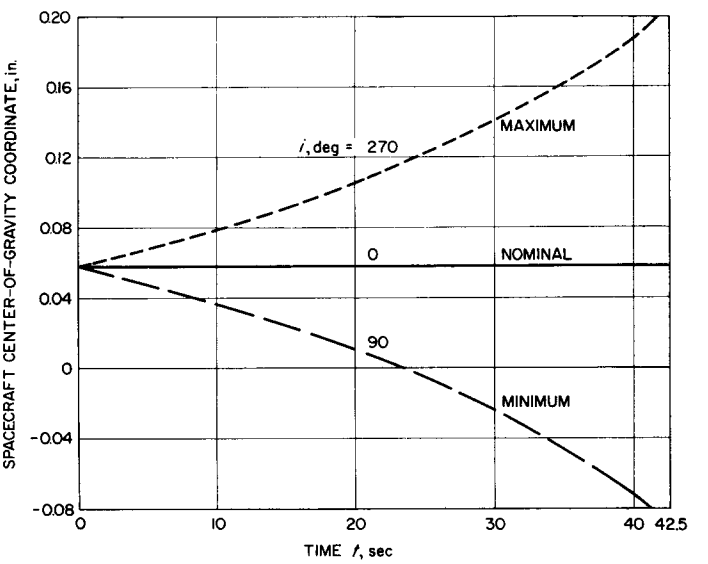

Fig. 10. Spacecraft center-of-gravity shift

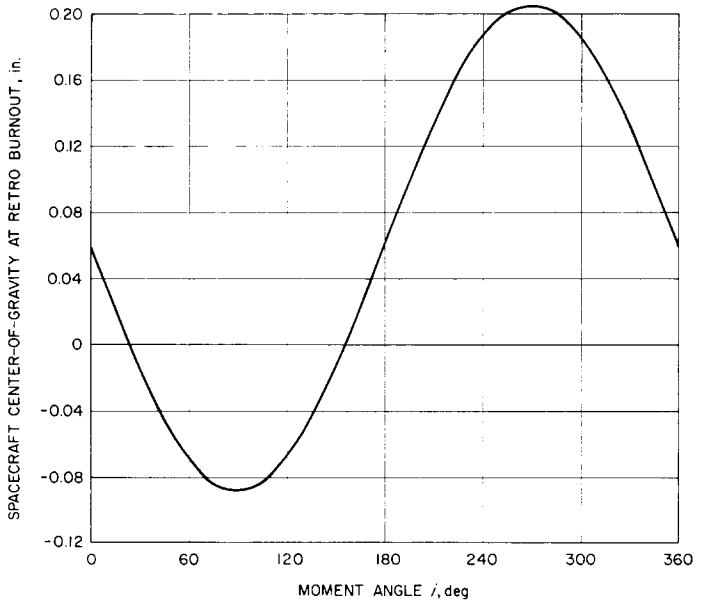

Fig. 11. Retro burnout center-of-gravity dependence on moment angle

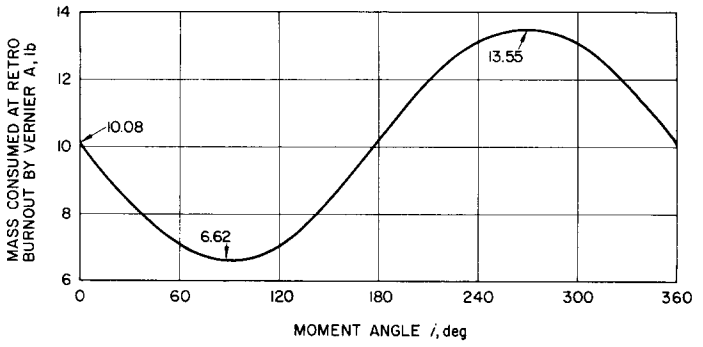

Fig. 12. Retro burnout mass consumption dependence on moment angle

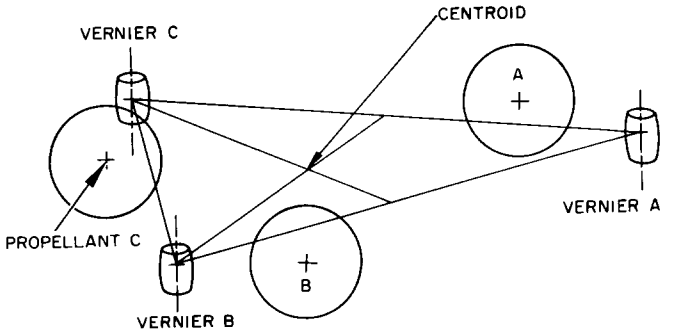

Fig. 13. Basic planform of vernier engines and propellant tanks

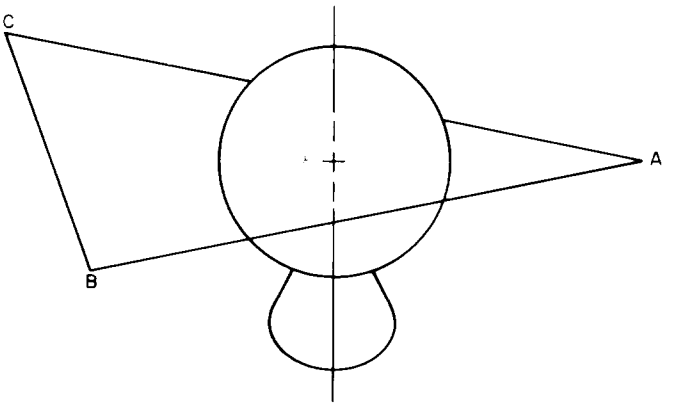

Fig. 14. Position of main retro engine

Also, the x-axis component of the mass center's migration is ignored. A complete list of assumptions follows:

(1) Initially, the mass center of retro fuel coincides with the total mass center.

(2) Initially, the mass center of vernier propellant is at centroid.

(3) During retro, the mass center of basic bus plus payload and the mass center of main retro fuel stay fixed.

(4) The mass ratio of oxidizer to fuel is the same constant for all three verniers.

(5) Specific impulse is the same constant for all three vernier engines, and is also constant for the main retro.

(6) The main retro thrust vector is constant relative to the spacecraft.

(7) The sum of vernier thrusts is constant.

(8) All vernier thrust is perpendicular to the plane of verniers.

(9) The spacecraft has no angular velocities during retro.

(10) The total mass center remains equidistant from the two Verniers B and C.

Assumptions 1, 2, 3, and 6 introduce only extremely small distortions of reality. Assumptions 4, 5, 7, 8, and 9 introduce somewhat larger distortions, but they are still small. Assumption 10 is expected to provide a slightly more optimistic result than the true one (but close to the true result), as a brief qualitative analysis of the system without Assumption 10 will reveal.

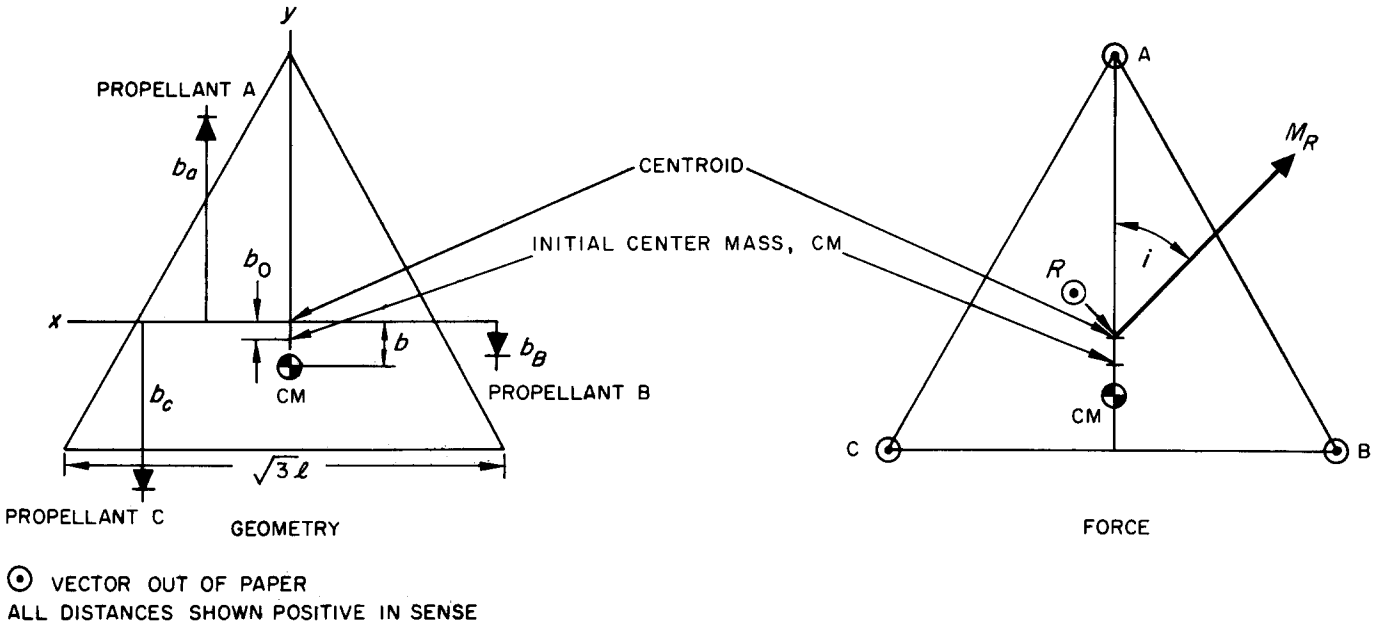

Fig. 15. Geometry and force diagrams

a. Basic equations. The location of the center of mass is given by

$$Mb = M_{RP}b_0 + m_I b_I + M_B b_B + m_C b_C - m_A b_A$$

The sum of moments about the x-axis through the center of mass is zero:

$$M_R \sin i + R(b-b_0) + A(\ell+b) - (B+C)(\ell/2 - b) = 0$$

Total vernier thrust is constant:

$$A + B + C = K$$

The rate of propellant consumption in any vernier motor is proportional to its thrust:

$$\left.\begin{matrix}\dot{m}_A \\ \dot{m}_B \\ \dot{m}_C\end{matrix}\right\} = \frac{-1}{I_{SP}g_0}\left\{\begin{matrix}A \\ B \\ C\end{matrix}\right.$$

By the two-dimensional assumption

$$B = C$$

The above equations can be combined to yield:

$$Mb - (b_B+b_C)m_B + m_A b_A - M_{RP}b_0 - M_I b_I = 0 \tag{1}$$

$$M_R \sin i + R(b-b_0) + A(\ell+b) - (K-A)(\ell/2 - b) = 0 \tag{2}$$

$$A + 2B = K \tag{3}$$

$$\left.\begin{matrix}\dot{m}_A \\ \dot{m}_B \\ \dot{m}_C\end{matrix}\right\} = \frac{1}{I_{SP}g_0}\left\{\begin{matrix}A \\ B \\ C\end{matrix}\right. \tag{4}$$

b. Maximization of single vernier propellant consumption. The desired result is an expression for the maximum mass of propellant that can be consumed by one vernier motor during retro fire. If A is the vernier motor under consideration, since $A + B + C =$ constant, A will vary with i, and therefore so will $\overline{m}_A$.

To find $\overline{m}_A(i, t)$, from Eq. (2)

$$A = \frac{2}{3\ell}\left[K\left(\frac{\ell}{2} - b\right) - R(b - b_0 - M_R \sin i\right]$$

$$\overline{m}_A(t, i) = \frac{1}{I_{SP}g_0}\int_0^t A\,dt$$

$$= \frac{2}{3\ell I_{SP}g_0}\int_0^t \left[K\left(\frac{\ell}{2} - b\right) - R(b-b_0) - M_R \sin i\right] dt \tag{5}$$

where b is itself a function of i and t.

Substitution of Eq. (1), solved for b, into Eq. (5) gives an equation which, when differentiated with respect to i and set equal to zero, gives $i = 3\pi/2$ for maximum consumption at Vernier A.

Analysis. From Eq. (5)

$$\overline{m}_A(t, i) = \frac{2}{3\ell_{SP}g_0}\int_0^t \left[-\frac{K+R}{\delta'}(\alpha'\,\overline{m}_A + \beta'\,\mathrm{t} + \gamma') + \frac{K\ell}{2} + M_R + Rb_0 \right] dt$$

where α', β', and γ' are constants, and δ' is a function of t. Differentiating $\overline{m}_A(t, i)$ with respect to time

$$\dot{\overline{m}}_A(t, i) = \frac{\overline{m}_A(t, i) + \eta\, t + \zeta}{\theta + \phi t} \tag{6}$$

where θ and ϕ are constants, and η and ζ are functions of i.

The solution to Eq. (6) is

$$\overline{m}_A(t, i) = \beta_1\left[(1 + \beta_2 t)^{\beta_3} - 1\right] + \beta_4 t \tag{7}$$

where

$$\beta_4 = \eta/(\phi - 1)\,, \beta_3 = 1/\phi, \beta_2 = \phi/\theta\,,$$

and

$$\beta_1 = (\dot{\overline{m}}_A \mid_{t=0} - \beta_4)/\beta_2\beta_3\,.$$

Since θ and ϕ are constants, β_2 and β_3 are constants, with β_1 and β_4 functions of i. Hence, for maximum consumption

$$\overline{m}_A(t, 3\pi/2) = \beta_1(3\pi/2)\left[(1 + \beta_2 t)^{\beta_3} - 1\right] + \beta_4(3\pi/2)t$$

Dependence on i. Eq. (7) can be written $\overline{m}_A(t, i) = \beta_1(i)\, k(t) + \beta_4(i)t$. So at any given time, $\overline{t}$, evaluating β_1 and β_4, $m_A(\overline{t}, i) = k_1 + k_2 \sin i$ (k_1, k_2 constants). Using conditions at $i = 0$ and $i = \pi/2$,

$$\overline{m}_A(t, i) = \overline{m}_A(\overline{t}, 0) + \left[\overline{m}_A(\overline{t}, \pi/2) - \overline{m}_A(\overline{t}, 0)\right] \sin i \tag{8}$$

Using $\overline{t}$ as retro burnout time, Eq. (7) can be used to evaluate the coefficients of Eq. (8), yielding an expression for burnout $\overline{m}_A$ as a function of i.

5. Probability of Stable Landing in Presence of RADVS Noise

A Monte Carlo simulation described in *SPS 37-33*, Vol. I has been modified to include the effect of radar altimeter and doppler velocity sensor (RADVS) noise output levels (T-2H and twice T-2H levels) on pretouchdown velocity and attitude. The probabilistic behavior of spacecraft velocity and attitude at attitude hold, and velocity, attitude, and angular velocity at vernier engine cutoff as a consequence of RADVS noise were determined from analog simulation studies. The current estimates of the noise-independent errors and the accompanying noise-dependent effects were incorporated into the Monte Carlo simulation to produce the joint probability density histograms for T-2H and twice T-2H levels.

Superimposing landing stability boundaries on the joint-probability density histogram for T-2H noise (Fig. 16) and counting the number of events that fall within the stable region out of the 10,000 Monte Carlo trial simulation, the probability of a stable landing for the T-2H level was determined to be greater than 0.999 (for the twice T-2H level the probability was about 0.996). The stable region of interest is above the 16 ft/sec boundary since the simulation demonstrated that the probability of longitudinal velocities exceeding 16 ft/sec is less than 0.001. Although the stability curves are functions of the angular velocities at touchdown, these curves are valid for the angular velocities encountered in the simulation (the probability that the total angular velocity is less than 3.2 deg/sec is approximately 0.99).

Although this analysis indicates acceptable system operaton in the presence of RADVS noise, the following should be noted:

(1) The margins between spacecraft control and landing performance have been substantially reduced.

(2) The lateral velocity resulting from the twice T-2H noise condition exceeds the 5 ft/sec (3σ) limit in JPL specification 30240D.

6. Capability of Surveyor Television System to Provide Pictures of Lunar Surface Using Earthshine Illumination During Lunar Night Operations

a. Introduction. Launch periods and landing constraints for the end of 1965 and early part of 1966 provide lunar night landings. In the absence of direct sunlight, the lunar surface will be illuminated from the Earth's reflected sunlight, called earthshine. Operation of the TV camera in normal and emergency modes and prediction of the signal-to-noise ratio (S/N) of the received television pictures have been considered for night landing. Optimizing earthshine illumination by appropriate selection of landing sites is also discussed.

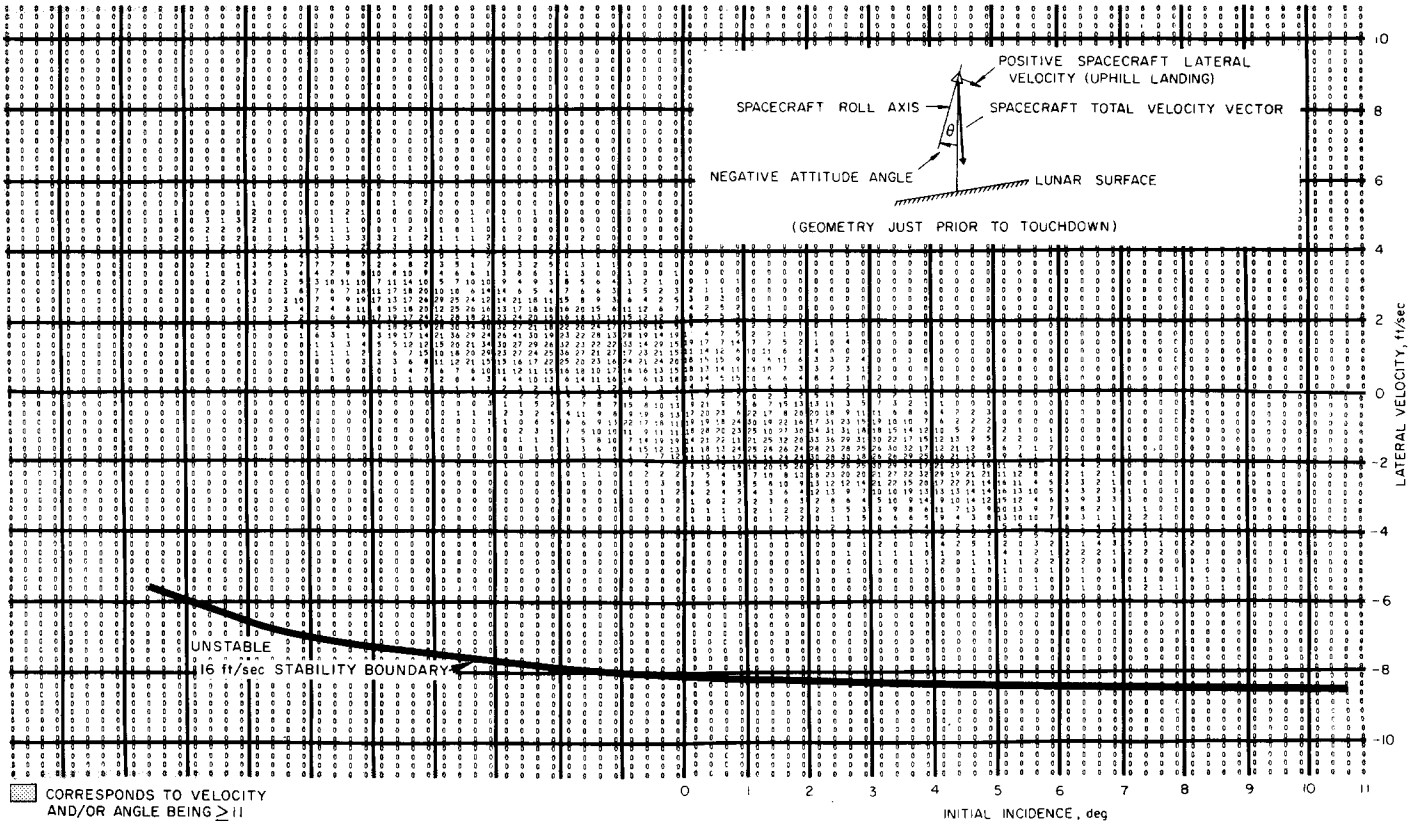

Fig. 16. Joint probability density of pretouchdown lateral velocity and initial incidence (T-2H noise)

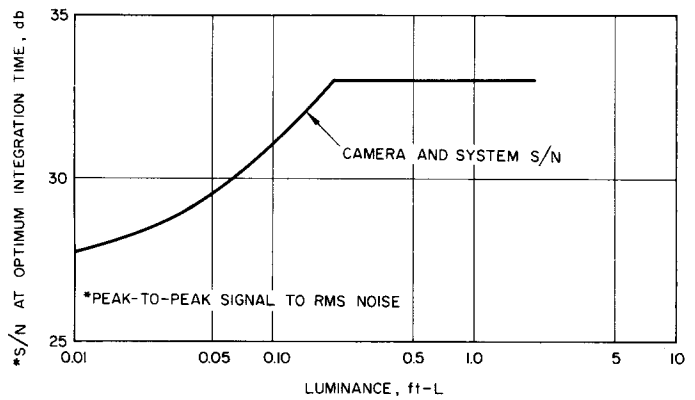

Fig. 17. Camera and system signal-to-noise ratio (normal mode) vs luminance

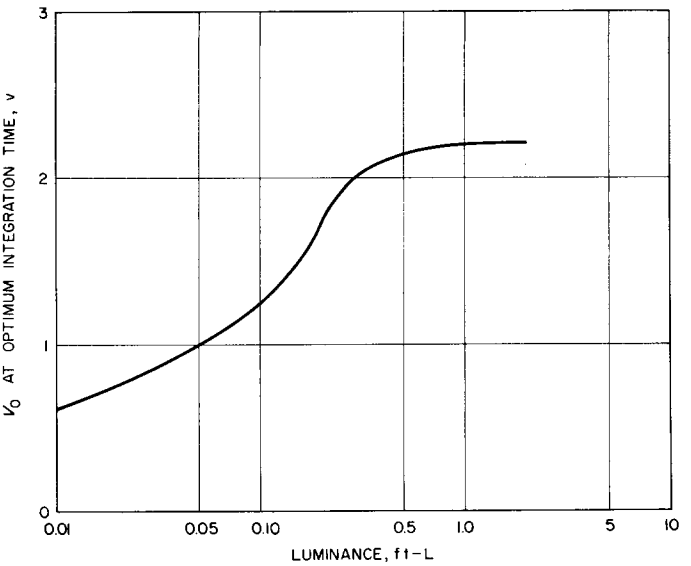

Fig. 18. Black-to-white transition vs V_0 (emergency mode)

b. Conclusions. Analysis of test data indicates that the *Surveyor* television system can provide TV pictures of the lunar surface in both the normal and emergency modes of operation. While the S/N of the normal mode pictures are approximately twice those taken with the emergency mode under worst conditions (Figs. 17 and 18), the normal mode requires the use of the planar array antenna, which may require an hour or more to position. Fig. 19 shows TV pictures taken in both modes of a low contrast Moon slide under low illumination conditions. The survey television camera will be warm enough to operate upon landing, if heated 5 hr prior to touchdown.

UNCLASSIFIED

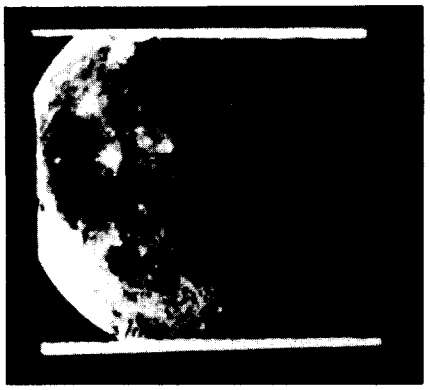

1. LUMINANCE = 0.05 ft-L
2. TRANSMISSION STOP, T5.6
3. INTEGRATION TIME = 8 min

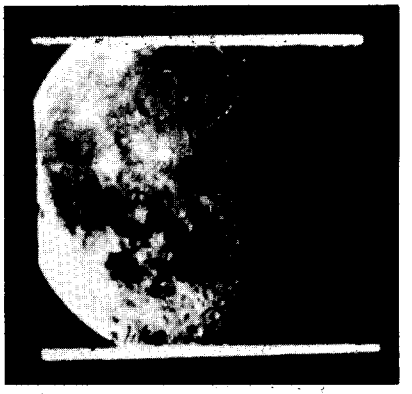

1. 0.05 ft-L
2. T8
3. 12 min

NORMAL MODE

1. 0.375 ft-L
2. T16
3. 18 min

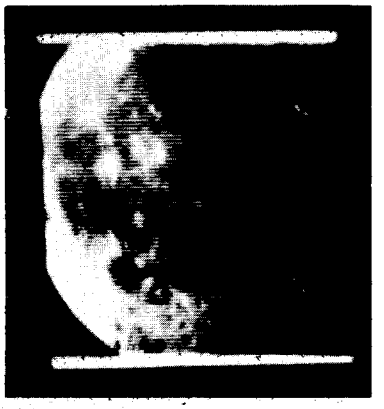

1. 0.05 ft-L
2. T8
3. 24 min

EMERGENCY MODE

Fig. 19. Low contrast Moon test charts

c. Expected luminance levels. The maximum illumination of the lunar surface by earthshine, for a full Earth is (Ref. 3)

$$E_{max} = 1.82 \times 10^{-3}\ \text{lm/cm}^2$$
$$= 1.69\ \text{lm/ft}^2$$

The maximum luminance of the 7% reflecting lunar surface (Maria) is therefore $B = 1.69 \times 0.07 = 0.12$ ft-L.

The television camera can view the surface at a maximum depression angle of approximately 60 deg (Fig. 20). The photometric function of the lunar surface (Fig. 21)

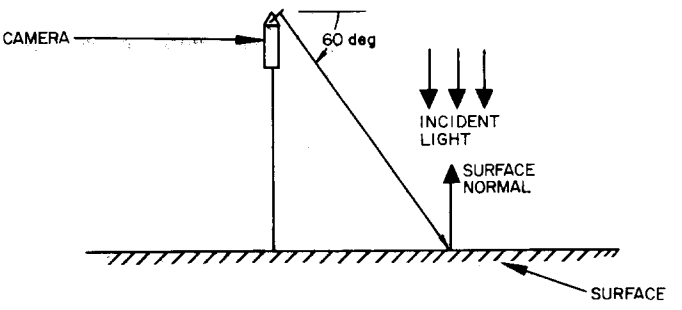

Fig. 20. Camera orientation with respect to nominal lunar surface

UNCLASSIFIED

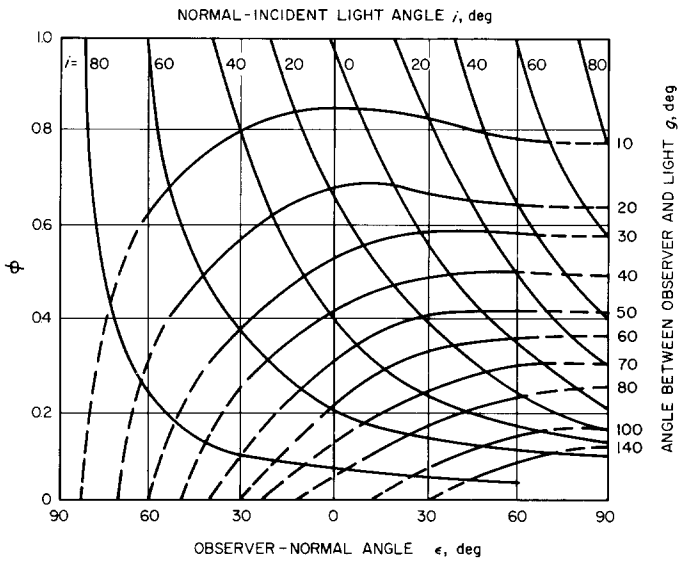

Fig. 21. Characteristics of lunar photometric function ϕ

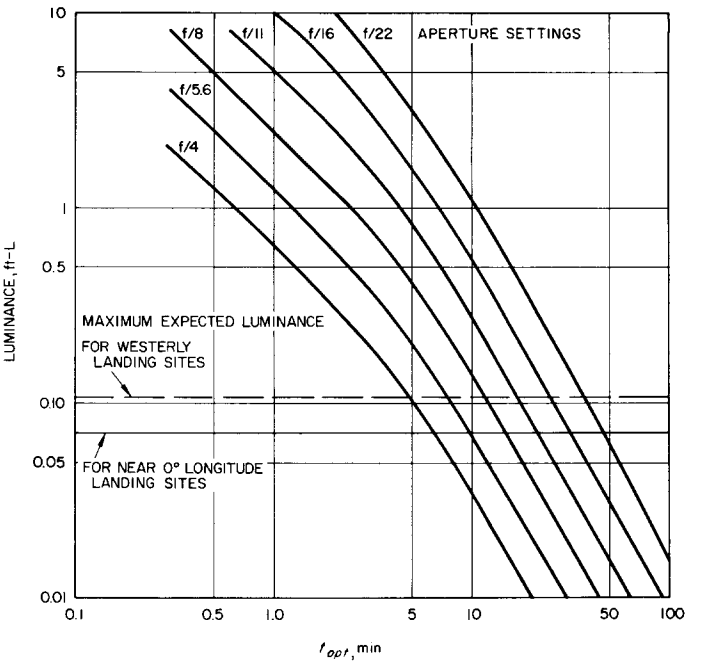

Fig. 22. Optimum integration time t_{opt} vs luminance (normal mode)

indicates that 58% of the total surface output will be reflected toward the camera if the incoming light is directly overhead, as is the case for near-0-deg longitude landings.

The luminance of the lunar surface as seen by the camera is $B_{max} = 0.12 \times 0.58 = 0.07$ ft-L based on a full Earth illuminating the lunar surface, and near-0-deg longitude landings.

d. Landing site selection. The selection of a landing site for night landing operations using earthshine can influence the maximum expected illumination levels (Fig. 22). The photometric function of the lunar surface (Fig. 21) indicates that it is possible to achieve a $\phi = 1$ if $g = 0$ deg. This implies that the incident light strikes the lunar surface along the line of sight of the camera. The maximum camera depression angle is 60 deg, which gives a minimum value of $\epsilon = 30$ deg for Fig. 21. Thus i_{min} is also 30 deg to produce $\phi = 1$. This could be accomplished by choosing westerly landing sites with a minimum longitude of 30°W. Landing sites west of 30 deg and up to 60 deg are suitable to produce large ϕ. Fig. 23 depicts the photometric function plotted in the camera azimuth plane for i to 40 and 60 deg, respectively. As can be seen in these plots, local areas of relatively high ϕ are found close inboard to the spacecraft.

e. Variation in Earth luminance. Landing windows (Ref. 4) have been plotted in Fig. 24, along with the relative luminance of the Earth[3] (Ref. 5). The landing windows at the ends of November and December 1965 are excellent for earthshine illumination conditions. Fig. 24 indicates that illumination levels less than 10% of full Earth are in most landing windows not meaningful, and the onset of lunar day takes place somewhere between 22 and 6% of full Earth for longitudes between 0 and 45°W. The average value of the onset of lunar day then is at 14% of full Earth, which is the approximate onset of lunar day at 40°W longitude. The following analysis is concerned with the capability of the camera to operate satisfactorily with levels of illumination from full Earth to 14% of full Earth, i.e., $0.017 \leq B \leq 0.12$ ft-L.

Normal mode TV.

Shuttered mode. The sensitivity S (that value of illuminance that causes vidicon saturation) of the SC-1 vidicon, is between 0.1 and 0.2 ft-c-sec for the normal mode and 150-msec exposure time. The required number of foot-lamberts input to the camera for a fully exposed picture at an aperture of $f/4$ is

$$B = \frac{4S\,(f/lb)^2}{T_e \Delta t}$$

[3]Lunlit program output of JPL ephemeris tape for the periods from January 1, 1965 to February 1, 1968.

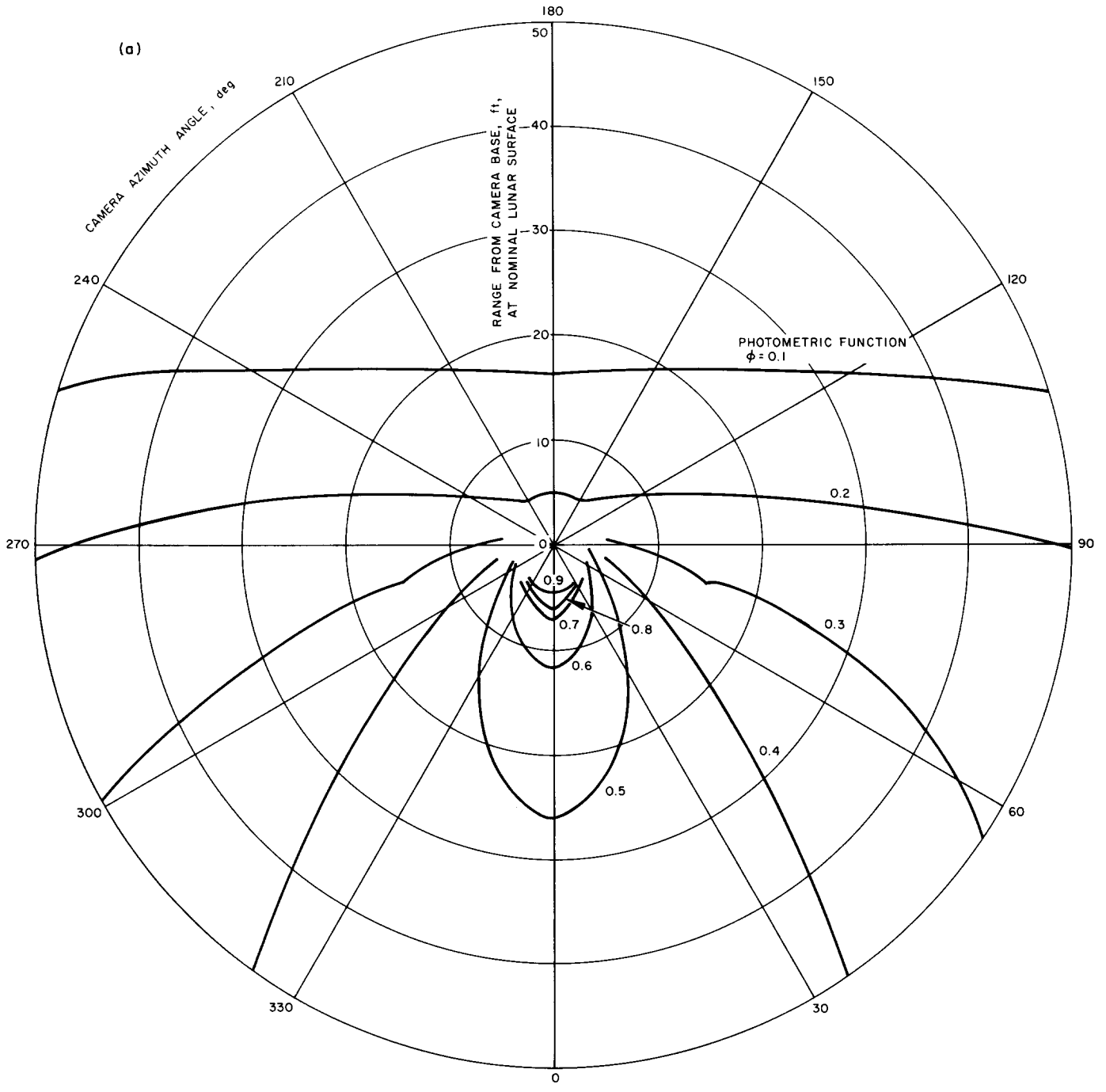

Fig. 23a. Photometric function ϕ plotted in spacecraft azimuth plane (i = 40 deg)

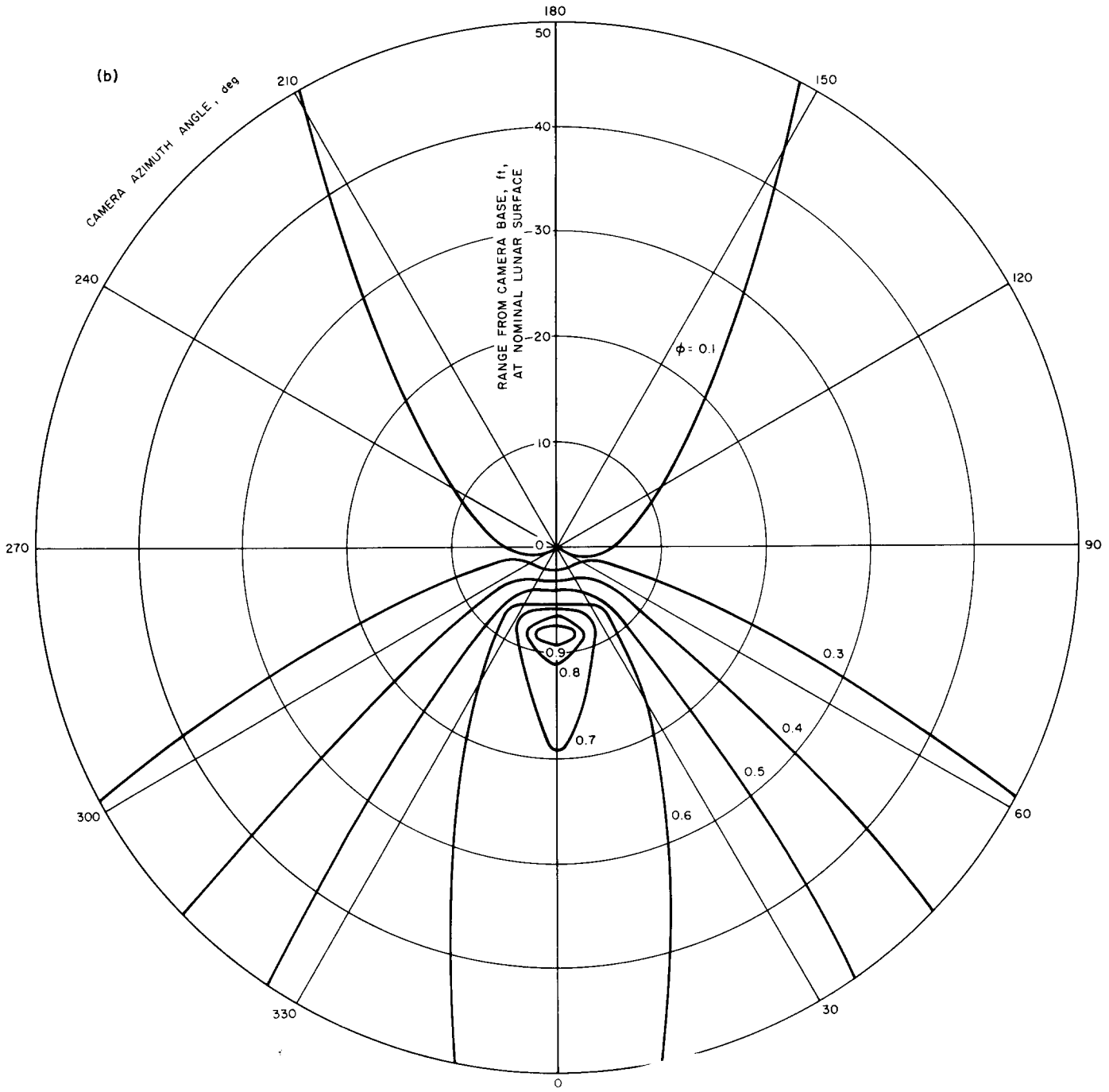

Fig. 23b. Photometric function ϕ plotted in spacecraft azimuth plane ($\dot{s}$ = 60 deg)

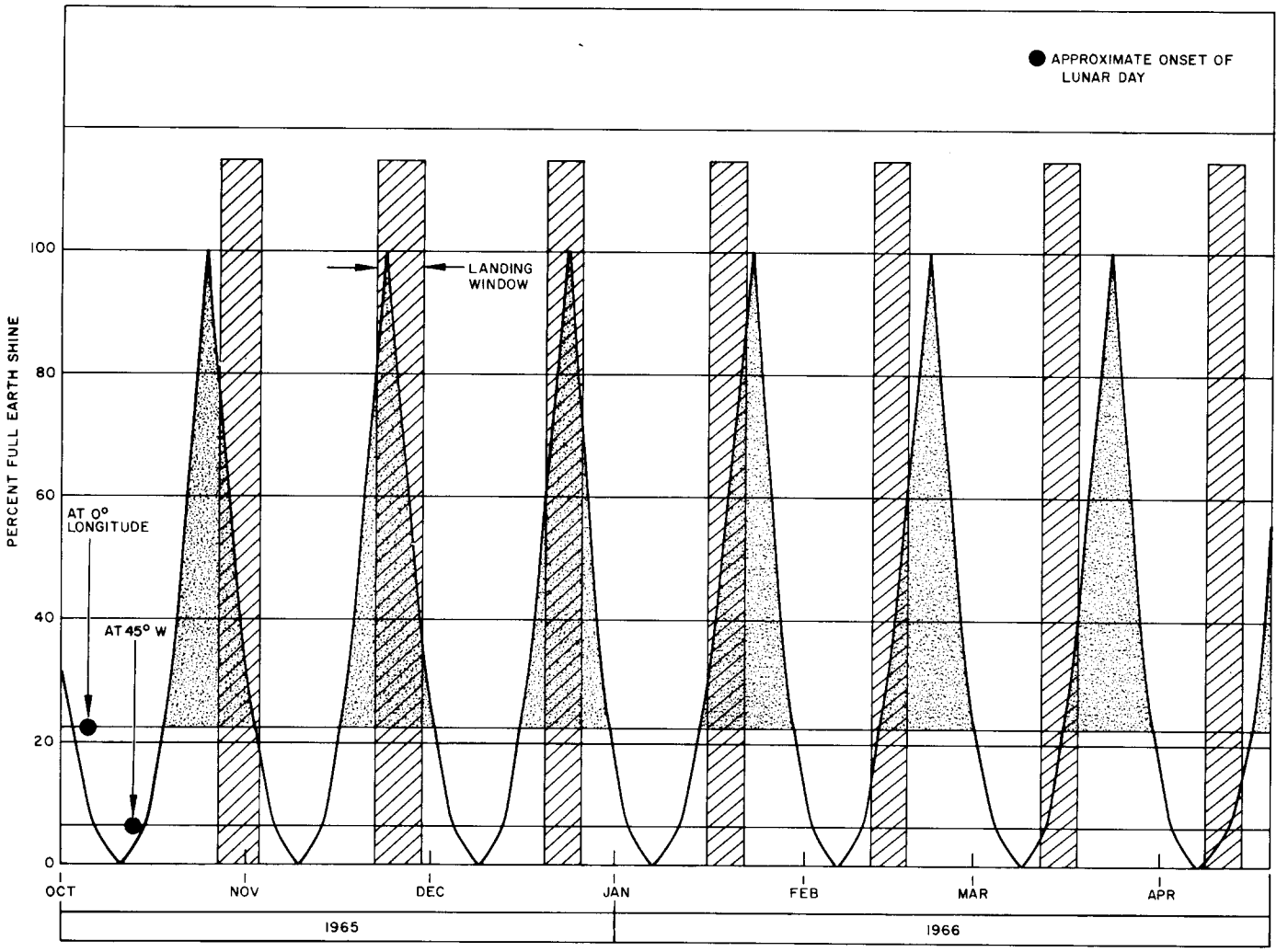

Fig. 24. Percent full Earth shine and landing windows (Oct.–Dec. 1965; Jan.–Apr. 1966)

where

B = surface luminance, ft-L

T_c = camera optical transmission coefficient = 0.5

Δt = exposure time

(f/lb) = 4, 5.6, 8, 11, 16, or 22

S = camera sensitivity, ft-c-sec

Thus

$$B_{min} = \frac{4 \times 0.2(4)^2}{(0.5)\,(150 \times 10^{-3})} \cong 170 \text{ ft-L}$$

which is about 2000 times the expected maximum luminance.

Open shutter. In the open shutter mode an exposure time of 1.2 sec yields an effective gain of approximately 11 in luminance. Thus the maximum luminance in this open mode is $B'_{min} = 170/11 = 15.5$ ft-L for a fully exposed picture, with a signal-to-noise ratio of approximately 36 db, peak-to-peak signal to rms noise. However, it is possible to underexpose a picture by approximately 3 f/stops and achieve an acceptable picture with a S/N of 18 db. Thus, $B'_{min} = 15.5/2^3 = 1.94$ ft-L. This is approximately 30 times greater than the expected maximum luminance.

Vidicon beam current blanking. The vidicon beam current could be inhibited in the open shutter mode; the effects of this change would be to increase the effective exposure time. However, since the beam current is blanked, the vidicon faceplate charges toward a positive potential independent of incident light. When the faceplate reaches the faceplate supply potential, the vidicon is saturated. Tests conducted by JPL on the 4.2.2 camera

have shown that saturation of the faceplate takes place in 10 min, for the case of no illumination on the faceplate. However, tests conducted for this study with a Hughes TV Laboratory camera using GEC vidicon SN 024421 indicates that a period of 20 min is required to notice a white level shift, and this does not appreciably affect the camera capability in the blanked beam current mode for the time periods required to obtain pictures of the lunar surface in earthlight. It is not presently known whether the saturation time is a function of individual vidicon tubes or of test conditions. Likewise, excessive spreading of pictorial elements due to the leakage between pictorial elements was noticed at JPL, but did not occur during the Hughes tests.

Open shutter—blanked vidicon current. The required exposure time to view the lunar surface, with $B = 0.07$ ft-L is, for the TV laboratory camera,

$$\Delta t = \frac{4S(f/lb)^2}{T_c B} = \frac{4 \times 0.1 \times (4)^2}{0.5 \times 0.07} = 183 \text{ sec} = 3.4 \text{ min}$$

However, the above computed exposure time fails to produce a usable TV picture. Fig. 22 indicates that 6.5 min are required to produce the optimum picture under these conditions. The above relationship fails to relate camera parameters in the blanked vidicon beam current mode. The optimum picture is that which produces the maximum signal-to-noise ratio. The curves of Fig. 22 were developed from test information obtained with a breadboard camera with an $S = 0.1$ ft-c-sec.

Using the experimental data of Fig. 22, a function P_N was determined to modify the normal exposure time so that good signal-to-noise ratio pictures can be obtained. Fig. 25 shows P_N versus B. The modified camera equation developed from the figure is

$$t_{opt} = \frac{4S(f/lb)^2}{T_c B}(3.88 + 1.5 \log B)$$

Blanked vidicon beam tests—normal mode. The Hughes tests were conducted under carefully controlled laboratory conditions to reduce the amount of stray light striking the test target or getting directly into the camera lens. No illuminating sources were permitted within the test area, and a black cloth shroud formed a complete tunnel-like cover between the camera lens and the test chart mounted in the light box. Illumination of the test chart was varied by using neutral density filters. Further variations in illumination on the vidicon faceplate were achieved by adjusting the camera lens T-stop setting. The illumination levels were determined by using a spot photometer pointed at the transparent center. A blue

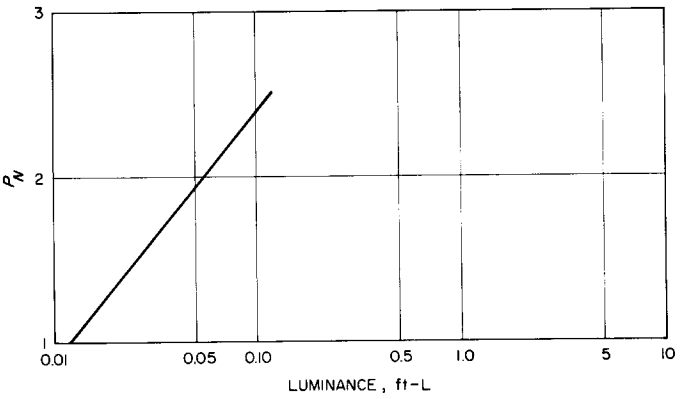

Fig. 25. Normal mode factor P_N vs luminance

80C filter was placed over the lens and photometer to achieve a 5000°K color temperature from the target. The test chart consisted of a wide black border with a transparent central portion. In the center of the transparent section was a bar chart with a 450 TV-line frequency.

The test data indicate that in the normal mode the camera can operate down in camera light levels equal to 0.012 ft-L, which corresponds to earthshine equal to 0.0207 ft-L or 17.3% of full Earth at 0-deg longitude, or 12.2% of full Earth with $\phi = 0.9$, and yield pictures of acceptable signal-to-noise ratio as shown in Fig. 17.

Emergency mode TV. Because of problems associated with establishing the antenna alignment necessary for normal mode TV, investigation of the possibilities of using the emergency-mode narrow-band TV to accomplish the task of lunar surface observations by earthshine was carried out. This TV mode uses the omni-antennas.

Open shutter mode. The readout time of each frame is 20 sec, with an additional 600 msec for a vertical blanking pulse. Thus the time between reading out a picture element is 20.6 sec. Using the camera equation, the minimum number of foot lamberts viewable of $f/4$ under these conditions is

$$B_{min} = K\frac{4 \times 0.2(4)^2}{0.5 \times 20.6} = 1.24\,K \text{ ft-L}$$

where K is the sensitivity factor.

The sensitivity factor takes into account the reduction in signal current due to the reduced rate at which the stored charge is read out. In this case, K can be found from the ratio of normal mode signal current to emergency mode signal current, i.e.,

$$K = \frac{i_n}{i_e} = \frac{dQ_N/dt_N}{dQ_E/dt_E} = \frac{dQ_N}{dQ_E} \times \frac{dt_E}{dt_N}$$

Since approximately the same amount of charge is found in both modes in a given frame,

$$K = \frac{dt_E}{dt_N} = \frac{20}{1} = 20$$

However, in actual vidicons the reduction in sensitivity in emergency mode is not so severe. The value of K in practice is found to be approximately 15. This variation from the theoretical is probably because in the emergency mode the scanning beam does not overlap adjacent lines as much as in the normal mode and hence less partial erasure of adjacent lines is encountered. The required luminance is

$$B_{E_{min}} = 1.24 \times 15 = 18.65 \text{ ft-L}$$

which is approximately 270 times the expected maximum luminance.

Open shutter—blanked vidicon current. Using a camera equation to calculate the required integration time for 0.07 ft-L yields at $f/4$, with the laboratory camera,

$$\Delta t = \frac{4S(f/4)^2}{T_e B} K = \frac{4 \times 0.1 \times (4)^2}{0.5 \times 0.07} \times 15$$

$$= 2850 \text{ sec} = 51 \text{ min}$$

Fig. 26 indicates that t_{opt} is 14 min; thus the camera equation must also be modified in the emergency mode.

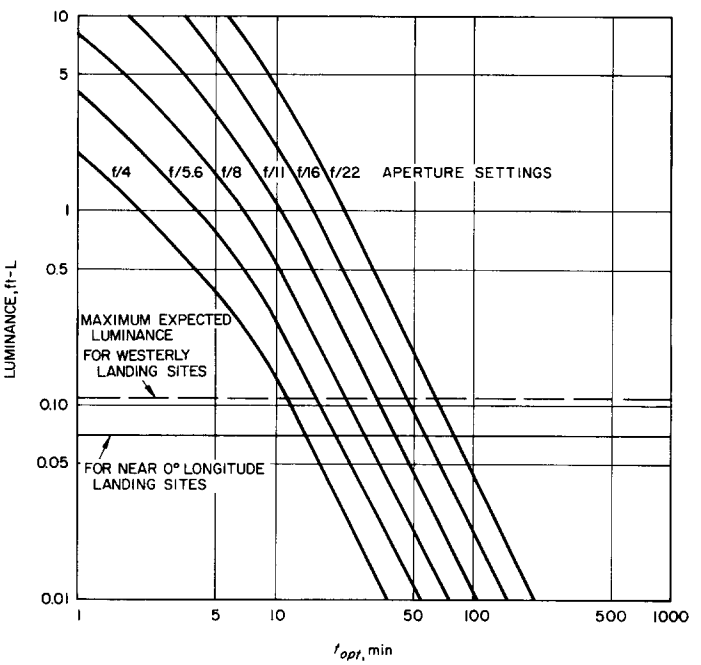

Fig. 26. Optimum integration time t_{opt} vs luminance (emergency mode)

Applying a similar approach used in the normal mode of comparing t_{opt} with ΔT to find P_E, i.e.,

$$P_E = \frac{t_{opt}}{t}$$

Fig. 27 shows P_E as a function of illumination. This relation can be expressed by the equation

$$t_{opt} = \frac{4S(f/lb)^2}{T_c B} (0.143 + 0.316 \log B)$$

Blanked vidicon beam tests—emergency mode. Similar test targets were used for emergency mode tests with the bar line frequency equal to 200 lines. Fig. 26 depicts

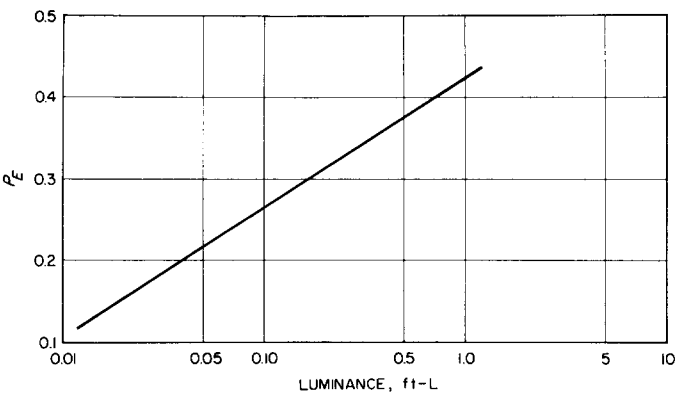

Fig. 27. Emergency mode time factor P_E vs luminance

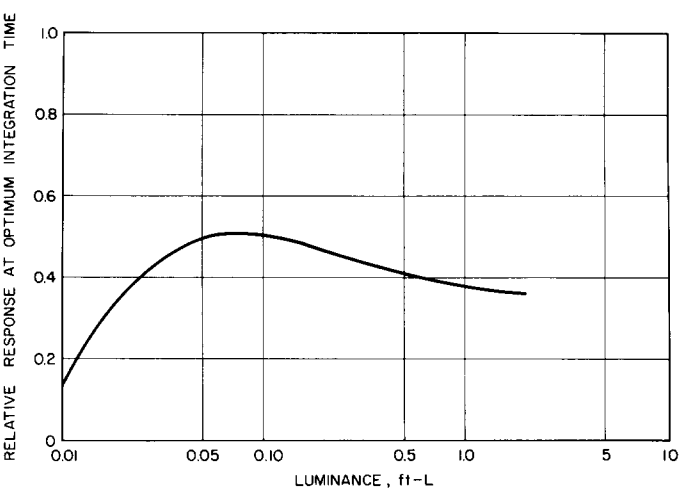

Fig. 28. Relative response to 200 lines vs luminance (emergency mode)

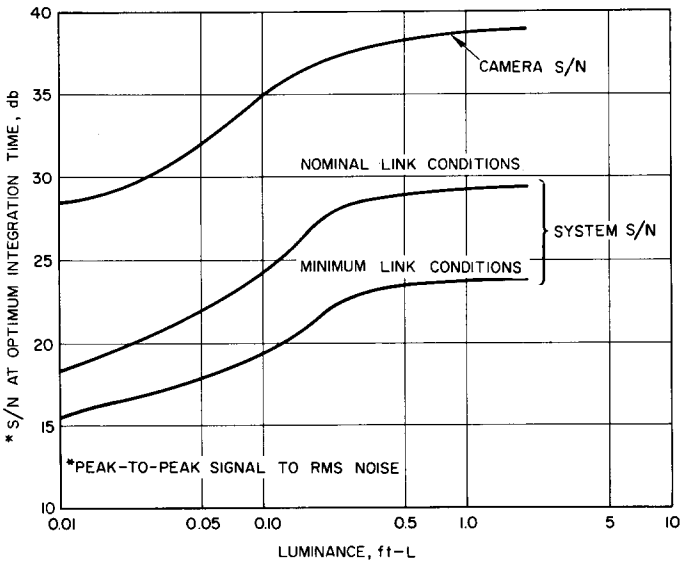

Fig. 29. Signal-to-noise ratio vs luminance (emergency mode)

the optimum integration time t_{opt} derived from test cases. The relative response is shown in Fig. 28, and the calculated camera signal-to-noise ratio in Fig. 29. The rms value of the noise, from the test data, was found to be 25 mv. The system signal-to-noise ratio is also shown for the cases of measured normal and minimum link conditions.

Quality of emergency-mode pictures. Fig. 29 indicates that the S/N of the received TV pictures ranges from 18.5 to 29.25 db for nominal link conditions, and from 15.5 to 23.5 db for minimum link conditions. Thus, under worst-case conditions (15.5 db) a TV picture of satisfactory quality can be obtained of the lunar surface. By appropriate postmission filtering, an additional 2 to 3 db can be gained for emergency mode pictures. By a judicious choice of landing window, one could expect to obtain emergency mode TV of 20 db under measured link conditions. Fig. 30 presents RETMA chart photos taken at low illumination levels. These photos show shading across the format. Although some degree of shading is present in TV pictures even under the best of conditions, the shading depicted here exceeds the allowable amount under normal light levels. The vidicon photo conductor anomalies are evidently exaggerated under these low light-level conditions. Several pictures at slightly different integration times, of course, could be taken of the same scene to produce a single photo with greatly reduced shading and noise. Another approach to reduce shading would be to calibrate the shading effects prior to launch.

7. Gyro Drift Error Compensation for Terminal Attitude Maneuvers

A computer program, Subroutine Drift, has been written which simulates the terminal attitude maneuvers and gyro drift rates. The basic output of the program is the alignment error of the spacecraft $+z$-axis to the desired thrusting direction at main retro ignition as produced by the gyro drift rates. This subroutine is used in the terminal command generation program to obtain terminal attitude maneuvers which compensate for the gyro drift errors. The usefulness of this gyro drift compensation scheme depends on two constraining factors. The subroutine accepts as inputs the gyro drift rates and directions about all axes of the spacecraft, which are assumed to be known at the time the terminal attitude maneuvers are initiated. Hence it is necessary to know the drift rate statistics at the time of the attitude maneuvers. The gyro drift error compensation scheme also depends on the assumption that the time between the completion of a given maneuver and the initiation of the next maneuver is determined and held constant. Consequently, the terminal attitude maneuver sequence must be held fixed with respect to these times; otherwise the computed attitude maneuvers which have been compensated for known gyro drift rates will be inaccurate.

a. Description of Subroutine Drift. The program accepts as inputs the gyro drift rates and directions about all axes of the spacecraft. The simulation is effected in the following manner: the spacecraft is rotated a small incremental angle about a chosen axis, which depends on the particular maneuver under consideration. The time to effect this incremental rotation is determined and the drift error during this time is simulated by appropriate rotations about the roll, pitch, and yaw axes. The small rotation angles about these axes are determined by the drift rates and directions and the time previously determined. This loop is repeated until the spacecraft has been rotated through the first part of the maneuver triad, e.g., the roll of a roll, pitch, roll maneuver. An input constant defines the time between the completion of the first maneuver of the maneuver triad and the beginning of the second. The gyro drift error obtained during this time is simulated by repeated small angle rotations about the spacecraft axes until the accumulated time associated with these rotations is equal to the total time between the first and second maneuvers of the maneuvers triad. The second and third maneuvers are simulated in like manner. For maneuvers in which sun lock is held—e.g., during the first roll of a roll, pitch, roll maneuver—the program (by means of an input) sets to zero the drift rates about the appropriate axes during the time Sun lock is maintained.

UNCLASSIFIED

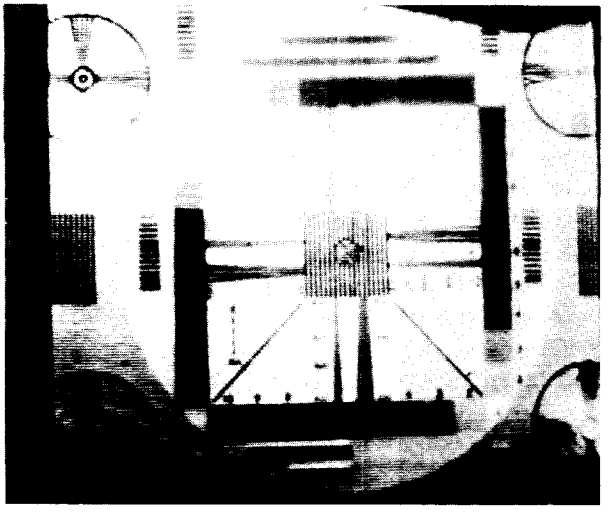

1. LUMINANCE = 0.4 ft-L
2. TRANSMISSION STOP, T8
3. INTEGRATION TIME, 6 min

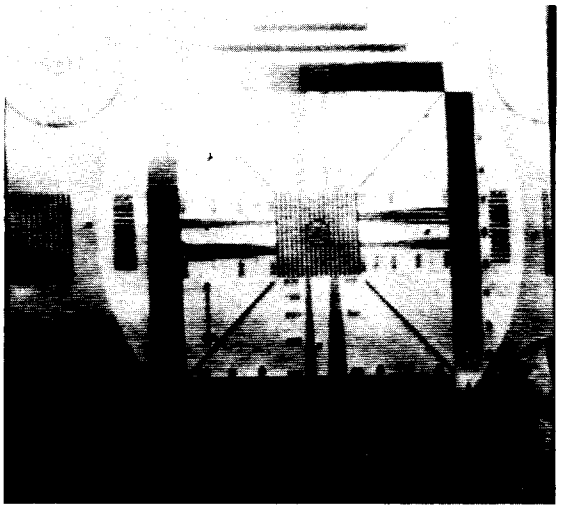

1. 0.05 ft-L
2. T8
3. 24 min

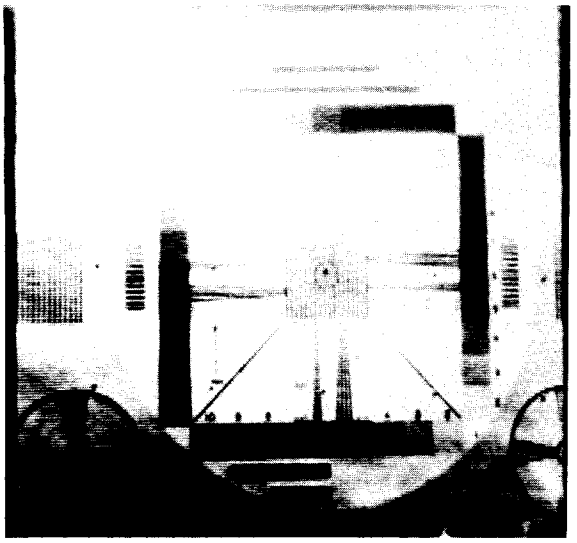

1. 0.375 ft-L
2. T16
3. 18 min

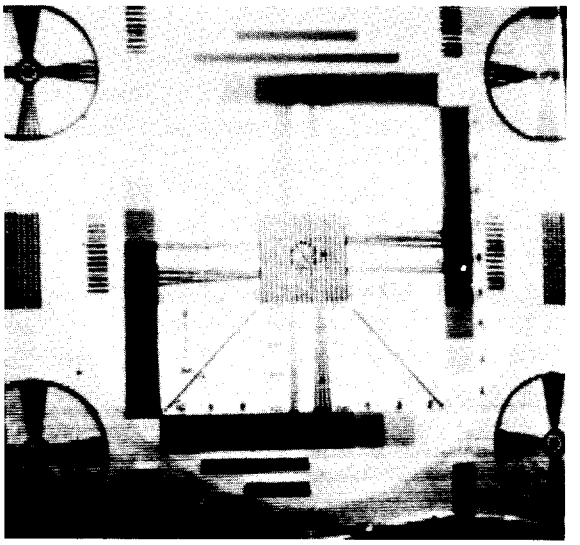

1. 4 ft-L
2. T8
3. 40 sec

Fig. 30. Emergency mode RETMA charts

After the complete maneuver has been simulated, the angle (*ANGD*) between the spacecraft $+z$-axis, and the desired thrusting direction is determined. An error vector ($\overline{DTH}$) is computed. This is simply the nominal thrusting direction ($\overline{TH}$) differenced by the spacecraft $+z$-axis direction after maneuver simulation.

b. Use of Subroutine Drift in terminal command generation program. A given set of "drift compensated" maneuvers is obtained in the following manner using a roll, pitch, roll (*RPR*) maneuver for illustration: A nominal *RPR* maneuver is computed which aligns the spacecraft $+z$-axis to the desired thrusting direction, assuming

UNCLASSIFIED

no gyro drift errors present. Using Subroutine Drift this maneuver is simulated, based on input gyro drift values. The angle *ANGD* is computed and if it is less than some input error threshold value, the nominal *RPR* maneuver will suffice to effect the desired spacecraft $+z$-axis alignment accuracy when gyro drift errors are considered. If *ANGD* is greater than the constraint value, a new "pseudo" thrusting direction equal to the previous thrust vector plus the error vector $\overline{DTH}$ is calculated. A nominal *RPR* maneuver is again calculated which aligns the spacecraft $+z$-axis to the new thrusting direction. Again the maneuver is simulated using Subroutine Drift and a new value for *ANGD* is computed. If the constraint on the value of *ANGD* is satisfied, the new computed *RPR* maneuver will effect correct alignment of the spacecraft $+z$-axis to within the input error threshold value. If not, the loop is repeated until *ANGD* does satisfy the constraint. The last computed *RPR* maneuver will then be the "drift-compensated" maneuver.

Mathematically, the iteration is given by the following relations:

$$\overline{TH}_{i+1} = \overline{TH}_i + \overline{DTH} \qquad i = 1, 2, \cdots,$$

$$\overline{DTH} = \overline{TH} - \overline{Z}$$

$$ANGD = \sin^{-1} \left| \overline{TH} \times Z \right|$$

where $\overline{TH}$ = the unit vector in desired thrusting direction, $\overline{TH}_i$ = the "pseudo" thrusting direction calculated in iteration, Z = the unit vector in direction of spacecraft $+z$-axis after maneuver simulation by Subroutine Drift, and $\overline{TH}_i = \overline{TH}$

A flow diagram describing the essentials of how Subroutine Drift is used in the terminal command generation program is given in Fig. 31.

8. Atlas/Centaur Surveyor Boost Simulation

Surveyor trajectory design is performed at Hughes Aircraft Company using a boost model fitted from sets of injection conditions obtained from General Dynamics/Convair (GD/C). If a change is made to the booster or its constraints a considerable time elapses before the new sets of data are available. In order to reduce this delay, and to provide a better understanding of the relationship between booster parameters and injection conditions, an effort has been made to develop a simple model which can provide trajectory characteristics of importance to *Surveyor*.

The first step toward this goal was to develop a fast, accurate boost simulation. This has been achieved with considerable success. An existing computer program has

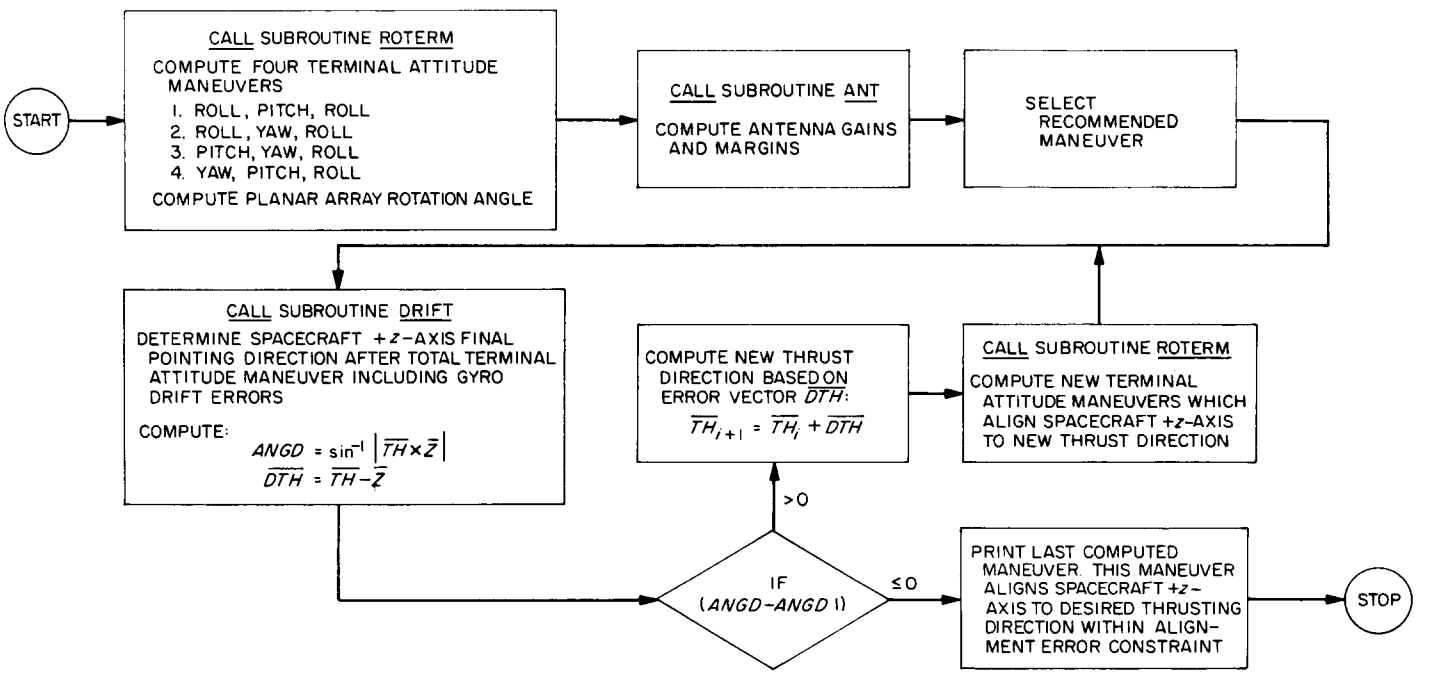
START
CALL SUBROUTINE ROTERM
COMPUTE FOUR TERMINAL ATTITUDE MANEUVERS
1. ROLL, PITCH, ROLL
2. ROLL, YAW, ROLL
3. PITCH, YAW, ROLL
4. YAW, PITCH, ROLL
COMPUTE PLANAR ARRAY ROTATION ANGLE
CALL SUBROUTINE ANT
COMPUTE ANTENNA GAINS AND MARGINS
SELECT RECOMMENDED MANEUVER
CALL SUBROUTINE DRIFT
DETERMINE SPACECRAFT +z-AXIS FINAL POINTING DIRECTION AFTER TOTAL TERMINAL ATTITUDE MANEUVER INCLUDING GYRO DRIFT ERRORS
COMPUTE:
ANGD = sin⁻¹ |TH×Z|
DTH = TH−Z
COMPUTE NEW THRUST DIRECTION BASED ON ERROR VECTOR DTH:
TH_{i+1} = TH_i + DTH
CALL SUBROUTINE ROTERM
COMPUTE NEW TERMINAL ATTITUDE MANEUVERS WHICH ALIGN SPACECRAFT +z-AXIS TO NEW THRUST DIRECTION
>0
IF (ANGD−ANGD i)
≤0
PRINT LAST COMPUTED MANEUVER. THIS MANEUVER ALIGNS SPACECRAFT +z-AXIS TO DESIRED THRUSTING DIRECTION WITHIN ALIGNMENT ERROR CONSTRAINT
STOP

Fig. 31. Terminal command generation program flow diagram

UNCLASSIFIED

been modified and refined to cater especially to the *Surveyor* boost phase. This simulation for the IBM 7094 can duplicate a sample GD/C trajectory within a maximum error in injection energy C_3 of 0.005 km²/sec², corresponding to about a 0.2-m/scc error in injection velocity, a 1.0-m/sec midcourse correction, and a 200-km miss at the Moon. Fractional errors in other injection parameters are even smaller. The program can run a case in 4 sec.

The next, and far more challenging step, was to predict the results of a change in the booster system. This was complicated by the fact that at the same time GD/C initiated use of the closed-loop guidance equations which will actually be used for the mission in their trajectory evaluations. These equations involve ten basic constants instead of the four originally used. This change resulted in a cessation of effort to exactly duplicate the GD/C trajectories using their choice of independent variables. Instead, it was decided to retain the four open-loop pitch variables which had been used in the first phase of the study (three pitch rates and total burn time), and attempt to match the GD/C closed ground traces with a yaw steering function involving a minimum number of new variables. This has been done successfully at the expense of two new variables. Thus sets of injection conditions may be obtained as functions of the seven basic independent variables: launch azimuth, three pitch rates, two yaw rates, and total burn time.

In summary, a simulation matching GD/C closed-loop trajectories has been accomplished and is available if difficulties arise in the use of the model fitted from *Centaur* trajectory data.

9. Six-Degree-of-Freedom Terminal Descent Digital Simulation

A six-degree-of-freedom digital simulation program for the terminal descent phase has been completed and checked out. The program is useful primarily for detailed design verification purposes and is presently being used in this capacity. It is also intended for use in postmission terminal descent spacecraft and trajectory analysis.

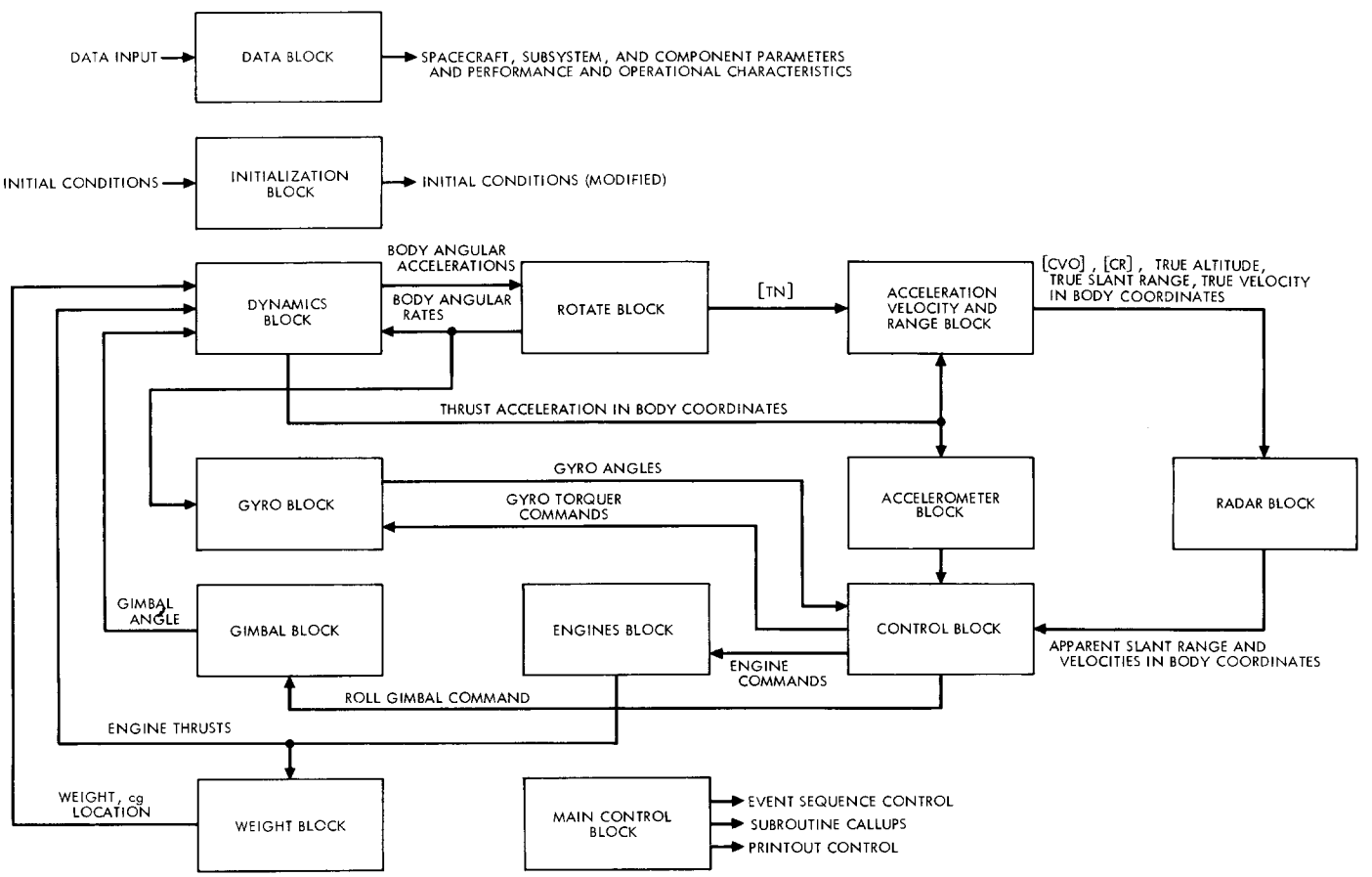

Fig. 32. Computational loop diagram

UNCLASSIFIED

The program is partitioned into subroutines, each major subroutine representing one of the blocks in the computational loop indicated in Fig. 32. The three auxiliary blocks shown in the diagram are:

(1) *Data block:* This block accepts basic input data such as spacecraft geometry, RADVS antenna-beamwidths, lunar reflectivity, control system gains and time constants, gimbal servo rate limits, main-retro thrust-time histories, etc., and these quantities are stored in memory so that they are available when required by the subroutines. Various spacecraft, subsystem, and component anomalies are also introduced through this block. These anomalies include such items as initial cg offset, RADVS antenna misalignments, RADVS tracker bias errors, RADVS db degradation, flight control sensor parameter variations, gyro torquer scale factor errors, vernier thrust gain variations, etc.

(2) *Initialization block:* This block accepts basic input initial conditions (body Euler angles, spherical position coordinates, velocity magnitude and direction relative to body coordinates) and converts these quantities into forms usable by the remaining blocks (initial direction cosines, inertial velocities and positions in rectangular coordinates, etc.).

(3) *Main control block:* The block provides primary control of the program, as shown in the diagram. By proper keying and providing the correct initial conditions, the terminal descent simulation can be started (and stopped) at any arbitrary point from vernier engine ignition to touchdown.

The basic computational loop shown in Fig. 32 is straightforward and the primary inputs and outputs of the subroutines, or blocks, are easily identified. Some program characteristics not evident in the diagram are described below:

(1) *Dynamic blocks:* The spacecraft inertia sensor is computed within this block. In the computation of the inertias and of the thrust and angular acceleration components, rigid body dynamics are assumed.

(2) *Rotate block:* The output [TN] is the coordinate transformation matrix between a Moon-centered inertial coordinate system and the spacecraft axes.

(3) *AVR block:* The basic thrust acceleration in body coordinates is transformed within this block to acceleration expressed in inertial coordinates. Velocity and range are derived and expressed in both inertial and spacecraft coordinates. A nonrotating Moon with constant gravitational acceleration (i.e., altitudes independent) is assumed. Various coordinate transformations relating the inertial coordinates, body coordinates, local vertical direction, and velocity direction are computed within this block.

(4) *Radar block:* True velocity in body coordinates is transformed to components along the radar beam axes. An option is provided in this block to compute power received for each beam as a function of velocity along the beam, beam incidence angle, lunar reflectivity, and RADVS performance parameters to test for tracker lockon. If one or two velocity trackers are not in lock, the system (and program) will operate in the conditional reliable mode. Under these conditions, the apparent velocities output from this block may be significantly different from their corresponding true input values. Under fully reliable operate conditions, the apparent and true velocities will differ only slightly due to the effects of the RADVS lags.

(5) *Control block:* Flight control system time constants less than $\frac{1}{30}$ sec are not included. In all other respects, the equations for this block have been written to preserve as much as possible the steady-state and transient stability characteristics of the present control systems design.

(6) *Weight block:* The fuel weight losses of the tanks associated with each of the vernier engines is computed separately, and overall spacecraft cg wander is determined. Inert losses are also accounted for in this block.

10. Maneuver Analysis Premission Data Program

An IBM 7094 computer program, the maneuver analysis premission data program, has been developed to generate graphical information regarding the terminal descent phase of *Surveyor* flight. The machine-plotted data include the following:

(1) Altitude versus time, from retro ignition to retro burnout.

(2) Velocity versus time, from retro ignition to retro burnout.

(3) Main retro thrust versus time.

UNCLASSIFIED

(4) Range versus velocity, from retro burnout to spacecraft touchdown, including burnout dispersion ellipses, descent segments, and radar constraints.

(5) Vernier engine specific impulse versus thrust.

(6) Retro burnout velocity versus unbraked impact velocity.

(7) Retro ignition altitude versus unbraked impact velocity.

(8) Propellant margin (reserve) versus unbraked impact velocity.

(9) Nominal vernier descent propellant consumption from retro burnout to touchdown versus unbraked impact velocity.

(10) Vernier propellant consumption dispersions versus retro burnout velocity.

The program is essentially the combination of two major subroutines, Parts A and B. Items 1, 2, and 4 above are generated in the former, and the remainder in the latter. (See Fig. 33 for program flow diagram.)

As can be seen from the flow diagram, Part A is composed of subroutines RETRO, VERN, KOVAR, LIPPS,

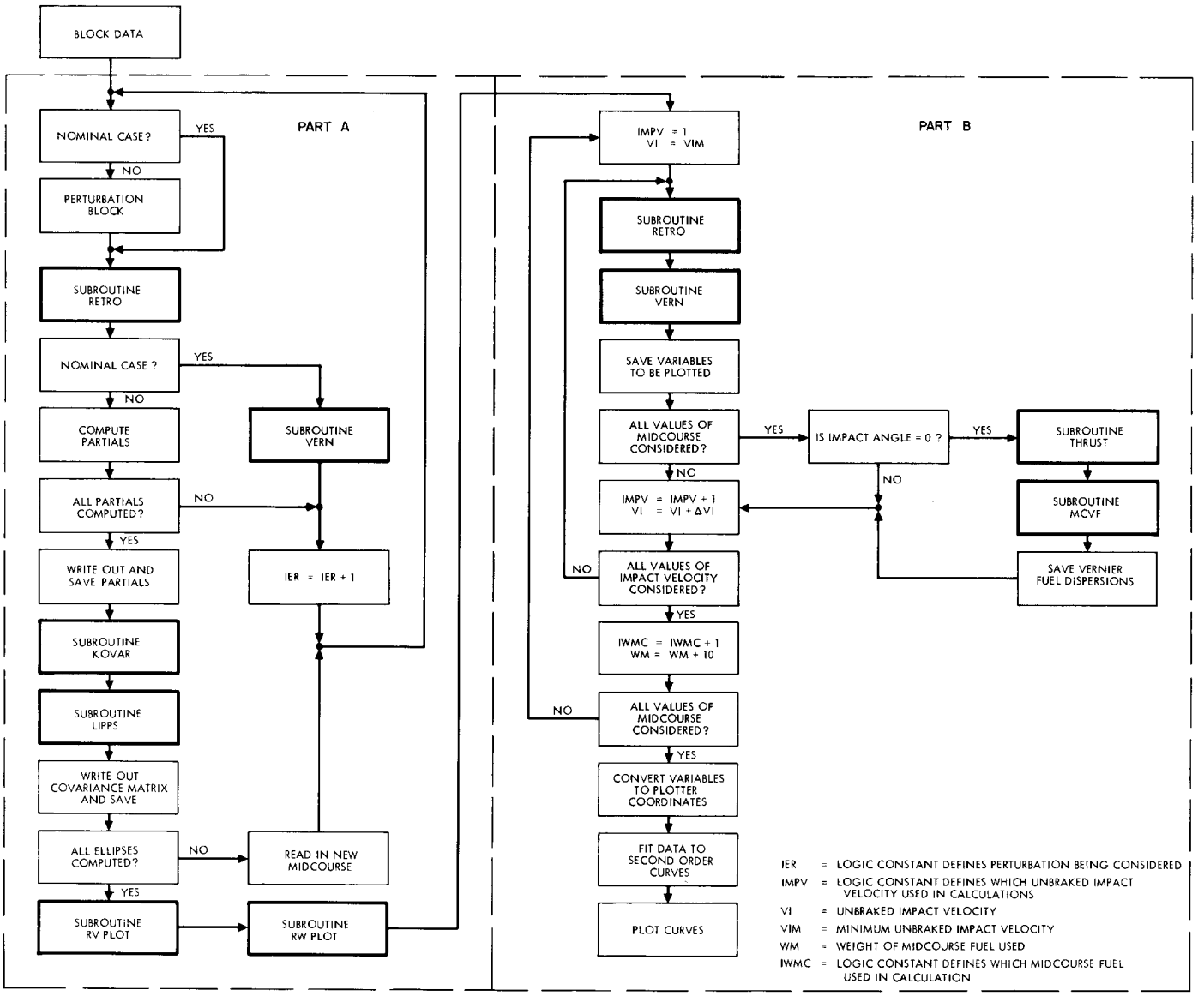

Fig. 33. Maneuver analysis permission data program flow diagram

UNCLASSIFIED

RVPLOT, and RWPLOT, plus linking logic and logic for computing partial derivatives of retro burnout conditions with respect to ignition conditions. The first two subroutines together form an integrating routine for the equations of motion for a 3-degree-of-freedom description of spacecraft motion during the terminal descent phase. Subroutine KOVAR computes the covariance matrix of main retro burnout range and velocity; conversion of the covariance matrix into burnout dispersion ellipses is effected in subroutine LIPPS. Subroutine RVPLOT generates the fourth plot above, while RWPLOT generates Items 1 and 2.

Part B is composed of subroutines RETRO, VERN, MCVF, THRUST, and GAUS 4, plus linking logic which effects the parameterization and plotting. MCVF is the Monte Carlo vernier fuel subroutine; THRUST computes average vernier thrust levels and specific impulse values to be used as inputs to MCVF. Subroutine GAUS 4 is a Gaussian random number generator used in MCVF.

11. Guidance and Maneuver Analyzer

A physical model has been designed and constructed which represents the *Surveyor* spacecraft and its associated flight geometry (Fig. 34). This model, known as the guidance and maneuver analyzer (GAMA), will be used to analyze the guidance and maneuver aspects of *Surveyor* flights during the missions, and is currently being used for development purposes and during premission tests. Although the model has immediate application to the *Surveyor* project, it may be used to analyze various phases of lunar and interplanetary missions in general. GAMA is an extension of a model being used at

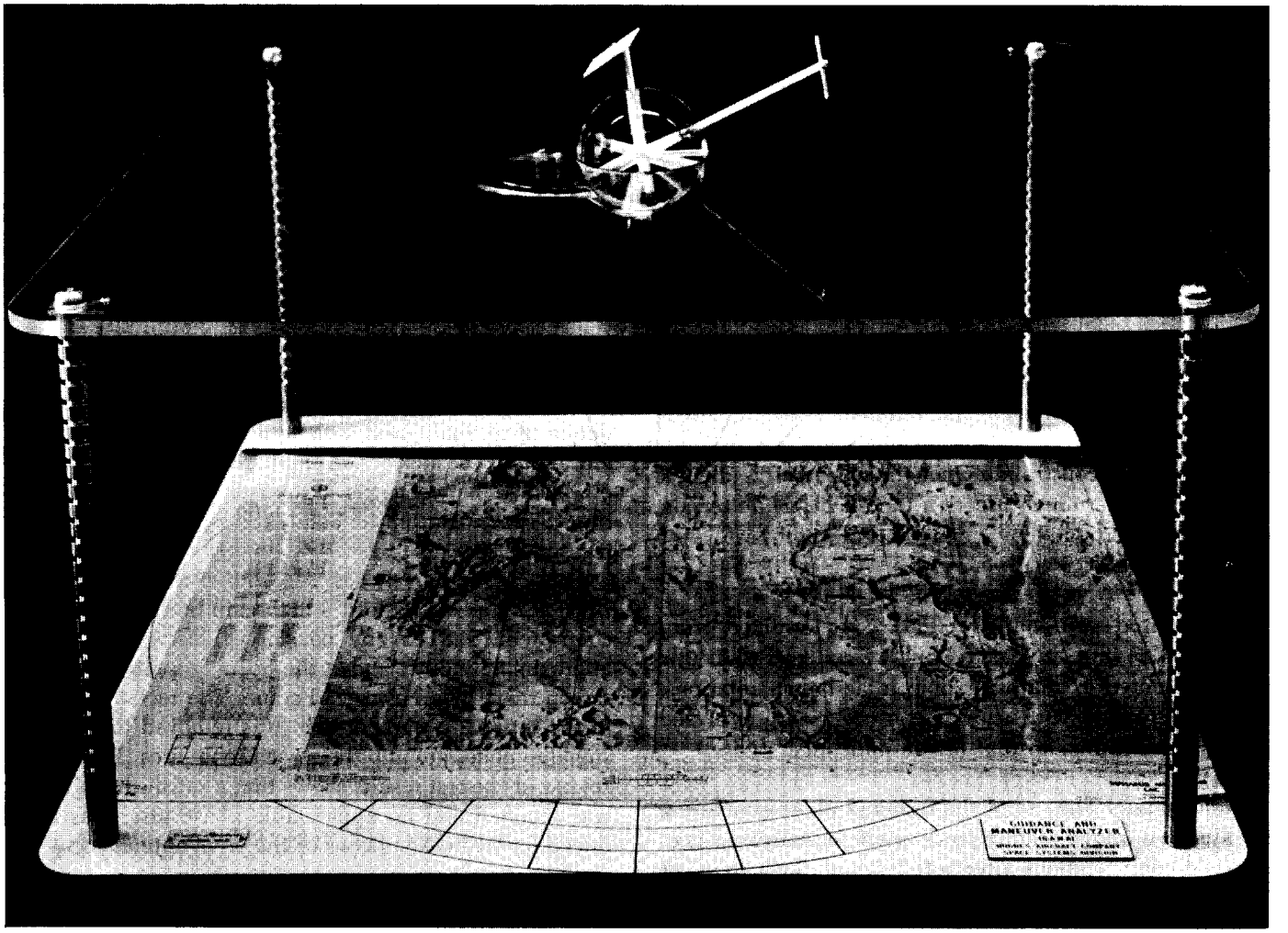

Fig. 34. Guidance and maneuver analyzer

UNCLASSIFIED

JPL (Ref. 7) modified to meet the needs of the *Surveyor* system.

a. Applications. The following applications entail a basic understanding of *Surveyor* midcourse and terminal guidance philosophy. (Ref. 8 is a convenient sourcebook.)

Midcourse phase. A velocity correction and set of spacecraft attitude maneuvers are computed during the midcourse phase of a *Surveyor* mission. In general, the maneuvers must satisfy various system constraints such as keeping the omnidirectional antenna being used pointed in the general direction of the Earth.

The velocity correction is constructed with GAMA in two steps. First, the critical plane velocity correction is constructed, based on knowledge of the initial miss and desired landing site. Next the "noncritical" component is derived from a consideration of the soft landing parameters and constructed with an appropriate scale.

Examination of the attitude maneuvers is begun by fixing the attitude of the sphere to represent the cruise mode of the spacecraft. It is convenient to measure the direction of the Sun, Earth, Canopus, and Moon in terms of angles with respect to the critical plane and noncritical direction. By using these angles, derived from trajectory computation, the protractor and boresight feature of the sphere can be used to mark points or position objects to represent the desired pointing directions.

Terminal phase. During the terminal phase of a *Surveyor* mission, the following items are of concern: cruise geometry, attitude maneuvers, terminal pointing direction, spacecraft-lunar surface geometry during descent, and geometrical constraints. Once the spacecraft is aligned to the desired terminal direction the effect of the terrain is quickly ascertained by using the boresight feature of the sphere.

The desired pointing direction, as determined from the unbraked impact velocity, and initial cruise attitude are represented as marks or objects and then rotations, and the interplay with various constraints are analyzed in a manner similar to that of the midcourse phase.

Lunar phase. The use of the terminal phase simulation as discussed above readily lends itself to analyzing geometrical considerations after soft landing. Such items as Sun and Earth position in spacecraft coordinates can be quickly estimated for purposes of positioning the solar panel and planar array.

Other applications. Various flyby situations can also be analyzed by using the terminal phase simulation. The TV coverage and quality along with attitude maneuvers can be quickly visualized and studied. Closely related to the flyby mission are the Lunar Orbiter and Apollo type missions; GAMA may be useful in studying various aspects of these and other lunar and interplanetary missions.

D. System Testing

1. T-21 Prototype Vehicle Tests

Data analysis effort during this period was directed toward preparation of the final T-21 system test reports. All of the results for the system functional test report have been compiled and included in the preliminary draft. The conclusions and recommendations section are being prepared. Tabulation of the test results for the vibration phase report is near completion. The results indicate that the vibration environment had little or no effect on the functional operation of the spacecraft.

2. SC-1 Flight Acceptance Tests

a. Mission sequence/electromagnetic interference tests (EMI). The last report period described two EMI tests performed on SC-1, completing a series of three tests. During this report period, data was analyzed and the phase report initiated. Also, a special RF link phase jitter test was performed. The objective of the test was to demonstrate that phase lock could be maintained during vibration of the spacecraft omni-antenna with an RF link established between the system test equipment assembly (STEA) transmitter and the spacecraft receiver-transmitter.

To accomplish this test a high-gain horn-type antenna, connected to STEA by coaxial cable, was suspended approximately 30 ft above the opening in the top of the screen room by an overhead crane. The rectangular door in the top of the screen room was removed to allow the signal to penetrate into the screen room area. Preliminary review of the test results shows that a satisfactory RF link was attained and no appreciable phase jitter was introduced for 5/16-in. excursions of the omni-antenna.

b. Vibration tests. Tables 9 and 10 summarize the vibration requirements and the operating sequence for the vibration test phase. Table 9 lists the vibration levels,

UNCLASSIFIED

Table 9. SC-1 vibration-phase flight acceptance test (FAT)

Test	Run Number	Axis of vibration	Sweep frequency	Sine level g peak	Random level g-rms	Test time, min	Octaves/ min	Run completed, date and hour
Low	1A	Longitudinal (z-axis)	5–100	0.25	None	4.25	1	Jun 11, 1965 15:40
FAT	2A	Longitudinal (z-axis)	5–50 50–100	1.5 1.33	None None	2.13	2 2	Jun 19, 1965 19:15
FAT	2B	Longitudinal (z-axis)	100–1500 1500–100	1.33 1.33	4.5 4.5	2.0 2.0	2 2	Jun 12, 1965 12:40
Low	3A	Lateral (along Leg 3)	5–100	0.25	None	4.25	1	Jun 13, 1965 11:52
FAT	4A	Lateral (along Leg 3)	5–50 50–100	0.7 1.33	None None	2.13	2 2	Jun 13, 1965 14:53
FAT	4B	Lateral (along Leg 3)	100–1500 1500–100	1.33 1.33	4.5 4.5	2.0 2.0	2 2	Jun 14, 1965 23:30
Low	5A	Lateral (normal to Leg 3)	5–100	0.25	None	4.25	1	Jun 20, 1965 09:28
FAT	6A	Lateral (normal to Leg 3)	5–50 50–100	0.7 1.33	None None	2.13	2 2	Jun 20, 1965 13:05
FAT	6B	Lateral (normal to Leg 3)	100–1500 1500–100	1.33 1.33	4.5 4.5	2.0 2.0	2 2	Jun 20, 1965 20:20

Table 10. Summary of vibration flight-acceptance-test sequence

(1) Functional test: a mission sequence EMI test performed as a substitution for the "Addends" tests of short system confidence check.

(2) Weight, balance, and alignment verification: these prerequisites performed at the optical dock during the EMI tests.

(3) Previbration alignment verification of TV cameras: performed with spacecraft mounted on vibration test fixture.

(4) z-axis vibration (prelaunch configuration established) with the following functional tests performed during vibration: FM mode—engineering interrogation; PM mode—phase jitter (telemetry hardline); transmitter frequency stability.

(5) Systems readiness test: postvibration, z-axis.

(6) Alignment check of TV cameras: postvibration, z-axis.

(7) Spacecraft mounted on lateral vibration fixture for vibration along Leg 3.

(8) Alignment of TV cameras: previbration, Lateral Axis 1.

(9) Lateral axis vibration (prelaunch configuration established) with the following tests performed during vibration: FM mode—engineering interrogation; PM mode—phase jitter (telemetry hardline); transmitter frequency stability.

(10) Systems readiness test: postvibration, Lateral Axis 1.

(11) Alignment check of TV cameras: postvibration, Lateral Axis 1.

(12) Spacecraft rotated on lateral fixture for vibration normal to Leg 3.

(13) Lateral axis vibration (prelaunch configuration established)[a] with the following tests performed during vibration: FM mode—engineering interrogation; PM mode—phase jitter (telemetry hardline); transmitter frequency stability.

(14) Systems readiness test: postvibration, Lateral Axis 2.

(15) Spacecraft rotated on lateral vibration test fixture (return to initial lateral axis position).

(16) Alignment check of TV cameras: postvibration, Lateral Axis 2.

(17) Short system confidence check: postvibration, conducted on the screen room test stand.

(18) System alignment verification: postvibration, performed at the optical dock.

[a] Flight compartment covers installed, squibs installed (except as noted), test access on Omni-antenna A and on auxiliary battery.

UNCLASSIFIED

test time, type of vibration, and date of test run for each axis of shake. Table 10 gives a broad summary of the steps followed to implement this test phase and the test procedures that apply to each step. The actual vibration runs were accomplished at the times listed in Table 9. In all cases, the actual vibration characteristics achieved were within specification requirements except for those deviations summarized in Table 11. These deviations were jointly assessed by Hughes and JPL during the operation as being acceptable and not requiring retest.

In each axis, sinusoidal vibration alone was used in test runs below 100 cps. Above 100 cps, to 1500 cps, sine plus random vibration was used. During test runs below 100 cps (Runs 1A, 2A, 3A, 4A, 5A, and 6A), the input level was maintained on the fixture immediately adjacent to a chosen spacecraft attachment point, except through certain frequency ranges where the vibration levels of the retro-motor case were limited to the nominal input level. This was accomplished through the Hughes Space Systems Laboratory developed SCAMP (selector, control, adjustable, multiple point). This device automatically switches the shaker control to that control accelerometer that at any instant of time experiences the largest response to shaker input excitation. Control accelerometer signals to the SCAMP included one accelerometer on the fixture and three accelerometers (in orthogonal axes) on the retro-motor case. Each SCAMP channel was set to take over control of power applied to the shaker at nominal specified vibration input level.

In vibration test runs above 100 cps (Runs 2B, 4B, and 6B) the retro-motor case was considered decoupled from the fixture, and recognizing the limited rigidity of the fixture, three control accelerometer signals were supplied to the SCAMP. Each control accelerometer was located on the fixture at a spacecraft attachment point.

A composite plot of the SCAMP input signals is therefore required to verify compliance with the vibration test specification. During these test runs, the SCAMP input accelerometer signals were filtered, using 50-cps bandwidth tracking filters. Random vibration level was established and maintained at one chosen control accelerometer.

Crosstalk, vibration normal to the input axis, was recorded during each run on the fixture at the spacecraft attachment points. Control accelerometer signals, safety limiting accelerometer signals (from the shaker armature acceleration limiter), signals from strain-gage confidence accelerometers, and signals from flight accelerometers installed in the spacecraft were recorded on magnetic tape for data reduction.

In following the test operation sequence outlined in Table 9, the summary of spacecraft anomalies occurring during the various subphases is presented in Table 12. A description of the various anomalies, when they occurred, and their disposition are related in this table.

c. Solar-thermal-vacuum test. All cables, test tees, etc, for the Hughes vacuum chamber have been fabricated. Thermocouples have been applied to the thermal model dummy retro. Cables for spacecraft external thermocouples have been cut and fitted. The ionization protective system designed to shut off spacecraft power in the event of major pressure changes has been installed. Auxiliary power in the event of a plant power failure will assist

Table 11. Summary of vibration test condition deviations

Run number	Type of test	Specification	Deviation
2A	Flight-acceptance level sine sweep, two axis	1.5 g from 5 to 50 cps; 1.33 g from 50 to 100 cps	Ran 1.5 g from 5 to 80 cps and 1.33 g from 80 to 100 cps
2B	Flight-acceptance combined sine/random, two axis	4.6-g rms random noise from 100 to 1500 cps (which with sharp cutoff at 100 and 1500 cps would be a noise density of 0.0145 g^2/cps)	4.6-g rms through a Krohnhite filter with cutoff at 0.2 and 1600 cps; gives a noise density of 0.011 g^2/cps
4B	Flight-acceptance combined sine/random, lateral axis along Leg 3	Random noise should be flat within 3 db between 100 and 1500 cps	At 700 cps, notch on Leg 3 accelerometer and peak on Legs 1 and 2 accelerometer were out of specification; total energy was probably in specification
6A	Flight-acceptance level sine sweep, lateral axis normal to Leg 3	g-level peak between 5 and 50 cps should be 0.7 g ± 10% (0.63 g minimum)	Because of instrumentation difficulties, actual levels turned out to be: 0.63g —5 to 8.2 cps; 0.61 g—8.2 to 9 cps; 0.68 g—9 to 50 cps

UNCLASSIFIED

chamber operation and provide limited power to the STEA for continuing spacecraft communication during this critical duration. Calibration of STEA (standard and special equipment) and solar beam mapping of the vacuum chamber have been accomplished.

It is presently planned to resume instrumentation on receipt of the spacecraft. This task will be completed approximately 11 days prior to pumpdown for Phases A and B.

d. Consent-to-ship tests. The SC-1 consent-to-ship test specification has been approved for release. Volume I of the supporting test plan books has been published. The plan of operation is to functionally exercise the spacecraft in a manner to satisfy the requirements of the short system confidence check. The test will be conducted under ambient laboratory conditions except as discussed in the following paragraphs.

The midcourse maneuver and terminal descent portion of the short system confidence check will be conducted while the spacecraft is being subjected to low-level vibration inputs which are representative of the vernier engine vibration levels expected. Vibration of the spacecraft along the axes of the three vernier engines will be accomplished using equipment and techniques developed in vibration testing on the S-8 and T-2N vehicles. The spacecraft will be on the screen room test stand using a soft airmount suspension. Three shakers operating from a common power amplifier will be attached to dummy vernier engines. The vibration level will be controlled from force transducers at the attachment points. The vibration level will be approximately 10-lb rms at each

Table 12. Spacecraft anomalies subsequent to start of vibration test phase

Unit	Description of anomaly	When anomaly occurred	Disposition	Revibration required
Prior to first shake				
Spacecraft	Leaks in He pressurization system		Repair prior to solar-thermal-vacuum test	Yes—performed on Runs 6A, 6B, and 5A
Boost regulator	29-v nonessential bus oscillates when commanded into the overload/undervoltage trip circuit		Study problem on GT-1 vehicle	
Antenna solar panel positioner	Catch on pin-puller is sprung		OK as is for solar-thermal-vacuum test; repair prior to delivery	
z-axis vibration				
Klystron power supply modulator (KPSM)	After low-level z-axis vibration, a screw was missing from KPSM cover	Run 1	Replace screw, torque per print, and revibrate	Yes—performed on all subsequent shakes
Flight control sensor group	Retro-separation inertia switch opened and closed three times at a vibration frequency of 50 cps	Run 2A	Normal occurrence	No
Spacecraft	Spacecraft sent several command enable indications via pulse code modulation telemetry when no commands were being sent	Run 2B	Cause unknown; problem under study; would have no adverse effect on mission	
TV 4	TV-4 alignment appeared to shift during vibration	Postvibration system readiness test	Problem under study; thought to be caused by magnetic field of shaker; TV 4 not used in SC-1 mission	
Transmitter A	Transmitter A switches from narrow band to wide band sometimes when high power is turned off	Postvibration system readiness test	A known problem that exists on Transmitter B	No
Flight control sensor group	One short low-dwell-level run was made with gyros at 115 to 120°F instead of 180°F		Check gyro drift when spacecraft is on mount in screen room	No

Table 12. Spacecraft anomalies subsequent to start of vibration test phase (cont'd)

Unit	Description of anomaly	When anomaly occurred	Disposition	Revibration required
Lateral axis vibration along Leg 3				
Flight control sensor group	Canopus lockon signal came on several times	Run 4A	None—this is a normal occurrence when there is no Sun in the sensor Sun channel	No
Spacecraft	After stop of vibration, spacecraft telemetry mode switched from coast mode to thrust mode without a command being sent	After Run 4A	Problem unknown—under study	
Spacecraft	Lost all commutated data from engineering signal processor and auxiliary engineering signal processor	Pre-4B equal run	Removed piece of aluminized mylar from engineering signal processor; both units now working OK; problem unknown on engineering signal processor auxiliary	
Flight control sensor group	Retro-separation inertia switch opened and closed again	Run 4B	None—a normal occurrence	No
Auxiliary battery	Pin 18 in auxiliary battery connection bent	Discovered after 4B	Pin was replaced; probable cause of intermittent auxiliary battery temperature prior to vibration	Yes—performed on Runs 6A and 6B
Spacecraft	RADVS D1 Gain-State 1 telemetry indicates ON even though RADVS is OFF; indicated OFF on previous system readiness test	Postvibration system readiness test	None—this is a normal occurrence	No
TV 4	TV-4 alignment appeared to shift during vibration	Postvibration system readiness test	Same as TV-4 *z*-axis vibration	
TV 3	Mirror elevation potentiometer has a bad spot at the extreme closed position	Postvibration system readiness test		
Spacecraft	Omni-antenna A transmitter power telemetry reads erratic	Postvibration system readiness test	Repair prior to solar-thermal-vacuum test	
Lateral axis vibration perpendicular to Leg 3				
Flight control sensor group	Acceleration error signal telemetry indicates incorrectly	Postvibration system readiness test	Problem unknown—under study	
Spacecraft	Screw worked loose and backed out of the foot pad assembly on Leg 3	Postvibration inspection		
Postvibration test				
Signal data converter	Radar altimeter tracker will not acquire signal in signal + noise-to-noise mode	Jun 22, 1965	Returned to Ryan for repair	
Doppler velocity sensor antenna	D1 Gain-State 1 Pin 18 reads 18,000 Ω; all other gain-state pins read 4000 Ω	Jun 22, 1965	Returned to Ryan for repair	
SC-1	Roll-axis launch-lock pin-puller squib blew when S and A switch 150 was moved from separated to mated condition	Jun 22, 1965	This problem was investigated using conditions in time-and-event log, and the configuration of the vehicle at time that this occurred substantiates it as being normal squib firing	
SC-1	Solar panel locked in transit telemetry, M11, did not light when lock pins seated	Jun 22, 1965	Microswitch was not properly adjusted	

dummy vernier engine, the summed and averaged force transducer signals being maintained at 0.05 lb^2/cps between 84 cps and 2 kc.

During the system readiness test portion of the short system confidence check, the spacecraft will be exposed to RF energy. This will verify the functional compatibility of the spacecraft to the expected radio frequency interference (RFI) levels to be encountered at Launch Complex 36 at AFETR, and to the expected RFI levels created by the *Atlas/Centaur* launch vehicle and its ground equipment.

e. Data analysis. Data analysis effort during this period was directed toward several tasks, including the following:

(1) Consent-to-test vibration reports.

(2) Analysis of vibration data.

(3) Performance verification report (consent-to-ship).

(4) Reduction of data from special tests.

(5) Reduction of mission sequence (MS)/EMI data utilizing a new data reduction program.

Consent-to-test vibration report. All data analysis was completed on SC-1 prior to the vibration test. The consent-to-test vibration report which summarized open test requirements (out of tolerance, under evaluation, partial data, no data) showed that the majority of these were in the no-data category. The primary reason for this was that many spacecraft units were replaced during the upgrade following the test period.

Analysis of vibration test data. Data taken during vibration have been analyzed and are being compiled into final report form. The results indicate that the functional operation of the spacecraft was not degraded during the vibration environment. A review of T-21 motion pictures of vibration testing indicated that inputs normal to Leg 3 produced solar panel responses most critical with respect to shroud clearance. Therefore the motion picture film of SC-1 flight-acceptance-test vibration phase was analyzed to determine margins within the dynamic envelope which has been defined (including the deviations which were requested from the original definition). Preliminary results indicate that the revised envelope can be met, although the original envelope was exceeded. Further study of the film will be undertaken to assure that the picture sequences selected for study included the worst cycle. Most of the data reduction required to describe vibration test control has been completed. However, several composite plots of the alternating control accelerometers are planned for the phase report. This work is under way. A review of flight accelerometer data indicated that there are some problems with saturating or clipping of accelerometer channels for those pickups at the attach fittings during combined sine and random operations, at 10-*g* rms. However, acceleration spectral density plots will be prepared and will still provide useful information.

Reduction of special test data. A number of special tests are being conducted to resolve numerous problems encountered during spacecraft testing. Analysis of this data is currently being performed.

Reduction of MS/EMI test data. A new data reduction computer program has been prepared for post-test data analysis. This program has the following capabilities:

(1) Plotting routine-automatic scaling and variable time base.

(2) Tabulation routine.

(3) Frame dumps.

(4) Status tabulation.

A program checkout has been accomplished by cycling the SC-1 62-hr mission sequence data. Analysis of the plotted data resulted in several program changes. Present results are very satisfactory, with only minor program changes anticipated. The significance of this program can be realized by the fact that all telemetry channels for a 66-hr mission can be individually plotted in approximately 3.5 hr. Thus, a rapid quantitative analysis of spacecraft performance can be accomplished.

3. SC-2 Flight Acceptance Tests

The SC-2 vehicle was in an upgrade program throughout the entire reporting period; therefore, no systems test operations were conducted. Units not previously group-tested and units previously group-tested which had failures, out-of-tolerance data, or significant modifications were regroup-tested for SC-2 on the Group Test-1 (GT-1) vehicle. Following completion of the upgrade program, SC-2 will be subjected to new and more extensive power and grounding checks. It will then start initial system checkout tests with STEA 4.

4. GT-1 Flight Acceptance Tests

a. Test operations. During the reporting period, GT-1 was utilized to support group test requirements for SC-2, SC-3, and SP-1. In addition, it was used as a test bed to

investigate problems arising from SC-1 system testing and to verify proposed modifications.

The following SC-2 units were group-tested: transmitters, receivers, boost regulator, battery charge regulator, RF transfer switch, central signal processor, and altitude marking radar.

The following units were subjected to special tests to verify modification design or to investigate problems in support of SC-1: transmitter wide-band/narrow-band switching; boost-regulator overload/undervoltage trip-circuit bypass regulator; and TV-4 horizontal sync.

The following SC-1, SP-1, and SC-3 units were group-tested: transmitter; receiver; engineering signal processor; low data rate auxiliary; signal processing auxiliary; auxiliary battery control; and boost regulator.

On delivery of the SC-2 spacecraft from the upgrade program, the GT-1 vehicle will be removed from STEA 4. GT-1 will then enter a short upgrade program to receive upgraded harness and additional substructure for flight control, TV cameras, and the antenna/solar panel positioner.

5. T-2 Descent Test Program

System testing of the first descent test vehicle, T-2N-1, was completed and the vehicle was shipped to the Air Force Missile Development Center on July 27. Weight, balance, and alignment checks were made, as well as functional tests, in preparation for the first operating test of the vehicle while tethered from a balloon.

Meanwhile, the recovery system test vehicle, T-2NR, has been tested four times in drops from a balloon. Recovery provisions have performed satisfactorily. Two additional tests will be made in mid-August, and it is planned to make the first test of T-2N-1 in early September.

E. Launch Operations

1. Air Force Eastern Test Range (AFETR)

a. T-21 Pathfinder Mission. During this reporting period the T-21 spacecraft was put through the Pathfinder Mission at AFETR. Pathfinder denotes the exploratory nature of the mission of utilizing schedules, procedures, operations, personnel, and equipment untried before in the AFETR environment. The seven phases of the mission were:

(1) Receipt, partial assembly, and electronics testing at the Spacecraft Checkout Facility.

(2) Propellant loading at the Propellant Loading Building of the Explosive Safe Facility.

(3) Final assembly, weight and balance, optical alignment, and encapsulation at the Final Assembly Building of the Explosive Safe Facility.

(4) Spacecraft mating to the *Centaur* simulator and system readiness and countdown tests at Launch Pad 36A.

(5) Decapsulate and partial disassembly at the Final Assembly Building.

(6) Propellant downloading at the Propellant Loading Building.

(7) Preparation for shipment at the Spacecraft Checkout Facility.

These phases are shown in Fig. 35 with actual dates for the major operations within each phase. In addition, special tests were run to establish confidence in certain operations, and unscheduled maintenance was required to correct spacecraft failures. These special events are also listed in Fig. 35.

The Pathfinder Mission was successful in that it exposed many areas that would have hindered AFETR operations on SC-1. As of July 21 there had been 140 Trouble Failure Reports (TFR) generated, of which 83 are against ground equipment, 54 are against the spacecraft, and 3 are against facilities.

Major operations are best described by reference to Figs. 36 through 45. Most of the effort in the Spacecraft Checkout Facility was concerned with the spacecraft mounted on the system test stand and interfaced with the system test equipment assembly. As of this report, the T-21 spacecraft was being prepared for shipment to Goldstone, California, on July 31 for mission operations testing.

b. Vernier propulsion system. The operations in checking the performance of the gas attitude control system and the vernier propulsion system resulted in numerous TFRs being written against major leaks of the quick disconnects on the vernier propulsion system. In addition to

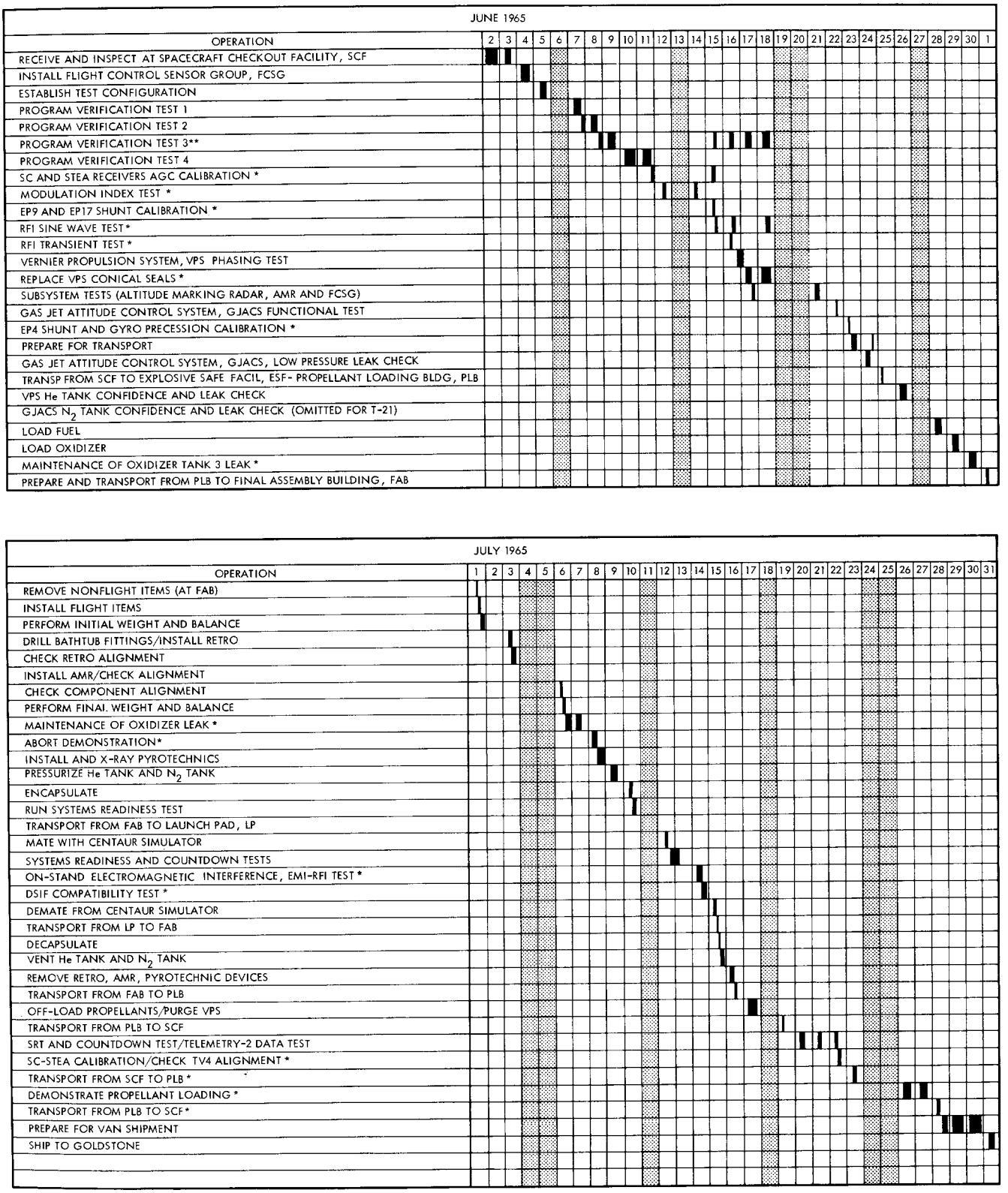
JUNE 1965
OPERATION
2 3 4 5 6 7 8 9 10 11 12 13 14 15 16 17 18 19 20 21 22 23 24 25 26 27 28 29 30 1
RECEIVE AND INSPECT AT SPACECRAFT CHECKOUT FACILITY, SCF
INSTALL FLIGHT CONTROL SENSOR GROUP, FCSG
ESTABLISH TEST CONFIGURATION
PROGRAM VERIFICATION TEST 1
PROGRAM VERIFICATION TEST 2
PROGRAM VERIFICATION TEST 3**
PROGRAM VERIFICATION TEST 4
SC AND STEA RECEIVERS AGC CALIBRATION *
MODULATION INDEX TEST *
EP9 AND EP17 SHUNT CALIBRATION *
RFI SINE WAVE TEST *
RFI TRANSIENT TEST *
VERNIER PROPULSION SYSTEM, VPS PHASING TEST
REPLACE VPS CONICAL SEALS *
SUBSYSTEM TESTS (ALTITUDE MARKING RADAR, AMR AND FCSG)
GAS JET ATTITUDE CONTROL SYSTEM, GJACS FUNCTIONAL TEST
EP4 SHUNT AND GYRO PRECESSION CALIBRATION *
PREPARE FOR TRANSPORT
GAS JET ATTITUDE CONTROL SYSTEM, GJACS, LOW PRESSURE LEAK CHECK
TRANSP FROM SCF TO EXPLOSIVE SAFE FACIL, ESF- PROPELLANT LOADING BLDG, PLB
VPS He TANK CONFIDENCE AND LEAK CHECK
GJACS N_2 TANK CONFIDENCE AND LEAK CHECK (OMITTED FOR T-21)
LOAD FUEL
LOAD OXIDIZER
MAINTENANCE OF OXIDIZER TANK 3 LEAK *
PREPARE AND TRANSPORT FROM PLB TO FINAL ASSEMBLY BUILDING, FAB
JULY 1965
OPERATION
1 2 3 4 5 6 7 8 9 10 11 12 13 14 15 16 17 18 19 20 21 22 23 24 25 26 27 28 29 30 31
REMOVE NONFLIGHT ITEMS (AT FAB)
INSTALL FLIGHT ITEMS
PERFORM INITIAL WEIGHT AND BALANCE
DRILL BATHTUB FITTINGS/INSTALL RETRO
CHECK RETRO ALIGNMENT
INSTALL AMR/CHECK ALIGNMENT
CHECK COMPONENT ALIGNMENT
PERFORM FINAL WEIGHT AND BALANCE
MAINTENANCE OF OXIDIZER LEAK *
ABORT DEMONSTRATION*
INSTALL AND X-RAY PYROTECHNICS
PRESSURIZE He TANK AND N_2 TANK
ENCAPSULATE
RUN SYSTEMS READINESS TEST
TRANSPORT FROM FAB TO LAUNCH PAD, LP
MATE WITH CENTAUR SIMULATOR
SYSTEMS READINESS AND COUNTDOWN TESTS
ON-STAND ELECTROMAGNETIC INTERFERENCE, EMI-RFI TEST *
DSIF COMPATIBILITY TEST *
DEMATE FROM CENTAUR SIMULATOR
TRANSPORT FROM LP TO FAB
DECAPSULATE
VENT He TANK AND N_2 TANK
REMOVE RETRO, AMR, PYROTECHNIC DEVICES
TRANSPORT FROM FAB TO PLB
OFF-LOAD PROPELLANTS/PURGE VPS
TRANSPORT FROM PLB TO SCF
SRT AND COUNTDOWN TEST/TELEMETRY-2 DATA TEST
SC-STEA CALIBRATION/CHECK TV4 ALIGNMENT *
TRANSPORT FROM SCF TO PLB *
DEMONSTRATE PROPELLANT LOADING *
TRANSPORT FROM PLB TO SCF *
PREPARE FOR VAN SHIPMENT
SHIP TO GOLDSTONE

*UNSCHEDULED OR SPECIAL EVENTS
** CLOSED LOOP TESTS RUN JULY 20 AND 21

Fig. 35. T-21 *Surveyor* prototype spacecraft operations at AFETR

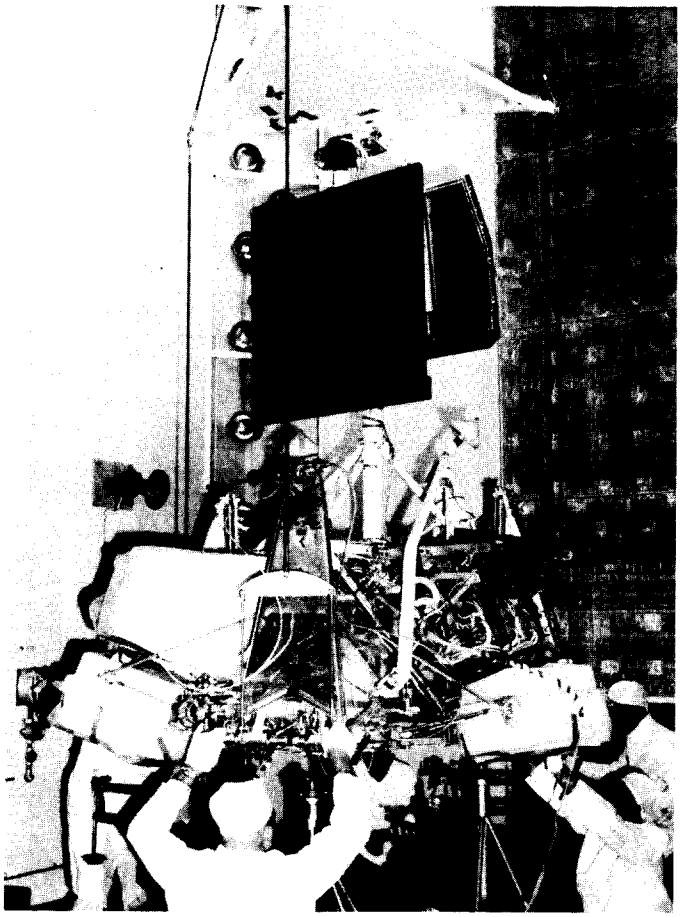

Fig. 36. T-21 spacecraft being placed on propellant weighing scales

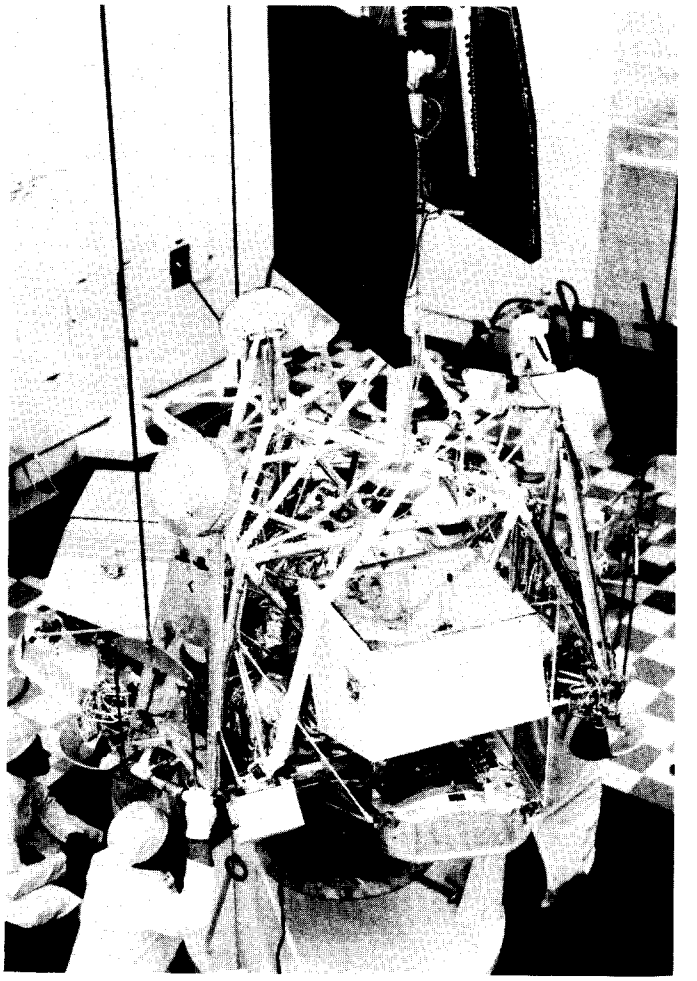

Fig. 37. Mating of inert retro-engine (T-21 spacecraft)

these leakages there were other leaks on the spacecraft, but they were primarily eliminated by insertion of different conical seals in the joints or by torquing to recognized torque valves.

The T-21 procedure for determination of total leakage rate in the vernier propulsion system is a pressure-decay-rate method. The vernier propulsion system is pressurized and its loss of pressure is rated and correlated to the total pressure quantity leakage. The same procedure will be used for SC-1.

c. Gas attitude control system. The gas attitude control system had numerous leaks but they were generally eliminated by correct torquing of all fittings. The leakage rates of GN_2 in the systems are excessive when checked with gaseous helium or bubble-o-meter, according to procedure. The current thinking is to pressurize the system to some nominal and/or operating pressure and observe the pressure decay rate of the system on the pneumatic control console.

d. Pneumatic control console. Gas pressure regulators 3, 4, and 5 had regulation and stability problems when used in servicing the spacecraft. The Marotta regulator was initially installed, found to be faulty, and reworked. It now appears best to use the conventional Grove regulator.

e. Precision weight system. Initial attempts to load propellants in the T-21 program resulted in an inaccurate amount of propellant placed aboard the spacecraft. Shut-off valves were placed in the propellant loading lines to isolate each tank during off-loading operations. This change and compensation for residuals in the loading lines established the proper accuracy.

f. SCAPE suits. The use of the self-contained atmospheric protection ensemble (SCAPE suit) was verified for use in operations with T-21. Because of earlier concern over lack of mobility with the SCAPE suit, lighter weight

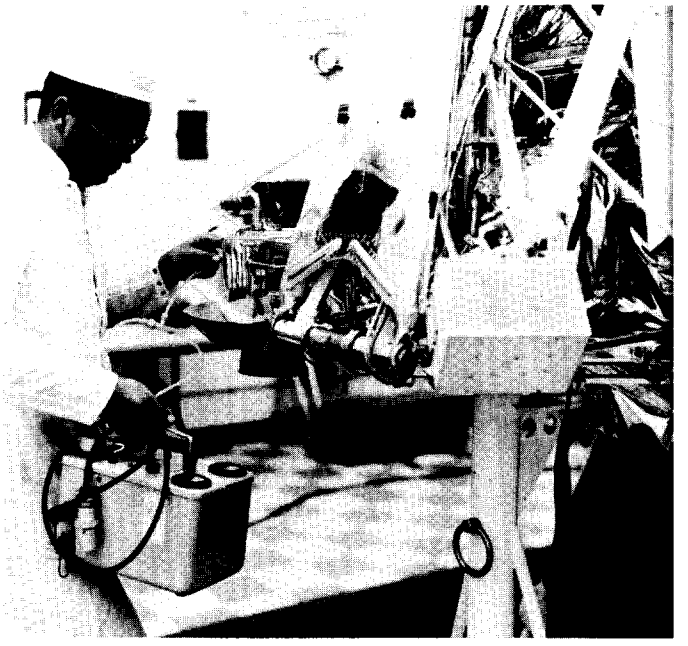

Fig. 38. Consolidated Electrodynamics Corporation leak detector in use on T-21 spacecraft

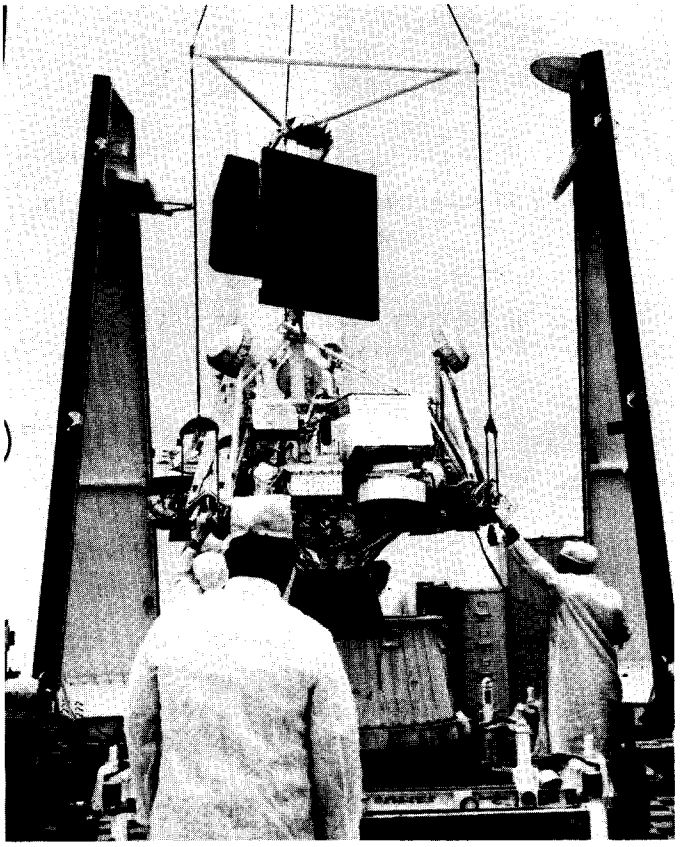

Fig. 39. T-21 spacecraft positioned for mating with upper *Centaur* adapter

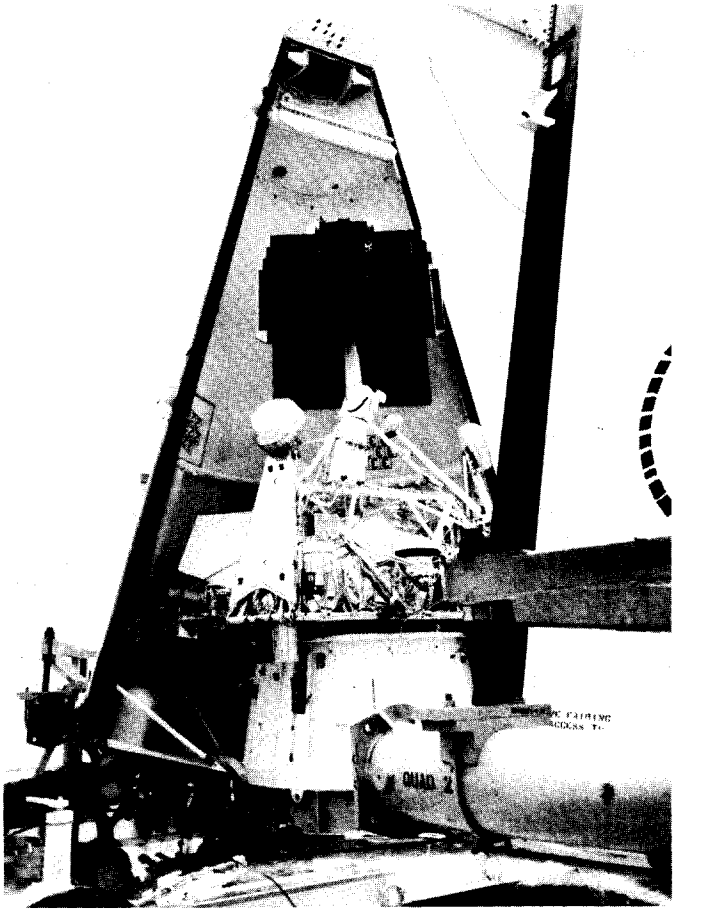

Fig. 40. Encapsulation of T-21 spacecraft mounted on GTV-2

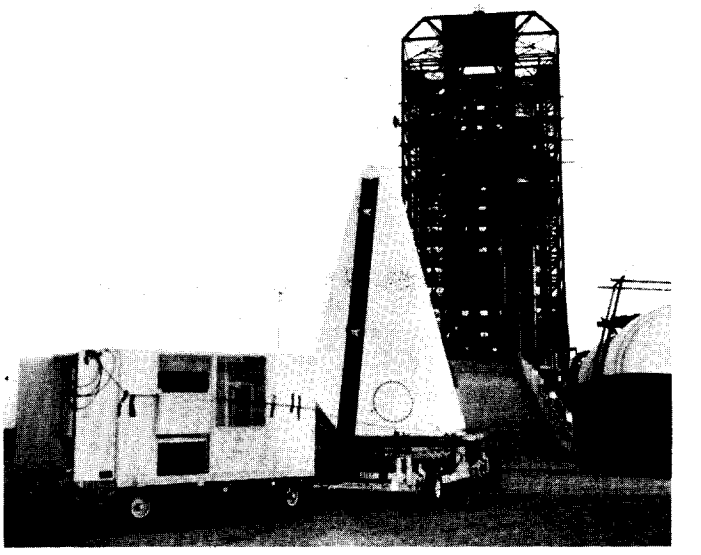

Fig. 41. T-21 spacecraft on GTV-2, mobile temperature control unit in tow, to Launch Pad 36A

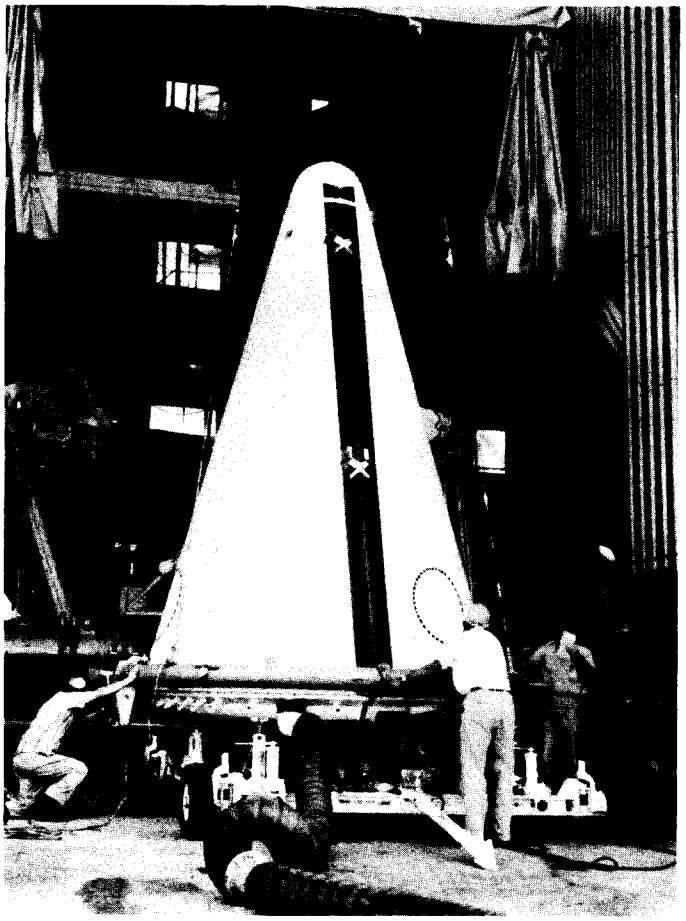

Fig. 42. T-21 spacecraft being lifted from GTV-2

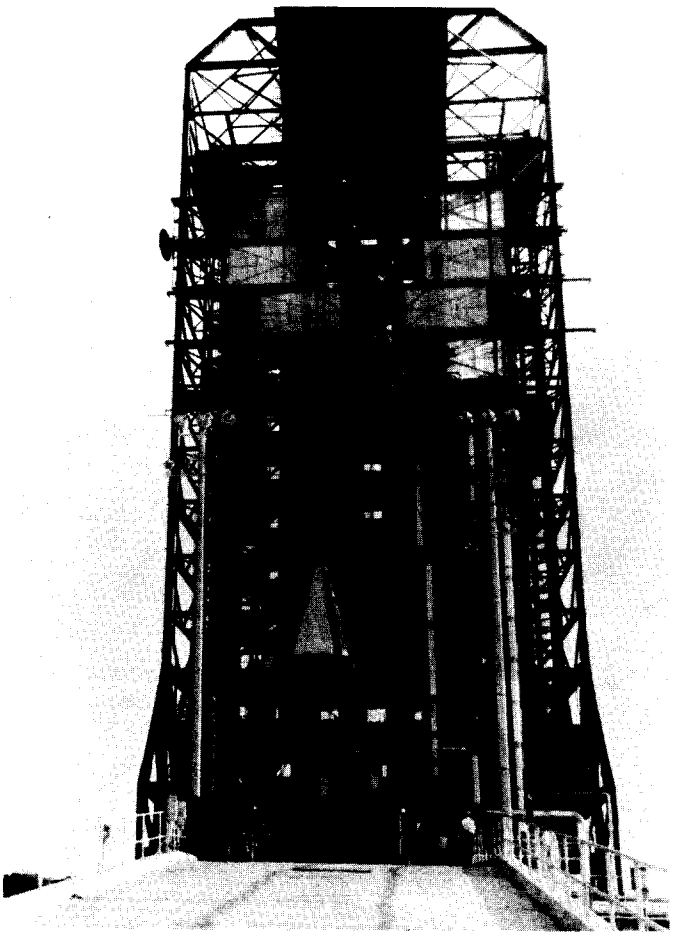

Fig. 43. T-21 spacecraft being raised for mating to simulator

acid suits were tried, but these proved cumbersome and unsafe when exposed to monomethyl hydrazine. SCAPE suits were then tried and appear to be satisfactory for propellant loading operations in the Propellant Loading Building.

g. Ground support equipment. The T-21 exercises brought forth some deficiencies in the ground handling and ground support equipment. The main deficiencies noted were as follows:

(1) The loading and tiedown of Ground Transport Vehicle 1 (GTV-1) in the air ride van proved to be a time consuming operation and subjected the spacecraft to unnecessary hazards. This brought forth a redesign of the equipment.

(2) The retro handling equipment proved to be deficient in minor respects. This equipment is currently being updated to reflect the experience gained from the T-21 operations.

(3) Some of the early designed optical alignment fixtures were discrepant in minor respects. Action is now under way to correct these deficiencies.

h. Optical alignment procedure. During the T-21 exercises at AFETR, the newly released optical alignment procedures were checked out for the first time in a field operation. In general, the procedures were adequate and those operations that could be performed proceeded smoothly. Minor revisions and additions are required to the procedures, and will be accomplished prior to arrival of the SC-1 spacecraft at AFETR.

i. Dynamic Model SD-2. At the beginning of the reporting period, SD-2 was in the Explosive Safe Facility at AFETR assembled and checked out, awaiting encapsulation. Significant accomplishments were:

(1) After uncrating and inspection, SD-2 was assembled and mounted on the payload adapter on

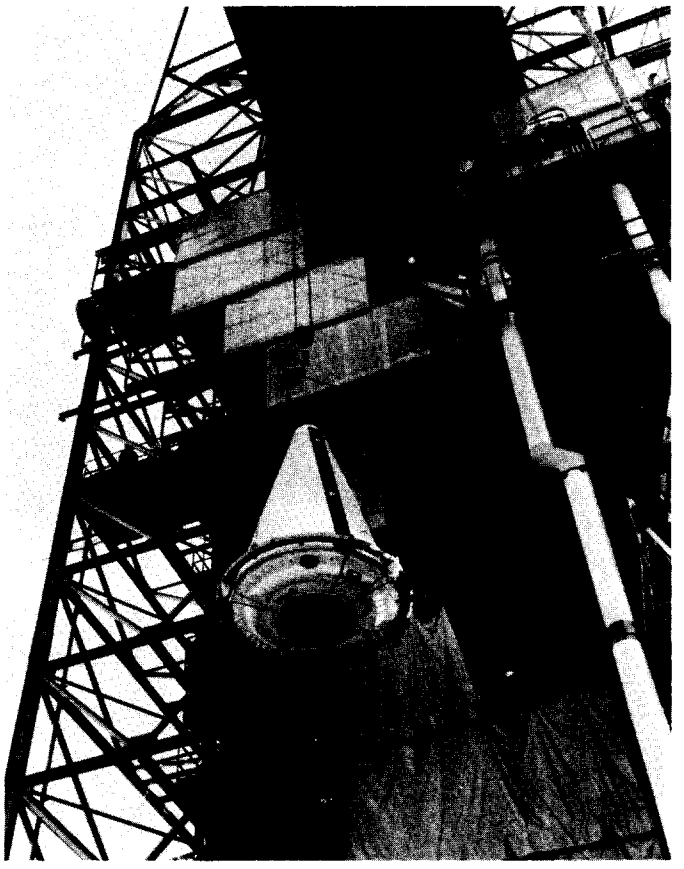

Fig. 44. T-21 spacecraft nearing top of gantry tower

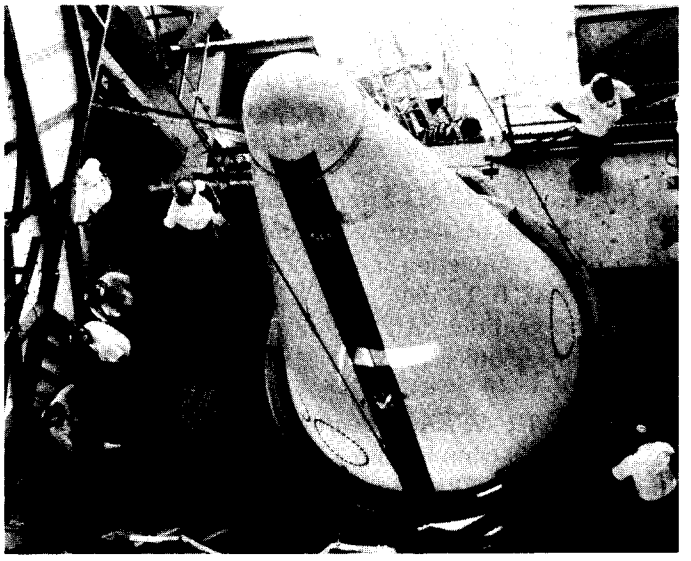

Fig. 45. Top view of T-21 spacecraft mounted on simulator

GTV-2 on June 10 (Figs. 46 and 47). Pre-encapsulation checkout of instrumentation and the transponder were completed by June 14.

(2) Special transponder parameter measurements for use by the Deep Space Instrumentation Facility (DSIF) were made in early June and the data transmitted to JPL.

(3) The spare omni-antenna was installed on SD-2 because there was doubt as to the original antenna performance due to possible physical damage.

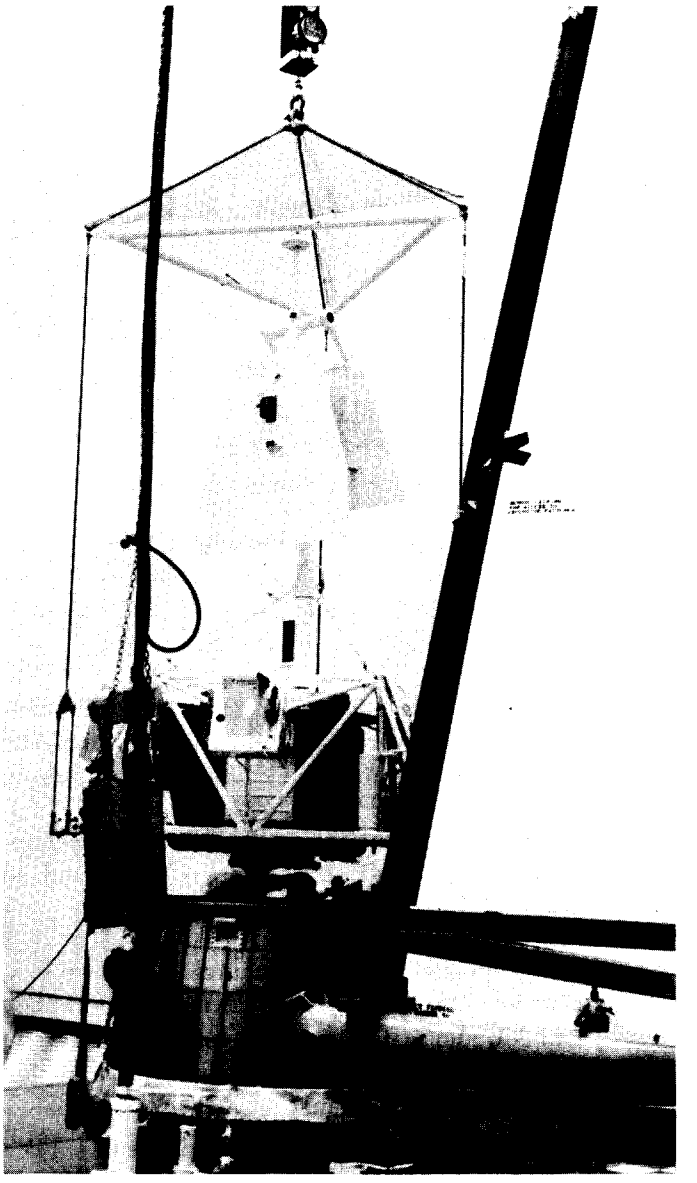

Fig. 46. SD-2 vehicle being lowered onto upper payload adapter

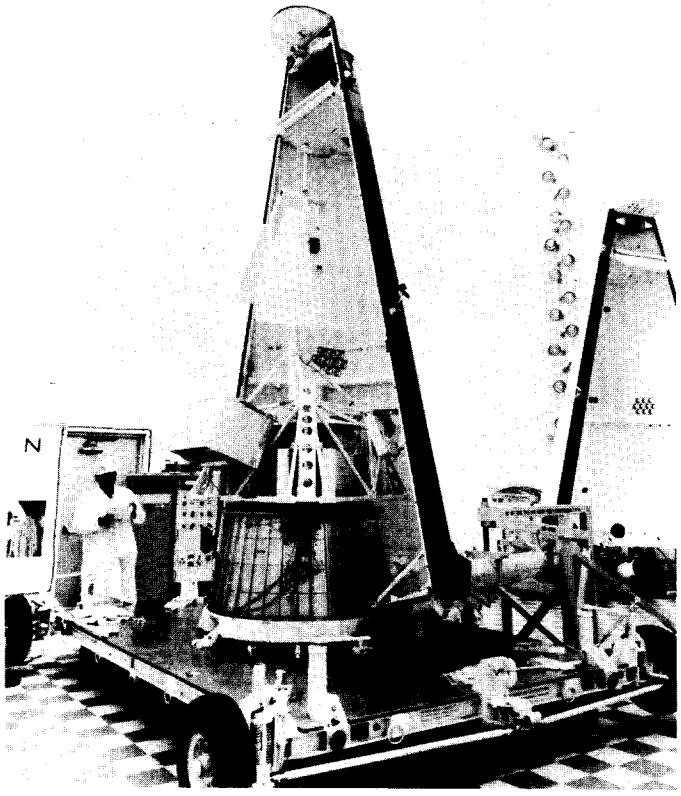

Fig. 47. SD-2 vehicle mated to upper payload adapter prior to encapsulation

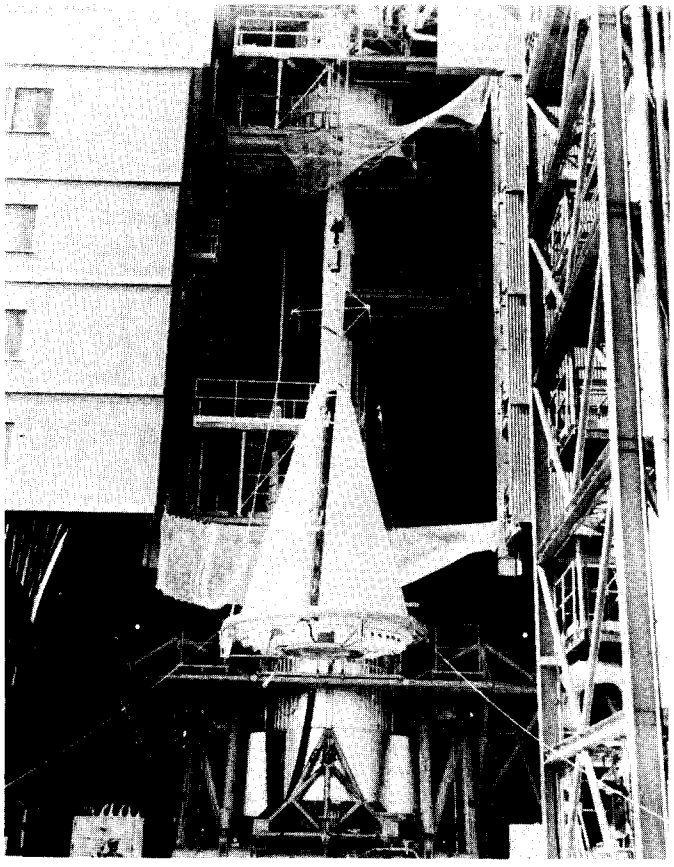

Fig. 48. SD-2 vehicle being hoisted into position for mating to AC-6

(4) The spare aerodynamic heating device was installed on SD-2. It replaced one that was electrically sound but had cracks around the edge and had been rejected by quality control.

(5) SD-2 was encapsulated and simulated countdown was successfully run on June 24. The simulated countdown validated the countdown procedure.

(6) SD-2 was decapsulated on June 30 to remove an excess length of instrumentation cable and to install flight latches.

(7) Re-encapsulation and a simulated countdown took place on July 8, and SD-2 was moved to Launch Pad 36B and mated to *Atlas/Centaur-6* (AC-6) on July 9 (Figs. 48 and 49). The transport and mating went according to plan.

(8) After mating, the tanking test was performed on July 13. A programmer malfunction and an *Atlas* failure at Vandenberg caused removal of the *Atlas* autopilot. It was returned to General Dynamics/Convair, San Diego for testing.

(9) The autopilot was returned and reinstalled. A special test to ascertain the results of random umbilical pulling was performed on July 26. The test resulted in damage to the programmer.

(10) As of July 27 SD-2 remains mated to AC-6 awaiting joint flight acceptance composite tests (J-FACT). Test completion should occur about 10 days after J-FACT. To date at AFETR, SD-2 has been in a go condition. All test delays have resulted from causes other than SD-2 readiness.

j. Phase III STEA activation. The Phase III STEA activation was completed on June 29 with the receipt of the remaining STEA racks in the Spacecraft Checkout Facility and the propellant servicing carts and weighing system in the Explosive Safe Facility. All areas were activated before the completion of the T-21 operations at AFETR.

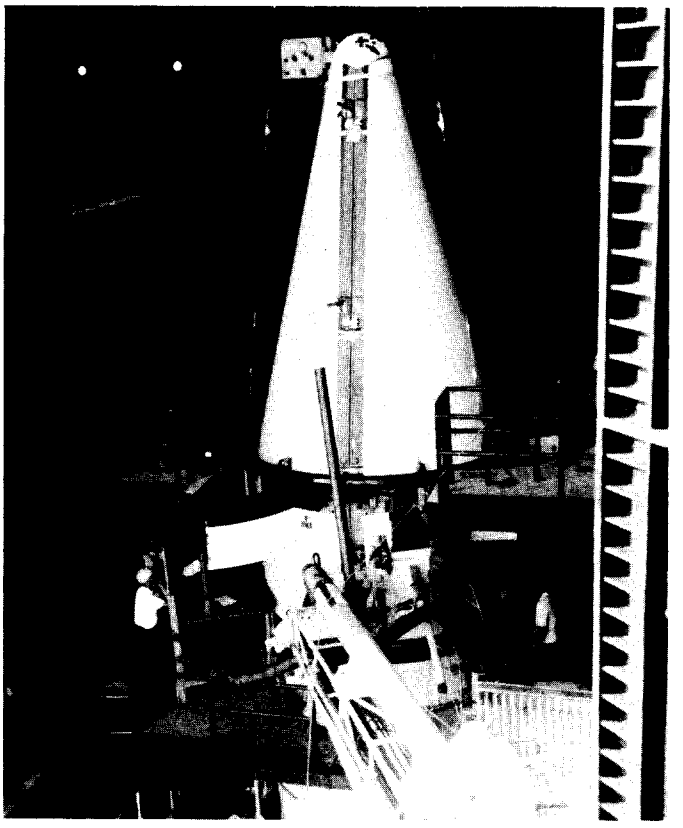

Fig. 49. SD-2 vehicle mated to AC-6

2. Surveyor Spacecraft Test Facility Activation at Goldstone

The *Surveyor* spacecraft test facility is located at a distance of approximately 7 mi from the Goldstone Pioneer Station. Natural site attenuation and adjustable attenuation simulate the realistic lunar distance for background or leakage radiation from the spacecraft. The physical arrangement of the site is shown in Fig. 50 and a drawing of the *Surveyor* Spacecraft Test Facility is shown in Fig. 51.

Activation of the Spacecraft Test Facility began on July 22, 1965 with the arrival of two 50- × 10-ft rental trailers. Activation of these trailers included installation of power and communication lines, and a checkout of the refrigeration units. The trailers are used for maintenance, bonded stores, and office facilities. The STEA trailer arrived at the spacecraft test facility on July 27, 1965. Facility activation included the installation, checkout, and verification of the equipment necessary to perform the T-21 DSIF-11/space flight operations (SFO) compatibility tests.

3. T-21 DSIF-11/SFO Compatibility Tests

The primary objective of the T-21 tests at Goldstone was to demonstrate the engineering and functional compatability between an actual flight equivalent spacecraft and the *Surveyor* SFO/Deep Space Network (DSN) system, and to provide operational training for the SFO/DSN personnel. The secondary objective of the tests was to establish the validity of spacecraft simulation techniques.

a. T-21 test vehicle configuration. The T-21 spacecraft was placed within the RF screen room on GTV-1 and assembled to flight configuration with the following exceptions:

(1) Altitude marking radar was not installed.

(2) Retrorocket was not installed.

(3) Test batteries were utilized.

(4) Propellant and gases were not loaded, except for 300 psi of nitrogen.

(5) Pyrotechnic devices were not installed.

(6) Shock absorbers were not installed.

(7) Hardline access was provided for prelaunch monitor rack and power supply rack.

(8) Solar panel/planar array was not installed.

(9) Omni-antennas were not electrically connected. Hardline RF access was provided to the STEA trailer and to the external 4-ft antenna.

b. Description of tests. The test series is divided into engineering and functional compatibility tests, operational training tests, Priority 2 tests, and Priority 3 tests.

Engineering and functional compatibility tests:

(1) RF compatibility test—to demonstrate the ability of the DSIF S-band system to communicate with the spacecraft for all spacecraft RF system configurations.

(2) Command compatibility tests—to demonstrate the ability of the DSIF S-band system to command the spacecraft in both spacecraft command configurations.

(3) Telemetry compatibility tests—to demonstrate the ability of the DSIF and CDC equipment to receive, detect, process, display, and record the PCM/FM/PM telemetry from the spacecraft.

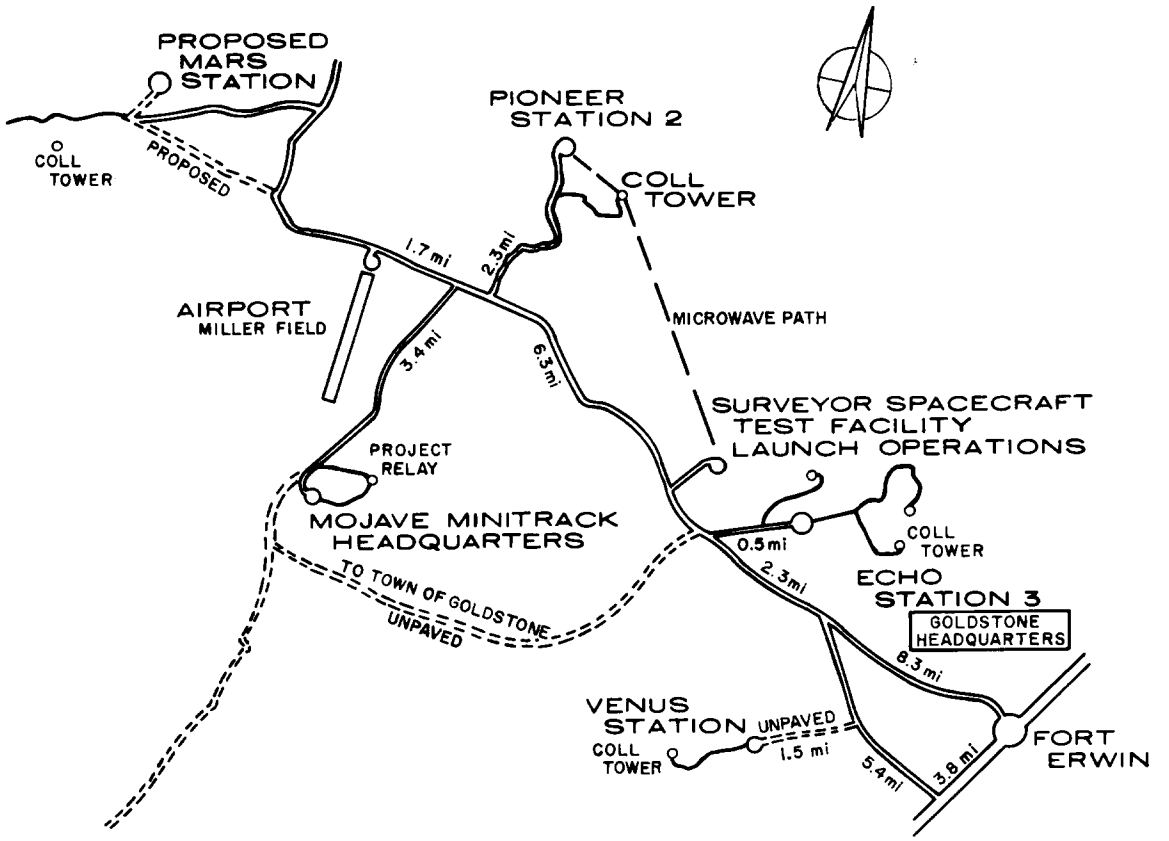

Fig. 50. Goldstone site showing *Surveyor* Spacecraft Test Facility location

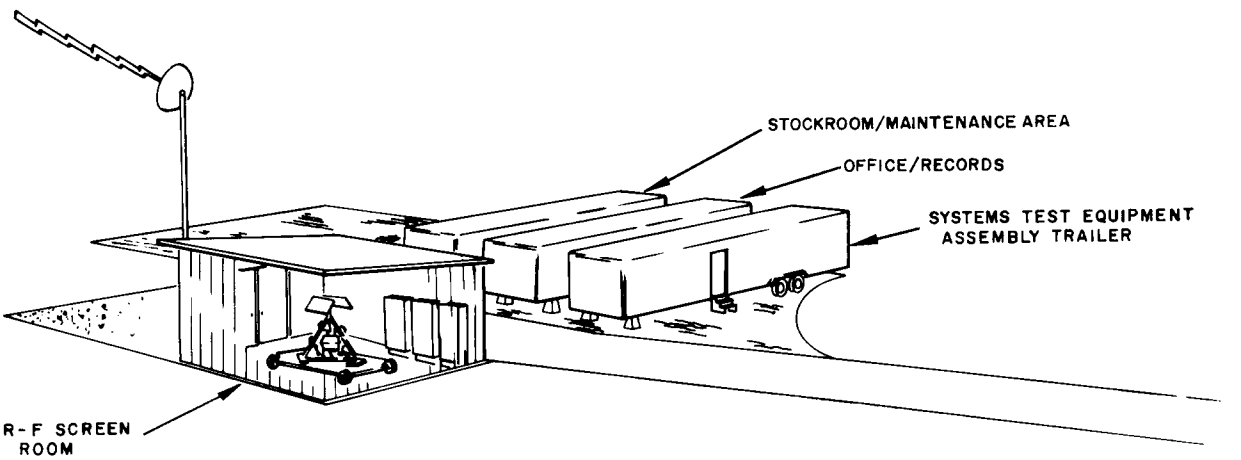

Fig. 51. Drawing of *Surveyor* Spacecraft Test Facility

(4) SFO compatibility tests—to verify the compatibility and functional operation of the concerned system tied in with SFOF.

Operations training tests. These tests provide an opportunity for DSIF-11 station personnel to practice and demonstrate proficiency in performing mission operations procedures, using the T-21 vehicle as a signal simulator.

Priority 2 tests:

(1) RF compatibility tests—the DSIF receiver is operated with the parametric amplifier instead of the maser.

(2) Command compatibility tests—involve command transmission during a backup telemetry mode and television mode.

(3) Telemetry compatibility tests—include the modes used during post-midcourse cruise, terminal descent, and post-landing engineering surveys.

Priority 3 tests:

(1) RF compatibility tests—to determine 2-way phase-lock threshold for conditions of various subcarriers on the downlink in both high and low modes, and for each spacecraft transmitter.

(2) Telemetry compatibility tests—to determine the performance of the analog telemetry subcarrier discriminators and the bit error performance of the 4400-bit/sec channel when multiplexed with the analog channels.

(3) Television compatibility tests—to utilize special test patterns in an attempt to obtain certain quantitative measures of the system performance and to focus the TV camera on landscape for effects of the microwave link transmission characteristics on the quality of the TV pictures.

F. Space Flight Operations

1. Command and Data Handling (CDC) System

The CDC/DSIF compatibility test results from Goldstone, Johannesburg, and Canberra were received by JPL during August 1965. Review and evaluation of these test results will be completed by October 1965.

More than half of the engineering change authorizations which are deemed necessary for incorporation in the DSIF CDCs before Mission A have been installed. The CDC configuration freeze now exists at DSIF 11, 42, and 51. No further changes to the CDCs at these sites will be permitted without explicit JPL approval.

The T-21 spacecraft testing at DSIF 11 started on August 9, 1965, and at the end of August was approximately half completed. A slip of four days has occurred, primarily due to the calibration of the RF link from DSIF 11 to the Spacecraft Test Facility (Fig. 52). The tests are primarily designed to verify the compatibility of the *Surveyor* spacecraft, as typified by T-21, with the *Surveyor* Mission operation system and portions of the Deep Space Network system.

On July 29, 1965 Hughes Aircraft Company was given a contract go-ahead to supply three additional "bare-bones" CDCs for DSIF stations.

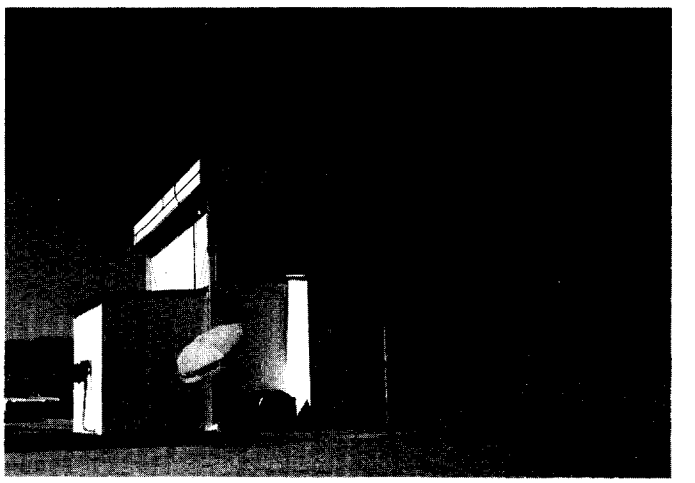

Fig. 52. Spacecraft Test Facility

G. Aerospace Ground Equipment

1. Operational Ground Equipment

a. Closed-loop simulation rack. Closed-loop simulation rack 277280-100, SN 003, was completed, checked out, and shipped to AFETR. Closed-loop simulation rack 277280-100, SN 002, was completed, checked out, and delivered to Systems Test Equipment Assembly 4 (STEA 4). This completed the manufacture of the closed-loop simulation racks with racks in place at STEA 1, STEA 4, and AFETR.

b. STEA 1. The thermal-vacuum chamber pressure sensing instrumentation has been integrated with the STEA 1 panic circuit to shut off spacecraft power in the event of chamber vacuum failure.

c. STEA 5. Preparations are under way for final acceptance testing, including power and grounding checks, on STEA 5. The presently scheduled activation date is August 6, 1965.

A comprehensive modification program of STEA 5 has reached its final stages with about 95% of the mandatory engineering change requirements installed and accepted by quality control. Some of the up-to-date equipment in the STEA 5 command and data handling console (CDC) has been transferred to the higher priority projects, and this means that STEA 5 CDC equipment must be updated again. Removal of this equipment for modification should not interfere with the first phase of STEA 5 operation.

d. Group test equipment assembly. Work is continuing on the group test equipment assembly (GTEA). The commercial equipment orders have been placed and the racks are being fabricated.

e. Operations console and launch control. The operations console and launch control rack assembly test and selloff for delivery to AFETR in support of T-21 has been completed. Modification kit drawings are being made for the incorporation of engineering change authorizations into the dynamic model operations console and launch control rack at Launch Pad 36B after the SD-2 launch. Assistance on functional drawings for operations console and launch control rack to the first active element has been completed.

f. Power and grounding. A complete power and grounding checkout on STEA 1 and an abbreviated power and grounding checkout on STEA 4 have been performed. The ground bus configuration for all STEAs has been reworked to more nearly approach a true star ground configuration.

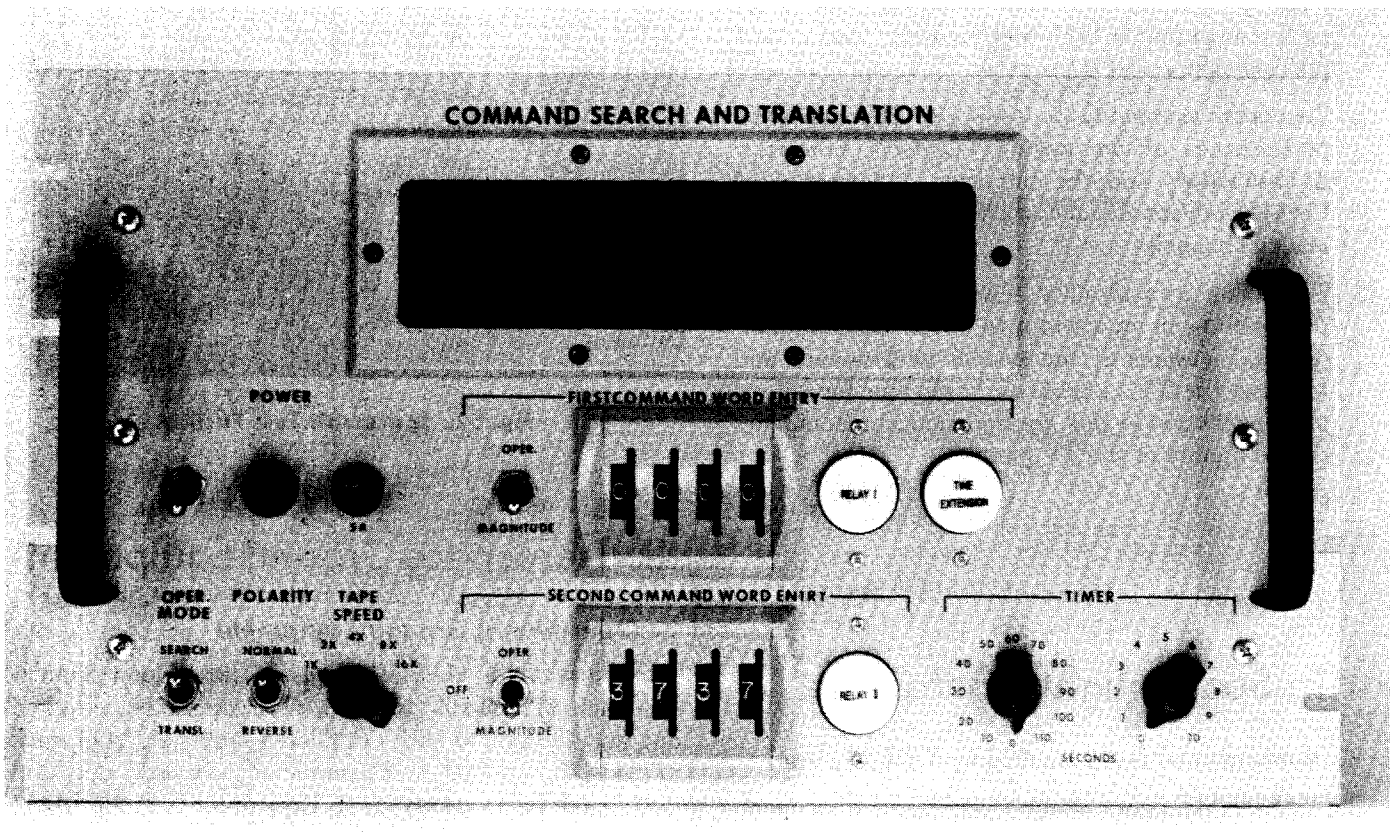

Fig. 53. Command search and translator unit

2. TV Survey Camera Target

Design of the target to be used in aligning the survey television camera on the spacecraft has been completed. Engineering has been released for fabrication. The first target has been scheduled for completion in late September.

3. Data Acquisition Center

Work continued on the documentation of interfaces between the STEA and the JPL computer data system. One piece of such interface equipment, the command translator rack, was recently added to the complex and is performing very satisfactorily. The core of the rack, the command search and translation unit, is illustrated in Fig. 53.

4. CDC Test Set

During the month of June the CDC test set was calibrated and evaluated at STEA 4. This test set was subsequently sent to AFETR to support the test operations there.

a. Description of equipment. The CDC test set is composed of three drawers mounted within a half-rack rollaway cabinet. These drawers are signal drawer, noise and output drawer, and noise source drawer. The test set generates signals that are necessary to test the CDC demodulator. Its 10-Mc output closely simulates the output of the RF STEA receiver. Both the 10-Mc signal circuitry and the noise source contain step attenuators. The noise summing (noise and output) drawer contains a power meter. By using this meter and the two step attenuators, a wide range of video, or 10-Mc output signal-to-noise ratios, may be selected. Also contained in the signal drawer are seven subcarrier oscillators that may be used to modulate the 10-Mc output from the test set.

b. Compatibility test. As part of the CDC test set compatibility tests conducted at STEA 4, a series of checks were made with the CDC FM demodulator to determine the signal-to-noise ratios that degraded operation of the demodulator. The CDC pulse-code-modulated (PCM) simulator was used to modulate the test set 70-kc subcarrier oscillator. The CDC test set 10-Mc output was connected to the CDC demodulator, discriminator, and decommutator as shown in Fig. 54.

Testing results indicated that the test set will be a very useful tool for testing and evaluating the CDC. A large portion of the CDC was exercised during the testing, and the test set provides a method of study for problems such as bit error.

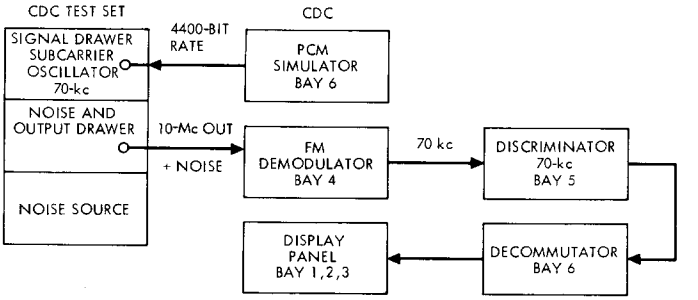

Fig. 54. CDC compatibility test arrangement

H. Flight Control

1. System Design and Testing

a. Radar noise during vernier descent. Analysis of the effects of radar altimeter and doppler velocity sensor (RADVS) noise during vernier descent has continued with the six-degree-of-freedom analog computer simulation. Computer determination of the dispersion of flight conditions at the point of transfer to inertial hold mode (following 10-ft/sec detector mark) was repeated for T-2H and twice T-2H noise levels to clear up some anomalies which appeared in data. The anomalies were traced to an error in data reduction. Corrected data are shown in Table 13, which describes the statistical dispersions in pitch and yaw attitude angles (θ and ψ, respectively) and lateral velocity components (V_x and V_y) which exist at the instant of transfer to inertial hold. These are presently being incorporated into the Monte Carlo digital simulation analysis of touchdown stability. No significant change from previous results is anticipated.

The effects of flight control system noise filters, which are presently scheduled for SC-3 and subsequent spacecraft, have been analyzed by means of the six-degree-of-freedom analog computer simulation. The scheduled noise filters are shown in Table 14.

The purpose of these filters is to reduce flight control system sensitivity to RADVS noise, and in particular to reduce vernier engine thrust excursions because of noise. Fig. 55 shows a comparison of vernier engine thrust excursions resulting from T-2H noise levels for each of three cases. The first trace shows Vernier Engine 2 thrust excursions when no noise filters are used, which is applicable to SC-1 and SC-2 spacecraft. The second and third

Table 13. Perturbation of attitude hold conditions caused by RADVS noise[a]

Noise level	Pitch attitude, deg		Lateral velocity V_y, ft/sec		Correlation coefficient, $\rho_{\theta V_y}$	Yaw attitude, deg		Lateral velocity V_x, ft/sec		Correlation coefficient, $\rho_{\psi V_x}$
	Mean θ_{av}	Standard deviation σ_θ	Mean $V_{y_{av}}$	Standard deviation σ_{V_y}		Mean ψ_{av}	Standard deviation σ_ψ	Mean $V_{x_{av}}$	Standard deviation σ_{V_x}	
Procurement specification	+0.02	+0.06	0.373	0.149	0.33	0	+0.07	0.399	0.145	−0.45
T-2H (Set I)	−0.16	−0.05	1.45	0.536	0.48	−0.07	+0.05	1.38	0.594	−0.51
T-2H (Set II)	+0.07	+0.01	1.32	0.445	0.44	−0.24	+0.02	1.54	0.502	−0.61
1.5 × T-2H	+0.33	+0.02	2.24	0.747	0.40	−0.26	−0.06	1.76	0.820	−0.35
2.0 × T-2H	−0.47	−0.11	2.74	0.904	0.23	−0.12	−0.21	2.74	0.961	−0.43

[a] Sample size of 60 analog runs per set.

Table 14. Scheduled noise filters

Channel	Filter		Filter location
	SC-3, 4	SC-5 and up	
V_x or V_y	$\frac{1}{1+0.156S}$	$\frac{1}{1+0.2S}$	Input to pitch/yaw precession command modulator
R and V_z	$\frac{1}{1+0.1S}$	$\frac{1}{1+0.1S}$	Descent amplifier

traces show the thrust excursions experienced when the noise filters are included in the flight control system. Satisfactory velocity and attitude control is maintained in all three of these cases, but it is evident from Fig. 55 that the noise filters effect a major reduction in vernier engine thrust excursions due to RADVS noise.

Analog computer results have verified that the noise filters will not measurably decrease the predominantly low-frequency dispersions in flight conditions (pitch/yaw attitude angles, lateral velocity) which exist at the instant of transfer to the attitude hold mode. Stability analyses have verified that adequate stability margins are retained in all control loops affected by the filters.

b. Velocity control system parameters for A-21A vehicle. Greater burnout weight of the A-21A vehicle (2450-lb injected weight) relative to SC-1 through SC-4 requires that certain parameters of the vernier descent velocity control system be modified to account for the attendant decrease in spacecraft deceleration capability. Analysis of the A-21A vernier descent phase has resulted in certain parameter modifications. As in the SC-1 configuration, appropriate allowances in the design have been made for RADVS and flight control system tolerances, lunar surface slope of up to 15 deg, and burnout flight-path angles of up to 45 deg from vertical. The

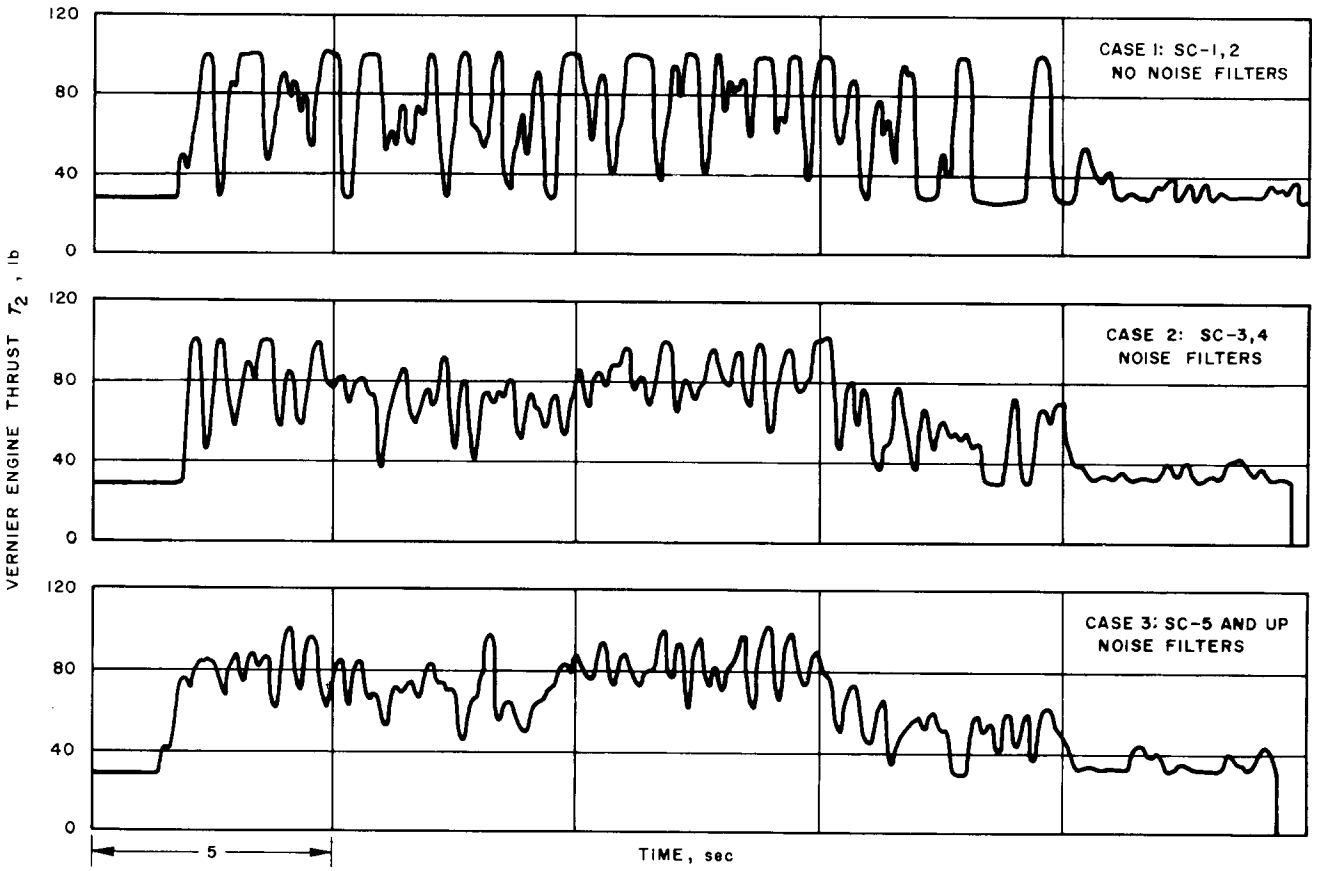

Fig. 55. Effect of noise filters on vernier thrust excursions

UNCLASSIFIED

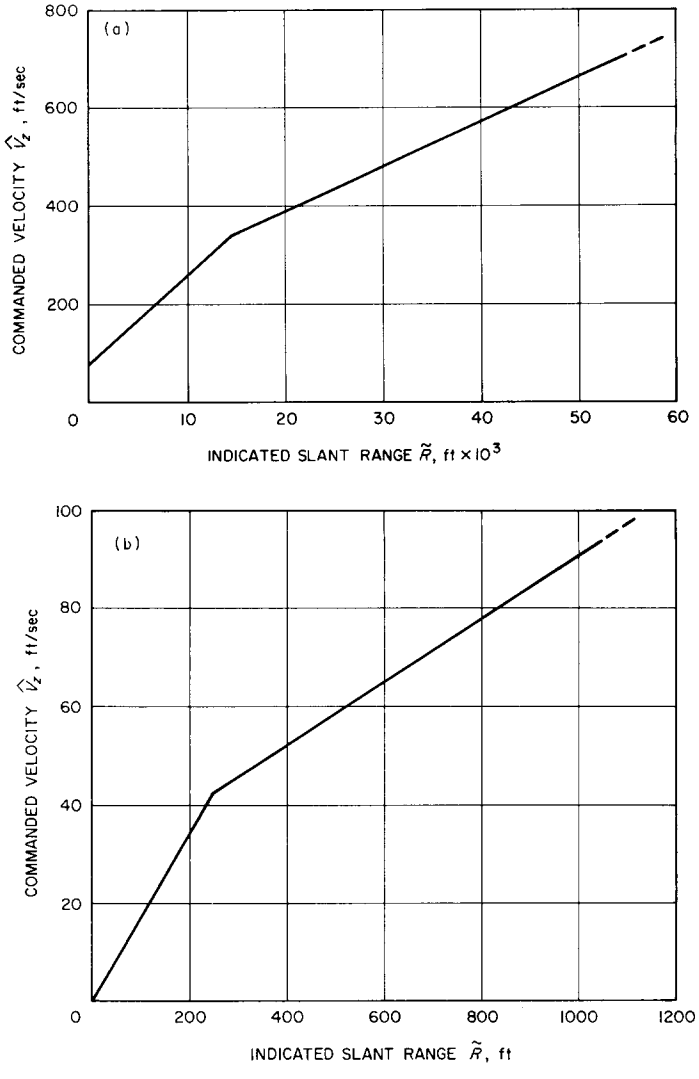

Fig. 56. Modified A-21A descent trajectory command segments (injected weight = 2450 lb max; burnout weight = 862 lb)

modified descent trajectory command segments to be used for A-21A are shown in Fig. 56.

c. Closed-loop testing with vernier engines. Although the closed-loop vernier engine test program conducted at Placerita Canyon (April to June 1965) produced satisfactory dynamical operation of the simulated flight control system, the following items render the term "satisfactory" conditional:

(1) The control loop gains as tested were 20 to 25% less than nominal (a noncritical test).

(2) Operational and scheduling problems precluded obtaining a baseline open-loop test of the same vernier engines used for the closed-loop test while burning propellants with minimum dissolved gas.

(3) In addition, the use of high-temperature propellants (greater solubility of gas, higher vapor pressure) is expected to contribute to some degree to the degradation of flight control subsystem dynamics.

A further closed-loop test series has been planned to improve knowledge of flight control subsystem performance while accounting for the above parameters. In particular, open- and closed-loop tests using both high and low dissolved gas content propellants at high temperature, for high, nominal, and low loop gains will be performed as part of the S-6 margin limit test program.

d. Vernier engine frequency response data. Vernier engine frequency response data covering two S-6 tests at Placerita Canyon and eight single-engine tests at Reaction Motors Division of Thiokol Chemical Corporation (RMD) has been reduced from magnetic tape via an analog computer. In addition to frequency, parameters considered were: (1) propellant temperature (ambient); (2) dissolved gas content (high); (3) oxidizer injection line size (both the design line and a reduced volume line were tested); and (4) thrust level. Data taken at frequencies below 5 cps and high-temperature propellants are needed to complete the frequency response picture. It is expected that data recently generated by RMD during the type approval test will fill this need.

2. Subsystem Testing

a. Flight control sensor group testing. The second model of the 235000-6 configuration was delivered to the spacecraft assembly area on June 25, 1965. This unit was initially destined for SC-2, but after the SC-1 flight control sensor group was damaged, the second model was installed on SC-1. The old SC-1 unit was found to be defective after the spacecraft high voltage problem. Although it now appears certain that the voltage levels determined to have been present on the spacecraft could not have caused the flight control sensor group damage, no other possible explanation has been established at this time. The investigation continues. The third flight model (235000-4 SN-1) is now in flight acceptance testing with delivery anticipated for mid-August.

All special tooling and test equipment for the flight control sensor group test position at AFETR have now been completed and checked out.

UNCLASSIFIED

b. Square-wave power compatibility tests. A production model of the new quasi-square-wave power supply was fabricated and compatibility tests were run with a complete flight control sensor group. The power savings, as expected, were found to be 14.7 w in coast phase and 15.6 w in thrust phase. The tests were concluded satisfactorily with no real problems revealed. There is yet the unanswered question of the possible effects of interferences at the spacecraft level.

3. T-2 Subsystem Tests

The first flight control electronics unit was returned from system test for upgrade. This upgrade was accomplished to incorporate the T-2 equivalent of the latest SC-1 changes (such as buzz fix). The unit has been reassembled, retested, and returned to the spacecraft assembly area for installation on T-2N-2. The second T-2 inertial reference unit was delivered for installation on T-2N-2.

Since radar noise magnitude is one of the system uncertainties, a study was undertaken to determine the comparative sensitivity to radar noise of T-2 and the spacecraft. In addition, studies were completed to verify that the design allocations for moment and thrust control were adequate.

a. Radar noise analysis. An analog computer study was conducted to upgrade the T-2 analysis on the effect of radar noise on the T-2N descent performance. The simulation consisted of a three degree-of-freedom planar study of the complete trajectory control system with one inner rate loop. All noise inputs were generated by random noise generators (three independent units) approximating a Gaussian distribution with power levels equivalent to the latest evaluation of the noise levels obtained during the T-2H (helicopter) test. Levels up to ten times T-2H levels were investigated.

In the trajectory control loop the noise level at the range and V_z outputs resulted in vehicle motions that are hardly noticeable (Fig. 57). The vehicle was able to acquire and track the command segments for noise levels as high as ten times T-2H. The loss of thrust command that can result from the rectification of noise in the acceleration command limiters was negligible.

The attitude-angle control loop receives radar noise from the lateral doppler velocity radar output resulting in somewhat random angular excursions. A listing of the peak excursion in angle, angle rate, and lateral velocity follows:

T-2H noise level	θ, deg	ω, deg/sec	V_y, ft/sec
X1	0.3	0.7	0.25
X5	1.4	4.0	1.0
X10	1.8	7.2	1.7

The excursions are, in general, quite small. The only possible problem arises because the angle which exists at the instant 10-ft/sec detection occurs will be held in the inertial mode. The lateral velocity will build up from that time until recovery or touchdown occurs. The present study did not include the inertial hold mode, and thus data on touchdown angles and velocities will require further study. The nominal increase in lateral velocity will be approximately 0.56 ft/sec^2 per degree-of-angle. The nominal time of inertial hold will be 6 sec and thus will result in a lateral velocity increase of approximately 3.4 ft/sec/deg. It was concluded, therefore, that T-2 performance is not significantly degraded by radar noise levels up to ten times those experienced in the T-2H program. This is in part because the noise transfer function (filtering properties) of the T-2 control systems are, in general, narrower and of smaller amplitude than those of the spacecraft. Fig. 58 shows the various transfer functions. The difference in the transfer characteristics is as follows:

The $\theta N/N_y$ curves are different because the difference in gain and inertia of the two crafts causes the natural frequency of T-2 to be higher than that of the spacecraft. $I \approx 25$ slug-ft^2 for T-2 and ≈ 165 for the spacecraft. The damping coefficient is also less for T-2 and this causes the peaking in the plot of $\theta N/V_y$ for T-2.

The difference in the L_x/N_y plot is due mainly to the large difference in the gain K_θ. $K_\theta = 3485$ ft-lb/rad for the spacecraft and 483 for T-2. The difference in the $\Delta T/N_y$ curves is due mainly to the larger gain in the accelerometer loop K_a. $K_a \approx 1260$ in the spacecraft and 406 lb-sec^2/ft in T-2.

c. Moment and thrust control margin study. During vernier descent, an amount of thrust must be allotted to control disturbance moments about the vehicle axes, reducing the total thrust available for deceleration. The principal contributors to these moments are the craft center-of-gravity (cg) offset, effective engine arm tolerance, engine thrust vector offset, and aerodynamic

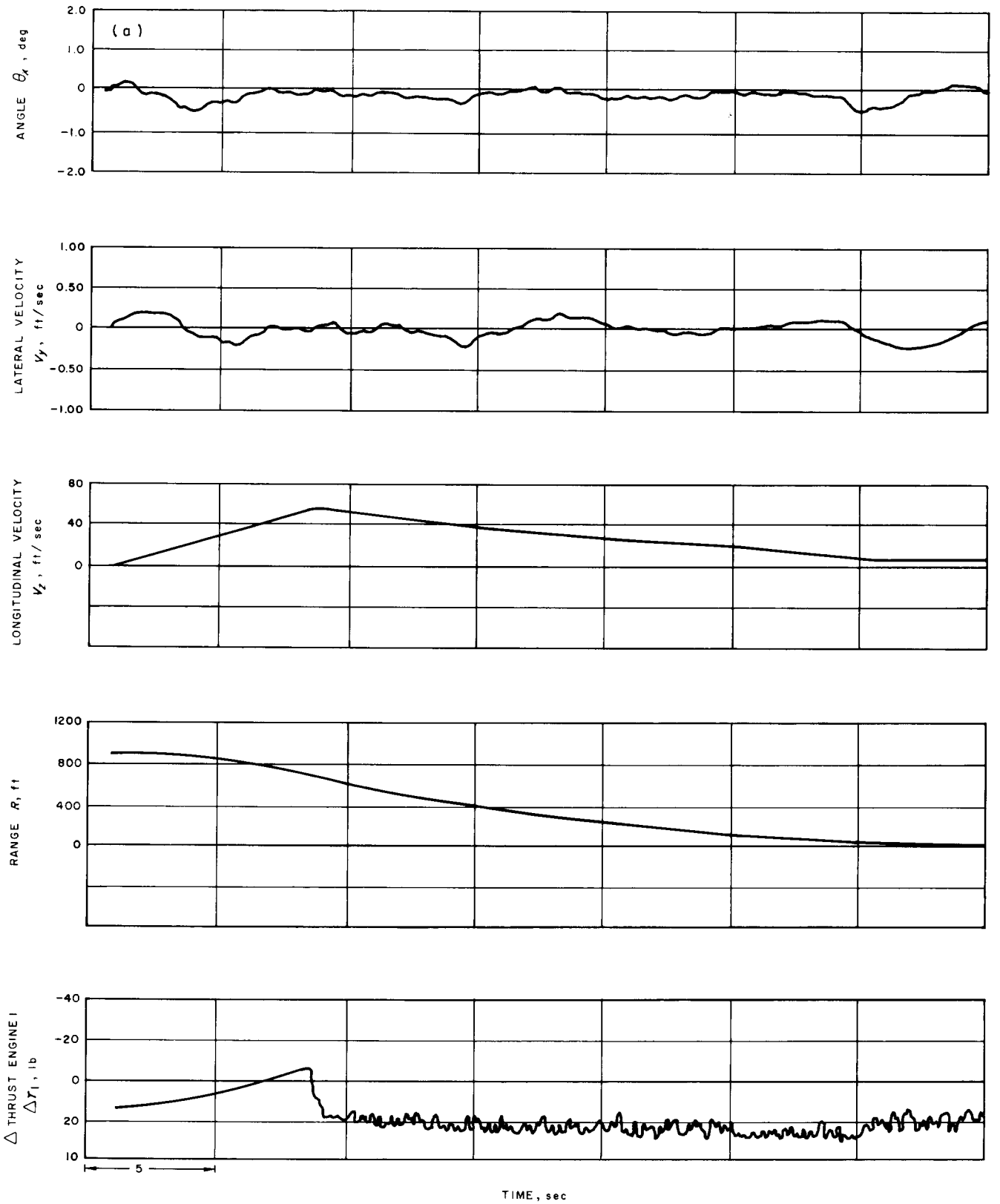

Fig. 57a. T-2N descent performance: radar noise at T-2H level

UNCLASSIFIED

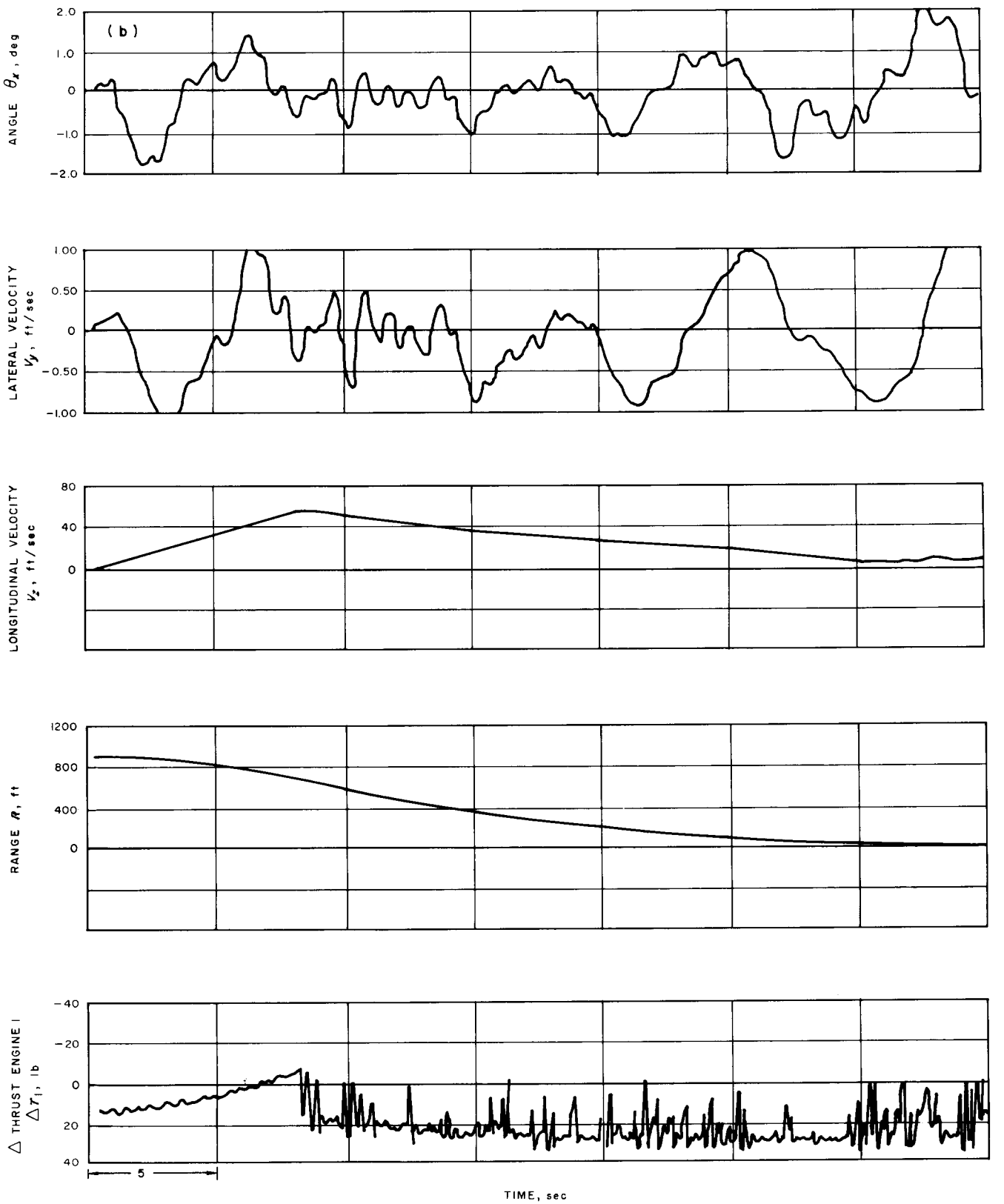

Fig. 57b. T-2N descent performance: radar noise at 5 × T-2H level

UNCLASSIFIED

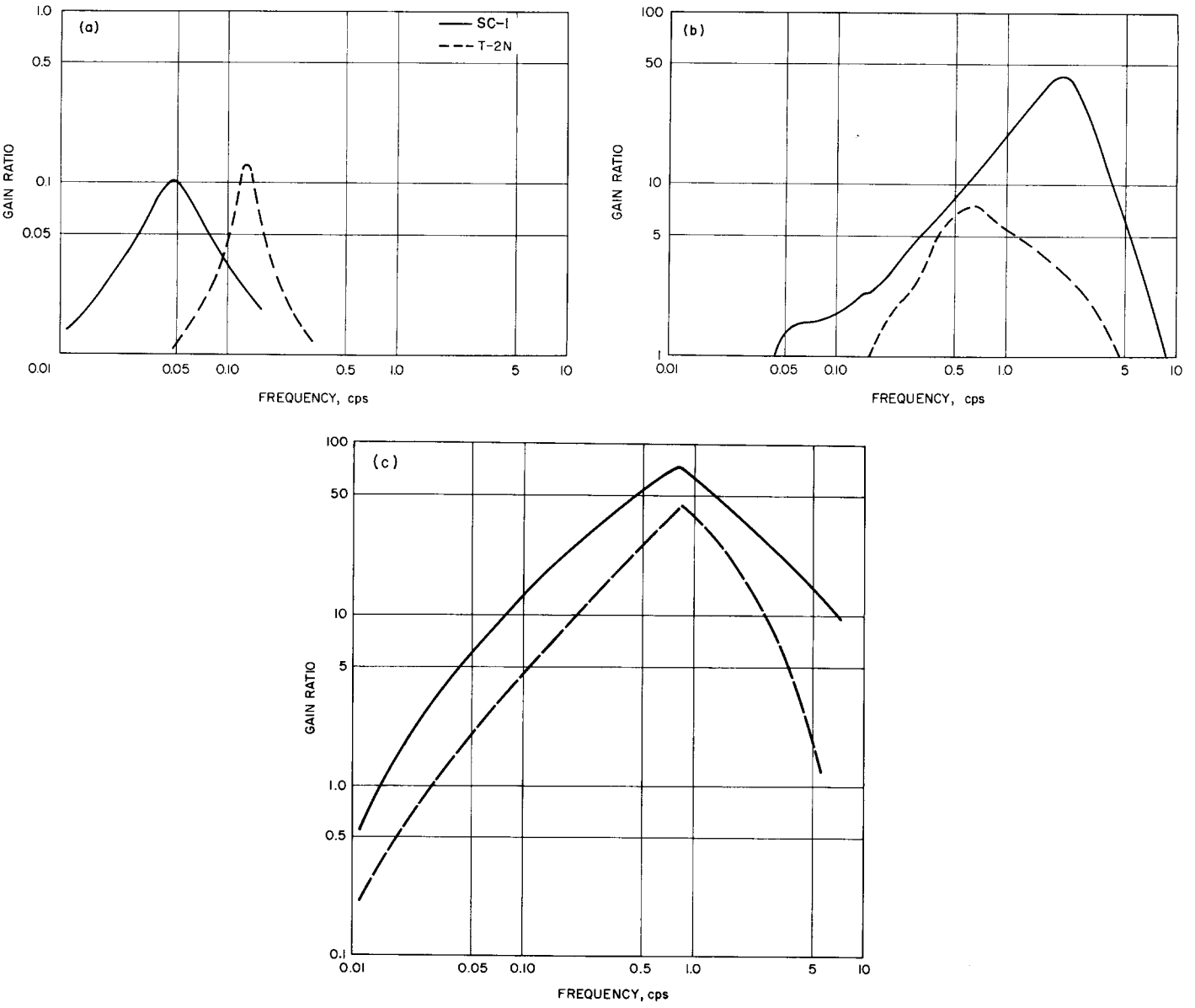

Fig. 58. Radar noise transfer functions for SC-1 and T-2N: (a) angle/noise $\theta N/N_y$; (b) moment/noise $L_x/_y$; (c) Δ thrust/noise at $\Delta T/N_y$

disturbances. Triangular boundaries of maximum cg excursion about the craft geometrical centerline (three axis) have been determined which will result in a maximum of 2 lb of thrust per engine required for moment control compensation. The effective engine arm tolerance is described by variations in the distance between the thrust vector of each engine and the three axes of the craft. An analytical procedure similar to that used for the cg offset was performed to obtain the thrust requirement listed in Table 15. The maximum moment because of the engine thrust vector offset was determined to be

Table 15. Thrust requirements

Contributor	Thrust	
	High, lb	Low, lb
Center-of-gravity offset	2.00	0.90
Engine arm length	0.75	0.35
Thrust vector offset	0.39	0.18
Aerodynamic disturbance	4.25	4.25
Total	7.39	5.68

26.5 in-lb. The thrust necessary to accommodate this is also shown in Table 15. The effect of aerodynamic forces on the T-2 vehicle is relatively unknown. An approximate value for the drag coefficient was obtained from previous T-2 tests and will be updated from the T-2NR test data. System design, with respect to the maximum drag force encountered, has been based on this value. The maximum aerodynamic moment was calculated to be 24 ft-lb by considering the location of the vehicle center of pressure with respect to the cg. The thrust required to account for this is listed in Table 15.

Based on Table 15, the differential thrust allocated for moment control is: high thrust—7 lb/engine; low thrust —6 lb/engine. Therefore, based on engines with a total thrust range of 27 to 80 lb, the maximum thrust available for vehicle deceleration is $T_a = 3(80 - 7) = 219$ lb, and the minimum total output thrust is $T_m = 3(27 + 6) = 99$ lb.

d. Descent segment design. The minimum and maximum acceleration commands were determined so that during vernier descent the total output thrust command would not exceed the thrust range of the vernier engine system. The loop errors such as accelerometer, limiter, and bias were considered in the calculation of the commands that are: $\Delta\hat{a}_{max} = 10.6$ ft/sec^2, $\hat{a}_{min} = 25.0$ ft/sec^2, where $\hat{a}_{max} = \hat{a}_{max} + \hat{a}_{min}$. The descent segments were inscribed in a nominal constant acceleration parabola in the range-velocity plane with $\hat{a}_{nom} = \hat{a}_{max}$. The acceleration parabola was reduced to account for radar, segment, and control system errors. The segments along with the various constant acceleration parabolas are shown in Fig. 59.

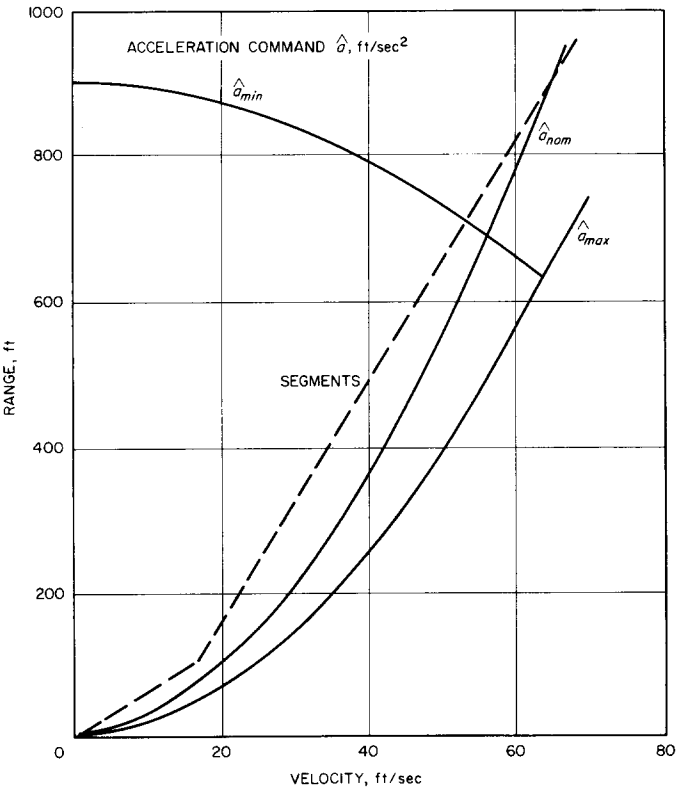

Fig. 59. T-2N descent segment parameters

4. Optical Sensors

a. Canopus sensor. A prototype model of the new production sunshade design has passed the required type-approval-test levels of vibration. The cg and mass moment of this shade are within 10% of the current production shade and in a more favorable direction to endure dynamic testing. The new configuration includes a greater number of baffles than the one previously tested. It is, therefore, intended that stray light and moonlight interference tests such as were performed on the developmental model be rerun employing this configuration. The results of these tests should show that this shade is as good or better than the developmental design evaluated previously.

The production shades were delivered. All sensors will be retrofitted prior to shipment to Cape Kennedy, but after completion of system testing. A brief investigation has been conducted on the effect of spacecraft particles that may enter the Canopus sensor field of view. The results of the investigation are being summarized.

b. Sun sensors. Type-approval-test results for the secondary and acquisition sensors were reviewed. The units were given complete acceptance as being flight-worthy. The primary Sun sensor received acceptance previously. All three sensors are being fabricated on schedule.

5. Inertial Sensors

a. Gyros. The last three of the five gyros involved in the gyro rebuild program have been accepted and have been allocated to SN-7 inertial reference unit, which is designated for the SP-1 (spare) flight control sensor group. The first of the 18 new gyros is due at the end of October. Besides *Surveyor*-qualified electronic components, these new gyros will have 26-gage wire in the external cable instead of the 30-gage wire used previously.

This increase in wire size was made to overcome difficulties in the inertial reference unit assembly and should improve the reliability of the wiring.

b. Accelerometers. The accelerometers on order for the A-21A program will be calibrated by the vendor for best accuracy at the new, lower midcourse acceleration of 0.08 *g*. Presently, the error band is specified at ±33 mv from the 30 v per *g* scale factor in the low *g* region, which yields 1% or better composite error down to only 0.11 *g*. The accelerometers for the A-21 *Surveyors* are meeting 1% at the 0.08-*g* point, so this further optimization can be achieved without affecting interchangeability of inertial reference units.

Type approval testing of two samples of the ±0.75-*g* accelerometers was conducted. After vibration the output of one of the samples was slightly outside the error band over a limited portion of the range. This instrument has been returned to the vendor for analysis and the out-of-tolerance condition has been verified. Pending the results of a teardown analysis, the second type-approval-test sample may be torn down also, since it exhibited similar shifts in output, although not exceeding the error band. These tests were run with a specified vibration input of 30-*g* sinewave, +4.5-*g* random which was known to be near the fragility level of the instruments.

c. Inertial reference unit. SN-3 inertial reference unit was delivered and is undergoing group-level flight acceptance testing with the SC-2 flight control sensor group. Testing to determine the characteristics of the thermal unbalance among the three gyro positions in the inertial reference unit is continuing. The thermal control model (TCM) and SC-1 solar-thermal-vacuum tests will be the proof tests of the added side radiator. For backup information, temperature sensitivity tests were run on one gyro over the temperature range from 172 to 188°F. The data are to be confirmed by tests on at least one gyro, but the results so far show reasonably low temperature sensitivities in the key gyro parameters. Transfer function sensitivity was 2.5%/°F and the torquer scale factor sensitivity was −0.07 deg/hr/ma/°F. Drift parameter changes over the +8°F temperature range were not identifiable as trends when plotted against temperature. Therefore, the sensitivity is less than the 0.3-deg/hr variations noted in the day-to-day test data.

6. Electronics Unit

The unit scheduled for use in SC-3 was retrofitted to the latest configuration and returned to system test. This unit is the first to incorporate the new 400-cps electronics control unit which generates 3-ϕ quasi-square-wave voltages to power the gyros. Unit SN-16, scheduled for use as SC-4, is in final stages of testing. This unit is identical to the SC-3 configuration.

Starting with SC-3, all units will incorporate the revised wiring harness with two additional connectors for squib circuits and one for test access. The dynamic model of the redesigned unit using dummy weights for the new harness passed vibration test at 1½ times type-approval-test levels. A model using the actual redesigned harness is undergoing vibration tests to determine adequacy of harness design.

The feasibility study to investigate the use of a contour cable for the flight control electronics unit wiring harness was completed. Since there were several developmental problems which would complicate an already difficult scheduling problem, it was decided not to attempt a switch to contour cable at this time. The decision was based on reasoning that for its incorporation to be economically attractive an SC-3 effectivity was essential. It is intended, however, to improve the fabrication techniques used on the present harness by specifying the exact lengths and routing of each wire.

7. Gas Jet System

a. Gas tank. The gas tank cleaning procedure was changed to require the installation of the gas charging fitting prior to the cleanliness test to eliminate the contamination that might be generated with installation of the fitting after cleaning. Twelve tanks were received prior to this change. Six tanks that were received with incorporation of this change will be used beginning with the SC-3 spacecraft. Tests are planned to investigate the effect the installation of the charging valve has on the tank cleanliness before deciding if the tanks without the change should have the fitting installed and then recleaned.

b. Pressure control. The pressure-control type-approval test was completed and the results were approved.

c. System test. The system test specified in the flight-control/TCM Integration 224697 Revision B were reviewed for adequacy of checking the pneumatic characteristics in view of difficulties encountered with the T-21 and SC-1 spacecraft. Additional tests including regulator lockup pressure, system leakage, and contamination are now planned.

8. Roll Actuator

The data from the roll-actuator type-approval program has been reviewed and the design has been judged acceptable. The unit used for the type-approval-test program has since been modified to correct the mounting deficiency, and the alignment pin that fractured was replaced by a press-fit pin bonded with an epoxy. In addition, the thermal shield and pin puller were added.

With the unit in this configuration, an additional 12 min of type-approval-test vibration was performed. The primary purpose of this additional exposure was to satisfy the new requirements for 48 instead of 36 min of vibration. A second reason for the additional tests was to evaluate the effect of the mounting provision changes on the weaker-type alignment pin. Visual inspection, as well as a quick preliminary checkout of the unit, has indicated no apparent damage. Since the weaker-than-flight-type alignment pin survived, confidence in the mounting changes has increased. Further functional checkouts are continuing on the unit. Following these checkouts, the unit will be subjected to additional flight-acceptance-test vibration exposure to gather data on fatigue life.

An additional vacuum firing test of a single vernier engine attached to a flight-type mounting bracket and an operating flight-type roll actuator was accomplished at the JPL Edwards Test Facility. Near maximum thrust, with several near minimum portions, was commanded during a maximum duration test while roll actuator responses to various inputs were measured. A modified thermal isolator assembly, replacing the assembly that failed during the previous firing test, was installed between the roll actuator/vernier engine bracket and support bracket. Additional thermal sensors were installed on the assembly, and flight-type strain gages were applied to the roll actuator/vernier engine bracket to measure thrust.

The results of preliminary data analyses indicate the following:

(1) Modified thermal isolator assembly showed no evidence of structural failure or overheating.

(2) Roll actuator responses are within normal range.

(3) Strain gages provide acceptably accurate measure of vernier engine thrust and vernier engine vibration due to combustion.

I. Electronics

1. Low-Gain Upper-Hemispherical Antenna

Consideration is being given to the addition of another antenna on the spacecraft to improve the overall performance of the telecommunications subsystem. This antenna, having a broad pencil beam and a small backlobe, will be mounted above the spacecraft, with the peak gain in the spacecraft $-z$ direction. Some of the benefits that will be realized with this antenna are:

(1) The patterns of the low-gain antenna will be influenced by the spacecraft to a much lesser degree than the patterns of the present omni-antennas because of the much smaller backlobe radiation of the low-gain antenna.

(2) A significant reduction of the lunar reflection problem should be realized.

The low-gain upper-hemispherical antenna will have right elliptical polarization and operate at both transmit and receive frequencies. System requirements have dictated the following design goals:

(1) Gain (as a function of half-cone angle θ), where θ measured from $-z$ axis ≥ -3.0 db for $0 \leq \theta \leq 80$ deg, and < -20.0 db for $100 \leq \theta \leq 180$ deg.

(2) Voltage standing wave ratio < 1.5 at 2295 Mc, and < 2.0 at 2115 Mc.

Development of this antenna is in progress. The antenna will consist of a turnstile antenna located one-quarter wavelength above a ground plane approximately 10 in. in diameter. Measurements to date show that to satisfy the backlobe goal the maximum half-cone angle within which a minimum gain of -3 db can be achieved is restricted to approximately 65 deg. These conditions give a peak gain of 5 to 6 db.

2. Auxiliary Antenna Switch

The auxiliary antenna switch selects between the upper-hemispherical antenna and the omni-antenna and is comprised of a single-pull double-throw (SPDT) switch and a solid-state drive circuitry to actuate the switch. This unit operates the same as the transfer switch and utilizes the same associated drive circuitry in the *Surveyor* transmitter.

The physical design of the unit is envisioned as follows. The overall dimensions will be 2.50 × 3.00 × 3.50 in. high. The package consists of a machined channel housing with the SPDT RF switch mounted in the module and a printed circuit board on each side. The input voltages (29 and 22 v) and the command signals will come through a nine-pin Cannon connector. The RF inputs and outputs are an integral part of the SPDT RF switch. The switch driver circuitry, comprising approximately 40 components, is located on the two printed circuit boards.

The design effort on the control item is about 90% complete. All of the components needed are already in-house.

3. Boost Regulator 274200-4 Series

ECA 111985 created the -4 configuration of the boost regulator. This engineering change increased the OTC bypass boost voltage by moving the bypass silicon controlled rectifier (SCR) gate driving circuit from the 30-v line in Module 284227 to the 33-v line. R12, the gate voltage divider resistor, was replaced with a higher wattage resistor (2 w). Since this resistor is too large physically to place in a module, it was mounted on the A1 chassis and renumbered R8. Rework to the module included removing R15, leaving this position vacant. R12 was removed also and replaced by a feed through wire. Diode CR1 was removed and replaced with a higher-conductance-type diode (988723-1). The module was freeze-coated and replaced in the boost regulator. R15 was replaced across the bypass SCR gate to the cathode and renumbered R9. An 0.01 capacitor from the flight control regulator base was added to the 33-v bus to increase the flight control output bus stability.

4. Wide-Band Modulator Change

A circuit study is underway to determine changes necessary to extend the frequency response of the present wide-band modulator from 220 to 265 kc because of the addition of a 250-kc subcarrier oscillator (SCO) on the SC-5 spacecraft and up.

A wide-band modulator breadboard has been built and circuit changes are being made to extend the frequency bandpass. The crystal in the voltage-controlled crystal oscillator will have to be replaced since the present crystal has unwanted spurious output around 250 kc. The complete circuit analysis is expected to be completed during the next report period.

5. Deletion of Pre-Emphasis in Wide-Band Modulator

In the original 231800 transmitter the wide-band modulator had a 6 db per octave pre-emphasis characteristic above 25 kc. System engineering found that the pre-emphasis had several degrading effects on the TV picture. The degrading effects were: (1) greater than 10 db over deviation of the carrier at high TV line rates, (2) overshoot and ringing of the sync waveform, and (3) undesirable slowing of the received sync pulse rise time. Therefore, the wide-band modulator has been redesigned to eliminate the pre-emphasis. Other improvements were added at the same time to the wide-band modulator to simplify and shorten the test time required to align this module. Transmitters containing the new wide-band modulators have been delivered for SC-1 and SC-2.

6. Voltage-Controlled Crystal Oscillator (VCXO)

The *Surveyor* transmitter was modified to desensitize the narrow-band VCXO command lines to transient pulses. The observed transients conducted on the command lines were caused by the RF transfer switch. A 10- to 15-v peak-to-peak pulse of narrow width existed on the narrow-band VCXO off-command line that was sufficient to switch the transmitter from narrow band to wide band when the transfer was actuated. This situation was corrected by adding an R-C filter in the input circuitry of the off switch. This additional delay makes the switch insensitive to pulses as generated by the transfer switch. Protection was increased by adding a block diode in the VCXO on-command line, making the narrow-band VCXO switches insensitive to a ±15-v 10-ms pulse.

7. Transmitter SN-18

Circuit analysis was performed on the SN-18 transmitter to determine the electrical stress that may have occurred on components during SC-1 failure on June 27, 1965. The analysis was performed for three conditions:

(1) 29-v bus rising to 54 v.

(2) 29-v bus rising to 70 v.

(3) 29-v bus rising to 130 v.

In Cases 1 and 2, a zener diode in the oscillator and associated resistors would be the only components overstressed. In Case 3, several transistors and resistors would be overstressed. The zener diode is being examined to determine the level of overstress. Also, several zener diodes of the same type are being stressed to determine

the time at each voltage case that the zener would have survived. The transmitter has been tested since it was returned and meets all specifications at room temperature.

8. Antenna Radiation Measurements[4]

a. Introduction. Hughes Aircraft Company has measured the *Surveyor* omni-directional spacecraft antenna patterns on their 3000-ft range. Resulting measurement errors, using this range and an early prototype spacecraft model, have produced uncertainties in the radiation patterns which are excessive. Therefore, a remeasurement program has been initiated at JPL. This program is required so that JPL can determine if the *Surveyor* telecommunications system is capable of supporting a standard *Surveyor* mission. The measurements are to be performed on the JPL 3300-ft antenna range utilizing a specially built full-scale *Surveyor* spacecraft model.

To acquaint the reader with the remeasurement task, the following topics will be discussed:

(1) *Surveyor* omni-radiation patterns.

(2) Measurement errors due to multipath transmission.

(3) Current progress of remeasurement task.

b. Surveyor omni-radiation patterns. The *Surveyor* spacecraft communication design and philosophy requires full spherical antenna coverage. This coverage is provided by two quasi omnidirectional antennas located 150 deg from each other in two different planes parallel to the x-y plane of the spacecraft coordinate system (Fig. 60). The primary radiation patterns have a basic cardioid shape. When coupled with the spacecraft, the resulting secondary pattern has the basic cardioid shape but with large serrations due to the primary pattern coupling with the spacecraft.

c. Measurement errors due to multipath transmission. Among the sources of error in the present *Surveyor* patterns is the error due to multipath transmission or what is more commonly known as range reflection and diffraction. This source of error is basically caused by energy reflected and diffracted off of the Earth and any other objects which might be located between the transmitter and antenna under test (Ref. 9). We can say that the antenna under test effectively sees multiple illuminating sources of varying phase and amplitudes being propagated from various angular directions. It is these "apparent" sources which give rise to error in the measurement. That multipath transmission can have serious effects on the resulting illuminating field is demonstrated by the curve of Fig. 61.

The pattern measurement error due to multipath transmission is a function of the gain level being measured (Ref. 9). The angular discriminatory nature of a high-gain antenna radiation pattern prohibits the reception of the total multipath transmission incident on the antenna, thereby decreasing the "error" or "multipath" energy detected at the antenna. On the other hand, the low-gain antenna is much less discriminatory in the angle over which it will receive energy. The resulting energy received at the low-gain antenna contains, therefore, a greater percentage of "error" voltage and the accuracy of measurement is degraded.

A significant source of field distortion at the JPL range is that due to the spacecraft support tower which supports and positions the spacecraft during the pattern measurements. A measurement program is currently underway to assess the effects of a support tower on the plane wave illumination at various locations about the tower. Knowledge of such effects will provide information concerning that volume of space through which the antenna may traverse without serious degradation due to support tower reflection and diffraction. A minimal spatial volume in which accurate measurements can be made is discussed in Part *d* that follows.

d. Current progress of remeasurement task.

Definition of spacecraft model. During the study phases of the remeasurement program it has been determined that a spacecraft model of higher quality than the early prototype originally used by Hughes Aircraft Company will be necessary if the increase in accuracy to be obtained with the JPL range is to be realized.

The higher quality model is defined in two respects:

(1) The spacecraft model will be required to have dimensional configuration integrity independent of orientation in a 1-g field. This has been defined as a $\pm$¼-in. dimensional tolerance.

(2) The spacecraft model to be used for pattern evaluation must appear as a nominal *Surveyor* spacecraft when illuminated at the command and telemetry frequencies. This implies an "external *Surveyor*" configuration with nominal reflectivity to S-band energy.

[4]Prepared by JPL Technical Section 336.

UNCLASSIFIED

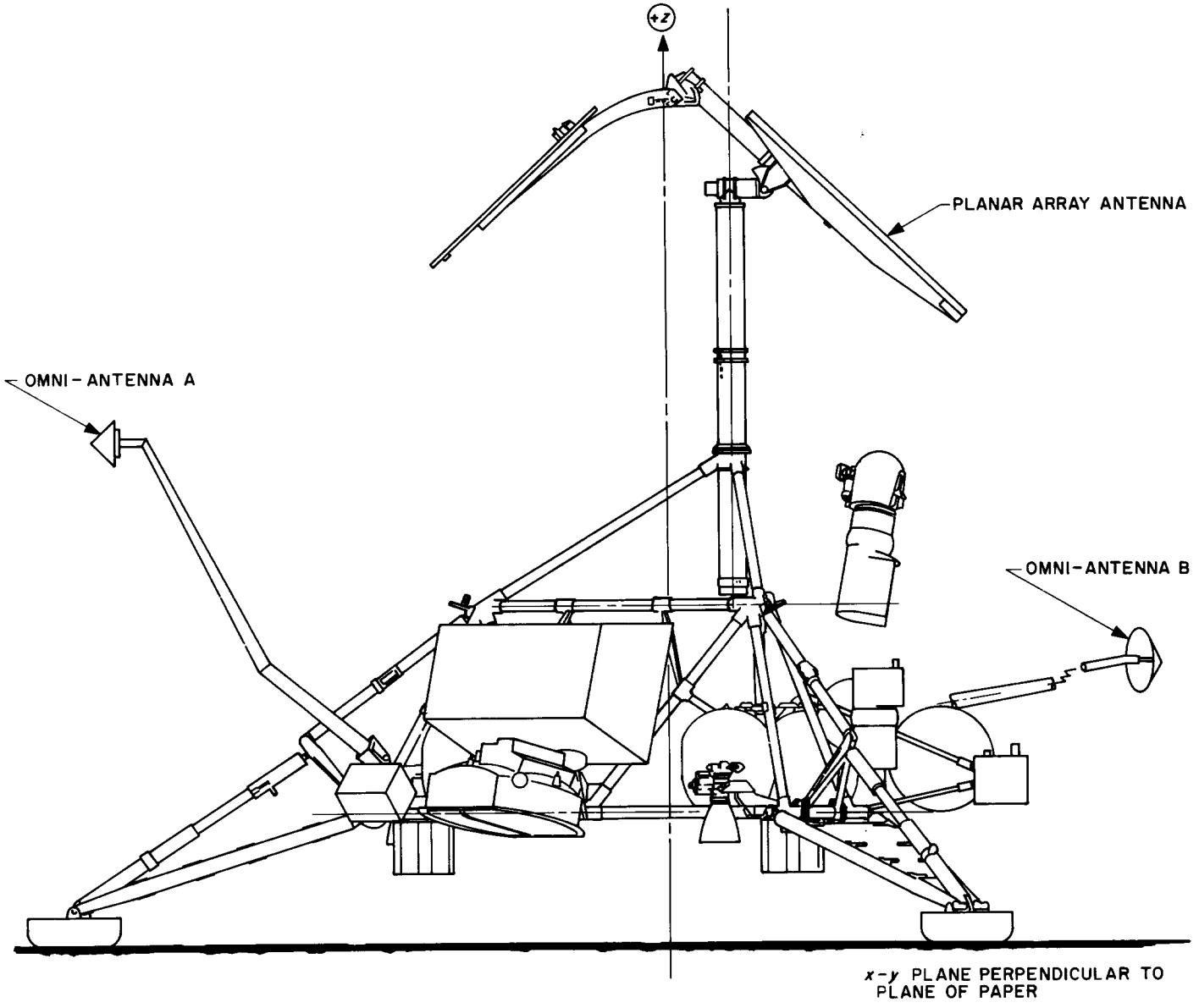

Fig. 60. *Surveyor* spacecraft communications antennas

A model of nominal reflectivity is required if radiation patterns which are heavily coupled to the spacecraft are to be accurately duplicated.

As previously stated, full spherical coverage is required for the *Surveyor* spacecraft. In the measurement scheme certain restrictions in antenna position limit the volume of space through which the spacecraft antenna may traverse while being measured. These restrictions are imposed by:

(1) The resulting diffraction produced by the mast and positioning mechanisms which are used to support the spacecraft during measurement.

(2) The reflections and resulting pattern distortion that would be produced if an antenna is directed toward the Earth during the process of measuring its pattern.

It then follows that the antenna under test must not enter the lower hemisphere or the quadrant of the upper hemisphere which lies behind the illuminated mast. It is desirable to record patterns only in the upper front quadrant of a sphere surrounding the spacecraft as viewed from the illuminating antenna (Fig. 62). These restrictions can be relaxed in some cases depending on the maximum allowable error which can be tolerated.

UNCLASSIFIED

The limited volume of space through which the antenna may traverse while being measured implies that the spacecraft must be capable of being mounted in more than one location if full spherical coverage is to be obtained. It further implies that, in the general case, the spacecraft roll axis must assume elevation positions varying from vertical to horizontal.

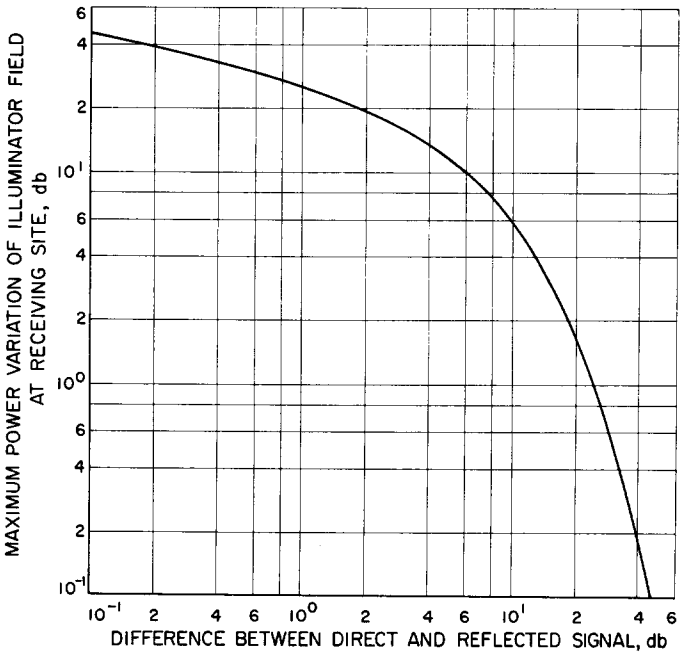

Fig. 61. Illuminated field variation vs reflected signal level

According to the consensus of opinion of JPL Engineering Mechanics Division representatives, mounting the *Surveyor* spacecraft in a horizontal position poses very severe deflection problems. If a flight structure is used for the tests, the antenna/solar panel positioner mast will suffer severe deflections and might ultimately break when mounted in a horizontal position. Components such as equipment boxes, batteries, etc, will also suffer deflections which would be intolerable from a pattern accuracy point of view. A structurally sound model is needed since horizontal suspension is necessary in recording patterns.

It has been decided to construct a special spacecraft model for the pattern measurements. A "*Surveyor* RF Modeling Quality Specification" has been written and defines the general guidelines and ground rules to be used for building the model. This model will be suitable in an RF reflectivity sense, and provide deflections which are adequately small when the spacecraft is orientated in a horizontal position.

Plans for construction of this new model are presently being initiated. The basic structure, including the solar

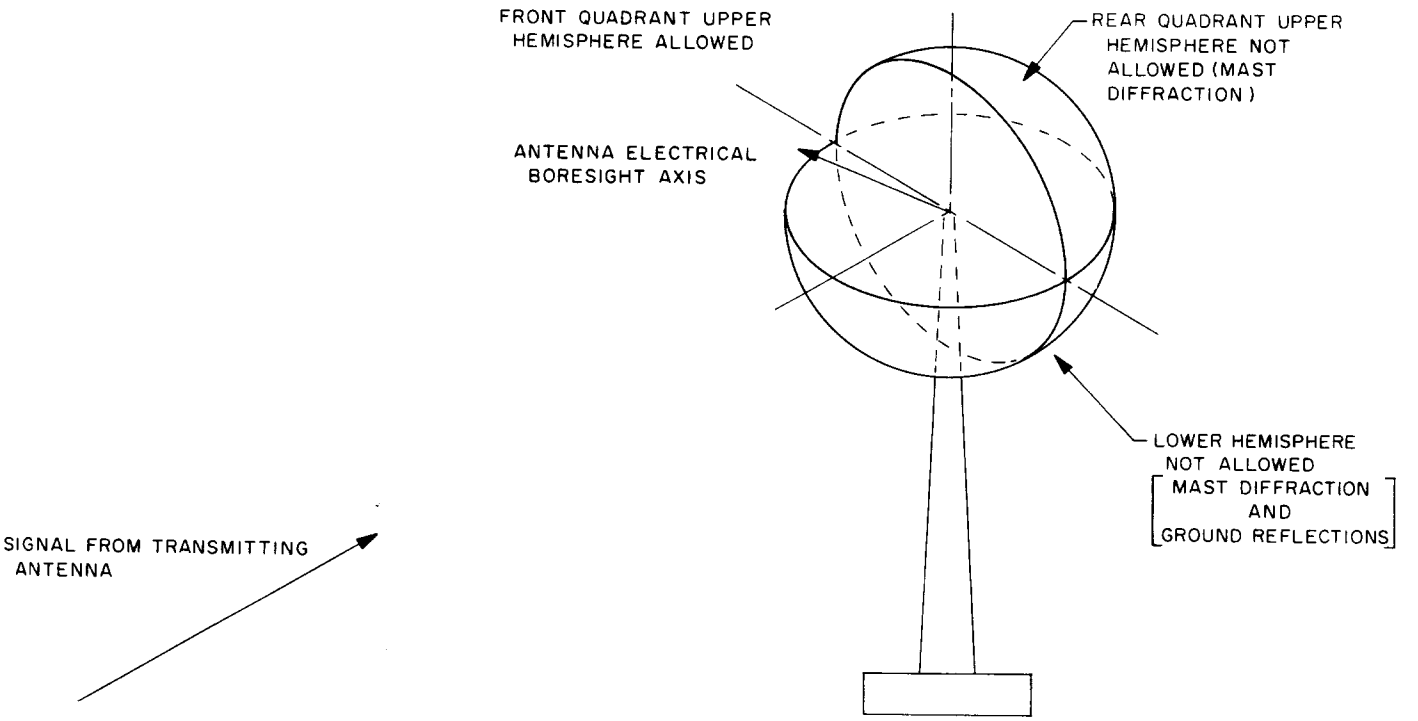
FRONT QUADRANT UPPER HEMISPHERE ALLOWED
REAR QUADRANT UPPER HEMISPHERE NOT ALLOWED (MAST DIFFRACTION)
ANTENNA ELECTRICAL BORESIGHT AXIS
LOWER HEMISPHERE NOT ALLOWED MAST DIFFRACTION AND GROUND REFLECTIONS
SIGNAL FROM TRANSMITTING ANTENNA

Fig. 62. Restricted region of antenna positions

panel/planar array mast, shall be mocked up with 4130 welded steel construction. Flight-type spacecraft components which are found unavailable for model use shall be mocked up with foam plastics, fiberglass, or wood coated with a suitable conductive surface.

Spacecraft support tower. A tower to support the spacecraft during measurements has been designed and is presently being released for fabrication. It has been designed to support a 1000-lb spacecraft during a 90-mph wind. There are two positioning degrees of freedom provided, which correspond to the cone and clock angles of the spacecraft coordinate system. The cone angle variation is provided by a heavy-duty azimuth rotator upon which the support tower is fixed. The clock angle is provided by a bearing and motor drive located inside the spacecraft retromotor.

Minimum spacecraft handling is accomplished by tilting the support tower about an axis at its base (Fig. 63) to a horizontal position and then placing the spacecraft over the retromotor which is pre-assembled to the support tower. After fastening the spacecraft to the retromotor, the support tower–spacecraft assembly is raised to a measurement position and locked in place. Support tower fabrication is to be completed October 4, 1965.

J. Electrical Power Supply

1. Solar Panel

a. Flight hardware. The status of flight panels is as follows:

(1) Solar Panel 1—being held as spare unit.

(2) Solar Panel 2—diode retrofit completed June 2, 1965; flight acceptance vibration test on the SC-1 spacecraft performed during June 1965; the panel is presently being prepared for SC-1 spacecraft optimum charge regulator integration testing.

(3) Solar Panel 3—dampener rod socket and grounding strap retrofit completed June 1965; diode retrofit completed July 1965; panel being prepared for repeat flight acceptance testing.

(4) Solar Panel 4—fabrication resumed on the basis of revised diode installation technique; flight acceptance testing to be initiated August 1965.

(5) Solar Panels 5 and 6—remain in storage.

b. Diodes. Eighteen pairs of diodes were installed on the S-2 dummy solar panel to evaluate possible solutions to the diode installation problem (*SPS 37-34*, Vol. I).

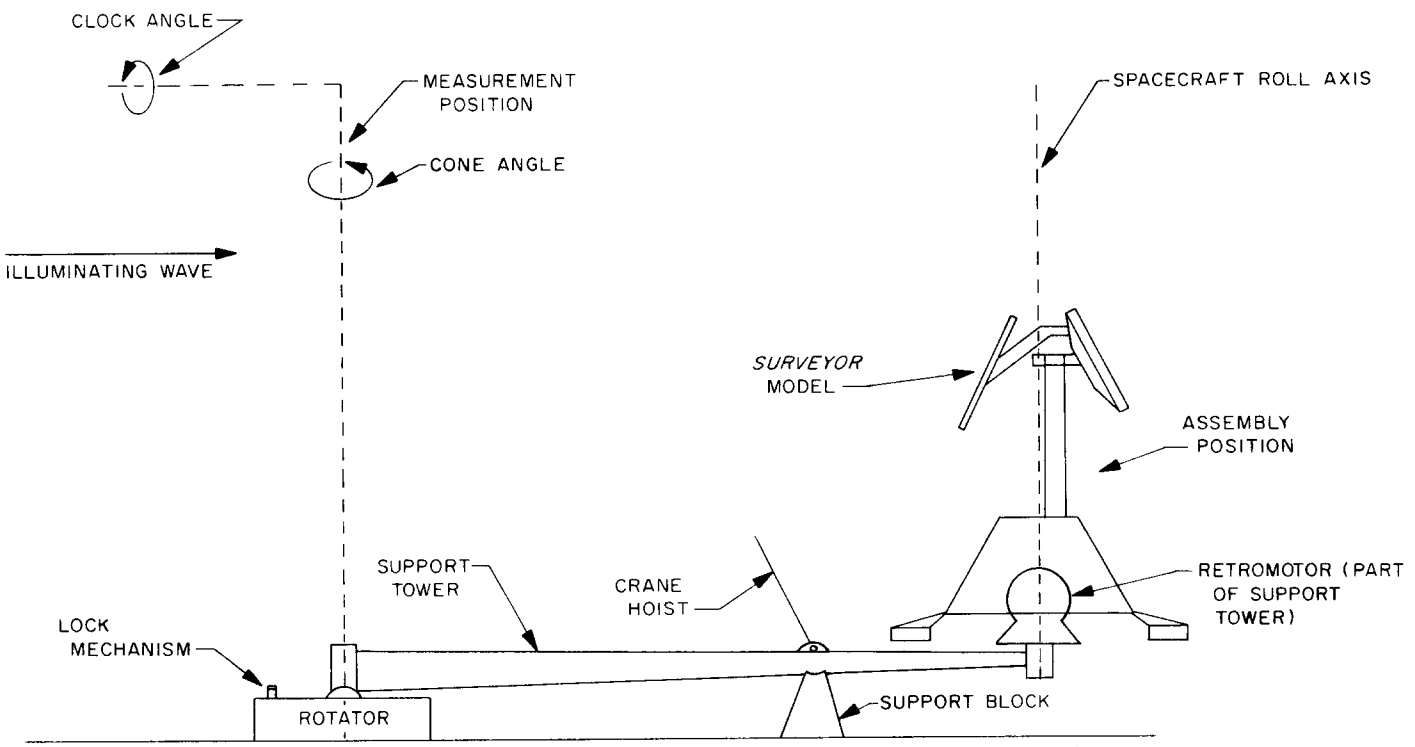

Fig. 63. Spacecraft support tower mounting procedure

Diode installations identical to the original design were included. After type-approval thermal-vacuum exposures of 100 hr at 235°F and 100 hr at −260°F at 10^{-6} mm Hg pressure, all diode installations of the original design had failed and all new test specimens had successfully survived the environments. One of the new test specimens that used the original potting material (RTV-731), but with multiple coatings of teflon release agent applied to the diode body, was chosen for use in flight solar panels. To minimize schedule slippage, diode retrofit was performed on solar panels SN-2, -3, and -4 in parallel with conduct of the qualification program. The retrofit will be fully qualified on completion of the S-2 dummy solar panel type-approval vibration testing which has been delayed approximately 2 mo because of unavailability of the antenna solar panel positioner (A/SPP) mast. No difficulty is anticipated with vibration qualification testing since diode failures have been shown experimentally and analytically to result from low-temperature thermal environments. Retrofit diode installations on solar panel SN-2 successfully underwent SC-1 flight-acceptance vibration testing. All retrofitted solar panels, with the exception of SN-2, will be subjected to a repeat flight acceptance test sequence on a unit basis.

c. Thermal shock test. Solar eclipse will subject the solar panel to rapid temperature changes. Solar eclipse tests were run in the Hughes Aircraft Company solar-thermal-vacuum chamber to determine the maximum temperature rate of change and to verify that the solar panel is able to withstand the thermal shock.

The thermal test consisted of two exposures. The first exposure began at 143°F (maximum transit temperature) followed by a cooldown to −130°F and a return to transit conditions. This represented a ½-hr eclipse which is the maximum spacecraft eclipse time. The second exposure was a cooldown to −195°F followed by a return to transit temperatures, corresponding to the 1-hr period during which the spacecraft may be randomly oriented while the solar panel is shadowed.

Fig. 64a shows temperature change during the initial 2 min of cooldown from +143°F. The solar panel temperature dropped 33°F in the first minute. During warmup from −130°F a thermal shock of 44°F/min occurred; during warmup from −195°F the solar panel experienced a thermal shock of 52°F/min. The warmup curves are shown in Fig. 64b.

Electrical performance tests of the solar panel were conducted in sunlight before and after the thermal shock

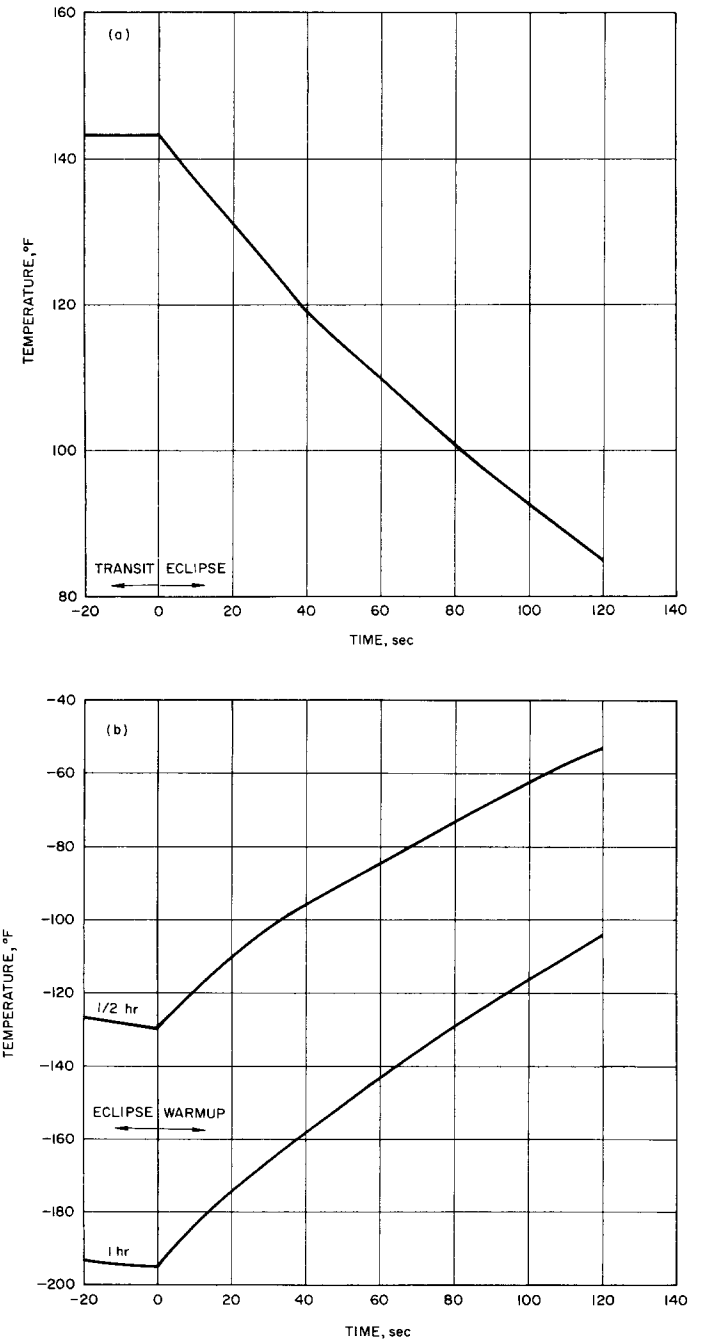

Fig. 64. Thermal shock on front (solar cell side) of solar panel: (a) cooldown during eclipse; (b) warmup following eclipse

tests; results are shown in Table 16. Total panel performance remained above absolute specification requirements. The reduction in total panel power was primarily caused by Subgroup V-5 degradation. An incipient failure in a V-5 solar cell existed prior to thermal shock testing and was not a result of the thermal shock exposure. Decreases

UNCLASSIFIED

Table 16. Electrical performance before and after thermal shock

Item	Power at 140 mw/cm², 25°C		
	Requirement, w	Pretest	Post-test
Total panel (less diodes)	54.0[a]	58.0	55.5
Subgroups			
V-1	10.79	11.87	11.52
V-3	10.79	11.54	11.52
V-5	10.79	11.52	10.18[b]
V-7	10.79	11.67	11.40
V-9	10.79	11.71	11.41

[a]Based on 5/9 of flight panel requirement since reliability panel was equipped with only five of nine subsystems.
[b]Intermittent defect noted prior to thermal shock testing.

in power output of three of the four remaining subgroups were noted although the subgroups continued to meet specification requirements.

Physical examination of the solar panel prior to and following thermal shock testing revealed no important damage. There was an increase in the number of cells having slight coverglass delamination. The white epoxy insulating finish on the front side of the solar panel was slightly yellowed by the xenon illumination.

d. Decompression tests. Four solar panel substrates were subjected to decompression tests to simulate the pressure change occurring at launch. The drop in test chamber pressure conformed to the pressure profile envelope shown in Fig. 65. There was no evidence of substrate damage following the exposure. Five more substrates will undergo decompression testing in early August.

e. High-temperature test program. Preparation for high-temperature tests is underway. Test apparatus consists of a solar panel container which has been redesigned to permit installation of a two-layer mylar window. To heat the panel to the predicted maximum lunar-day temperature of 230°F either a forced-air heating system or radiant heaters will be employed. The merits of the two heating systems are being evaluated. The use of two layers of mylar separated by a ⅜-in. air space rather than one layer of mylar reduces the heat loss through the window from 6 to 1 kw. Addition of the mylar will cause approximately 28% transmittance loss in useful solar illumination. However, test results are expected to give a good indication of solar panel performance at elevated temperatures.

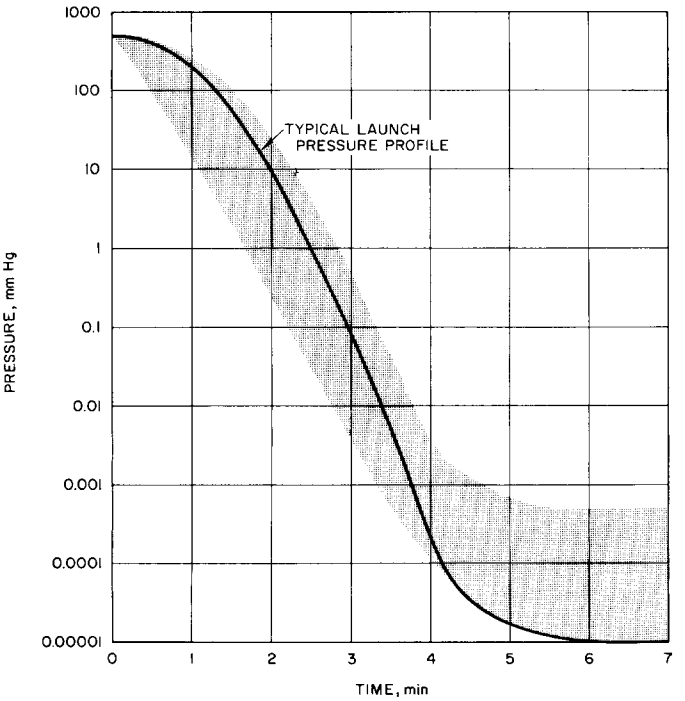

Fig. 65. Panel decompression test — pressure profile envelope

When the test container is completed, a sunlight test will be performed utilizing the type-approval solar panel. The greenhouse effect of the mylar window is expected to raise the panel temperature to approximately 170°F without additional heating. No heaters will be employed in the first phase of the test program to check this expectation. After completing the first phase, the selected heating system will be installed and the lunar day environment will be simulated by heating the panel to 230°F.

f. Eastern Test Range (ETR) operations. Solar panel tests were conducted at ETR during May 1965. Operations included short-circuit current tracking between primary standard cells and the reliability solar panel, checkout of the test console built by launch operations, and sunlight performance testing of the solar panel. The JPL solar simulator was uncrated, assembled, and adjusted for use. Success of the operations demonstrated the feasibility of solar panel sunlight performance testing at ETR.

g. Systems testing. Solar panel SN-2 underwent SC-1 spacecraft flight-acceptance vibration testing during June 1965. Following the test, one partially cracked solar cell was found at location V9-19A, as shown in Fig. 66. Cause of the cracked cell has not been determined. Following

UNCLASSIFIED

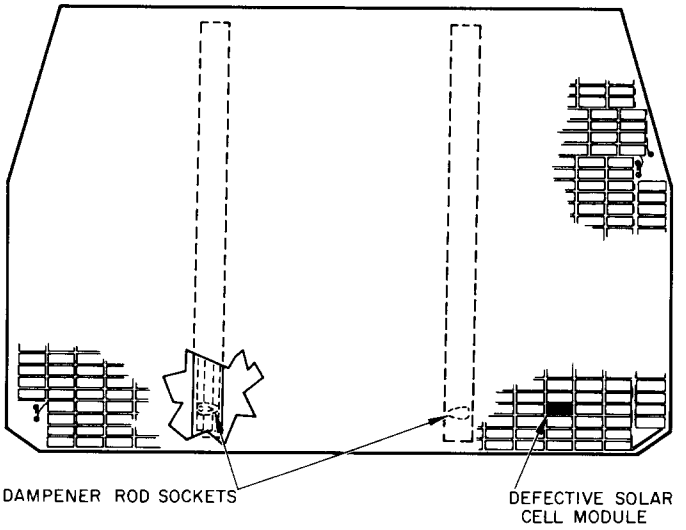

Fig. 66. Location of defective solar cell module on SN-2 solar panel

replacement of the defective solar cell module and electrical performance retest in sunlight, the solar panel will undergo optimum charge regulator electrical integration testing on the SC-1 spacecraft under xenon illumination.

h. Design review. A special solar panel design review was held in June. Panel design modifications were discussed as well as present manufacturing status. The major portion of the review was devoted to a discussion of topics recommended by JPL, including components selection, qualification and flight-acceptance test programs, electrical performance, data reduction procedures, inspection procedures and acceptance criteria, reliability, and failure reports.

2. Batteries

a. Main battery. Flight acceptance testing was performed on SNs 19 through 28. SNs 19 and 20 were shipped to ETR for use on the SD-2 flight vehicle. Both batteries have an aluminized outer wrapping for thermal control. A third battery, SN-26, is also being prepared for SD-2 flight availability.

Five batteries are undergoing a reliability test program. After successful completion of flight acceptance level vibration testing, the batteries were placed on an automatic charge-discharge sequence simulating lunar mission conditions. At present, the batteries are functioning under simulated second lunar day requirements. Data reduction and analysis is expected to be completed in the next report period. The last four reliability batteries are in fabrication, with vibration testing scheduled early in August.

b. Auxiliary battery. Auxiliary battery SN-2 was delivered for use in testing of the SC-1 spacecraft. During conduct of special tests on the spacecraft, a high voltage condition occurred on the regulated bus and resulted in failure of some units. Special tests were conducted on the battery to determine whether the battery was in or out of the electrical subsystem at the time of the high voltage condition and to determine the ability of the battery to accept charge. The battery was shown to be capable of accepting charge currents up to at least 5.0 amp without a large increase in voltage; the battery presented a low impedance to the charging source.

As a further study, another auxiliary battery (SN-26) was charged at various battery capacity levels to determine the maximum battery on-charge voltage that would be reached in a 15-min charging period. Charging was performed at a 2.0-amp rate utilizing the solar panel simulator. Discharge was performed at a 6.0-amp rate and was continued until the battery charge was reduced by 20% from its previous charged state. Charge and discharge cycles continued until the battery was completely discharged. The results are tabulated in Table 17.

Table 17. SN-26 auxiliary battery maximum charge voltage test summary

Battery capacity, %	Charge rate, amp	Charge time, hr	Maximum charge voltage, v
100	2.0	0.25	27.43
80	2.0	0.25	24.50
60	2.0	0.25	22.25
40	2.0	0.25	22.25
20	2.0	0.25	22.50
0	2.0	0.25	22.40

Flight acceptance testing is underway on SNs 18 through 25, and 27 through 29.

c. T-2 batteries. T-2 main batteries SN-104 through -113 met flight acceptance test requirements and have been used in various T-2 vehicle engineering and environmental tests. Ten additional batteries have been ordered from Electric Storage Battery Company to fulfill system requirements. T-2 recovery batteries SN-4 through -25 met flight acceptance requirements and have been used in T-2 vehicle environmental tests. Ten recovery batteries were sent to Holloman AFB to be used in T-2 descent tests. Twenty-five additional batteries have been ordered from Eagle-Picher Company.

UNCLASSIFIED

Table 18. Battery life test

Battery SN	2-hr soak temperature, °F	Voltage, v	Current, amp	Voltage, v	Current, amp	Voltage, v	Current, amp	Voltage, v	Current, amp
		3 days		4 days		5 days			
43	40	10	5	11	5	9	4		
35	Ambient	14	5	14	5	14	7		
32	Ambient	15	6	16	7	16	7		
37	100	15	7	18	8	17	8		
		6 days		7 days		8 days		9 days	
43	40	10.5	4	10.5	4	11.5	5	11	5
35	Ambient	16	6.5	16.5	6.5	15	6.5	15	6
32	Ambient	15.5	7	16.5	6.5	15	6	14	5.8
37	100	18	7.8	21.0	7	18.5	4.7	18	7

Tests were conducted on the T-2 recovery battery to establish length of battery life under intended mission use conditions. Four batteries were used for tests in different temperature environments and pulse discharged for 5 sec at rates between 4 and 8 amp. Three of the batteries were refrigerated overnight and allowed to stand for 2 hr at different temperatures. After refrigeration, SN-43 was exposed to 40°F, SN-35 was exposed to ambient temperature, and SN-37 was exposed to 100°F. SN-32 was kept at ambient temperature at all times. The results of this test are shown in Table 18. No noticeable degradation in voltage resulted as the activated stand time was increased from 3 to 9 days.

3. Main Power Switch

During this reporting period six units were subjected to qualification testing; four units completed all tests with no failures. SN-3 failed to operate after vibration testing and was returned to the vendor and disassembled to determine the cause. Potting material, used to seal the case, was found on the gears and the interior of the case. A dark area, on the bottom of the case, was a varnish-like material deposited by the motor when it was overheated in an attempt to get the switch to transfer.

Possible causes of failure are as follows:

(1) Improper brake setting (because of vibration).

(2) Potting material in gears causing motor to stall.

Exact cause of failure is still to be determined and investigation is continuing.

SN-6 would not pass the dielectric withstanding voltage test after 10,000 transfer operations. The defect showed as leakage between the two positive motor terminals.

K. Propulsion

1. Main Retrorocket Engine

a. Flight engine fabrication. Three retro-engines have been loaded in support of SC-1. All engines were loaded to a nominal 1250 lb of propellant. Both the flight engine and the acceptance test engine will be cut back to the required flight loading as determined by Hughes Aircraft Company.

The flight, acceptance, and flight spare engines were selected through a joint Hughes/JPL/Thiokol meeting on July 13, 1965. Loaded case LSU-52 was tentatively designated the SC-1 flight engine with LSU-54 as flight spare. Cutback of the acceptance test engine, LSU-49, has been accomplished. The final cutback propellant weight, as measured, will be specified in the next report; target weight was 1235.7 lb.

The precutback physical characteristics of the three engines are indicated in Table 19.

b. T-21 retro ETR operation. During the period from June 1 to June 23, inert retro-engine Serial No. A21-E successfully underwent a complete handling, inspection,

UNCLASSIFIED

Table 19. Precutback engine characteristics

Case number	Total inert weight, lb	Precutback propellant weight, lb
LSU-49	139.44	1249.86
LSU-52	140.08	1250.04
LSU-54	140.71	1250.20

and thermal control installation operation at ETR during the T-21 Pathfinder Mission. The three basic operational phases were: (1) safe and arm functional checkout; (2) retrorocket X-ray inspection; and (3) thermal control blanket installation. Modifications were found to be necessary to some of the retro handling equipment for a safer and more expeditious operation; this equipment has been redesigned and rebuilt for use with flight spacecraft.

The applicable handling, testing, and installation procedures are being upgraded based on the T-21 operations.

c. Safe and arm devices. Two flight-quality safe and arm devices (SN-700 and -701) for SC-1 flight retro and spare have completed thermal control preparation at Hughes and have been delivered to Thiokol/Elkton for installation on the flight and flight spare retro-engines.

d. Retrorocket conditioning tests. The temperature conditioning tests, conducted with the thermal-control-model inert engine and simulating the ETR operations sequence, were halted before completion because the engine was required for SC-1 solar-thermal-vacuum tests. The completed conditioning tests established the retro-engine assembly thermal time constant at 50 hr. It follows that the 72-hr minimum prelaunch conditioning period at 95±3°F would be sufficient to heat the retro from the 75°F nominal explosive-safe-area ambient temperature to the required launch temperature range of 85±5°F.

In the event of an abort requiring removal of the spacecraft to the explosive safe area for repairs, the planned 72-hr conditioning period could be reduced to as little as 14 hr. In this event, the retro would not be exposed to the 95±3°F-conditioned environment for a long enough period to guarantee the minimum launch temperature.

It is therefore concluded that resistance heaters will be required on the retro case to provide a minimum launch temperature of 80°F under any circumstance.

2. Vernier Propulsion System

a. Vernier system engineering.

System developmental test program. In the last report period, four closed-loop and two dynamic profile open-loop tests were conducted. Data from all these tests were analyzed with regard to system performance. No problems were noted in the closed-loop tests except that the overall attitude loop gain was set at a low rather than a nominal value. Adequate stability was demonstrated with helium-saturated propellants; however, confirming tests at nominal and high loop gains will have to be run on the S-6 spacecraft following the type-approval-test program.

During the open-loop dynamic run (for the purpose of defining the dynamic characteristics of the system), the chamber pressure tap burned through on one of the engines. Post-test analysis of the data and films revealed an engine instability at approximately 80 cps when commanded to −60 ma. The burnthrough apparently occurred 1 sec after a subsequent step to 80 ma (maximum thrust). Reaction Motors Division (Thiokol Corp.) had an identical failure. As a result, until a complete explanation is available, similar thrust profiles are prohibited during systems tests. Phase shift and gain attenuation data have been reduced by semiautomatic means from both open-loop tests resulting in a significant reduction in data scatter. Gain attenuation during Run S-6-055 at 5 cps with helium-saturated propellants is still less than the specification value of 0.85 minimum; however, phase shift was always less than 40 deg at 5 cps and less than 50 deg at 10 cps.

Uncommanded thrust excursions which occurred on all three engines during Run S-6-055 were analyzed to be the result of helium sucked into the feed system from the top of each oxidizer tank. This helium was liberated during a venting procedure peculiar to the test operation and cannot occur from this cause during a real mission.

System type-approval-test program. Class IV vehicle upgrades were accomplished on the S-6 and S-7 spacecraft and the vehicles entered the checkout portion of their test phases during this report period. S-6 will undergo a 100°F mission cycle and a 0°F mission cycle (less the vibration phase), while S-7 will undergo an ambient mission cycle including the boost and retro vibration phases. Testing on S-6 will be accomplished at Hughes' Placerita Propulsion Test Facility while S-7 will be tested at JPL's Edwards Test Station.

b. Components.

Helium tank and valve assembly. The helium tank and valve assembly installed on the T-21 vehicle completed

the pressurization cycle and hold requirements of the Pathfinder Mission at AFETR.

The assembly which was installed on the SC-1 vehicle was removed and replaced during the report period. The decision for replacing the SC-1 tank assembly was based on the fact that the type-approval-test helium tank and valve assembly configuration differed from the original SC-1 installation. The difference between the original installation and the present installation is the use of charging valves instead of quick-disconnects at the helium fill and regulator test locations, and a modified check valve is now utilized. The helium tank and valve assembly which was removed from the SC-1 vehicle is currently allocated as a spare for the S-6 and S-7 programs.

Six units are being processed through the thermal finishes and flight acceptance test programs with minimum difficulties. One assembly exhibited excessive check valve leakage following vibration testing and this discrepancy is being evaluated.

Helium regulator. The regulator assembly continues to perform in a satisfactory manner. No difficulties have been experienced during the report period.

Relief valve. Carleton Controls Corporation has delivered all but six relief valves required by existing purchase orders. Delivery of the remaining valves is no longer a pacing item for tank assembly production. Component type approval tests have been completed, and the test data obtained is being analyzed.

Check valve. Four check valve assemblies fabricated by Pneu-Hydro were received, cleaned, assembled, and acceptance-tested during this period. Nine additional valve assemblies have been received from Pneu-Hydro and are in process for delivery to bonded stores.

Component approval tests on the modified check valve design have been delayed and are now scheduled to commence approximately mid-August. Because the new check valve configuration has only minor design changes over the original design, consideration is being given to penalty testing instead of a complete type-approval-test program.

Filter assembly. The component approval tests for the filter assemblies have been completed without discrepancy. An adequate supply of filter assemblies is in stock.

Quick-disconnects. The reacceptance program for quick-disconnects allocated to the T-2, S-6, S-7, and SC-2 vehicles is continuing. Completion of all quick-disconnect work is expected to be accomplished by the end of September.

The charging valves which replace the helium fill and regulator test quick-disconnects have completed development testing and type approval tests are scheduled to begin approximately in mid-August. Development tests on the charging valves for other locations on the vernier propulsion system, i.e., the propellant tanks, helium pressurization lines, and thrust chamber assemblies, are in progress. Type approval tests on these valves are expected to begin early in September.

Squib valve. Sufficient squib valves are in bonded stores to support the needs for S-6, S-7, the helium tank and valve assemblies type approval test, and flight vehicles up to and including SC-4.

c. Tank development.

A-21. Propellant and helium tanks are complete except for closeout of paper work. Nitrogen tanks are complete except for delivery of last three tanks.

T-2N. All three helium tanks have been delivered. The CO_2 tanks are complete except for closeout of paper work.

A-21A/114. Bids were received on the helium and propellant tanks from Airite, Airtek, and Solar, with California General and Pressure Systems, Inc., declining to bid. The technical evaluations have been completed.

d. Thrust chamber assemblies (TCA). Flight thrust chamber assemblies for the SC-1 vehicle were received and thermal-painted. These units will be used for SC-1 solar-thermal-vacuum and supplemental SC-1 penalty vibration testing. Filters were changed on these units to assure cleanliness. A "pull tape test" was performed on SN-541 to demonstrate that the gold plate adherence was satisfactory.

Thrust chamber assemblies for the S-6 and S-7 test program have been received and the thermal paint applied. These units are available for the S-6 and S-7 vehicle test programs.

Upgrade of the Hughes TCA Interface Document was continued. Remaining areas of work are TCA dynamic performance and mixture ratio control. This item is expected to be completed during the next report period.

e. T-2N vehicle. The T-2N-1 propulsion system was subjected to two functional and leakage tests prior to and following the vehicle environmental test program. The system was subjected to vibration, humidity and temperature, and simulated landing shock tests. The T-2N-1 vehicle was shipped to the Air Force Missile Development Center (AFMDC) in preparation for the first tether and descent tests. Spares were shipped to AFMDC to support the propulsion system during the test program. Three TCAs were delivered to AFMDC to complete the total provided for this program.

All of the components for the T-2N-2 control items have been delivered. Buildup of these assemblies is expected to be completed during the next report period.

f. A-21A/114. The helium tank shell design is nearing completion. Investigation was initiated to increase the volume of this tank from the proposed value of 1750 in^{-3} to a new value of 1850 in^{-3} to compensate for the increased feed pressure required by JPL Action Directive 128.

The propellant tank shell design is nearing completion. Investigation is pending regarding the increase of nominal working pressure to 910 psi, by incorporation of Action Directive 128, to accommodate a slightly higher plumbing pressure drop which may be experienced on incorporation of the lunar vent/antimigration system. A change in the location of tank-to-bladder seals to reduce leakage problems has been incorporated.

Modifications to the regulator and relief valve settings (50 psi) are nearing definition for appropriate specification changes. No problem is anticipated with the regulator. Existing relief valve designs have been reevaluated in the light of proposed relaxed specification tolerances and a more realistic leakage budget for various system components. A final choice of relief valve designs will be made in the next report period. It is anticipated that A-21A hardware requirements can be met by rework of assemblies already procured.

Redesign of the propellant tank bladder and standpipe has been completed and is in release. Negotiations for bladder procurement have been initiated.

Propellant line routing has been determined, and the plumbing design of the vernier propulsion system is essentially complete. The system under investigation includes crossfeed manifolding with precision check valves being used to prevent propellant migration.

The A-21A/114 system will be designed to provide rapid overboard ejection of liquid propellant at touchdown by firing a pair of squib-actuated valves. This feature was made necessary by recent thermal studies which indicated that TCA temperatures may exceed 300°F after landing. The integrity of the TCA valve seals is in doubt under these conditions, making a rapid, controlled, propellant jettison desirable.

JPL has planned tests to define the probable temperature at which seal failure will occur. Studies of propellant concentration in the vicinity of the spacecraft during jettison have been made by Hughes, and tests to determine the effect on other components are being planned.

Consideration is being given to the procurement of a more compact helium filter to reduce the height of the component "stackup" mounted on the helium tank. Shortening of this assembly should materially decrease vibration amplitudes in this area, resulting in more reliable sealing.

g. Ground support equipment (GSE). The first set of propulsion GSE was used operationally to load the T-21 vehicle during the Pathfinder Mission at AFETR. The equipment functioned satisfactorily but several difficulties were encountered which require resolution prior to propellant loading of the SC-1 spacecraft.

The difficulties were: (1) the spill sleeves used for protecting the spacecraft thermal finishes were not entirely adequate, (2) quick disconnect coupler leakage, and (3) propellant loading accuracy was not achieved.

A short term program has been established at AFETR to evaluate revised loading techniques. Results of this program are not available at this time.

The inadequacy of the spill sleeves during loading is being evaluated. It is believed that the spill sleeves were not properly installed which caused the propellant to spill on the spacecraft thermal finish.

The QDs, which were utilized for the T-21 loading operations, were not retrofitted to the latest configuration. For SC-1 operations, the modified couplers will be employed, which should alleviate the leakage problem.

The second set of GSE for use at JPL Edwards Test Station has completed acceptance tests and has been delivered to Hughes. During acceptance testing, minor

leakage was experienced on one valve in the oxidizer servicing cart. Other than this discrepancy, no other difficulties were encountered.

3. Dissolved Gas Effects on the RMD Thrust Chamber Assembly Dynamic Performance[5]

a. Summary. Analytical models of the *Surveyor* vernier engine, used in previous analog computer simulations of the spacecraft control dynamics, have not included the effects of gas dissolved in the propellants.

A linearized analytical model of the RMD[6] vernier thrust chamber assembly (TCA) with helium-saturated propellants has been developed. When expressed in transfer function form, the analytical model appears as:

$$\frac{\Delta(\text{thrust})}{\Delta(\text{TV input current})} = \frac{\tau_1 S + 1}{\tau_2 S + 1}$$

where τ_1 and τ_2 are dependent upon and vary with thrust level. This model was derived for incremental variations about any thrust level over the throttling range of 30 to 104 lb.

b. Introduction. Previous analog computer simulations and stability calculations used an analytical model of the vernier engine which did not include the effects of gas dissolved in the propellants. These simulations are now considered inapplicable since data from vernier propellant feed system tests performed by Hughes Aircraft Company indicate that the propellants will become completely saturated with helium within 4–20 hr after pressurization. These times are much shorter than will exist between midcourse maneuver and terminal descent during a *Surveyor* mission.

The objective of this analysis is to develop an analytical model of the engine, including the effects of dissolved helium, which can be used to evaluate spacecraft control system performance when this engine model is used in the simulation. A linearized analytical engine model was developed for this purpose. The linearization necessary to yield a mathematical model in closed form makes this model accurate only for small amplitude variations about the operating point. Such a model is adequate for spacecraft control system stability analysis but is not adequate for a complete simulation of the control system when large thrust excursions are involved. Because of complexity, the large thrust excursion rise time is presently being considered as a separate problem, and eventual results will be subsequently compared with the small-amplitude step response times.

c. Linearized analytical model development. It has recently been ascertained that helium permeates the present bladders of the spacecraft vernier fuel and oxidizer feed system. This occurs in much shorter time intervals than will exist between midcourse maneuver and terminal descent during a *Surveyor* mission. Because of the sustained high helium pressurization condition following midcourse maneuver (700 to 840 psia), significant quantities of helium can be dissolved in the propellants.

Recent laboratory tests performed at JPL regarding helium solubility in propellants give results as shown in Figs. 67 and 68. As the pressure of the propellants is reduced, gas is released from solution, creating the existence of a two-phase mixture. The lower the pressure of the propellant, the greater the amount of gas that comes out of solution. Since the solubility of helium in the fuel is considerably less than in the oxidizer, and since the back pressure regulator in the fuel flow circuit maintains all but a very small volume in the flow circuit at a pressure of 450 psia or higher, the volume of gas which comes out of solution on the fuel side is much smaller than on the oxidizer side. The major effect of dissolved gas on TCA dynamics is caused by gas coming out of solution on the oxidizer side. The oxidizer is capable of initially absorbing more helium; and since there is not an oxidizer back pressure regulator, the volume between the second stage of the throttle valve

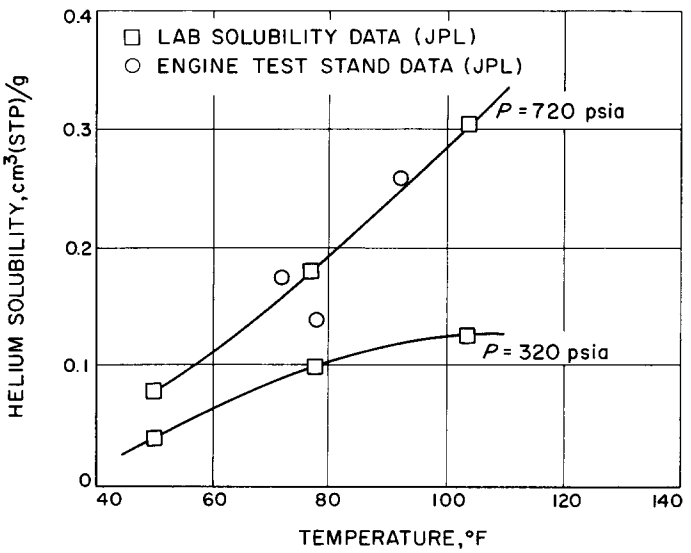

Fig. 67. Helium solubility in MMH-hydrate

[5]Prepared by JPL Technical Section 384.
[6]Reaction Motors Division of Thiokol Chemical Corporation.

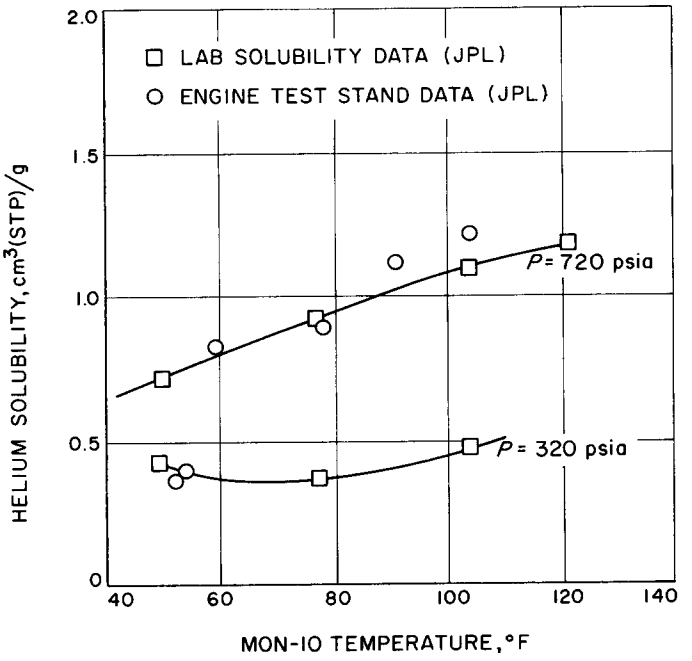

Fig. 68. Helium solubility in MON-10

and the injector can contain a considerable amount of free gas, especially at low thrust where the pressure can be as low as 90 psia.

Fig. 69 is a flow schematic diagram of the RMD TCA.

The oxidizer side of the TCA shall first be considered. The following assumptions were made:

(1) The oxidizer at tank pressure is saturated with helium gas.

(2) The fuel is completely free of dissolved gases.

(3) The specific impulse is independent of small variations in mixture ratio.

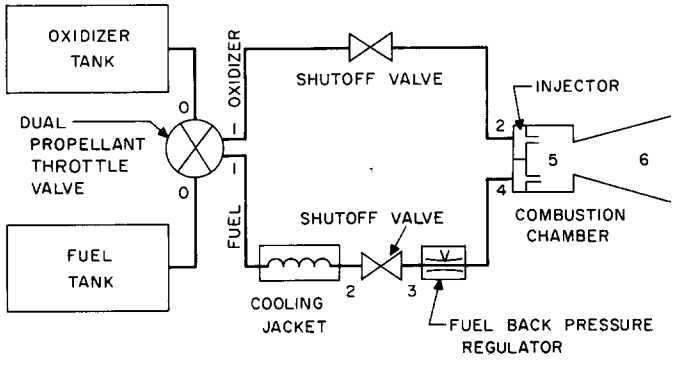

Fig. 69. RMD TCA flow schematic

(4) The characteristic velocity c^* is independent of small variations in mixture ratio.

The pressure in the oxidizer line can become as low as 90 psia at the minimum thrust condition, allowing the major portion of dissolved gas to come out of solution. This condition creates a very compressible mixture of helium and oxidizer downstream of the throttle valve on the oxidizer side.

The density of the mixture in this region can be expressed as

$$\rho_m = \frac{M_h + M_o}{V_h + V_o} = \frac{1+f}{\frac{1}{\rho_o} + \frac{fR_hT_m}{P_h}} \tag{1}$$

where $f = M_h/M_o$. See Table 20 for definition of symbols.

From the energy and path equations for a reversible flow process without external work

$$d\left(\frac{v^2}{2g}\right) = -\frac{dP}{\rho_m} \tag{2}$$

Combining Eqs. (1) and (2), the velocity v_5 of the mixture entering the combustion chamber, assuming initial velocity v_2 negligible, is

$$\frac{v_5^2}{2g} = -\int_{P_2}^{P_5}\left(\frac{1}{\rho_o(1+f)} + \frac{fR_hT_m}{P_h(1+f)}\right)dP \tag{3}$$

Assuming that the variation in mixture temperature T_m across the injector is negligible and also that no additional helium comes out of solution in the injector orifice, Eq. (3) can be simply integrated as

$$\frac{v_5^2}{2g} = \frac{P_2 - P_5}{\rho_o(1+f)} + \frac{fRT}{1+f}\ln\frac{P_2}{P_5} = \frac{\dot{w}_{m5}^2}{2g\rho_m^2 A_i^2} \tag{4}$$

Because f is very small compared to unity, Eq. (4) can be rewritten

$$K_1\dot{w}_{m5}^2 \cong P_2 - P_5 + K_2\ln\frac{P_2}{P_5} \tag{5}$$

where

$$K_1 = \frac{\rho_o}{2g\rho_m^2 A_i^2} \tag{6}$$

and

$$K_2 = f\,\rho_o\,R_h\,T_m \tag{7}$$

Table 20. Definition of symbols

A_i	effective injector area	V_h	volume occupied by helium
A_t	thrust chamber throat area	V_m	medium volume
c^*	characteristic velocity	V_o	volume occupied by oxidizer
f	ratio of helium mass to oxidizer mass	V_T	total volume occupied by medium
g	gravitational constant	$\dot{w}_f$	fuel mass flow rate
K	gain attenuation defined by Eq. (35)	$\dot{w}_m$	medium mixture mass flow rate
K_1	constant as defined by Eq. (6)	$\dot{w}_o$	oxidizer mass flow rate
K_2	constant as defined by Eq. (7)	$\bar{\dot{w}}_f$	fuel flow rate at nominal operation level
K_3	constant as defined by Eq. (8)	$\bar{\dot{w}}_o$	oxidizer flow rate at nominal operating level
K_4	constant as defined by Eq. (28)	$\bar{\dot{w}}_T$	total propellant flow rate at nominal operating level
M_h	helium mass	α	incremental normalized fuel flow rate variation
M_o	oxidizer mass	α_0	amplitude of fuel flow rate as defined by Eq. (31)
P	pressure	β	incremental normalized pressure variation
P_h	helium pressure	γ	incremental normalized oxidizer flow rate variation at combustion chamber entrance
$\bar{P}$	pressure at nominal operating level	ϕ	phase lag as defined by Eq. (32)
R_h	helium specific gas constant	ρ_m	medium density
S	conventional LaPlacian operator	ρ_o	oxidizer density
T	thrust	τ_1, τ_2	time constants
$\bar{T}$	thrust at nominal operating point	ψ	incremental normalized oxidizer flow rate variation at throttle valve exit
T_m	medium temperature	ω	angular velocity
t	time		
v	medium velocity		

The chamber pressure can be expressed as

$$P_5 = K_3 (\dot{w}_{o5} + \dot{w}_{f5}) \tag{8}$$

where

$$K_3 = \frac{c^*}{gA_t} \tag{8a}$$

Combining Eqs. (5) and (8) gives

$$K_1 \dot{w}_{m5}^2 = P_2 - K_3 (\dot{w}_{o5} + \dot{w}_{f5}) + K_2 \ln \left[\frac{P_2}{K_3 (\dot{w}_{o5} + \dot{w}_{f5})} \right] \tag{9}$$

For small perturbations about any operating condition, Eq. (9) can be linearized and finally expressed as

$$(\bar{P}_2 + K_2) \frac{dP_2}{\bar{P}_2} = \left[K_3 \bar{\dot{w}}_{f5} + \frac{K_2 \bar{\dot{w}}_{f5}}{\bar{\dot{w}}_T} \right] \frac{d\dot{w}_{f5}}{\bar{\dot{w}}_{f5}} + \left[2K_1 \bar{\dot{w}}^2 + \frac{K_2 \bar{\dot{w}}_{o5}}{\bar{\dot{w}}_T} \right] \frac{d\dot{w}_{o5}}{\bar{\dot{w}}_{o5}} \tag{10}$$

Defining the differential terms of the previous equation so that

$$\frac{d\dot{w}_{f5}}{\bar{\dot{w}}_{f5}} = \alpha \tag{11}$$

$$\frac{dP_2}{\bar{P}_2} = \beta \tag{12}$$

and

$$\frac{d\dot{w}_{o5}}{\bar{\dot{w}}_{o5}} = \gamma \tag{13}$$

the time derivative of Eq. (10) is

$$(\bar{P}_2 + K_2) \frac{d\beta}{dt} = \left[K_3 \bar{\dot{w}}_{f5} + \frac{K_2 \bar{\dot{w}}_{f5}}{\bar{\dot{w}}_1} \right] \frac{d\alpha}{dt} + \left[2K_1 \bar{\dot{w}}_{o5}^2 + \frac{K_2 \bar{\dot{w}}_{o5}}{\dot{w}_T} + K_3 \bar{\dot{w}}_{o5} \right] \frac{d\gamma}{dt} \tag{14}$$

Because of the compressibility of the medium, the volume from the exit of the second stage of the throttle valve to the face of the injector orifice acts as a capacitor. For this region, the total volume, which is constant, can be expressed as

$$V_{2T} = \frac{M_o}{\rho_o} + \frac{M_h}{\rho_h} = \frac{M_o}{\rho_o} + \frac{M_h R_h T_m}{P_2} \tag{15}$$

Under the assumption that the temperature of the fluid in this volume T_m remains constant, the time derivative of Eq. (15) becomes

$$\frac{dV_{2T}}{dt} = 0 = \frac{1}{\rho_o}\frac{dM_h}{dt} + \frac{1}{\rho_h}\frac{dM_h}{dt} - \frac{V_h}{P_2}\frac{dP_2}{dt} \tag{16}$$

where

$$\frac{M_h R_h T_m}{P_2} = V_h \tag{17}$$

The time rates of change of oxidizer (dM_o/dt) and helium (dM_h/dt) in the space V_{2T} are essentially the instantaneous difference in flow rates between Station 1 and 2 so that

$$\frac{dM_o}{dt} = \dot{w}_{o1} - \dot{w}_{o2} = \dot{w}_{o1} - \dot{w}_{o5} \tag{18}$$

$$\frac{dM_h}{dt} = \dot{w}_{h1} - \dot{w}_{h2} = \dot{w}_{h1} - \dot{w}_{h5} \tag{19}$$

Inasmuch as at any given quasi-steady-state operating condition

$$\frac{\dot{w}_h}{\dot{w}_o} = \frac{M_h}{M_o} = f \tag{20}$$

and further because

$$P_2 = \bar{P}_2\left(1 + \frac{dP_2}{\bar{P}_2}\right) = \bar{P}_2(1+\beta) \tag{21}$$

and

$$\dot{w}_{o5} = \bar{\dot{w}}_{o5}\left(1 + \frac{d\dot{w}_{o5}}{\bar{\dot{w}}_{o5}}\right) = \bar{\dot{w}}_{o5}(1+\gamma) \tag{22}$$

and

$$\dot{w}_{o1} = \bar{\dot{w}}_{o1}\left(1 + \frac{d\dot{w}_{o1}}{\bar{\dot{w}}_{o1}}\right) = \bar{\dot{w}}_{o1}(1+\psi) \tag{23}$$

then Eq. (16) can be written as

$$\frac{V_h \bar{P}_2}{\bar{P}_2(1+\beta)}\frac{d\beta}{dt} = \left[\bar{\dot{w}}_{o1}(1+\psi) - \bar{\dot{w}}_{o5}(1+\gamma)\right]\left[\frac{1}{\rho_o} + \frac{f}{\rho_h}\right] \tag{24}$$

But

$$\bar{\dot{w}}_{o1} = \bar{\dot{w}}_{o5} \tag{25}$$

therefore

$$\frac{V_h}{(1+\beta)}\frac{d\beta}{dt} = \bar{\dot{w}}_{o5}\left[\psi - \gamma\right]\left[\frac{1}{\rho_o} + \frac{f}{\rho_h}\right] \tag{26}$$

Assuming the percent variation in fuel flow α is equal to the percent variation in oxidizer flow ψ and further that β is small compared to unity, then Eq. (26) can be written

$$\frac{d\beta}{dt} = \bar{\dot{w}}_{o5}\left[\alpha - \gamma\right]K_4 \tag{27}$$

where

$$K_4 = \left[\frac{1}{\rho_o} + \frac{f}{\rho_h}\right]\frac{1}{V_h} \tag{28}$$

A linearized equation for thrust involving the nominal thrust and the non-dimensionalized variations in fuel and oxidizer flow rates can be simply derived as

$$\frac{T}{\bar{T}} = \frac{\bar{\dot{w}}_{f5}}{\bar{\dot{w}}_T}\alpha + \frac{\bar{\dot{w}}_{o5}}{\bar{\dot{w}}_T}\gamma \tag{29}$$

Eliminating $d\beta/dt$ between Eqs. (14) and (27) and then combining the results with Eq. (29) gives, after some maneuvering, the expression in the transformed domain,

$$\frac{T}{\bar{T}} = \alpha\left[\frac{\dfrac{4K_1\bar{\dot{w}}_{o5}}{5(K_2+\bar{P}_2)K_4}S + 1}{\dfrac{(2K_1\bar{\dot{w}}_{o5} + K_2/\bar{\dot{w}}_T + K_3)}{(K_2+\bar{P}_2)K_4}S + 1}\right] \tag{30}$$

Eq. (30) is the linearized transfer function of thrust for small perturbations in fuel flow rate at the throttle valve exit.

For a cyclic disturbance in fuel and oxidizer at the throttle valve exit, the fuel flow rate

$$\alpha = \alpha_o \sin \omega t \tag{31}$$

and the thrust phase lag ϕ is

$$\phi = \tan^{-1}\omega\tau_1 - \tan^{-1}\omega\tau_2 \tag{32}$$

where

$$\tau_1 = \frac{4K_1\bar{\dot{w}}_{o5}}{5(K_2+\bar{P}_2)K_4} \tag{33}$$

UNCLASSIFIED

and

$$\tau_2 = \frac{2K_1\bar{\dot{w}}_{05} + \frac{K_2}{\bar{\dot{w}}_T} + K_3}{(K_2 + \bar{P}_2)K_4} \tag{34}$$

and ω is the driving frequency in rad/sec.

In terms of τ_1, τ_2 and ω, gain attenuation is

$$K = \frac{\tau_1}{\tau_2}\left[\frac{\omega^2 + \frac{1}{\tau_1^2}}{\omega^2 + \frac{1}{\tau_2^2}}\right]^{1/2} \tag{35}$$

Because K_4 is inversely proportional to the volume occupied by the helium V_h as seen in Eq. (28), τ_1 and τ_2 are directly proportional to V_h. Therefore, at any one frequency and nominal operating level, the gain attenuation, as expressed in Eq. (35), will decrease with increasing V_h while phase lag, which is not monotonic with ω for this transfer function, will peak at various frequencies as determined by the amount of helium released from solution (Fig. 70).

The current engine requirements are that at 5 cps the phase lag $\leq$32 deg and the gain attenuation $\geq$0.85. These numbers are based on a first-order lag transfer function $[1/(\tau S + 1)]$ which is assumed independent of thrust level. Eq. (30) shows that the phase lag and attenuation are definitely a function of thrust for which the lowest level is the most critical. Table 21 displays 5-cps phase lag and attenuation calculations at several thrust levels for a nominal propellant mixture ratio of 1.5. The worst condition exists at the lowest thrust level, but improves with increasing thrust.

The aforementioned analysis assumed negligible vapor pressure in comparison with the partial pressure of the helium released from solution. This is a good assumption at low temperatures, but at the maximum propellant feed temperature of 100°F, the high oxidizer vapor pressure causes a large increase in the volume of gas downstream of the throttle valve. Consequently, the volume V_h in Eq. (28) would be replaced by V_m where

$$V_m = V_h + V_v \tag{36}$$

and where

$$V_v = V_h \frac{P_v}{P_h} \tag{37}$$

Engine dynamic performance is degraded even more at the high propellant temperatures due to the larger volume of gas downstream of the throttle valve. Table 22 shows 5-cps phase lag and attenuation calculations at two thrust levels for a nominal propellant mixture ratio of 1.5.

An analysis identical to that presented above was conducted for the fuel side of the TCA. Conclusions drawn

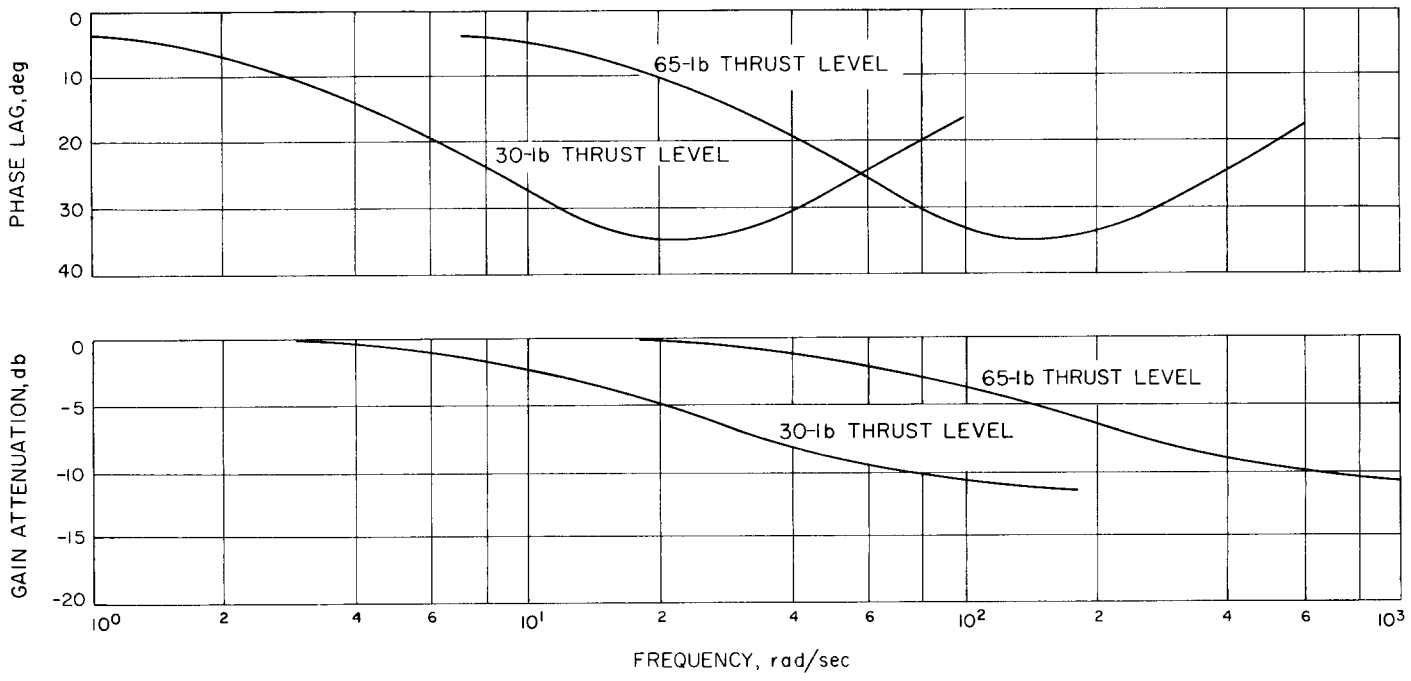

Fig. 70. Phase lag and gain attenuation vs frequency for the 30- and 65-lb models of Table 21

UNCLASSIFIED

Table 21. Numerical calculations for negligible oxidizer vapor pressure effects

Total volume V_T, in.^{3}	Thrust level, lb	Numerical transfer function	Phase lag, deg at 5 cps	Gain attenuation at 5 cps
0.83	30	$\frac{T}{\bar{T}} = \alpha \frac{(0.0237S + 1)}{(0.0859S + 1)}$	33	0.43
0.83	40	$\frac{T}{\bar{T}} = \alpha \frac{(0.0128S + 1)}{(0.04615S + 1)}$	34	0.61
0.83	46	$\frac{T}{\bar{T}} = \alpha \frac{(0.0106S + 1)}{(0.0365S + 1)}$	30	0.69
0.83	65	$\frac{T}{\bar{T}} = \alpha \frac{(0.00415S + 1)}{(0.01345S + 1)}$	16	0.93
0.83	100	$\frac{T}{\bar{T}} = \alpha \frac{(0.00066S + 1)}{(0.00199S + 1)}$	2	1.00

Table 22. Numerical calculations including oxidizer vapor pressure effects at 100°F

Total volume V_T, in.^{3}	Thrust level, lb	Numerical transfer function	Phase lag, deg at 5 cps	Gain attenuation at 5 cps
0.83	30	$\frac{T}{\bar{T}} = \frac{(0.0372S + 1)}{(0.138S + 1)}$	28	0.34
0.83	41	$\frac{T}{\bar{T}} = \frac{(0.023S + 1)}{(0.082S + 1)}$	33	0.45

from this analysis were that there would be negligible phase lag and attenuation contributions from the fuel side; since the solubility of helium in the fuel is considerably less than in the oxidizer (Fig. 67) and since the pressure regulator in the fuel circuit maintains all but a very small volume in the flow circuit at a pressure of 450 psia or higher, the volume of gas quantities which comes out of solution on the fuel side is very much smaller than on the oxidizer side.

The theoretical transport and combustion lags were neglected in this analysis. They have been shown to be small and would not significantly add to the engine characterization. Therefore, the linearized transfer functions shown in Tables 21 and 22 are most realistic for use in describing the dynamic TCA performance when the propellants are saturated with helium.

d. Experimental substantiation of model. A more representative transfer function of the TCA with helium dissolved in the propellants could be obtained by combining the transfer functions of Table 21 (for low temperatures) or of Table 22 (for high temperatures) with a throttle valve transfer function. However, suitable throttle valve transfer functions in transfer function form are presently unavailable due to the complexity of the analysis. Data at 5 cps with little or no dissolved helium in the propellants, however, show small phase lags and little or no attenuation. This means that the model developed for helium dissolved in the propellants does satisfactorily represent the *Surveyor* vernier engine at or near 5 cps. Figs. 71 and 72 show small-signal attenuation and phase lag versus frequency data for helium-saturated propellants as well as gas-free propellants with the model predictions superimposed.

The gas-free propellant curves of Figs. 71 and 72 essentially represent the throttle valve characteristics. When these effects are included with the model predictions, the long-dashed curves are the results.

e. Conclusion. The linearized analytical model of the RMD vernier thrust chamber assembly with helium-saturated propellants developed herein appears to be satisfactory for assessing spacecraft control system performance for small-amplitude variations about the operating point.

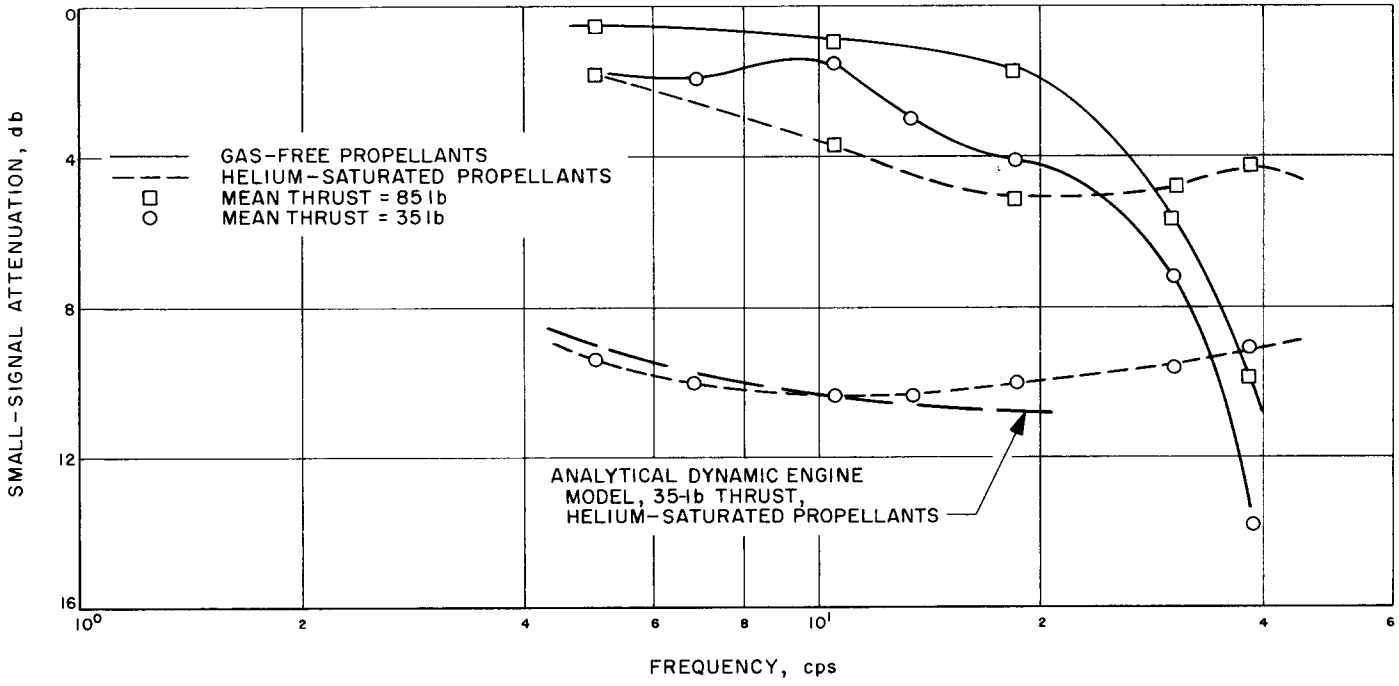

Fig. 71. Effects of dissolved gas on *Surveyor* vernier engine dynamic performance (small-signal attenuation vs frequency)

4. *Vernier Propulsion Subsystem*[7]

Work was continued on the program to perform limited environmental tests of selected upstream system components for the purpose of evaluating, on an independent basis, the capability of these components to meet the *Surveyor* requirements. A helium regulator (Carleton Controls Corp.; Hughes Aircraft Company Part Number 254080) was acquired on a loan basis from Hughes Aircraft Company and became the first test object in the evaluation program. The initial results were presented in *SPS 37-32*, Vol. I.

The program has progressed through completion of regulator testing. Functions recently completed include life cycle tests, vibration, blowdown, leak tests, lock-up, disassembly, and inspection. Tests previously reported evaluated the regulator characteristics under temperature extremes.

The life cycle tests consisted of 100 regulated flow cycles with leak checks after every 20 cycles. Results of the life cycle tests showed that in the first cycle of each 20 cycles, the regulated pressure was 5 to 7 psi above the upper limit at low flow rates, then remained within tolerance until the end of each series.

The present regulator design (a design more recent than the model under test) incorporates a precalibrated spring package which gives a flatter regulator output. This enables the regulator to be calibrated so that the pressure will be within the limits.

The regulator sustained type-approval-level vibration in three axes with no detrimental effects. The regulation performance after vibration was essentially the same as before.

The disassembly and inspection of the component parts after environmental test revealed that the anodized seat was eroded at the edge of the orifice, resulting in excessive leakage. A scratch which was noted adjacent to the seat was apparently the result of a foreign particle flowing through the component. These observations emphasize the importance of adequate inlet filtration.

Both sides of most of the Belleville springs exhibited excessive corrosion. In the modified-design regulator presently being employed in the flight spacecraft, the spring material has been changed and this condition has been corrected.

The design of the regulator which was tested was also found capable of being improved in the following specific

[7]Prepared by JPL Technical Section 384.

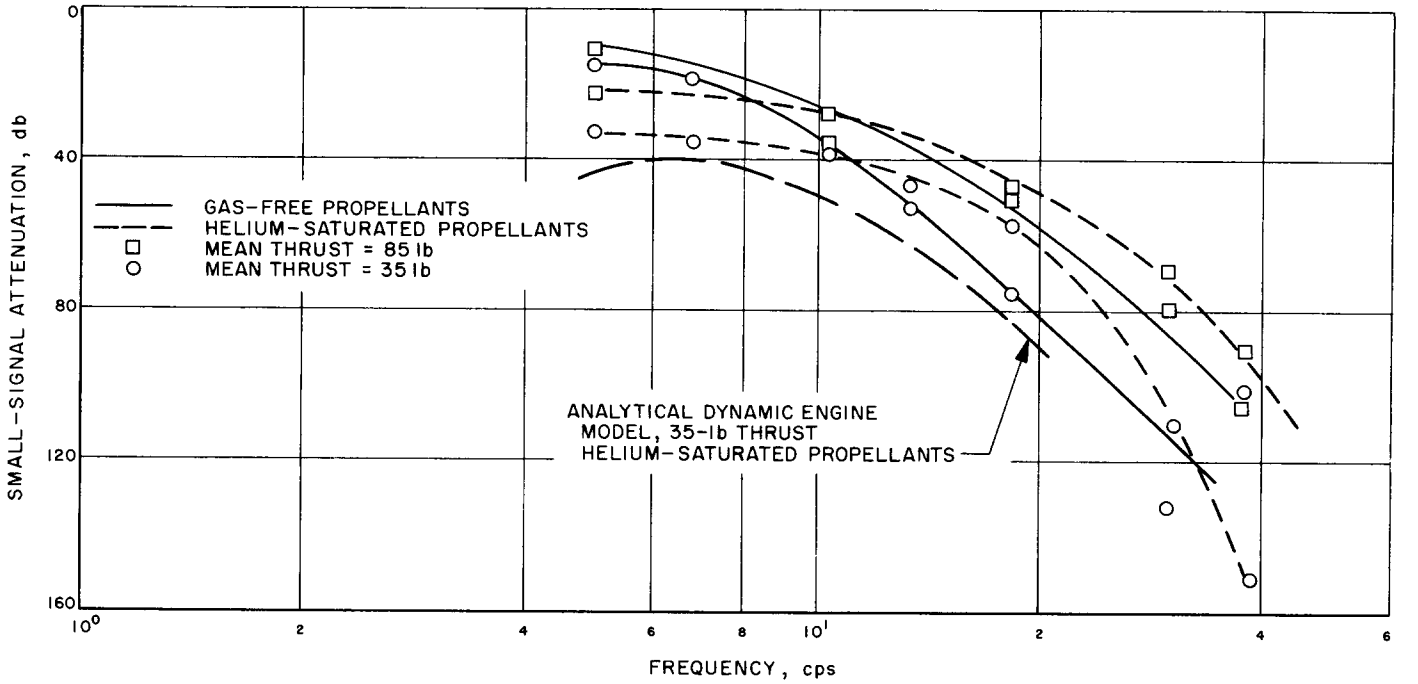

Fig. 72. Effects of dissolved gas on *Surveyor* vernier engine dynamic performance (small-signal phase lag vs frequency)

areas. The two interconnecting push-pull rods are not positively locked at the diaphragm-piston end attachment point. The external ring for retention of the diaphragm is not locked by any means. Although the modified regulator does not incorporate changes in these areas, the type-approval tests of both the old-design and modified-design regulators have not shown any failures attributable to these areas. These modifications will be considered in the future units.

The evaluation with the present unit is considered complete with these tests. Although the regulator evaluated is no longer of the latest modification, the results of these tests have influenced the design of the present flight unit.

The second component to be evaluated under this program is the helium relief valve. The purpose of these valves in the system is to prevent overpressurization of the propellant tanks in the event of a malfunction of regulator lock-up. Two units (M. C. Manufacturing Company; Hughes Aircraft Company Part Number 262703) have been acquired. One unit will undergo type-approval tests in its present design condition, and one will undergo type-approval tests with a modified seal design. Results will be reported as they become available.

5. *Thrust Chamber Assembly*[8]

As a part of a continuing evaluation of the *Surveyor* vernier engines (RMD Model No. TD-339), eight tests were performed at JPL Edwards Test Station during July and August. The tests are arranged in groups according to test goals.

Group	Test No.	Test date	Purpose
9	G-4	6-22	First test in single-engine vibration test program
9	G-6	7-8	Second test in single-engine vibration program
10	DY 72-75	7-12 to 7-26	Engine dynamics with saturated propellants
11	F 1-2	7-21	Engine operation during static acceleration
12	DY-76	8-2	Pre-chilled molybdenum-wrought nozzle extension tests

[8]Prepared by JPL Technical Section 384.

a. Group 9. Following Test G-4 (previously reported in *SPS 37-34*, Vol. I), SN-42 thrust chamber assembly (TCA) was subjected to a three-axis simulated boost vibration test. Variable frequency sine wave acceleration levels were 18 *g* between 50 to 150 cps and 6 *g* between 150 to 1500 cps. Random white Gaussian acceleration vibration levels were 6.75 *g* (rms) between 100 to 1500 cps. These tests were performed with the TCA filled with solvents under a pressure of 700 psi. There was no indication of leakage as a result of vibration. Solvent flow tests of the engine after vibration showed essentially no change in the engine flow characteristics.

The engine was remounted on the shaker fixture and test fired (Test G-6) on July 8. During this firing, the engine was subjected to simulated retromotor vibration pulses. The only effect of the simulated boost and retro-vibration on the engine was a shift in mixture ratio from 1.5 (Test G-4) to 1.41 (Test G-6). This change in mixture ratio falls within the allowable limits of 1.4 to 1.6.

A similar shift was found on a TCA used in pre-qualification testing at RMD. Both were due to the inability of the self-locking adjustment screws to hold during severe vibration. This design has been changed to incorporate a positive lock by epoxy seals. The revised design has completed type-approval and additional testing without evidence of failure. This change has been incorporated into all TCA's by means of a field modification order.

b. Group 10. This group of tests was performed with flight engine SN-538 and helium-saturated propellants to determine the effect upon TCA dynamic response of a reduced-volume oxidizer line located between the throttle valve and the shutoff valve. An additional objective was to determine if raising the propellant temperatures would degrade the dynamic performance.

A mathematical model of the engine utilizing dissolved helium gas had indicated that there should be improvement in dynamic performance by reducing the oxidizer line volume and that high propellant temperature would represent the worst-case condition. Preliminary RMD test data also had indicated some improvement in dynamic response under ambient temperature conditions with helium-saturated propellants when utilizing the reduced-volume line.

Accordingly, SN-538 engine was retro-fitted with a reduced-volume line and tested over a representative dynamic profile. Tests DY-72 and DY-73 were performed with 100 and 40°F helium-saturated propellants, respectively. Following these tests, the original-volume oxidizer line was reinstalled on the engine to provide comparative dynamic data. Tests DY-74 and DY-75 were performed with 100 and 40°F helium-saturated propellants, respectively.

Analysis of the test data indicated that the presence of helium dissolved in the propellants had a significant effect on dynamic response, particularly at the low-thrust levels. The major effect of a reduced-volume oxidizer line was an improvement in response during step thrust changes. Other than this, the improvements in dynamic response were small. The test results confirmed the analytical predictions that the high propellant temperature would give the worst dynamic performance.

c. Group 11. Following the vibration test of SN-42 engine, the engine was mounted on the rotating arm of a centrifuge unit to determine its operability when subjected to a constant 12-*g* acceleration in simulation of the condition at retromotor burnout. Two tests were performed in July to demonstrate that start and shutdown characteristics, performance, and dynamic response would be unchanged in an acceleration field. The results of these tests when compared with previous firing data (Tests G-4 and G-6) for this engine, indicated no detectable difference in operating characteristics. It is of interest that SN-42 engine, which had been subjected to the vibration and acceleration tests, has operated successfully for an accumulated firing time of over 25 min at RMD and JPL.

d. Group 12. A group of tests similar to those described under Group 2 (*SPS 37-33*, Vol. I) are planned to determine the suitability of the flight-type stress-relieved (no recrystallization) wrought-molybdenum nozzle material when test-fired after having been pre-chilled to successively lower temperatures. The tests performed previously under Group 2 had employed a partially recrystallized molybdenum nozzle. The lowest temperature planned for this series of tests is −100°F. Test DY-76, the first test of a series of four, was successfully completed in August at ambient temperature. Joint conductance and nozzle interior emissivity measurements before and after test firing are a part of the work being conducted with this particular engine.

L. Spacecraft Vehicle and Mechanisms for Basic Bus

1. Vehicle Status

S-6 vernier propulsion system qualification vehicle. This vehicle was returned from the Placerita Canyon

Test Facility for an upgrade period. The vernier propulsion system was replaced with a flight quality system for the beginning of type approval tests. This upgrade was completed and the vehicle was returned to test near the end of July.

S-7 vernier propulsion system qualification vehicle (Fig. 73). This vehicle differs from S-6 in that it is fully ballasted to simulate the flight spacecraft (for purposes of structural dynamic simulation during live firings of the vernier engines). It was fitted with a fully flightworthy (Class IV) vernier propulsion system and was delivered to the cognizant engineering activity for type approval testing.

S-9 engineering payload structural test model. This vehicle makes use of a flightworthy spaceframe and substructure formerly assigned to the SC-3 spacecraft. It is currently being fitted with dummy components (ballast), some of which had been used on the S-2 structural test model. This vehicle will be used for further verification of the dynamic structural responses and structural integrity of the A-21 series spacecraft.

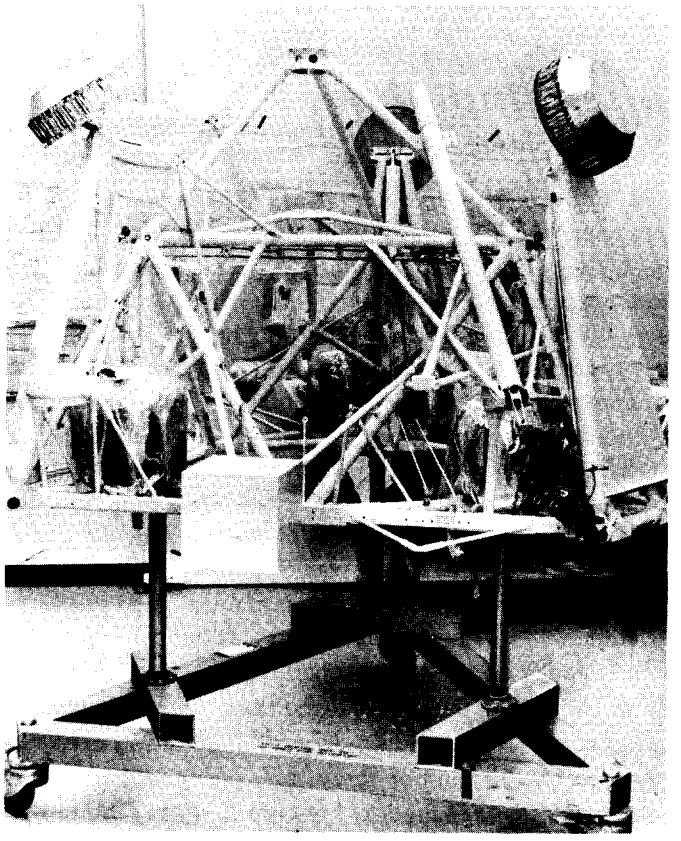

Fig. 73. S-7 vernier propulsion system qualification vehicle

S-10 thermal test model. This thermal test vehicle has suffered delays in final assembly caused primarily by emphasis being placed on higher priority flight vehicles. It is now scheduled to be completed in mid-August.

T-21 system type-approval-test vehicle. This vehicle was shipped to Eastern Test Range during the last reporting period.

SC-1 first flight spacecraft. The first flight spacecraft has been in system test during the majority of this reporting period. Near the end of the period it was prepared for the thermal vacuum test phase and returned to testing.

SC-2 second flight spacecraft. The upgrade on the SC-2 spacecraft has continued with delivery to system test expected near the end of July. Delays were in general incurred due to top priority placed on SC-1 and T-21 and the necessity to divert some mechanical and electrical components from this vehicle to SC-1 as spares. Parts of the vernier propulsion system such as plumbing lines and tanks are an example of parts diverted to repair SC-1.

SC-3 third flight spacecraft. Fabrication effort on this vehicle has been continued at a relatively low level due to higher priority assigned to the SC-1 spacecraft and its associated test vehicles. The original spaceframe assigned to SC-3 was converted to S-9. The new SC-3 spaceframe fabrication progress is shown in Fig. 74.

2. Vehicle Testing

a. T-2 series drop test vehicle airbag test. A new airbag configuration referred to in *SPS 37-34*, Vol. I has been designed, developed, and flight-acceptance-tested. Fig. 75 shows schematically the basic mechanical differences between the old and new design. The new airbag is trapezoidal rather than rectangular and has the following advantages over the original design:

(1) More stability under both straight compression and side loading due to its tapered construction.

(2) Requires less CO_2 gas to fill, which means quicker filling of bags and a greater margin of reserve gas supply.

(3) The internal gas pressure rises more rapidly and uniformly as the smaller tapered end initially strikes the ground, resulting in a consistent control of the diaphragm rupture pressure. Thus, more precise control of landing shocks are predicted by uniform release of the CO_2.

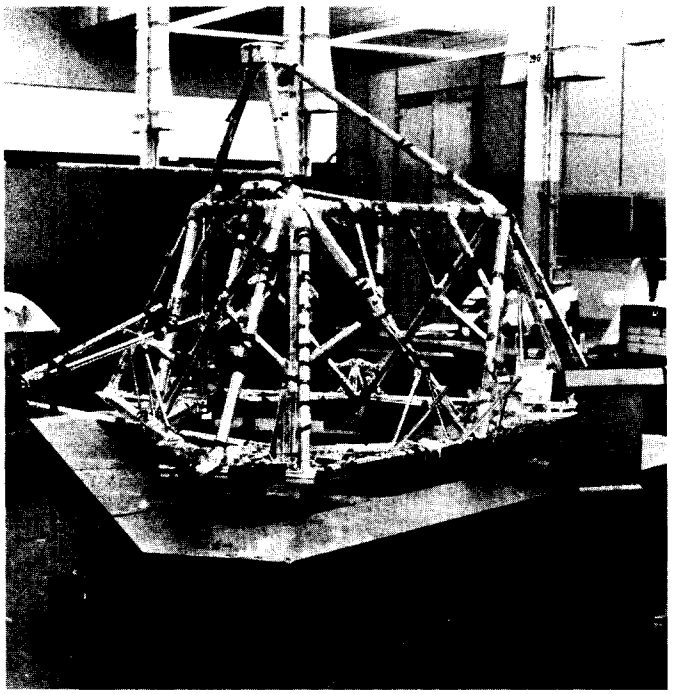

Fig. 74. SC-3 spacecraft spaceframe

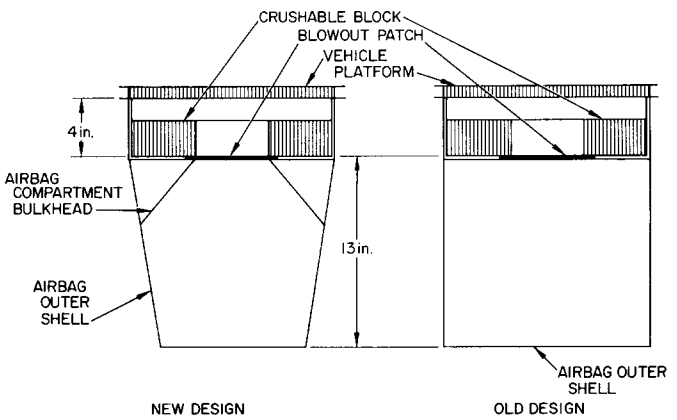

Fig. 75. Mechanical differences between old and new T-2 airbag configuration

(4) Internal corner pockets have been designed within the bag which provide additional energy absorbing control during last stages of airbag collapse, and remove the high "g" spike from the system which had been observed in some of the tests with the original design. Fig. 76 illustrates the comparison of load absorptive qualities of the old and new design plotted against an ideal curve.

The new airbag design was tested both at Culver City at the Structure Test Laboratory and by an actual drop

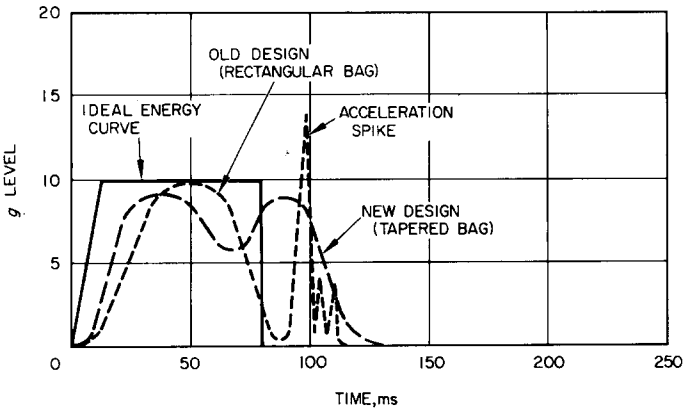

Fig. 76. Comparison of load absorptive qualities of old and new T-2 airbag configuration

with T-2NR at Holloman Air Force Base; it will be the design used for the remainder of the T-2 series tests.

b. T-2 parachute recovery system. Drop tests with the "iron maiden" parachute test vehicle at Holloman Air Force Base indicated that the use of a four-canopy parachute recovery system resulted in a sinking rate of 22 to 23 ft/sec (above the 20-ft/sec requirement for T-2 tests). A five-canopy system was employed which brings the sinking rate within specification. This system will be used for the remaining T-2 series tests.

c. Retrorocket separation test. Separation tests were run using the T-1 spaceframe and a retrorocket that had been thermally covered to flight engine dimensions. The tests were run in three phases. In the first phase, the retro was lifted vertically upward from the spaceframe by a cable attached at its center of gravity. The spaceframe was level and no attempt was made to impede the separation. In the second phase, the retro was still attached at its center of gravity. This time, however, deliberate attempts were made to keep it from separating from the spaceframe. The insulation was hooked on one of the separation devices, the frame was tipped at vernier angles, and the retro was wedged in place. In the third phase, an attempt was made to simulate a condition of separation which could occur if two separation devices functioned on the first firing impulse and the third one functioned on the second firing impulse. A simulated retrorocket was fastened to only one of the attach positions and a separation device was fired to separate it (Fig. 77).

Separation, in all phases, was completely successful and exceeded all specification requirements.

Fig. 77. Retrorocket engine separation test using T-1 spaceframe

3. Mechanisms for Basic Bus

a. Omnidirectional antenna mechanisms. The two omnidirectional antenna mechanisms (designated A and B) use tapered fiberglass cloth tubes bonded to aluminum hinge bracket assemblies. They deploy and lock the two omnidirectional antennas into operating position before separation from the *Centaur* stage.

Omnidirectional Mechanisms A and B have been delivered and installed on the T-21 and SC-1 vehicles. The mechanisms for SC-2 have been delivered to bonded stores. The Mechanisms A and B for the SP-1 (spare) units have been delivered into bonded stores. Mechanisms A and B for the SC-3 vehicle are in assembly.

b. Antenna/solar panel positioner. The antenna/solar panel positioner (A/SPP) provides mounting, positioning, position indicators, and launch and landing locks for the planar array antenna and solar panel. The antenna support structure has four controllable axes. The roll, elevation, polar, and solar axis drives use a solenoid stepper motor for power and a wire-wound potentiometer for position indication.

The A/SPP (SN-1) has been delivered to the SC-1 spacecraft. The SN-2 unit has completed electrical checkout and functional/overload testing. An engineering unit (X-1) has been structurally upgraded to the current SC-1 configuration for use in the S2-A spacecraft drop tests.

The design phase of a structural/functional upgrade of the positioner is 90% complete. This upgrade will ensure adequate margins for the entire structure; the previous partial structural redesign covered only the area of failure which occurred during the S-2A drop test. Some existing hardware items will be strengthened using doublers, some will be unchanged, some eliminated, and some replaced. The roll and elevation axis pin pullers are relocated such that they mount parallel to the centerline of the axis they lock with the locking pin extending through a flange. The functional portion of this upgrade provides improved alignment and efficiency through the following:

(1) Increased spread between elevation axis bearings with bearing parts interchangeable with the roll axis.

(2) Single piece construction of polar axis worm and gear support structure.

(3) Revised worm gear bearing arrangement.

(4) Upgraded drive assembly with an all-aluminum planetary transmission and a commercial potentiometer; all parts are usable interchangeably at roll and elevation axis.

c. Separation sensing and arming review. Three separation sensing and arming devices per spacecraft provide redundant interruption for the post-separation squib firing circuits and vernier-engine solenoid circuit until after the spacecraft separates from the *Centaur*.

Sets of hardware (three devices per set) through Mission D (Flight Spacecraft SC-4) had been flight-acceptance-tested and delivered to bonded stores. These units are in process of rework to incorporate customer requested changes. The sets for SC-1, SC-2, and SP-1 (spare) have been redelivered to bonded stores.

d. Pyrotechnic devices.

Manual pin-puller assemblies. A complete drawing package of a modified, manual pin-puller configuration has been released. It was required by some changes in the mounting provisions. Items for SC-1 have been reworked to the latest configuration and delivered to the spacecraft.

Pyrotechnic switch. The pyrotechnic switch type-approval test results were reviewed and accepted as flight qualified.

Electric squib. The electric squib (PN 236472-1) type-approval-test results were reviewed and accepted as

flight qualified. A complete set of *Surveyor* electric squibs has been shipped to Eastern Test Range. These units are being utilized for evaluation and test as part of the Pathfinder Mission requirements.

Pyrotechnics for T-2 vehicle. Thirty squibs from each squib configuration (120 total) have been subjected to the type-approval-test environments. This includes temperature shock, vibration, mechanical shock, temperature, and humidity. Nondestructive electrical tests have been completed on every squib after each environment. Approximately 50% of the tested units have been fired at various temperatures and all-fire currents to acquire squib performance data. All squibs fired were satisfactory.

Ten sets of pyrotechnic devices have been flight-acceptance-tested. The following units have been delivered to Holloman Air Force Base:

Name	Usage
Electric squib	Airbag inflation
Electric squib	Recovery chute deployment
Thruster	Recovery chute deployment
Electric squib	Helium dump
Electric squib	Helium release Oxidizer manifold dump Fuel manifold dump
Electric squib	Ten stabilizing chutes
Pin-puller subassembly	Assemblies jettison

M. Scientific Payload

Activities during this reporting period have been devoted largely to incorporation of subsystem current limiting changes, review of new experiment requirements, activation of payload system tests, and system design of the touchdown dynamics instrumentation subsystem.

1. Alpha Scattering Experiment Subsystem

The alpha scattering experiment will be used for compositional analysis of lunar surface materials. The experiment provides a capability to measure materials at several locations on the lunar surface when used in conjunction with the soil mechanics/surface sampling experiment.

The experiment subsystem consists of an instrument, instrument auxiliary, instrument sensor deployment mechanism, mounting substructure, and associated cable harnesses. The instrument consists of a sensor head assembly (deployed onto the lunar surface) and an electronics unit (mounted in thermally-controlled Compartment B).

a. Subsystem integration. Recent Hughes Aircraft Company/JPL coordination meetings have resulted in 20 proposed changes to the alpha scattering instrument interface specification. Descriptions of these changes will be presented in *SPS 37-36*, Vol. I.

b. Instrument auxiliary. Changes to provide current limiting of the 29-v nonessential bus, and a fuse to protect the 22-v unregulated bus have been authorized. Detailed changes to the alpha scattering instrument auxiliary are:

(1) A current limiting switch will be added to control the 29-v power to the alpha scattering instrument and auxiliary.

(2) The 22-v input power line will be fused.

c. Instrument sensor deployment mechanism. Based on new deployment requirements and instructions to utilize a lazy tongs/escapement mechanism, a redesign of this mechanism has been initiated. A preliminary design layout is shown in Fig. 78.

In the new design, the instrument support arm and diagonal brace arm (with an adjustable locking lever) provide an arrangement for clamping the skirt of the alpha scattering instrument to the supporting structure. An extension on the instrument support arm contains the electrical cable (accordion folded) within an open box. This extension also bears against one end of the pallet locking lever, causing the other end to block the pallet from moving. This prevents the escape wheel and the spool on which structural wire is wound from rotating, thus keeping the wire taut. The other end of the wire goes through a teflon-lined wire tube and then through a wire lock which is clamped to the wire at the other end of the tube. The wire lock permits some slack to exist between the tube and the instrument knob to which the end of the wire is attached. The tube is attached to the outer link of a spring-driven lazy-tongs device. A slotted nut rides on a threaded extension of the spool shaft and a pin puller rides in the slot.

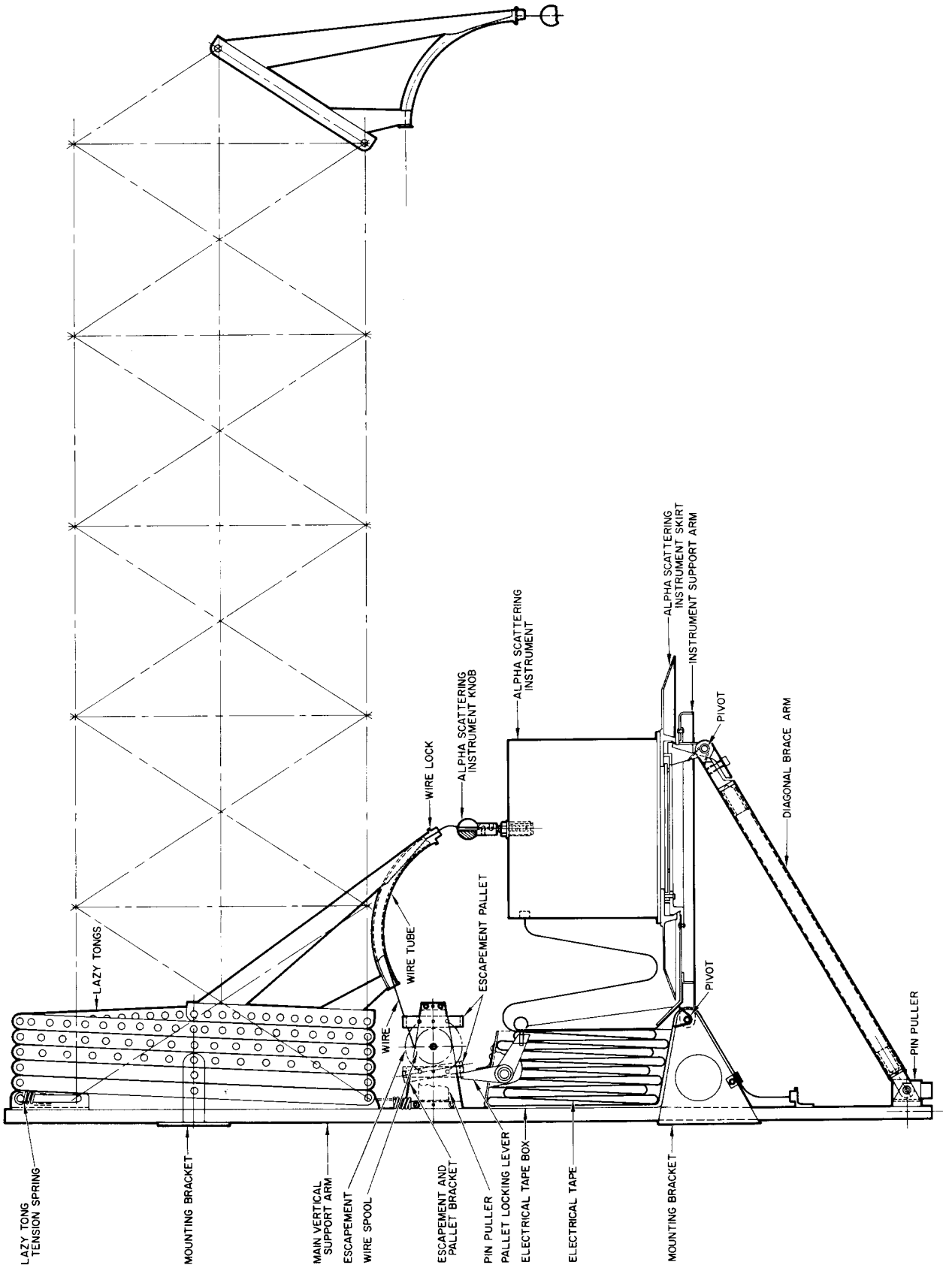

Fig. 78. Alpha scattering instrument sensor deployment mechanism

d. Instrument operational mode. Following touchdown, the alpha scattering instrument is deployed to a "background count" position away from the spacecraft and above the lunar surface. This is accomplished by an Earth command which actuates the pin puller at the diagonal brace arm. When the pin is withdrawn, the diagonal brace arm drops away from the main vertical support, rotating the locking lever out of the instrument skirt and thus leaving it free. The instrument support arm also falls away, rotating about its pivot point near the main vertical support. When the instrument support arm falls away, it opens the door on the electrical harness storage box and releases the pallet lock, thus allowing the spool wire tension to operate the escapement.

The lazy tongs are driven to the extended position by helical and leaf springs. The escapement controls the rate at which the alpha scattering instrument moves to the background count position. At this point the slotted nut reaches the end of the threaded portion of the shaft. Further rotation of the spool is prevented by the second pin puller. The alpha scattering instrument is deployed from the background count position to the surface position by Earth command. This command operates the second pin puller, releasing the wire spool, and allowing the escapement to unreel the wire at a maximum velocity of 0.7 ft/sec until the alpha scattering instrument is lowered to the lunar surface. After lunar surface operation, the surface sampler can be moved over the instrument knob, picking up the instrument and relocating it.

2. Seismological Experiment Subsystem

This subsystem is designed to supply several kinds of information, including seismicity, background noise level, elastic properties of the Moon, internal lunar construction, and the distribution of meteorite impacts on the lunar surface. The subsystem consists of an instrument, instrument auxiliary, mounting substructure, and associated cable harness. The instrument consists of a sensor

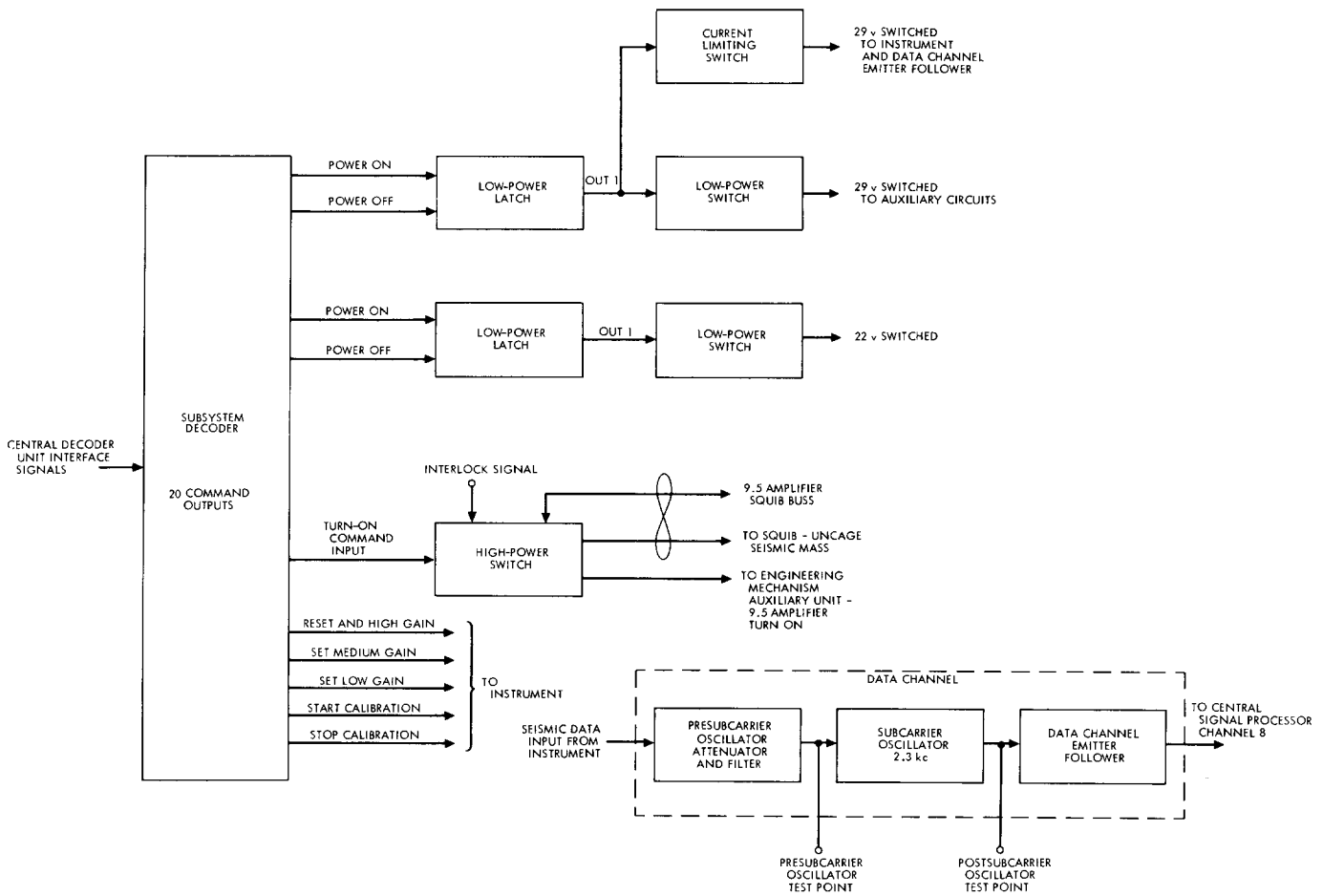

Fig. 79. Single-axis seismometer auxiliary block diagram

(mounted on a rigid portion of the spaceframe) and an electronic unit (mounted in thermally-controlled Compartment B).

a. Subsystem integration. The seismometer interface specification was revised to include a requirement for current limiting. This change provides the experiment with current limiting (up to 200 ma) on the regulated bus, and fusing (200 ma) on the unregulated bus.

During this period, other changes were proposed to the interface specification. They include:

(1) Instrument outline and mounting changes.

(2) Instrument weight changes.

(3) Instrument source impedance changes.

The new sensor outline and mounting will require a modified mounting substructure on the spacecraft. Sensor weight has increased from 5.8 to 7.4 lb. The instrument electronics unit has been reduced from 1.2 to 1.0 lb. The instrument source impedance has been reduced from 5000 $\pm$250 Ω to 200 Ω or less.

b. Instrument auxiliary. Recent auxiliary design activity has been related to the incorporation of current limiting, fusing, and the modification of a data channel attenuator to accommodate a 0- to 200-Ω driving source impedance. A block diagram depicting these changes is shown in Fig. 79.

c. Unit and subsystem testing. The seismometer and auxiliary units were tested on the M-13 spaceframe. At completion of unit testing, a gross subsystem integration test was accomplished. Lack of accurate and precise information on the prototype seismometer instrument operating characteristics has made data analysis very difficult. The experiment test data has not indicated any major new problems in integrating the subsystem with the spacecraft. High ambient seismic noise levels prevent complete test of the experiment since the sensor must remain caged.

3. Micrometeorite Ejecta Detection Experiment Subsystem

This subsystem will provide data regarding the number, momentum, and kinetic energy of individual lunar ejecta resulting from meteoroids impacting the lunar surface. The experiment subsystem consists of an instrument, instrument auxiliary, mounting substructure, and a subsystem cable harness. The instrument consists of a sensor assembly (mounted on the upper portion of the spacecraft) and an electronics unit (mounted in thermally-controlled Compartment B).

a. Subsystem integration. The micrometeorite ejecta detector interface specification was revised to include a requirement for current limiting. This change will provide protection for the main spacecraft power distribution in case of an experiment subsystem malfunction. The instrument operating current is now specified to be regulated at not more than 200 ma under short-circuit conditions. Recent Hughes Aircraft Company/JPL technical coordination meetings have led to further changes in the interface specification. These changes are summarized as follows:

(1) *Thin film protection voltage.* This change will require a -12-v "keep alive" voltage to be generated in the instrument auxiliary. The voltage, monitored by telemetry, will be applied to the instrument thin film plates for protection against impact shorts during all times that instrument power is off. The change also includes elimination of the sensor heater circuit and modification of the experiment subsystem cable harness.

(2) *Instrument design improvement.* A noise coincidence circuit and an X-10 mike circuit have been added to the instrument design. The noise coincidence circuit will provide for a substitute bit in the output data format to indicate when mechanical noise on the spacecraft is of sufficient level to trigger the micrometeorite sensor circuits. The X-10 mike signal will improve the dynamic range of the impact momentum measuring circuits in the instrument. The experiment subsystem cable harness will be affected as well as test and operational procedures.

(3) *Data format.* The instrument clock accuracy of $\pm$2% and the latest ejecta data format will be added to the interface specification.

(4) *Operating temperature.* The sensor assembly upper operating temperature is changed from 207 to 213°F to agree with the results of a recent instrument thermal analysis.

(5) *Electronics unit.* The outline and mounting dimensions of the electronics unit are changed to represent the latest instrument design.

(6) *Automatic readout.* The instrument design now provides for a readout sequence to occur automatically once every 10 sec during instrument operation.

b. Instrument auxiliary. Recent activity on the instrument auxiliary has included engineering design to incorporate current limiting and fusing in accordance with a recent contract modification. Specific items accomplished during this report period are:

(1) Initiated qualification program for special components.

(2) Purchased components for breadboard fabrication.

(3) Released preliminary circuits.

(4) Completed preliminary design review.

The auxiliary modification (to provide current limiting and fusing) is shown in Fig. 80. The current limiting switch provides limiting of currents to both instrument and auxiliary circuits. The fuse provides spacecraft power protection in case of a malfunction in the instrument heater circuit.

c. Unit and subsystem testing. Unit level testing of the micrometeorite ejecta detection auxiliary and instrument has been completed and resulting test data is now under analysis. Integration testing of the auxiliary and instrument as a subsystem is now in progress. Unit level testing is scheduled for the next reporting period. Modification of the instrument strain-gage amplifiers to flight configuration (gain and bias) will be required before testing can be completed.

4. Soil Mechanics/Surface Sampling Experiment Subsystem

This subsystem is designed to examine the lunar surface in a limited area near the *Surveyor* spacecraft for the purpose of determining the general contour and mechanical properties of the lunar soil. The subsystem consists of a soil mechanics/surface sampler, an electronic auxiliary, a wiring harness, and mounting substructure.

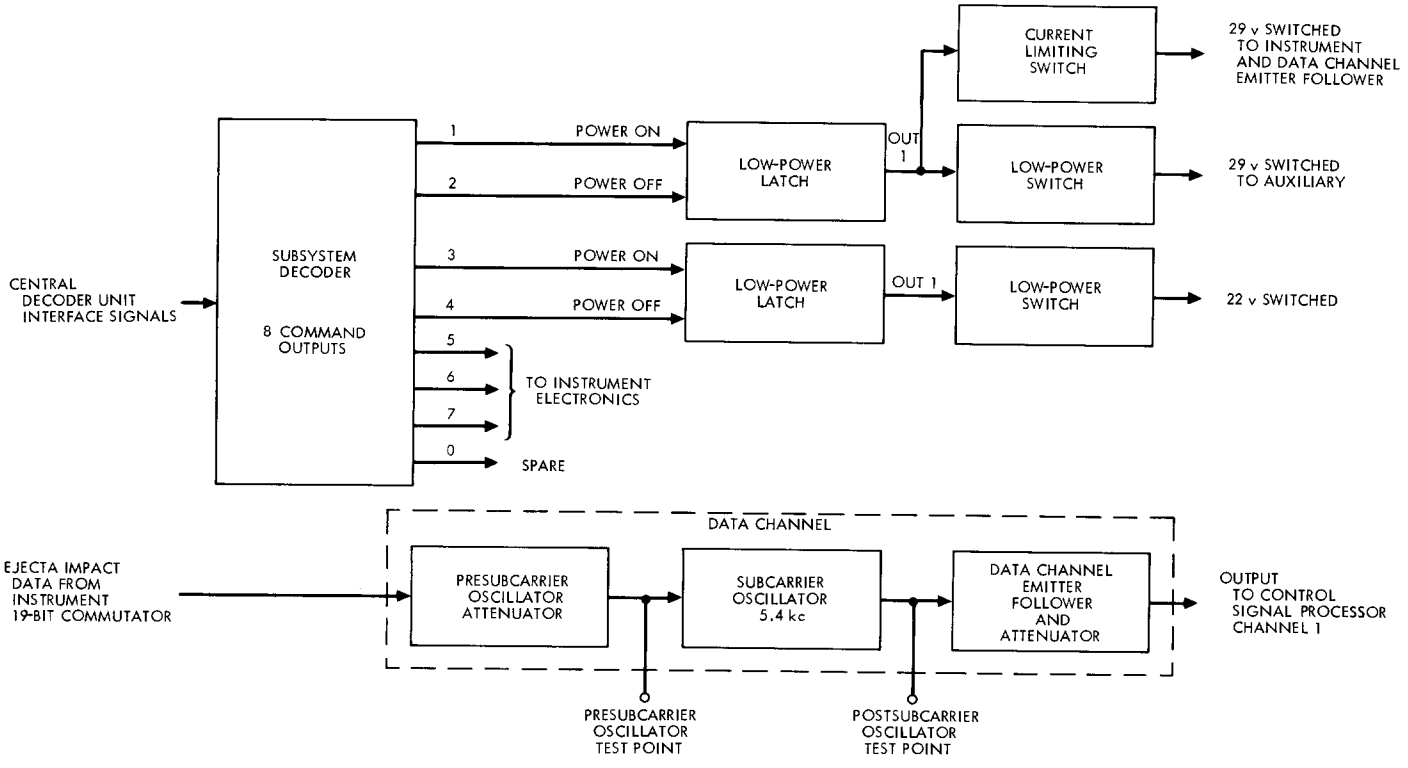

Fig. 80. Micrometeorite ejecta detector auxiliary block diagram

The soil mechanics/surface sampler is designed for digging, scraping, and picking over an area of approximately 20 ft² of the lunar surface. The mechanism is comprised of an electric-motor-driven pantograph arm and a scoop. The arm is operated by independent electric-motor drives in elevation, radial extension, and azimuth. A separate motor provides for opening and closing the scoop. An acceleration measuring system is used to indicate scoop deceleration during picking action. Two strain-measuring systems indicate radial and vertical digging forces. Potentiometers are used to provide scoop position data.

All flight-quality drive motors have been received and flight acceptance testing is now in progress. All tests are expected to be complete by the end of August. Proposals have been received on both the strain and acceleration measuring systems. It is expected that orders will be placed during August. A stress analysis is expected to be completed during the next reporting period.

The soil mechanics/surface sampler auxiliary provides command decoding, signal processing, power management, squib firing, and control of the instrument motors. Circuit and product design were essentially complete, then an auxiliary design change was approved to incorporate current limiting of all 29-v regulated power and fusing of the 22-v motor excitation lines. New circuits have been designed and component qualification initiated.

The soil mechanics/surface sampler wiring harness electrically interconnects the instrument auxiliary and basic spacecraft. A nonflight harness has been fabricated and delivered to the Payload Systems Laboratory for use on the M-13 spacecraft mockup.

A mounting substructure for the soil mechanics/surface sampler is designed to support the instrument during transit and lunar operational phases. In the original design an incompatibility between the soil mechanics/surface sampler and its mounting substructure was discovered. The substructure was redesigned to correct this incompatibility and to meet present instrument interface requirements. Drawings have been completed and a stress analysis is in progress.

5. Touchdown Dynamics Instrumentation Subsystem

The functional objectives of this subsystem are:

(1) Determine spacecraft motion.

(2) Determine surface bearing shear strength and penetration of lunar surface.

(3) Determine lunar surface contour.

a. Motion of spacecraft reference axes. An inertial reference system, having its vertical axis parallel to the local lunar gravity force vector, is required. The initial velocity of the spacecraft at touchdown, expressed in this inertial reference system, will be calculated using data derived from on-board instrumentation together with the knowledge that during the free-fall period the only external force acting on the spacecraft is lunar gravity. With the initial conditions of velocity known for both the body and inertial reference systems, the initial Euler angles relating these two reference systems can be calculated. Time histories of the variations of the Euler angles and angular velocities subsequent to initial touchdown will be obtained from the instrumentation subsystem. Linear accelerations measured in spacecraft coordinates will also be obtained from the subsystem. This data will then be integrated and combined with angular data to obtain the linear velocity and linear displacement of the spacecraft center-of-gravity in the body reference system. The center-of-gravity motion will then be transformed to the lunar inertial reference system using the known Euler angles.

b. Bearing strength, shear strength, and penetration of lunar surface. Information on the bearing strength of the lunar surface will be obtained from an analysis of footpad load components normal to the resultant velocity vector of each footpad. Information on shearing resistance or coefficient of friction of the lunar surface will be obtained from an analysis of the load components parallel to the footpad resultant velocity vectors. The quantities required for this analysis are the magnitude and direction of the resultant load applied to each footpad in contact with the lunar surface and the magnitude and direction of the resultant velocity of each footpad. Motion data will be derived from a knowledge of landing gear position and the vehicle center-of-gravity motion described in the preceding paragraph. In addition, during the period in which no more than two of the crushable blocks are in contact with the lunar surface, it will be possible to obtain the resultant loads and velocities associated with the blocks from the space vehicle acceleration and angular rate data. Therefore, a similar analysis of the bearing and shearing loads can be made for the crushable blocks. This will increase the amount of lunar surface data obtained, and also indicate whether the shape of the impacting body has a significant effect on the applied

loads. Information relative to the impacting bodies' lunar surface penetration will also be based on an analysis of the load components parallel and normal to the direction of their resultant velocity vectors. For example, if the surface in the landing area is hard enough to prevent penetration, the ratio of the parallel load to the normal load will increase as the resultant velocity decreases (coefficient of friction while sliding is less than the static value). If, however, significant penetration occurs, this ratio will tend to increase with an increase in resultant velocity (increased inertia forces will result from imparting motion to the surface material).

c. Surface contour. Six points of relative lunar surface elevation will be established by noting the position of each footpad and each crushable block at the instant when they contact the lunar surface. Furthermore, if the surface is hard (i.e., it is determined that the penetration is not significant), the contour of the surface traversed by the footpad and crushable blocks will be described by the respective displacements.

d. Subsystem function and description. The function of the touchdown dynamics instrumentation subsystem is to measure and record certain physical parameters during the period from generation of the spacecraft 1000-ft mark through touchdown on the lunar surface, store the data, and on command, transmit the physical data to Earth. The parameters are as follows:

(1) Three mutually orthogonal components of translational acceleration.

(2) Three mutually orthogonal components of angular velocity.

(3) Axial forces in six spacecraft leg struts and three shock absorbers.

(4) Angular position of each spacecraft leg (relative to spaceframe).

(5) Initial contact time of each footpad and crushable block with lunar surface.

The following outputs from spacecraft basic bus units will be recorded:

(1) The three components V_x, V_y, and V_z of spacecraft translational velocity (outputs of RADVS).

(2) Vernier engine cutoff signal.

The experiment subsystem will consist of the following units:

Unit	Location
22 channel tape recorder and associated electronics	Touchdown dynamics compartment
Gyro accelerometer package, containing three rate gyros and three linear accelerometers and associated electronics	Touchdown dynamics compartment
Three strain-gage amplifier and power supply packages, each containing one power supply and three amplifiers	Touchdown dynamics compartment
Nine strain-gage bridges	Leg 1, 2, 3
Three leg position potentiometers	Leg 1, 2, 3
Six contact switches	Crushable blocks and footpads
Subsystem auxiliary	Touchdown dynamics compartment

The touchdown dynamics subsystem is shown in Fig. 81, which gives the *Surveyor* spacecraft stowed, midcourse, and postlanding configurations.

e. Operating modes. The record mode is used to record data from receipt of the 1000-ft mark through touchdown on the lunar surface. The retro separated signal turns on power to the gyro/accelerometer package (to allow time for the motors to attain operating speed) and also enables record logic. A manual backup command can be used if necessary. The 1000-ft mark from the RADVS turns on the remainder of the instrumentation, the auxiliary unit, and the tape recorder. The auxiliary then generates a 3-sec Calibrate 1 signal which is sent to all instrumentation units. At the conclusion of this signal a 1-sec Calibrate 2 command is generated. At its completion, data recording begins and continues for approximately 1 min. An end of tape sensor in the recorder generates a turnoff signal which deenergizes all subsystem power.

Data stored on the tape will be played back (on command from Earth) after touchdown on the lunar surface.

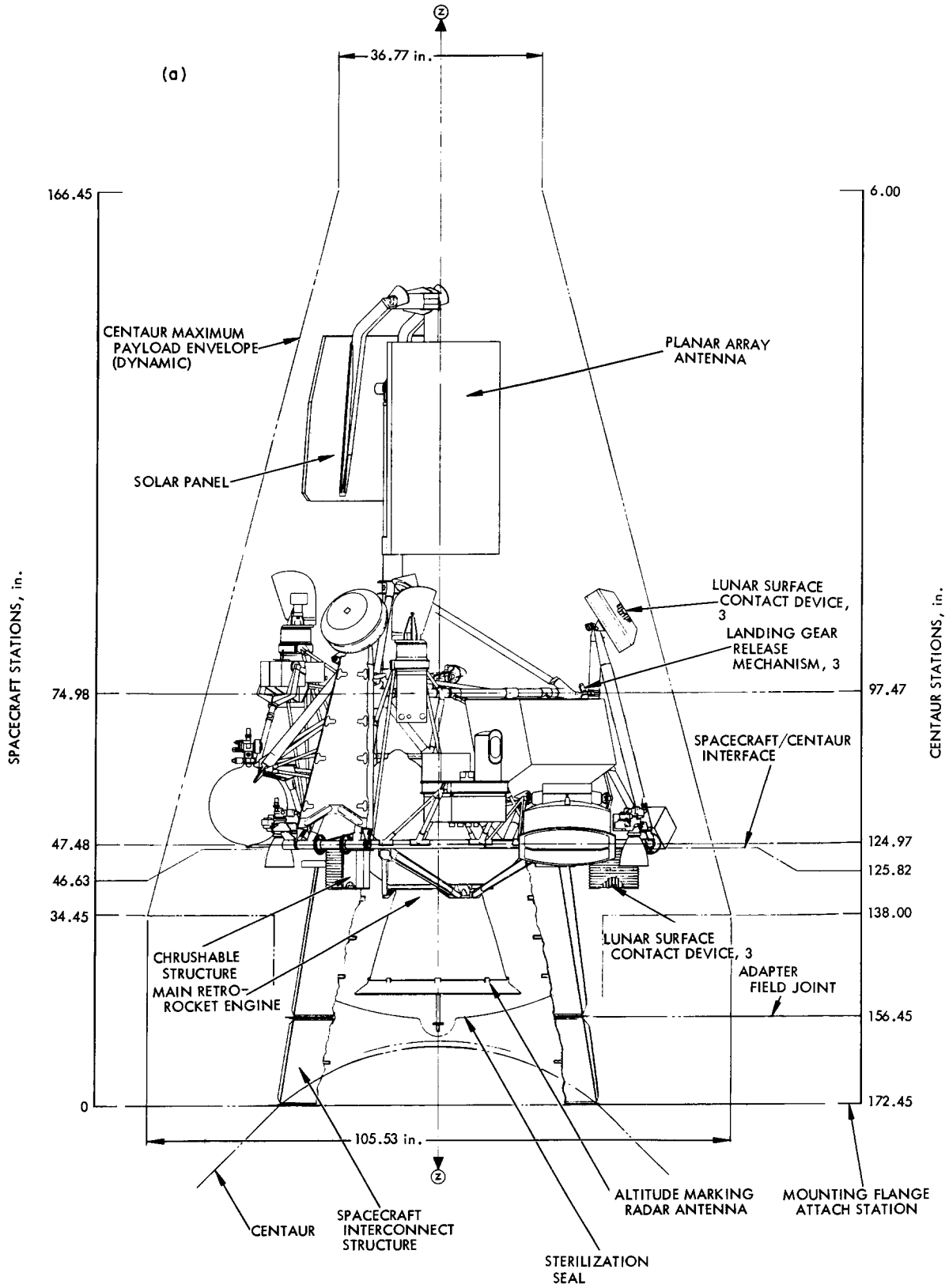

Fig. 81a. *Surveyor* spacecraft stowed configuration

UNCLASSIFIED

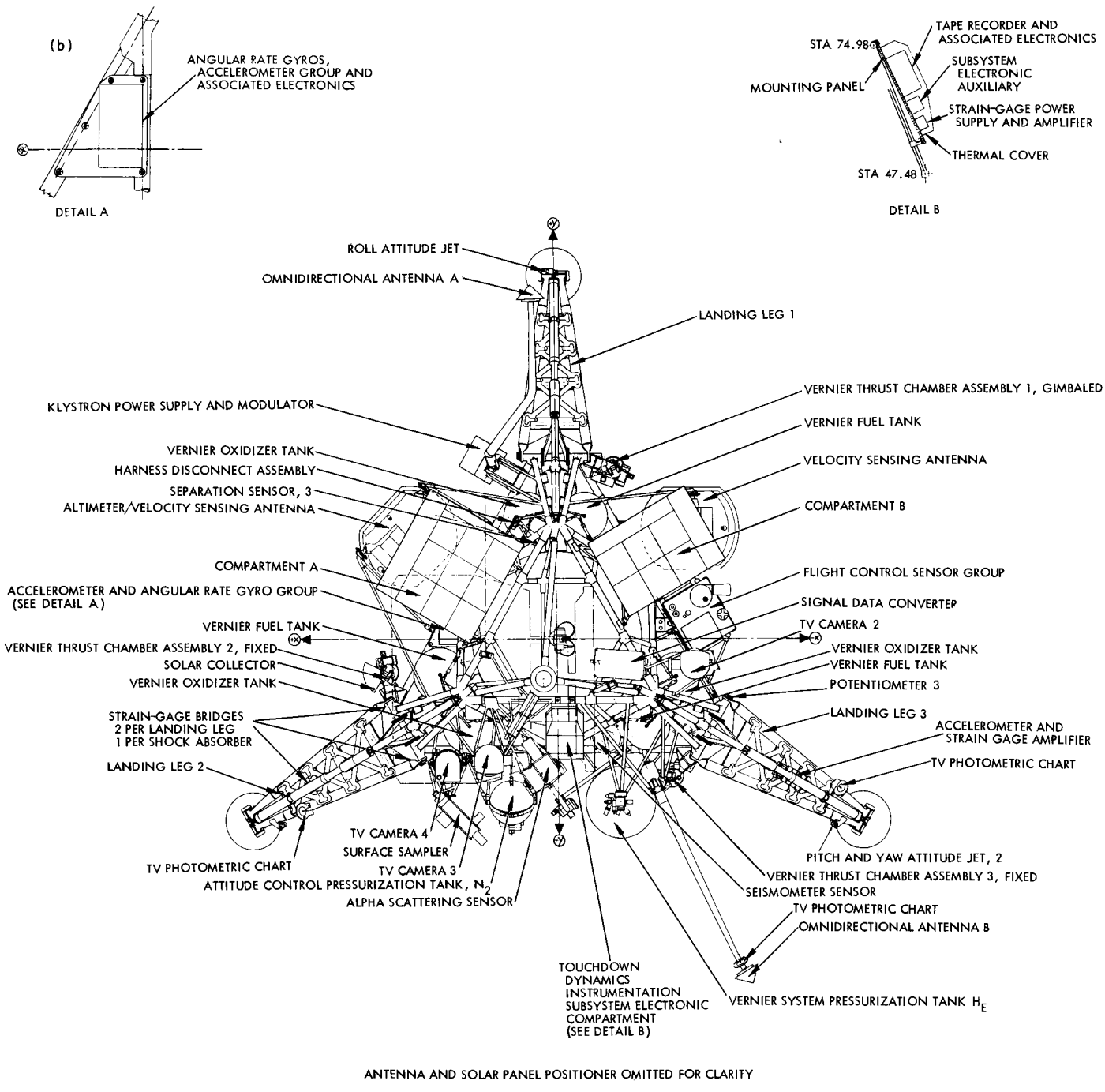

Fig. 81b. *Surveyor* spacecraft midcourse configuration

The preferred mode of data transmission is use of the spacecraft low-power transmitter with the planar array, but the telemetry design is such that the high-power transmitter with an omni-antenna also provides acceptable performance.

The recorder will be mechanized to play back only one data channel and a time reference channel at a time. A solid-state head-switching network will be advanced one step each time the end of tape sensor is energized. Playback and recording will be at the same type speed.

UNCLASSIFIED

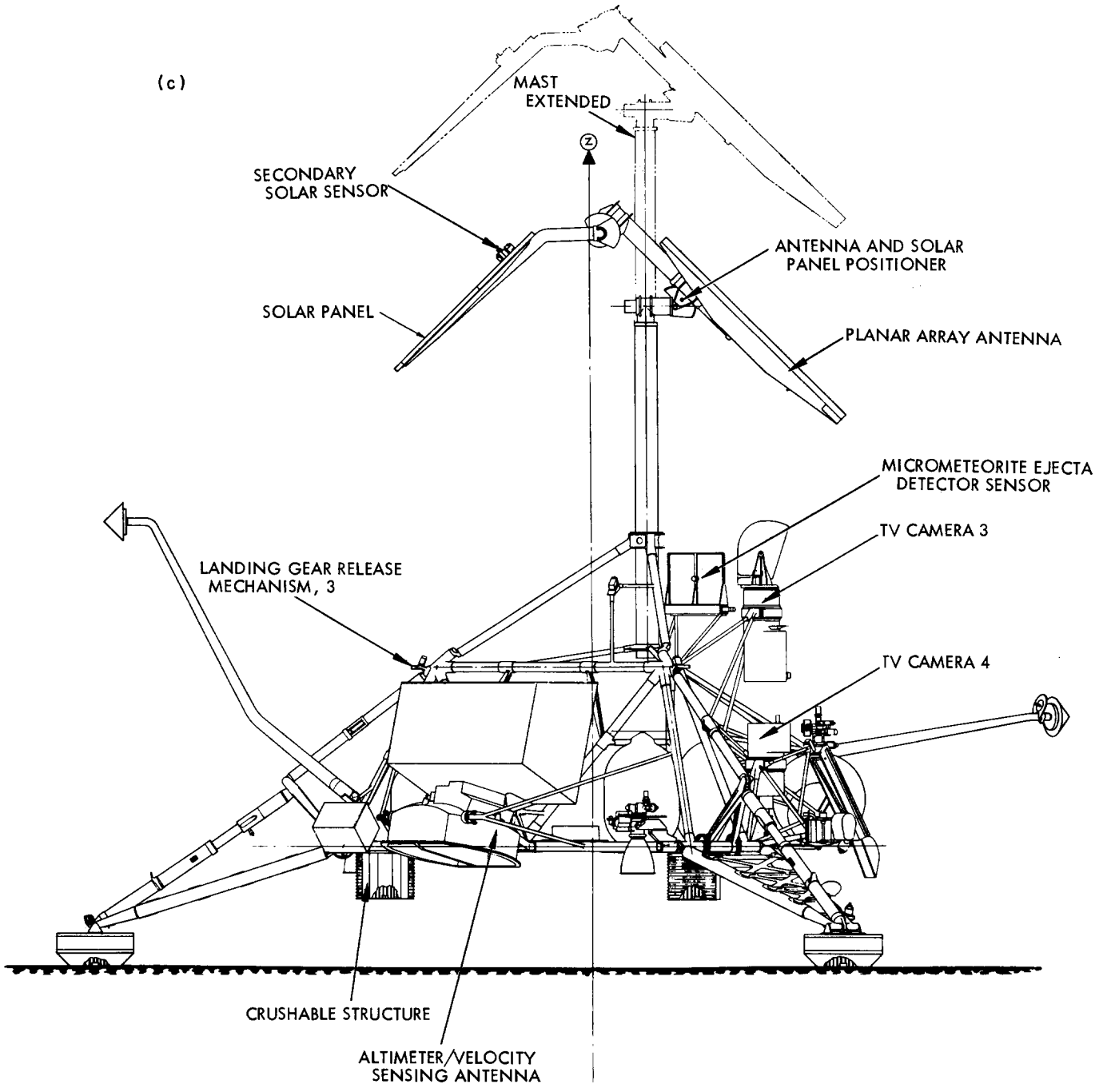

Fig. 81c. *Surveyor* spacecraft postlanding configuration

Therefore, about 21 min will be required to play back 21 data channels.

The output of the data channel will be a ±40% deviation frequency modulated signal, 900-cps center frequency. The time reference channel output will be a narrow-band 2-kc center frequency signal. These will be fed to the summing amplifier in the central signal processor for modulation of the main carrier.

f. Tape recorder performance. The recorder and associated electronics will be capable of simultaneously

recording 21 channels of analog data, and one time-reference channel, using FM saturation recording. Sequential playback will be provided, with the time reference and one selected data channel being played back each time. The recorder will use an endless tape loop and will have an end-of-tape sensor. The recorder will be capable of recording a minimum of 70 sec of continuous data and will play back at the same tape speed as is used for recording.

The recorder will have one playback amplifier connected to the time-reference channel head and a second playback amplifier which can be switched to sequentially play back each of the recorded data channels. Sequencing will be internal to the recorder. The frequency-modulated signal obtained from the heads on playback will not be demodulated but will be filtered and amplified only. The tape recorder will be self-contained, requiring only 22-v power, pulse commands, and signal input and output connections.

The recorder will provide a record time of 70 sec for 21 data channels and one time-reference channel. The recorder will operate within specifications within 1 sec after application of power. Long-term speed stability will be $\pm 0.5\%$. The record will be an FM saturation type, using a voltage-controlled-oscillator center frequency of 900 cps for data channels and a 2-kc signal for a time-reference channel.

A record command and 22-v power will be applied simultaneously to the recorder. At the same time a calibrate command will be applied to each sensor (e.g., items such as gyros and accelerometers, which are not part of the tape recorder). After 3 sec, a second calibrate command to generate another calibrate level will be applied to all sensors for 1 sec. When this command is removed, normal data recording will commence and continue through spacecraft touchdown. End of the tape loop in the recorder will generate a turnoff signal that will be utilized by the experiment auxiliary unit (not part of the tape recorder) to turn off all power to the recorder and all sensors. Subsequent tape playback will be initiated by manual command from Earth. This command will apply 22-v power to the recorder and will also supply a playback command (pulse) to the recorder.

The recorder will then play back sequentially each data channel, one at a time, using inertial switching and logic to select each playback head in turn. The time-reference channel will be played back simultaneously with each data channel. Two separate signal outputs from the recorder will be provided, the selected data channel and the time-reference channel.

g. Landing gear strain gages, amplifiers, and power supplies. Strain-gage bridges will be located on each of the landing gear struts to sense axial compression/tension forces. Each of the three landing gears includes two leg struts and one shock absorber strut; nine strain gages are therefore required. The three gages on each gear will be excited by a single power supply and their outputs amplified by three independent amplifiers.

h. Landing gear position potentiometers. Three position potentiometers (one mounted at the hinge-line of each landing gear leg) will be used to determine the angular relationship between each landing gear strut and the main spaceframe. The relative directions of the forces measured in the struts can thus be determined.

i. Gyro, accelerometer, and associated electronics. The gyro/accelerometer package consists of three rate gyros and three linear accelerometers mounted in precise relationship to sense roll rates and linear accelerations about three mutually orthogonal axes. The package includes all electronics and power conversion circuitry necessary to enable the units to operate from the *Surveyor* spacecraft 22-v power bus and to provide signal outputs compatible with the spacecraft telecommunications system.

j. Touchdown dynamics instrumentation auxiliary. This device is designed to provide those electrical functions required to accomplish the electrical tie-in of subsystem components with the basic spacecraft system. Specifically included are the following:

(1) Master power switching, control logic, and sequence control for the total subsystem.

(2) Command decoding for the entire subsystem.

(3) Subcarrier oscillators and associated filtering for six real-time channels.

(4) Pulse forming of event-marking signals.

(5) Position potentiometer excitation.

(6) Time correlation marker signal generation.

(7) Automatic switching of RADVS signals at engine cutoff.

k. Contact devices. To sense the time at which the various points of the spacecraft initially contact the lunar surface, contact sensors will be located in each of the three footpads and three crushable blocks. In addition

to that instrumentation provided exclusively for the touchdown dynamics experiment, other data pertinent to the experiment are derived from basic bus system elements as follows:

(1) Radar altimeter and doppler velocity sensor (RADVS)—to express spacecraft motions relative to the lunar surface, RADVS velocity outputs are required. These outputs are designated V_x, V_y, V_z, and R.

(2) Vernier-engine strain gages—shutdown time of a vernier engine is desired. This information is derived from an existing strain gage located on the engine mounts.

A typical recording sequence is as follows:

Time, sec	Event
$T - 30$	Recorder electronics on
$T - 29$	Recorder motor on
$T - 27$	Start calibrate
$T - 25$	Stop calibrate
$T = 0$	Touchdown
$T + 30$	System off

l. Equipment location and general arrangement on spacecraft. The touchdown dynamics subsystem, unlike other *Surveyor* instruments, consists of a set of elements located at several points on the spacecraft. Strain-gage bridges are located on each of the three landing legs as are the three position-indicating potentiometers. One contact-indicating device is located on the bottom of each crushable block and landing gear pad.

Specified angular tolerances between the rate gyros and linear accelerometers dictate their being mounted on a common support. As shown in Fig. 81, the rate gyro package and three accelerometers are mounted to a common rigid plate. This plate is mounted at the most rigid point available on the spaceframe. It is expected that the gyro/accelerometer package will be furnished as a unit for installation. Therefore, angular tolerance and coordinate location control need to be maintained only at the installation interface, not with respect to individual sensitive axes. Proper installation will require precise optical tooling to maintain the positional tolerances.

Because of the requirements for complete scientific experiment subsystem autonomy and the necessity of providing an independent location for all payload elements, an additional equipment compartment is required. It will house the tape recorder and associated electronics, the electronic auxiliary, and the strain-gage amplifiers. This compartment, located in Section II, will consist of an aluminum honeycomb platform fastened to the spaceframe by low thermal conductance isolators and covered with a thin outer shell to provide passive thermal control.

m. Wiring harness. The concept of experiment subsystem autonomy requires electrical and physical independence of the subsystem, including the wiring harness. It is expected that a three-branch harness will be required: one interconnecting spacecraft Compartment B and the new equipment compartment, one interconnecting the accelerometer and three gyro units and the new compartment, and one interconnecting the landing gear and crushable block mounted sensors and the new compartment. In addition, an umbilical disconnect (similar to that provided for each of the other scientific experiment subsystems) will be required. This connector, located in Compartment B, will provide the link between the proposed instrumentation subsystem and the basic bus telecommunications, central command decoding, and central power subsystems.

n. New equipment compartment. Equipment will be located in a compartment whose temperature is controlled within the range of -20 to $+165°$F throughout transit and for a period of at least 2 hr after touchdown.

The tape recorder and electronics must operate for a maximum total time of approximately 21 min (1-min record, 21-min playback). The total thermal dissipation rate within the compartment (during the recording cycle) will be 46.4 w. The recorded information will be played back at a rate of one channel per cycle and the thermal dissipation rate during the 21 playback cycles will be approximately 21 w. The bulk temperature rise of the equipment inside the compartment, following 19 min of such operation, will be approximately 5°F. There will be no thermal dissipation within the compartment until approximately 30 sec prior to landing.

A passive thermal design will provide the required compartment temperature control. The equipment mounted in the compartment will have sufficient heat capacity to survive the solar eclipse prior to landing and for at least 2 hr after landing. The tape recorder and electronic components will be mounted on a honeycomb panel attached to the spaceframe with low conductance supports. The panel will be designed to provide a high thermal conductance on the mounting surface side. An outer shell will provide the required thermal radiation shield and will also serve as a dust cover.

UNCLASSIFIED

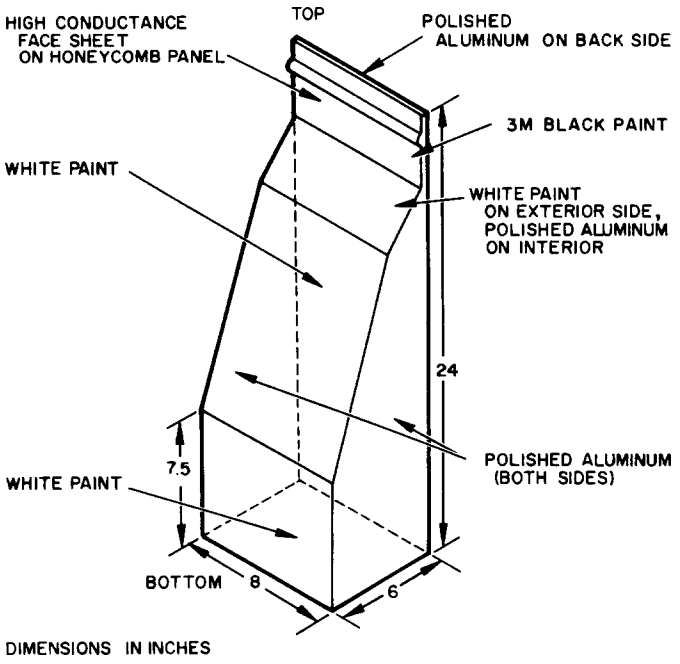

Fig. 82. Touchdown dynamics instrumentation subsystem

Based on calculations, the thermal finish definition shown in Fig. 82 would provide a nominal compartment temperature of approximately 100°F. This temperature would be entirely compatible with equipment requirements since the maximum temperature drop expected during a 1-hr eclipse is 30°F, and during a period of 2 hr following a lunar night landing the compartment temperature would drop no more than 60°F.

o. Compartments A and B. The A-21A spacecraft is expected to land with the temperature of the thermally-controlled Compartment B at near maximum because of the high electrical power dissipations occurring within the compartment during thermal descent. At touchdown, average Compartment A and B thermal tray temperatures of 94 ±13 and 112 ±13°F, respectively, are predicted. (Maximum operating tray temperatures are specified at 125°F.) Since the principal playback operational constraint will be that imposed by Compartment B temperature at landing, the optimum postlanding operations will be determined by the extent to which the compartment thermal transient capability can be utilized as well as by the steady-state compartment dissipating capability available under the solar lighting conditions which exist at touchdown.

p. Power and electrical energy. Expected electrical power requirements for the touchdown dynamics subsystem are estimated in Table 23. The electrical power utilized during the record/real-time data transmission period result in a load increase of approximately 1.0 amp on the spacecraft (29-vdc nonessential) regulated bus. The minimum usable electrical energy remaining in the A-21A spacecraft battery at touchdown is presently estimated at approximately 2000 w-hr. The record cycle is expected to consume approximately 1 w-hr and the playback cycle approximately 11 w-hr. This represents approximately 0.6% of the available electrical energy reserve.

Table 23. Power requirements for touchdown dynamics subsystem

Unit	Electrical power required, w	
	20 v	22 v
Tape transport and associated electronics		14.4
Electronic auxiliary	5.0	2.0
Three-axis gyro/accelerometers and associated electronics		10.0
Strain-gage power supply and amplifiers	20.0	
Total	25.0	26.4

q. Thermal energy. The recorded touchdown dynamics data will be transmitted in either the high-power omnidirectional antenna mode or the low-power planar array mode. The effects of either of these operational modes on compartment thermal constraints are functions of lighting conditions which exist at touchdown.

If it is desired to utilize the low-power mode of telemetry transmission, playback must be delayed approximately 1 hr to allow Earth acquisition with the high-gain antenna and completion of desired basic bus posttouchdown operations. Under worst-case lunar-noon lighting conditions, a steady-state thermal environment could be approached 1 hr after touchdown. The recorder playback would then be restricted by Compartments A and B steady-state dissipating capabilities. Transmission in this mode is restricted only during a relatively narrow range of solar angles centered about lunar noon. Proper orientation of the solar panel could provide increased compartment thermal dissipation during the critical time interval.

If immediate playback of the recorded data is of prime importance, use of the high-power omnidirectional antenna mode would permit transmission within a few

UNCLASSIFIED

minutes after touchdown under most lighting conditions. Postlanding power shutdown operations, verification of telemetry status, and the playback of touchdown dynamics data would require approximately ½ hr of high transmitter power operation. With Compartment B at 112 ± 13°F at touchdown, the allowable duration of continued operation in the high-power mode is presently unknown. A detailed transient thermal analysis would be required to provide this definition. Near lunar noon, the compartment may be cooled to a lower initial temperature by positioning the planar array and solar panel to partially shade the radiators or to reduce the thermal energy reradiated to the compartments from the panels. For other landings, a cooldown period may be necessary to provide lower initial compartment temperatures. In either case, delay of playback would be required.

In summary, if data playback can be delayed for all landings, use of low transmitter power with high-gain antenna would be advantageous. The lower electrical power dissipations in the thermally-controlled compartments would result in a significant reduction in the rate of temperature rise near lunar noon, and nonstandard solar panel positioning (for improvement in compartment dissipating capability near noon) would become significantly more effective. Low transmitter power operation is generally more desirable because continuous operation during a major part of the lunar day would not be constrained. The major disadvantage lies in the necessity to delay data transmission until the Earth is acquired by the high-gain antenna. This delay is estimated at 1 hr or more.

r. Hardware description. As shown in Table 24, equipment comprising the touchdown dynamics subsystem is contained in several units. Unit names, quantities, and physical characteristics are given.

6. Preparations for Analyzing Surveyor Video Data[9]

a. Introduction. The *Surveyor* Space Science Analysis and Command (SSAC) group in the Space Flight Operations organization is responsible for the organization and conduct of the portion of the *Surveyor* mission related to operation of the scientific instruments on the payload, and for the evaluation of the data resulting from the instruments. For the first mission, the instrument payload consists of a survey television camera.

The Television Performance Analysis and Command (TelPAC) group is part of the SSAC organization. This is a group of technical specialists who analyze and evaluate instrument performance, and also control the engineering performance of the television experiment.

b. Video analyst responsibilities. One of the technical specialists in the TelPAC group is the video analyst. His primary task is to monitor the video data displays, analyze the data, and determine the electronic performance of the television instrument.

[9] Prepared by JPL Technical Section 323.

Table 24. Touchdown dynamics instrumentation subsystem

Unit	Number required	Size, in.	Weight, lb
Equipment compartment structure, including attaching hardware	1	24.0 × 6.0 × 8.0	2.25
Tape recorder and associated electronics	1	6.00 × 7.00 × 6.00	8.0
Electronic auxiliary	1	3.00 × 3.00 × 5.30	2.50
Gyro/accelerometers, associated electronics and mounting plate for gyro/accelerometers	1	4.50 × 5.50 × 2.0	4.00
Strain-gage power supply/amplifier (3 at 0.5 lb each)	3	1.70 × 2.50 × 2.00	1.50
Strain gage (9 at 0.10 lb each)	9	0.50 × 1.0	0.90
Leg position potentiometers (3 at 0.25 lb each)	3	0.75 × 1.25	0.75
Contact switches (6 at 0.25 lb each)	6	0.50 × 1.0 × 1.0	1.50
Wiring harness for subsystem	—		2.25
			23.65

UNCLASSIFIED

After a successful lunar landing and prior to opening of the mirror on the television instrument, an analysis of the video data will determine:

(1) The amount of noise in the video signal.

(2) The dark signal level or black reference.

During a picture-taking sequence with the television mirror stepped open, the video analyst will determine:

(1) The nominal signal-to-noise level at any specific time.

(2) The video signal amplitude as a percentage of full saturation level.

(3) The sharpness of focus (electronic and optical).

(4) Video content and contrast in the data.

(5) Malfunctions or anomalies with the instrument operation.

The video analyst must be prepared to detect anomalies, analyze the cause of the anomaly, and recommend corrective action. Examples of such anomalies are:

(1) Dark picture — underexposed.

(2) Saturated picture — overexposed.

(3) Picture is out of focus.

(4) Shaded picture.

(5) Video data that is inconsistent with TV identification data or with commands transmitted to the spacecraft.

c. Equipment. The video data displays presently consist of a slow-scan television monitor, and a type 564 storage oscilloscope. These are shown in Fig. 83. These pieces of equipment are eventually to be part of an engineering console to be used by the TelPAC group.

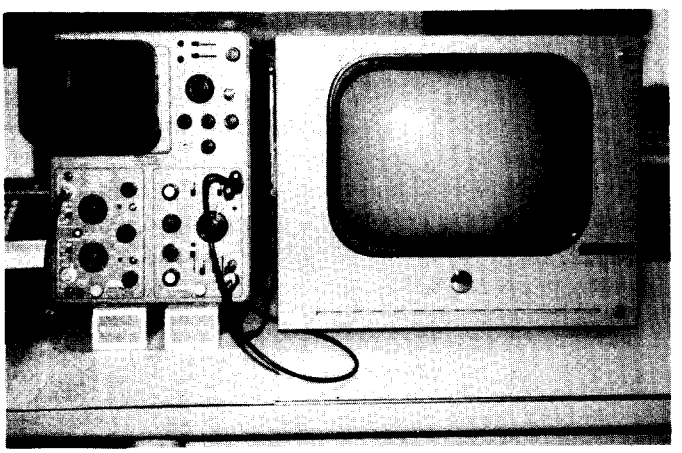

Fig. 83. Storage oscilloscope and slow-scan monitor

The slow-scan monitor is capable of operating at either the *Surveyor* television normal-mode 1.2-sec frame time, or the 20-sec emergency-mode frame time.

It will be necessary during a mission to obtain photographs of the video data displayed by the slow-scan monitor and by the oscilloscope. During training exercises, it has been difficult to monitor the video data and photograph it using the one set of display equipment. It is planned to obtain another slow-scan monitor and oscilloscope with polaroid oscilloscope cameras to obtain the required photographs.

d. Training. Many training exercises have been conducted in order that the members of TelPAC could become proficient in their tasks. A prototype *Surveyor* television camera known as the 4.2.2 camera is used as the source of video. The video data is displayed on the monitoring equipment in a similar manner to a real mission. The A-trace display on the oscilloscope allows the video signal to be seen in analog form. This display is valuable for determining signal-to-noise ratio, video signal amplitude, the black-level and white-level amplitudes, and the sharpness of focus. The monitor display exhibits picture content and contrast.

During the training exercises, the 4.2.2 camera has been used in three different configurations. In the first configuration, the camera is positioned and focused on a screen where an image is projected by a 35-mm slide projector using the rear projection technique. The azimuth and elevation positions of the camera mirror are not physically changed, but appear to change from an analysis of the video data. This realism of the data is due to the projection of different images or scenery. The iris and filter wheel are physically changed at various times to adjust for image intensities.

In the second configuration, the camera is installed inside a large circular area called the panorama. Inside the panorama is a photographic display of scenery which is illuminated by floodlamps. Fig. 84 shows the 4.2.2 camera inside the panorama. Fig. 85 is a view of the panorama and camera from the top edge of the panorama. During training exercises with this arrangement, the camera mirror is stepped in both azimuth and elevation, thereby simulating a real mission.

In the third configuration, the camera and mounting tripod are set on the roof of the Space Flight Operations

UNCLASSIFIED

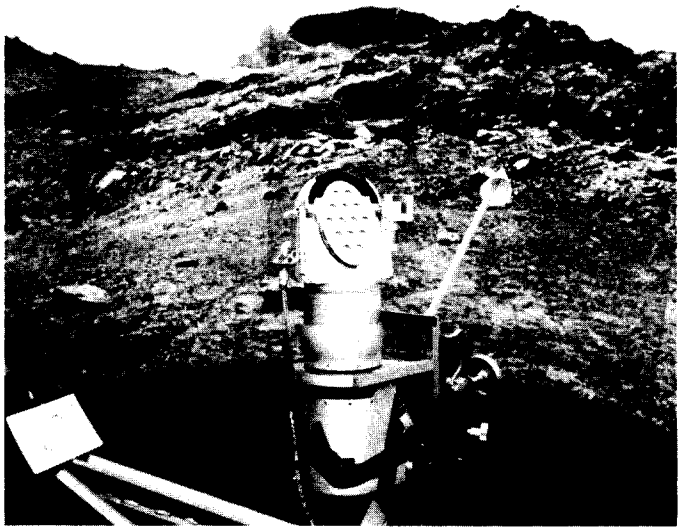

Fig. 84. Prototype *Surveyor* camera inside panorama

Fig. 85. Prototype *Surveyor* camera and panorama from top edge of panorama

Facility building. In this arrangement all the operating functions of the television camera are utilized. The only disadvantage of this configuration is the presence of distinguishable familiar items in the video data such as buildings, automobiles, etc.

An important part of the training exercises has been the simulation of malfunctions and anomalies with the television camera. After an anomaly or malfunction has been recognized by TelPAC, corrective action is recommended such that a particular camera survey could continue and usable video data be obtained. Many different problem situations have been simulated during the exercises. From the experience of working under these non-standard situations, sets of corrective action and failure flow diagrams have been generated by the TelPAC group to aid in quick solutions. These sets include:

(1) Underexposed pictures, above and at noise level.

(2) Saturated pictures.

(3) Shaded picture.

(4) Torn or noisy picture.

(5) Filter interrogation sequence.

(6) Iris interrogation sequence.

(7) Auto iris failure.

(8) Manual iris failure.

(9) Shutter failure.

(10) Focus failure.

(11) Mirror azimuth failure.

(12) Mirror elevation failure.

(13) Focal length failure.

(14) Filter wheel failure.

e. Future plans. The training exercises are scheduled to continue using both standard and non-standard situations. The 4.2.2 camera is being modified to operate in the emergency mode and also in a new mode known as the star integration mode. These modes are both possible operating modes for the first *Surveyor* mission. Training exercises will be conducted utilizing these modes of operation with the 4.2.2 camera.

A tape recording has been made of the video signal from the flight camera aboard the first flight spacecraft. A complete first survey was made with this camera during the recording. The playback of this video data from the recording will allow the members of TelPAC to become familiar with flight camera data and also to be able to distinguish parts of the spacecraft that are within the camera's field of view.

N. Thermal Control

1. Subsystem Thermal Analysis and Design

a. Radar altimeter and doppler velocity sensor (RADVS). After readjusting the T-21 solar-thermal-vacuum test data for the seven previously reported intensity discrepancies, the RADVS system thermal response is within the predicted range. The klystron power supply and modulator (KPSM) temperature spread about the nominal was ±7°F and not the expected ±13°F. The signal data converter (SDC) internal temperature spread was ±6°F. The comparison of the ±6°F with the predicted ±11°F is a matter of further study since the cover-to-cover temperature gradient was ±15°F. The gradients found on the receiving transmitting antennas were considerably less than predicted.

The signal data converter thermal finish pattern was changed from its T-21 design to increase its expected flight temperature to a 72°F bulk nominal. The SC-1 thermal finish pattern for all other units is identical to the T-21 design.

The RADVS thermal design has been based on the corrected Phase II and III T-21 solar-thermal-vacuum test data. The correction applied is equivalent to a 7% high reading of the radiometers. The corrected T-21 results are presented in Table 25.

Table 25. T-21 RADVS thermal design data

Unit	T-21 pretest predictions, °F			T-21 test results,[a] °F		
	Simulated transit coast phase			Simulated transit coast phase		
	Bulk nominal and predicted uncertainty	Temperature spread about nominal	ΔT after 30-min solar eclipse	Bulk nominal	Temperature spread about nominal	ΔT after 30-min solar eclipse
KPSM						
Main package without doppler-velocity-sensor klystron tube assembly	21 ± 23	±13	−15	39	±7	−15
Doppler-velocity-sensor klystron tube assembly	25 ± 40	—	−25	39	—	−15
SDC						
Mother board assembly	65 ± 26	±11	−5	75	±6 (internal T/C) ±15 (cover to cover)	−8
Low-voltage power supply	65 ± 26	±8	−20	75	—	−18
R-T assemblies						
Altimeter/velocity-sensor antenna						
Dish and skirts	(−140 to 125) ±42	—	−40	−25 to 114	—	−10 (min) to −105 (max)
Septum (2)	(−85 to 20) ±42	—	−40	−32 to 25	—	−20
Feedhorn	(−12 to 8) ±42	—	−40	—	—	—
Preamplifier and crystal holder	38 ± 35	±10	−30	21 to 47	—	−30
Velocity-sensor antenna						
Dish and skirts	(−140 to 125) ±42	—	−40	−32 to 83	—	−10 (min) to −100 (max)
Septum (2)	(−85 to 20) ±42	—	−40	−24 to 1	—	−10
Feedhorn	(−20 to 0) ±42	—	−40	—	—	—
Preamplifier and crystal holder	30 ± 35	±10	−30	11 to 35	—	−20
Waveguide assembly	—	—	—	23 to 50	—	−24

[a]Temperatures are corrected for solar intensity measurement discrepancy of approximately 7% high reading of radiometer.

A preliminary analysis was performed on the RADVS antenna to determine the thermal effects that would result from the closing of the antenna aperture with radio-frequency transparent, light-diffusing cover. This analysis was performed, primarily, to compare the transit coast-phase temperature rise of the existing antenna without a shield to the temperature rise of the antenna with a shield placed initially so as to completely cover the aperture and then secondly moved up into the aperture so as to just cover the parabolic surface.

In the case where the shield completely covered the aperture, a maximum temperature increase (over an unshielded antenna) of approximately 25°F was calculated. When the shield was moved up into the aperture, the corresponding temperature increase was approximately 5°F. The reason for the drop in temperature difference is that in the former case the shield acts as a barrier to radiation losses from the high-emittance microwave absorber located on the inside of the antenna while in the latter case only the parabolic surface within the aperture is covered leaving the microwave absorber free to radiate. Effects on the functional performance of the antenna of this latter configuration remain to be determined.

The minimum expected temperature of the existing antenna is −50 to 140°F. With the cover emplaced over the aperture the temperatures increase to −26 to 176°F but drop down to −47 to 144°F when the cover is placed only over the parabolic surface.

b. Thrust chamber assemblies (TCA). The thermal designs for SC-1 checkout and flight TCAs have been defined. The individual thermal designs are predicated on point values of interface joint conductance and extension cone inner surface emittance for each TCA. Paint patterns and reflector sizes have been designed to maintain TCA temperatures (excluding the nozzle extensions) between 0 and 165°F during all engine inoperative periods. A transit steady-state temperature of 130°F has been selected as the design point nominal for the head end of the TCA. TCA thermal design parameters and the nominal thermal performances are tabulated in Table 26 for SC-1 flight and checkout TCAs.

During receiving inspection, SN-537 was found to be unacceptable for use on the SC-1 spacecraft. SN-541, a backup flight-qualified TCA, will be used to replace SN-537 at Leg 2 on the SC-1 flight vehicle. The thermal performance of SN-541 is expected to parallel the thermal behavior of SN-537. Interface joint conductance, nozzle-extension-cone inner-surface emissivity, and nozzle-extension-cone outer-surface emissivity for SN-541 have been determined to be 2.00, 0.19, and 0.78 Btu/hr-°F, respectively. The thermal parameters of SN-541 are sufficiently similar to the thermal parameters of SN-537 that no change in the thermal design is required.

Table 26. Thermal design and predicted temperatures of SC-1 thrust chamber assemblies for flight conditions

TCA					Predicted temperatures (nominal values)						TCA thermal design parameters					
											Thermal finish			Reflector		
					Coast phase			After $T-$ min solar eclipse[a]			Head end					
Serial number	Joint conductance, Btu/hr—°F	Extension cone inside emissivity, ϵ_n	Extension cone outside emissivity, ϵ_n	Spacecraft leg number	Head end, °F	Bottom barrel, °F	Top of cone, °F	Head end, °F	Bottom barrel, °F	Top of cone, °F	Black paint, in.^{2}	White paint, in.^{2}	Remaining TCA area gold plate[b]	Mirror angle ϕ deg	Mirror depth, in.	Mirror projected area, in.^{2}
Checkout																
501	1.24	0.30	0.788	1	131	58	38	100	45	24	0.00	4.50	$\alpha-0.28$	NA[c]	NA	NA
502	1.95	0.30	0.788	2	129	87	79	98	41	25	2.80	0.00	Gold	54.5	3.50	20.0
504	1.37	0.30	0.788	3	131	56	41	96	32	11	3.50	0.00		36.2	2.30	8.0
Flight																
536	2.33	0.24	0.788	1	123	46	33	91	32	20	0.00	4.50		NA	NA	NA
537	2.33	0.21	0.788	2	133	92	85	102	45	31	2.80	0.00		54.5	3.50	20.0
539	2.66	0.26	0.788	3	132	56	49	96	31	20	3.50	0.00		36.2	2.30	8.0

[a]Eclipse duration: 33 min—TCA-1, -3; 39 min—TCA-2.

[b]An α gold of 0.36 was used in the study to account for cavity effects on top of the TCA's.

[c]NA = not applicable.

A parametric study was made to determine the influence of variable barrel/nozzle-extension-cone interface joint conductance values ($0.5 \leq C \leq 3.0$ Btu/hr-°F) and nozzle-extension-cone inner-surface emittance ($0.02 \leq \epsilon \leq 0.38$) on TCA steady-state transit temperatures. The results of the study indicate that the TCA temperature range of 0 to 165°F will be exceeded if a wide range of interface joint conductance and emittance values are imposed on TCA temperature control. Based on the above ranges of thermal parameters, the TCAs will have a total temperature in the range 0 to 165°F; the bandwidth of conductance and emittance values must be restricted or point values must be known. A tolerable range of conductance and emittance values are $C = 2.50 \pm 0.50$ Btu/hr-°F and $\epsilon = 0.23 \pm 0.04$, respectively.

Because of a failure of the vernier-engine bracket isolation hardware during a simulated-altitude engine firing at Edwards Air Force Base, steps were taken to increase the strength of the isolation hardware by substituting stainless steel washers for laminated plastic washers in two places, and to protect the isolation hardware from direct infrared heating from the vernier nozzle cone by inserting a 0.1-in. polished aluminum heat shield between the nozzle cone and the thermal isolation hardware. These changes were compatible with thermal control requirements. On June 21, 1965 this redesign performed successfully during a 200-sec simulated-altitude engine firing at Edwards Air Force Base. Thermal data from the above test (such as temperature versus time plots) is being evaluated and will be presented in the next *Space Programs Summary*.

c. Propellant feed system. Analysis of the thermal control system for the anti-migration propellant feed system is in its final stages. Included in the analysis is a study to determine the thermal feasibility of replacing the vapor-deposited aluminum (VDA) on the propellant lines with a polished surface which would be more resistant to physical degradation. Preliminary results (steady-state) show little temperature effect on those lines connecting to TCAs 2 and 3; it is felt that a substitution will be possible. However, on those lines connecting oxidizer and Fuel Tank 1 to TCA 1, a paint pattern comprised of organic white and polish will be required to maintain proper thermal control on the lines. The temperature requirements of the propellant lines were heretofore specified to be 0 to 100°F during all phases of the flight; the minimum expected temperature was set by the thermostat actuation temperature (16°F). In view of the recent increase in maximum allowable TCA temperature to 165°F during inactive portions of the flight, sections of the lines immediately adjacent to the TCA will exceed 100°F because of conduction coupling. This situation has received attention in recent proposed amendments to the Hughes Aircraft Company/JPL TCA interface document. It is the objective of the current thermal finish optimization studies to minimize the length of line above 100°F consistent with the goal of employing a thermal finish that is highly resistant to degradation. In addition, it may be necessary to relocate the thermostat on this set of lines if the paint and polish pattern is substituted for VDA. For the SC-1 system (VDA), no thermal problems are expected; complete predictions for both steady-state and transient phases of flight are to come.

Because of installation problems (i.e., only a limited number of turns of heater wire can be wrapped per inch of line) a modification has been made to the heater requirements for the anti-migration propellant feed lines (Table 27).

Table 27. Heater requirements for anti-migration propellant feed lines

Line	Heater line length, in.	Power density, w/ in.	Power capability/ line, w
Oxidizer Tank 1	23.2	0.094	2.18
Fuel Tank 1	13.3	0.032	0.45
Oxidizer Tank 2	28.0	0.08	2.24
Fuel Tank 2	19.0	0.06	1.14
Oxidizer Tank 3	26.0	0.075	1.95
Fuel Tank 3	18.0	0.019	0.34

d. Helium tank. *SPS 37-34*, Vol. I inadvertently indicated that maximum temperatures would occur on the outboard surface of the SC-1 tank. The maximum tank temperatures actually occur on the inboard surface. Considering the possibility of 140 and 115°F existing on the tank and valve assembly, respectively, the present upper temperature limits of the tank (115°F) and valve assembly (100°F) are being evaluated with the objective of increasing the upper limits, if possible. If increased limits are not possible, a redefinition of the paint pattern will be necessary.

The analytical model of the tank and valve assembly is in the process of being upgraded, with the ultimate objective of developing an optimized paint pattern. Of prime interest is the possibility of replacing the VDA with a thermally suitable material or process which will more readily withstand normal handling and testing.

UNCLASSIFIED

e. Main retro-engine. A thermal analysis has been made of the A-21 main retro-motor to determine maximum propellant temperatures at the time of ignition. The factors contributing to upper-bound-terminal propellant temperatures were a maximum allowable propellant temperature of 90°F at launch and higher temperature boundary conditions on the outside of the super insulation blanket consistent with the use of an electrostatic grounding conductive mesh.

To evaluate the thermal aspects of the electrostatic grounding, solar absorptance and emittance property measurements (before and after 100 hr of ultraviolet irradiation) were made on samples of 2-mil aluminized teflon with a conductive mesh sewn to it. The solar absorptance before ultraviolet irradiation increased to 0.18 and 0.19 on a sample with the mesh, compared to 0.16 on a sample without the mesh. The solar absorptance after ultraviolet irradiation further increased to 0.21 and 0.22 on the conductive mesh sample and remained constant at 0.16 on the sample without the mesh. The emittance remained constant at 0.69 and 0.70 independent of the presence of the mesh and ultraviolet exposure.

The increase in solar absorptance after ultraviolet irradiation will result in higher boundary temperatures on the exterior of the retro. For this analysis, it was assumed that these higher boundary temperatures existed throughout the entire transit period. (All previous retro propellant calculations were based on 80°F start temperatures because the minimum temperatures at the time of ignition were of interest.) The maximum propellant temperature distribution at retro ignition was sought and the propellant temperatures at launch were changed to 90°F. The appropriate changes were made to the three-dimensional retro heat transfer program and the resulting propellant temperatures were determined. The analysis indicated that at the end of 66 hr the head-end propellant temperature was 75 ±5°F, the minimum temperature adjacent to the skirt attach point at spacecraft Leg 2 was 42 ±11°F, and the temperature at the aft burning surface was 45 ±11°F. About 50% of the propellant mass was in excess of 70°F, the bulk temperature limit given in the retro procurement specification. The temperature at all propellant locations was shown to have increased from 9 to 13°F above those previously reported. Approximately two-thirds of the increase is because of higher initial temperatures and about one-third is caused by increased boundary temperature resulting from the conductive mesh. The bulk propellant temperature is estimated to be 65 ±5°F. The highest temperature at which the retro has been qualified for flight is 70°F.

The detailed temperature distribution has been provided to the propulsion and systems analysis activities for review to determine if the local and bulk temperatures are within specification and qualification temperature limits.

f. Auxiliary battery. Results obtained during T-21 solar-thermal-vacuum test were employed to estimate the maximum anticipated SC-1 flight temperatures. The maximum cover plate temperature is not expected to exceed 110°F during steady state and no power dissipation is expected. Although preliminary analysis indicates the possibility of overheating (> 130°F) during dissipative battery modes, it is felt that the analysis is too conservative. Thus, the analytical model of the auxiliary battery is being modified for the purpose of performing detailed T-21 data evaluation studies of the auxiliary battery design and ultimately predicting flight temperatures.

g. Altitude marking radar. First-order calculations indicate heat losses of approximately 0.5 to 1.0 w occur because of a 0.6-in. gap between the altitude marking radar electronics deck and the thermal hat. Action has been taken to determine an efficient means of eliminating this gap. Electrical energy requirements may be reduced by 15 to 30% from the current energy dissipation levels if this change can be accomplished.

h. Antenna/solar panel positioner (A/SPP).

A/SPP solar-thermal-vacuum test. A solar-thermal-vacuum test was conducted using the X-1 A/SPP hardware mounted in a holding fixture in the JPL 25-ft space simulator. Analysis of the test data has not been completed; however, some preliminary results are presented in the following paragraphs.

Fig. 86 presents a summary of the raw test data and Fig. 87 presents a summary of the current SC-1 flight temperature predictions. The SC-1 flight temperature predictions were generated with a computer model that was revised to incorporate the modified thermal characteristics needed as indicated by the test data. The approach used in analyzing the test data was to reproduce the test results using the computer model. Solar mapping data recorded prior to and following the test were used to revise heat inputs to various model elements. After the computer model was revised to yield temperatures which approximate the actual test data, the

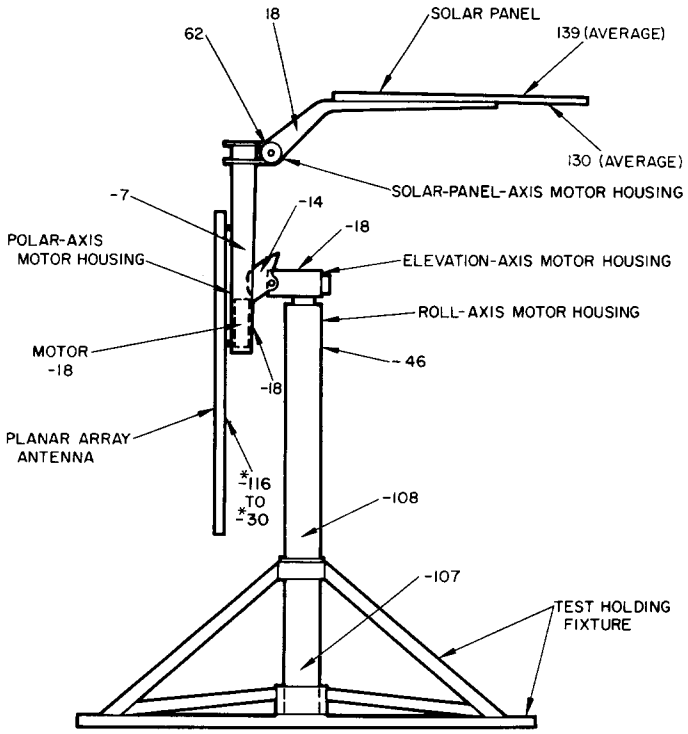

Fig. 86. Model X-1 antenna/solar panel positioner solar-thermal-vacuum test data

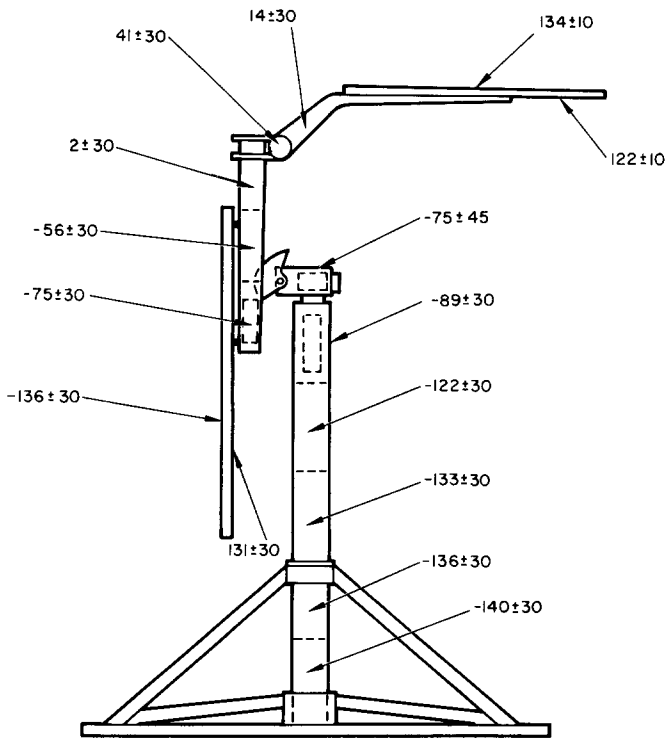

Fig. 87. Model SC-1 antenna/solar panel positioner flight temperature predictions

environmental changes between test and space were subtracted from the model inputs and the resulting computations represent the SC-1 flight predictions.

The majority of the mismatch between flight and test environment was caused by solar energy side loading on the vertical surfaces of the hardware due to solar beam divergence and chamber reflections. Such inputs have very little effect on the solar panel temperature and a relatively large effect on the planar array antenna and positioner mechanism.

The data obtained during operation of the special test heater provide a means of evaluating the thermal conductance across some questionable interfaces. The results of such analysis have been incorporated into the computer model. The conductances are representative of maximum values since the contact conductances in question are higher in Earth gravity than in a zero gravity condition.

Based on the data analyzed to date, the flight temperatures appear to be warmer than anticipated and temperature gradients throughout the mechanism appear to be lower than anticipated. Temperature differences of less than 5°F were observed among the sector gear, worm gear, and elevation-axis motor housing. The solar panel temperature was as predicted (approximately 140°F with no electrical power being used), and the temperature difference between the cell side and the back side of the solar panel was a maximum of 12°F (a 6°F-ΔT was predicted). The cell side of the panel dropped 50°F during the first minute of the solar eclipse. This temperature drop corresponds with temperature drop measurements made previously on the panel.

Based on the current understanding of the test results, the minimum drive-motor temperatures are presented in Table 28 for the first flight spacecraft. Evaluation of the test data is continuing and the temperatures in Table 28 may undergo some modifications at the completion of the data analysis. Temperature tolerances are based on engineering judgment augmented by thermal information obtained during the test data reduction process.

Antenna/solar panel positioner redesign. The thermal control efforts in the A/SPP redesign have been centered

Table 28. Predicted flight temperatures — SC-1 A/SPP drives

Drive motor assembly	Minimum temperatures, °F	
	Transit coast mode	Touchdown (assumes 1/2-hr solar eclipse)
Roll axis	−119	−132
Elevation axis	−120	−135
Polar axis	−120	−123
Solar axis	10	−66

around the positioner motor-drive assemblies. The proposed redesign thermally isolates the stepping motors and drive assemblies from the motor housings and results in a potential overhead problem when the motors are operated continuously for 30 min as specified in Hughes Specification 224510. Motor coil temperatures as high as 550°F have been indicated by coil resistance measurements after 15 min of continuous stepping. The coil wires are teflon-coated and will suffer degradation in insulating characteristics at temperatures over 400°F.

Thermal control has proposed a thermal conductance strap to be attached between the motor case and housing of each drive mechanism. Such a device will lower the motor-case temperature and also lower the motor-winding temperature during operation. Various methods of improving the conduction coupling between the motor winding and case are being investigated. A thermal test is planned to evaluate the proposed methods of increasing coil to motor case conductances.

2. T-21/SC-1 System Test Support

A detailed thermal-control evaluation report has been prepared discussing the results, conclusions, and recommendations from the T-21 solar-thermal-vacuum tests. The evaluation is being released as part of the overall T-21 Phase Report. Support of the SC-1 solar-thermal-vacuum flight acceptance tests has consisted of selecting the solar intensity levels for all the test phases; performing an evaluation test to determine effective radiation properties under a xenon source; determining acceptance criteria for the spacecraft thermal control systems; providing data display requirements for the computer data system, which provides flight thermal sensor data in real time and in engineering units; and defining a black-plate radiometer installation to complement the Eppley solar monitors.

a. SC-1 solar intensity levels and effective radiation property data under xenon spectrum. The SC-1 solar-thermal-vacuum flight acceptance test will consist of three phases. The first two phases are consecutive nominal mission sequences (one at a low solar intensity and the other at a high solar intensity) with a full complement of functional test equipment. The third phase is an abbreviated mission sequence at a nominal solar intensity. This phase is a "plugs-out" test devoid of most test equipment and hardline harnesses.

The solar intensity levels will be 88% of a solar constant in the low intensity phase, 100% of a solar constant in the nominal intensity phase, and 113% of a solar constant in the high intensity phase referenced to a black-plate standard. These levels correspond to 80, 92, and 105% of a solar constant measured on the Eppley radiometer SN-5509. Effective radiation properties of thermal finishes under a xenon source have been determined from the 6-kw xenon evaluation test. For most finishes, property values under a xenon source are close to those resulting from the actual Sun. The match in properties is superior to those obtained with a mercury-xenon source.

b. SC-1 thermal control system acceptance criteria. The thermal acceptance criteria have been developed; the details are presented in the A-21 flight acceptance plan for the solar-thermal-vacuum test phase; and a summary is presented in the subsequent discussion.

Many differences exist in a solar-thermal-vacuum environment compared with a space environment. In the post-test evaluation period it will be necessary to make adjustments in the temperature results for the differences which exist between the test environment and the space environment. The effects of environmental conditions for which testing is not performed, such as off roll-axis orientation of the vehicle during maneuvers and the approach to a hot lunar surface, will have to be added to the adjusted temperature range. In addition, a further allowance must be made for temperature uncertainties not eliminated by test such as the potential contamination of thermal finishes between conclusion of testing and launch.

Flight thermal sensor data, although considered the basic data, will be supplemented by thermocouple data as required. The data evaluation procedure consists of transposing and adjusting the data to a flight environment, and comparing the results to temperature limits. In general, it is anticipated that temperature requirements will be satisfied and thermal acceptance will be achieved. If temperature performance does not satisfy its thermal requirements, a disposition will have to be made. If a unit has demonstrated proper functional performance during the vehicle solar-thermal-vacuum tests despite

UNCLASSIFIED

temperature limits being exceeded, or if a unit supplier can prove that proper functional performance can be obtained at temperatures outside the stated limits, it will be possible to use the unit as is. If temperature excesses cannot be tolerated, modifications will be made to the thermal control system and verification testing may have to be performed.

c. Computer data system. In addition to the auxiliary data monitoring system, which provides temperatures measured by thermocouples in near-real-time during SC-1 flight-acceptance-test operations, a computer data system (CDS) will be available for near-real-time display of temperatures measured with flight thermal sensors. Flight sensor temperatures will be displayed on a character printer at the test site whenever an averaged group of temperature samples changes by $\pm 3°F$ from the previous printout or whenever an alarm limit is exceeded. In addition, a dump of all sensor data on the various commutators will be displayed on a line printer whenever an engineering interrogation is made. Thermal support for this activity has consisted of providing thermal sensor calibration data, temperature alarm limits, and the number of data samples to be averaged as a function of telemetry bit rate. The thermal calibration data was provided in terms of scaling coefficients obtained from curve fits of calibration data provided by the manufacturer. An additional capability of the CDS is to provide post-test automatic plotting of SC-1 thermal sensor measurements.

d. Black-plate radiometers. Two black-plate radiometers are to be installed in the Hughes vacuum chamber to supplement Eppley solar intensity monitors during *Surveyor* flight spacecraft solar-thermal-vacuum tests. Comparison of solar intensity values obtained with Eppley radiometers and black plates indicates a difference of 7 to 10%. The relative response of the plates and radiometers will serve as a further verification of the intensity and prevent testing with erroneous solar intensity levels due to an instrument malfunction as occurred in the T-21 solar-thermal-vacuum tests.

The two plates are mounted in a horizontal plane side by side above the normal transit position of the solar panel support arms (155 in. above the chamber I-beams). Two thermocouples and a heater are bonded to the bottom of the plate, which is then covered with 10 sheets of aluminized mylar.

Three steady-state temperature conditions will be established at each solar intensity level, two with heater power applied. From this data, the constants, including solar intensity, can be determined.

3. Spacecraft Performance Analysis and Command (SPAC) Support

The thermal management program was developed as an analytical tool that could be used during the *Surveyor* mission to predict and compare spacecraft temperatures, and to predict heater power requirements for the power management program. The Thermal Management Program Test Specification has been prepared, describing in detail four test models that will be used to verify operation of the program features during the thermal program certification test. All of the test models have been checked out satisfactorily at Hughes Aircraft Company, and the program is judged to be ready for usage in the SPAC mission control tests. After satisfactory results during program integration tests at JPL in the current reporting period, the certification tests for the thermal analog models will take place. To meet a constraint placed on the amount of computer core storage available to the thermal management program, it has been necessary to delete the part of the program that allowed for automatic data plotting at JPL of program results. This deficiency is expected to be corrected for missions subsequent to SC-1.

The thermal sensor data for Phase 2 of T-21 solar-thermal-vacuum testing has been reduced from programmed automatic telemetry evaluator tapes and published. This data along with data previously published on T-21 Phase 3, and data to be obtained from SC-1 flight-acceptance solar-thermal-vacuum tests during the week ending July 30, will be used to evaluate the predictions made by the thermal management program for the *Surveyor* transit model.

4. S-10 (Temperature Control Model) Test Program

a. Thermal control model (TCM) vehicle status. The *Surveyor* TCM has been scheduled for a solar-thermal-vacuum test at the Hughes Aircraft Company and the JPL space environment facilities before the first *Surveyor* spacecraft flight. The TCM spaceframe subassembly, including thermal finishes, is complete and mock-up temperature sensors with built-in thermocouples are installed. Support brackets for the remaining control item units are planned. Delivery of the TCM to thermal control for final thermocouple installation is anticipated by late August 1965.

UNCLASSIFIED

b. Test facilities. Test facility equipment, test operation instrumentation fabrication, and checkout are in various states of completion. Close coordination is underway to ensure compatibility of the TCM and TCM test equipment to the new 10-ft JPL space environment simulator. Various 10-ft diameter chamber rework tasks are presently being completed to comply with the TCM test environment, vehicle mount, and LN_2 shroud requirements. After the 10-ft chamber rework has been completed, an evaluation test of the chamber will be conducted before testing the *Surveyor* TCM. The evaluation test will measure the chamber effective wall temperatures as seen by radiation coupling to flat plates in the chamber center, collimation of the solar simulator beam, apparent solar absorptance of various typical *Surveyor* thermal finishes when irradiated by the xenon lamp through the associated optic system, and the chamber vacuum capability.

c. Data acquisition instrumentation. Instrumentation for the TCM data acquisition is nearly completed. Presently, checkout is being completed on the power control console and the Automatic Data Monitoring System (ADMS) Scanner 4 for acquisition of approximately 50 electric thermal mockup heater power dissipation levels. The completion of this power ADMS will represent an advancement in the state of acquisition of large quantities of accurate power data and data reduction into various tabulated formats in real test time. The first three scanners of the ADMS will monitor about 800 thermocouples on the TCM, reduce the thermocouple temperature millivolt signal to degrees Fahrenheit within real test time and tabulate the results in selected formats. A variety of duty cycle instruments for recording the TCM thermostatically-controlled active heater power operation periods are being investigated for lease or procurement. The TCM A/SPP pulse commander will be integrated with the TCM A/SPP unit and checked out before installation on the TCM vehicle.

d. Special TCM test equipment. The T-21 liquid-nitrogen solar-panel simulated-shadow shroud systems will be used in the TCM testing. One additional shroud will be mounted under the RADVS velocity sensor antenna to obtain empirical data on the effect of the reflected solar radiation from the Hughes chamber end bell LN_2 shrouds into the altitude velocity sensor dish. A second shroud system will consist of three TCM LN_2 cylindrical shrouds wrapped around the three TCM hard-mount legs between the end bell attach point and the TCM vehicle attach point. Each support leg will be wrapped with aluminum foil before the shrouds are installed. These three shrouds will reduce the thermal energy radiation loss from the existing bare fiberglass epoxy legs.

A vernier-engine nozzle-cone heating simulator is being developed for simulating the effect of midcourse maneuver and terminal descent firing radiant heat effect on spacecraft subassemblies adjacent to the engines. The simulated nozzle configuration is an 80-20 nickel-chrome alloy ribbon-wound ceramic core heater. The heating-element temperature response time required to reach about 2000°F is estimated to be less than 30 sec. The heater will be capable of repeated firings under a space-simulated environment. The first development tests in a space environment are scheduled for about the first week of August. On final acceptance of the nozzle heater, three models will be built, one for each engine location, for testing on the TCM during the scheduled Hughes Aircraft Company Phase I tests.

e. S-10 test plan. Table 29 summarizes the S-10 test plan by defining the test vehicle configuration and major test objectives for each phase. Three phases are planned at the Hughes space simulator to be followed by three phases at the JPL 10-ft simulator. The total test time will be approximately 190 hr. The total vehicle instrumentation has been defined and the detailed test procedure is in progress.

5. Retrorocket Exhaust Plume Radiation Study

A heat flux of 0.12 Btu/ft²-sec was previously reported on the RADVS antennas from the variable radiosity retrorocket exhaust plume. This incident flux applies to the antenna dishes; it would cause a maximum temperature rise of 13°F and does not represent an overheating problem (Table 30).

The microwave absorber material on the inside of the RADVS antenna skirts is sensitive to the retro exhaust plume radiation because it has a high absorptance, low heat capacity, and a view to the high radiosity part of the retrorocket exhaust. The retrorocket exhaust radiation flux incident on the outboard part of the microwave absorber is higher than the flux incident on the dish because the microwave absorber has a view to the exhaust adjacent to the retrorocket exit while the dish does not. A scale model of the exhaust plume was used to determine the maximum incident flux on the microwave absorber. A 1/40 scale model of the 13-deg-angle truncated exhaust cone, 20-exit-diameters high was divided into 10 sections (10 truncated cones) of equal height. The maximum view factors from the antenna inner skirt (i.e.,

Table 29. S-10 (TCM) test program

Phase number	Facility and vehicle configuration	Solar constancy, %	Run number	Mode number	Time, hr	Test objectives	Comments
Hughes Aircraft Company I	Facility: Hughes vacuum chamber Solar source: xenon				(18)	Determine effects of vernier-engine cone heating	
	Vehicle configuration: complete vehicle with following exceptions:	100		1	8	Establish coast-mode steady-state conditions on vehicle and simulate 51-sec engine burn	51-sec burn corresponds to nominal midcourse correction
	Foot pads deleted from legs Shadow shrouds and vehicle support tube shrouds installed	100		2	2	Establish coast-mode steady-state conditions and simulate 240-sec engine burn — maximum thrust	240-sec burn corresponds to maximum specified engine burn time at maximum thrust
	Flight vernier-engine cones replaced with special cones for hot cone testing	100		3	4	Establish coast-mode steady-state conditions and simulate 310-sec engine burn — maximum thrust	310-sec burn corresponds to time required to burn all propellant at maximum thrust
	Facility limitations: Landing gears extend into reduced solar intensity region of beam Vehicle will not fit in chamber with foot pads on	100		4	4	Establish coast-mode steady-state conditions and simulate 476-sec engine burn	476-sec burn corresponds to time required to burn all propellant at minimum thrust
Hughes Aircraft Company II	Same as Hughes Aircraft Company Phase I except for the following:	100	1		(95) (66)	Subsystem margin testing	
	Flight-type vernier-engine cones will be installed					Simulate complete mission duration in transit coast-mode environment	Entire 66-hr flight duration is required for tests on the main retro and propellant tanks since thermal control depends on heat capacities
	Altitude velocity sensor antenna cold shroud will be installed						
	Solar panel and planar array will be removed from positioner			1	8	Obtain steady-state thermal data on all subsystems with coast-mode power in Compartments A and B	
				2	51	Perform special high-power and low-power compartment tests Perform RADVS special tests Perform vernier system special tests Perform flight control sensor group special tests and atitude marking radar special tests	Several tests in mode will be performed in parallel for units that are thermally independent

Table 29. S-10 (TCM) test program (cont'd)

Phase number	Facility and vehicle configuration	Solar constancy, %	Run number	Mode number	Time, hr	Test objectives	Comments
Hughes Aircraft Company II (cont'd)				3	6	Perform survey and approach camera warmup cycles	TV camera heaters will be turned on according to actual mission requirements
						Reduce compartment system power to zero and observe thermal switch opening temperature	
		0	2		1	Perform 1-hr solar eclipse	TV heaters will remain on during eclipse to simulate night landing
		120	3		(16)	Perform subsystem margin testing by testing under solar intensity greater than one solar constant	
				1	8	Establish steady-state conditions on all subsystems (coast mode)	Coast-mode power in compartments
				2	8	Perform special subsystem tests using special test heaters	Subsystem testing not completed in Hughes Aircraft Company Phase II, Run I, can be continued here
		0	4		1	Perform 1-hr solar eclipse	
		80	5		(13)	Perform subsystem margin testing using solar intensity less than one solar constant	
				1	8	Establish steady-state conditions on all subsystems (coast mode)	Coast-mode power in compartments
				2	4	Increase lower spaceframe temperature using special test heaters on retro-engine attach points	Observe effects of increased spaceframe temperature on main retro propellant and other subsystems
Hughes Aircraft Company III	Facility: Hughes vacuum chamber				(17)		
	Solar source: xenon	120	1		6	Obtain steady-state temperatures on landing gear assembly, leg mounted nitrogen lines, and attitude jet	
	Vehicle configuration: complete vehicle with following exceptions:	100	2		5		
	Leg 1 and 2 removed	0	3		1	Determine transient thermal characteristics of landing gear assembly during solar eclipse	Perform 1-hr solar eclipse
	Omni-antenna removed						
	Vehicle location in chamber shifted to illuminate entire Leg 3	80	4		5	Obtain steady-state temperature data on landing gear assembly	Compartment system thermal losses will also be observed during Run 4
	Install "live" shock on Leg 3						
	Cold shrouds not required for this phase						
	Facility limitations: Only that portion of spacecraft near Leg 3 will be in solar beam						

Table 29. S-10 (TCM) test program (cont'd)

Phase number	Facility and vehicle configuration	Solar constancy, %	Run number	Mode number	Time, hr	Test objectives	Comments
JPL I	Facility: JPL 10-ft simulator Solar source: xenon				(26)	Perform subsystem margin testing in JPL 10-ft simulator	Comparison will be made between results of Hughes and JPL facility tests
	Vehicle configuration: same as Hughes Aircraft Company Phase II except landing gears must be removed and omni-booms replaced with studs	80	1		8	Establish coast-mode steady-state conditions on all subsystems	Repeat Hughes Aircraft Company Phase II, Run 5, Mode 1
	Facility limitations:	100	2		8	Establish coast-mode steady-state conditions on all subsystems	Repeat Hughes Aircraft Company Phase II, Run 1, Mode 1
	Vehicle will not fit into simulator with landing gears or full-length omni-beams installed	0	3		1	Perform 1-hr solar eclipse	
		120	4		8	Establish coast-mode steady-state conditions on all subsystems	Repeat Hughes Aircraft Company Phase II, Run 3, Mode 1
		0	5		1	Perform 1-hr solar eclipse	
JPL II	Facility: JPL 10-ft simulator Solar source: xenon	100			(15)	Perform test with solar panel and planar array antenna installed on vehicle	No shadow shrouds
	Vehicle configuration: same as Hughes Aircraft Company Phase I except no landing gear assemblies and no shadow shrouds		1		10	Establish coast-mode steady-state conditions with solar panel and planar array installed on vehicle	Observe differences in temperature distribution when cold shrouds are replaced by solar panel and planar array
	Facility limitations: same as JPL Phase I		2		2	Reposition solar panel and planar array to 45 deg from Z-axis for 2-hr period to observe subsystem effects	Determine effects of repositioning solar panel and planar array during terminal descent
			3		2	Actuate all positioner motors and move panels through a series of motions to observe transient response of subsystems	Observe positioner motor thermal responses
		0	4		1	Perform 1-hr solar eclipse	
JPL III	Facility: JPL 10-ft simulator Vehicle configurations: same as JPL Phase II except retro-engine removed and propellant tanks will be drained	0	1		20	Establish lunar night heat losses from compartment system	Heat loss will be determined by monitoring power required by thermal control and heater assembly in each compartment; the command receiver in Compartment A will remain on

microwave absorber) to these 10 sections were determined with a form-factometer. The radiosity of each of the sections was calculated from the known maximum radiosity adjacent to the retrorocket exit (6.5 Btu/sec-ft^2) and the hypothesis that the radiosity decreases inversely as the square of the distance from the apex of the exhaust cone. The incident flux at the inside antenna skirt due to any one of the 10 sections of the exhaust cone is equal to the product of the view factor from the skirt to that section times the radiosity of that section. The

Table 30. RADVS dish maximum temperatures

RADVS dish	Temperature, °F
Maximum steady-state transit (T-21 data) (only 110°F for the velocity sensing antenna)	140
Uncertainty in coast phase	±45
ΔT rise because of Moon (lunar noon landing)[a]	50
Maximum ΔT rise because of retrorocket landing	13
Maximum temperature	203 ±45

[a]Temperature drop for terminator landing is $6°F < T < 42°F$.

maximum total incident flux at the inside antenna skirt was calculated to be 0.36 Btu/ft²-sec by summing the incident fluxes from the 10 different sections. Actually, the first four sections were the only significant ones; the view factors to the other six sections were negligible.

Previous tests were made of 3-in. diameter samples of the microwave absorber and dish materials. The microwave absorber samples were heated in a vacuum of 10^{-4} torr with heat flux intensities of 0.8, 1.2, and 1.5 Btu/ft²-sec for 50 sec. No surface degradation was visible. A sample of the microwave absorber material delaminated after exposure to 1.2 Btu/sec-ft² for 150 sec (this is almost 4 times the duration of the retrorocket firing and the flux is 3.3 times higher than expected).

The microwave absorber was not damaged when exposed to 1.5 Btu/ft²-sec for 50 sec. This flux level is 4 times higher than the flux from the retrorocket exhaust. The test samples of microwave absorber were not damaged until the flux level was 3.3 times higher than the flux from the retrorocket exhaust and the heating duration 3.7 times the retrorocket firing duration. Therefore, the retrorocket firing is not expected to be a problem. The recorded temperature at this time for this extreme heat test was 350°F, but the actual surface temperature (without the heat capacity and conduction losses of the thermocouple) probably was higher than 350°F. It is concluded that the microwave absorber can survive the lunar noon landing where the maximum calculated temperature at this time is 365 ±45°F (Table 31).

Table 31. RADVS skirt inner surface (microwave absorber) maximum temperature[a]

Condition	Lunar noon landing, °F	Terminator landing, °F
Maximum steady-state temperature in transit (outboard skirt)	45	45
Uncertainty in coast phase	±45	±45
T rise because of Moon	80	0
T rise because of direct sunlight	0	50
T rise because of retrorocket	240	240
T rise because of vernier engines	0	0
Maximum temperature	365 ±45	335 ±45

[a]Location with maximum view to retro-exhaust

O. Engineering Mechanics

1. Shock Absorbers

The National Waterlift Company (NWL) has completed the recalibration of strain gages on shock absorbers MS 13, 14, and 15 used on the T-21 vehicle. The shock absorbers have been returned to Hughes. Shock absorbers MS 32, 33, and 34 have completed flight acceptance tests and have also been shipped to Hughes. MS 32 completes the set for the SC-1 spacecraft, since one of the original SC-1 units (MS 27) was returned to NWL because of a discoloration in the weld, which could indicate brittleness. MS 33 and 34 are scheduled for use on SC-2. The third unit to complete the SC-2 set is in assembly.

Previous welding difficulties resulting in porous welds initiated a change to an automatic welding procedure. All future welding of cylinder to tube assemblies will be done by Airtek Dynamics of Compton, California, utilizing automatic welding equipment. Weldments SN 24, 25, 30, 32, 34, and 35 have been rewelded successfully using the new procedure. The remaining nine cylinder and tube assemblies for the A-21 program are being remachined and X-rayed prior to being rewelded.

Shock absorber MS 27 (the suspected brittle weld) will be drop-tested at reduced temperature during August in preparation for the low-temperature qualification drop tests. In addition, NWL will burst-test three helium gas chambers.

Strain gages have been installed on cylinder and tube assemblies SN 24, 25, 30, 32, 34, and 35. Shock absorbers MS 20, 21, and 22 (type approval test) are presently undergoing the flight acceptance test prior to shipment to Hughes for thermal finishing.

In compliance with a new specification, the basic A-21A shock absorber material has been changed to type 6A1-4V titanium. Also incorporated within the new specification is the low-temperature drop test and man-rated burst test of the helium gas chamber.

2. Landing Dynamics

a. Three-dimensional touchdown stability. The three-dimensional lunar landing program which is being developed by the Bendix Products Aerospace Division, South Bend, Indiana, under JPL subcontract 951304, is nearing completion. It is expected that the results of five check cases will be available within the next three weeks. Three of the five check cases have been run on the Hughes Aircraft Company two-dimensional lunar landing program, the other two on a three-dimensional extension of that program, which Hughes developed on their own initiative.

After verification of the Bendix program by means of the five check cases, phase two of the Bendix contract will be initiated. Phase two consists of 2,500 computer runs designed to establish comprehensive three-dimensional *Surveyor* landing stability boundaries.

b. Two-dimensional studies. The analysis to investigate vehicle landing stability as a function of extreme temperatures of the landing system has been continued. Stability boundaries have been determined for a vehicle having shock absorbers at 120°F, crushable blocks at −50°F, and vehicle centers-of-gravity of 18.5, 18.0, and 17.0 in. above the leg hinge plane. The results are shown in Fig. 88; the current 3σ landing dispersion ellipse and projected design ellipse are also shown as references.

The preliminary stability boundaries which were shown in *SPS 37-33*, Vol. I were based on an insufficient number of data points and should be replaced with Fig. 88.

c. A-21A landing gear design. Because the landed weight of the A-21A vehicle will be significantly greater than the weight of A-21, a redesign of the A-21 shock absorber is necessary. The greater weight of the A-21A requires increases in the shock absorber compression damping, return damping, spring constant, and hydraulic preload. This results in greater pressure loads in the shock absorber. Space restrictions on the vehicle remain identical to those of the A-21, so that the increased pressures require internal increases in wall thickness. The new shock absorber will be designed to carry loads in the 8500- to 9000-lb range.

Because of the necessity to modify the shock absorber parameters, an optimization study is underway to obtain

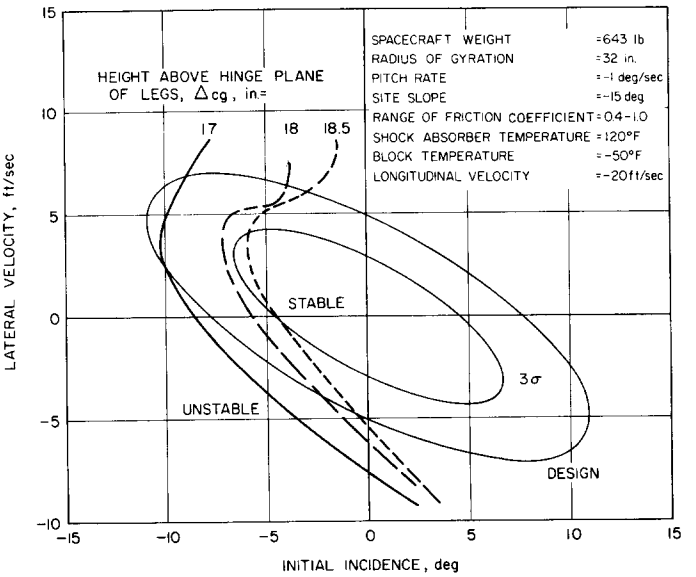

Fig. 88. Lunar landing stability boundaries

parameter values which give the best possible stability while keeping the loads within the acceptable range. To date, stability boundaries have been determined for the A-21 shock absorber scaled up 14% for the heavier A-21A vehicle. Stability boundaries have also been determined considering increases of 5 and 10% in compression damping, rebound damping, and spring rate above the values for the scaled-up A-21 shock absorber. These results are shown in Fig. 89 for longitudinal velocities of 20 and 18 ft/sec. Also shown for reference are the 3σ and design dispersion ellipses.

d. Three-dimensional touchdown stability drop tests. After completion of separation tests at General Dynamics/Convair, the T-1 vehicle is to be returned to Hughes for upgrade prior to the stability drop tests, at which time the vehicle designation will become S-15. A triaxial gyro system for determining vehicle attitude during the drop tests has been selected. The gyros used for this system are Model FG23-2101-1 supplied by Humphrey, Inc., and can measure up to 360 deg of rotation with a resolution of less than 0.5 deg, and can be remotely caged and uncaged. Work is underway to design a mounting platform for this gyro system for integration into the S-15 vehicle.

Design of the body-block load-measuring device continues. One of the most promising designs makes use of strain gages on the block supporting structure in conjunction with a commercial load cell to measure the forces imparted to the spaceframe by the crushable body blocks. The major problem is the space limitation in the vicinity of the block spaceframe interface. Present plans

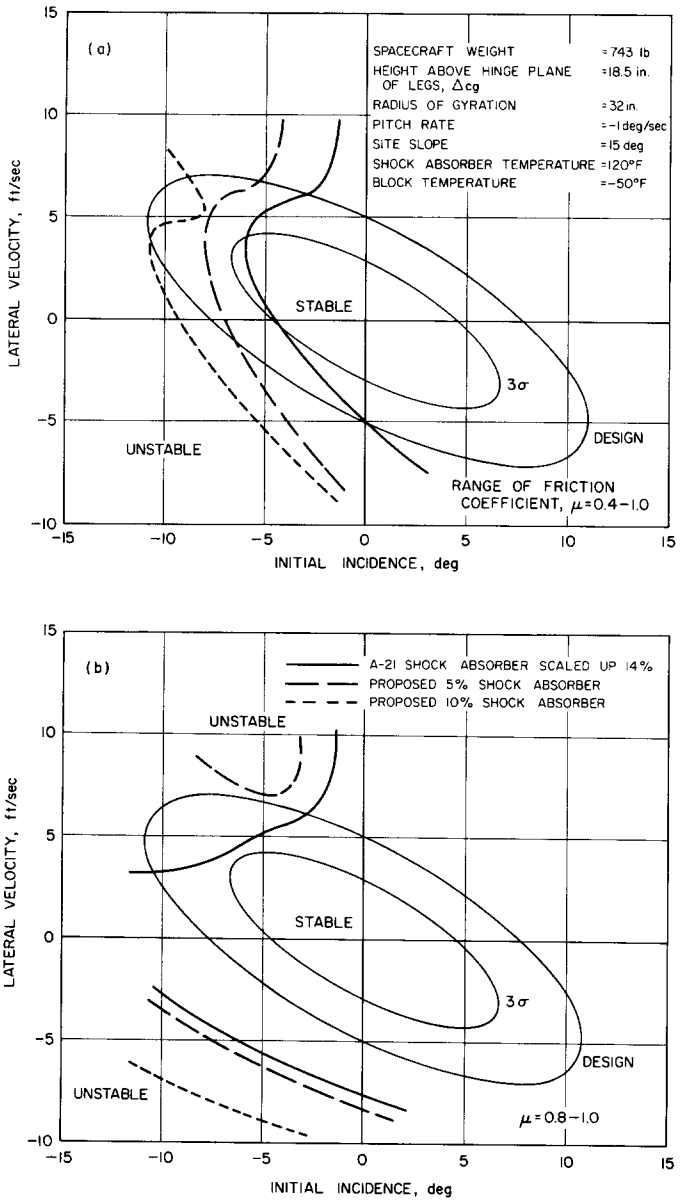

Fig. 89. A-21A spacecraft stability boundaries: (a) longitudinal velocity = −20 ft/sec; (b) longitudinal velocity = −18 ft/sec

call for conducting a development program on a prototype design during unit block tests before incorporating similar devices on the vehicle.

Plans have been completed for modifying the existing steel scaffold at the drop test facility to allow for an enlarged landing platform. This scaffold is an integral part of the mechanical system, which elevates the vehicle prior to each drop and partially supports the vehicle during a drop test to simulate lunar gravity. The landing area must be enlarged from 20 × 40 ft to 40 × 40 ft to allow for crosshill lateral velocity at touchdown, a prime requirement for three-dimensional stability studies.

Preliminary design of the new, enlarged landing platform for the drop test facility has begun. This new platform is to be of a circular shape with a 40-ft diameter, sloped 15 deg from the horizontal, and capable of rotating 90 deg to either side of the preferred direction of the vehicle lateral velocity, which remains fixed in inertial space. To make the landing surface as inelastic as possible, the primary platform surface will be made of 12- × 12-in. wooden beams with secondary supports of steel I-beams. Preliminary calculations estimate that the weight of the platform will be 40 tons.

The test series will consist of approximately 25 two-dimensional and 25 three-dimensional drops. Commencement is presently scheduled for November 22 (2-D) and December 27 (3-D).

3. Dynamic Analyses

Analyses of the current series of S-2A drop test conditions have been made to predict structural bending moments. The drop test conditions are shown in Table 32. Mathematical models of the spacecraft with the planar antenna in the required locations were developed and used to predict the expected strain-gage readings during these remaining drop test conditions. Table 33 gives the maximum and minimum values of the eleven bending moments expected during Drop Tests 5 through 9. Fig. 90 defines the bending moments listed in Table 33 and shows their relationship to the strain gages used for the drop test measurements.

The mathematical models of the spacecraft were used to study the effect of the reduction of vertical touchdown velocity during the lunar landing conditions listed in Table 34. The absolute maximum of the critical bending moments on the antenna/solar panel positioner (A/SPP) are listed in Table 35. Definitions of these bending moments are also given in Fig. 90.

For Lunar Landing Cases 1 through 4 and 9 through 12 the significant antisymmetric bending moments (M_4, M_6, M_{13}, M_{15}, M_{19}, M_{21}, M_{23}) decreased as the touchdown velocity decreased since these cases were with Leg 1 downhill, which excites the antisymmetric motion of the A/SPP. Similarly, the symmetric bending moments decreased for the Lunar Landing Cases 5 through 8 since these cases were with Leg 2 downhill, which excites both the symmetric and antisymmetric bending moments.

Table 32. Earth drop tests to simulate lunar landings

Test conditions	Spacecraft orientation	A/SPP position, deg	Worst-case lunar landings				Equivalent Earth drop tests (without horizontal velocity)			
			Touchdown velocities, ft/sec		θ_0, deg	Slope of surface, deg	Vertical touchdown velocity, ft/sec	θ_0, deg	Slope of surface, deg	Drop height, ft
			Longitudinal	Lateral						
5	Leg 1 downhill	65	20	2	2	15	18.0	0	15	5.04
6	Leg 1 downhill	45	20	2	2	15	18.0	0	15	5.04
7	Level	0	20	0	0	0	18.6	0	0	5.38
8	Leg 1 downhill	0	20	2	2	15	18.0	0	15	5.04
9	Leg 1 downhill	0	20	2	2	15	18.0	0	15	5.04

Table 33. Predicted bending moments, 1000 in.-lb, on A/SPP for S-2A drop tests

Bending moments (Fig. 90)	Moments description (Fig. 90)	Drop Test 5[a]		Drop Test 6		Drop Test 7		Drop Test 8		Drop Test 9	
		Minimum	Maximum	Minimum	Maximum	Minimum	Maximum	Minimum	Maximum	Minimum	Maximum
M_4	S/G 107	−5.9	5.9	−7.5	7.4	−1.79	2.0	−9.1	9.8	−8.8	9.0
M_5	S/G 104	−3.3	2.4	−2.4	1.8	−2.6	1.0	−2.6	1.4	−2.3	0.98
M_6	S/G 103	−4.0	4.9	−5.0	5.8	−1.1	0.88	−6.4	5.3	−5.8	4.9
M_{13}	S/G 175	−6.8	4.2	−11.0	9.5	−1.4	1.65	−7.5	6.9	−7.4	6.8
M_{14}	S/G 174	−2.4	1.5	−2.3	1.4	−1.1	0.72	−1.2	1.2	−1.5	0.76
M_{15}	S/G 178	−6.9	5.5	−5.6	4.9	−2.2	2.3	−14.3	12.4	−13.8	12.4
M_{19}	Mast torsion	−6.4	5.5	−10.9	9.4	−1.5	1.6	−6.7	5.9	−6.7	5.9
M_{20}	Mid-mast bend at Y-axis	−2.4	3.5	−2.0	2.9	−1.9	1.5	−4.3	4.5	−2.9	3.3
M_{21}	Mid-mast bend at X-axis	−20.3	14.8	−19.1	10.4	−4.7	3.9	−23.6	22.2	−23.5	22.2
M_{22}	Lower mast bend at Y-axis	−3.5	4.9	−2.6	4.2	−3.2	2.7	−7.4	7.7	−4.9	5.4
M_{23}	Lower mast bend at X-axis	−32.2	21.9	−29.5	14.6	−6.4	5.1	−3.0	29.3	−30.4	28.9

[a] Data was interpolated from models with the A/SPP positioned at 55 and 70½ deg.

Therefore, the significant bending moments are decreased as the vertical touchdown velocity is decreased.

4. Dynamic Tests

a. S-2A vehicle. The drop test conditions have been revised for completing the simulated lunar touchdown tests on the S-2A vehicle. The program is expanded to include five drops with the upgraded A/SPP. Three of the revised drop conditions are given in Table 32 as Drop Tests 5, 6, and 8. Drop Test 7 is similar to Drop Test 8 except that the drop height is 3.32 ft, producing a vertical touchdown velocity of 14.6 ft/sec, corresponding to a lunar touchdown velocity of 17 ft/sec. Drop Test 9 is also similar to Test 8 except that the polar axis of the A/SPP is positioned with the planar antenna 36 deg from the vertical axis of the mast.

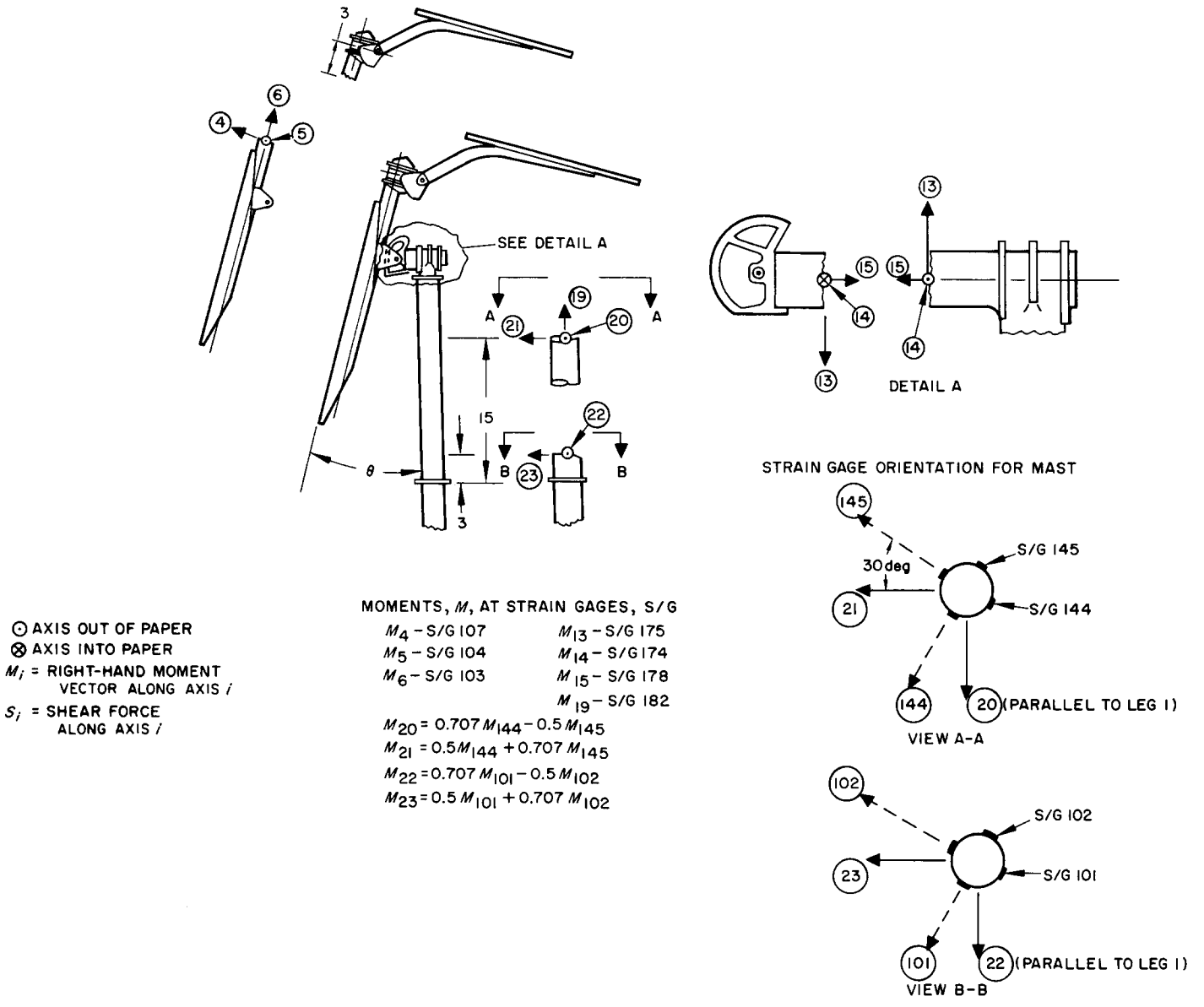
SEE DETAIL A
DETAIL A
STRAIN GAGE ORIENTATION FOR MAST
30 deg
S/G 145
S/G 144
(PARALLEL TO LEG 1)
VIEW A-A
S/G 102
S/G 101
(PARALLEL TO LEG 1)
VIEW B-B
⊙ AXIS OUT OF PAPER
⊗ AXIS INTO PAPER
M_i = RIGHT-HAND MOMENT VECTOR ALONG AXIS i
S_i = SHEAR FORCE ALONG AXIS i
MOMENTS, M, AT STRAIN GAGES, S/G
M_4 - S/G 107
M_5 - S/G 104
M_6 - S/G 103
M_{13} - S/G 175
M_{14} - S/G 174
M_{15} - S/G 178
M_{19} - S/G 182
$M_{20} = 0.707 M_{144} - 0.5 M_{145}$
$M_{21} = 0.5 M_{144} + 0.707 M_{145}$
$M_{22} = 0.707 M_{101} - 0.5 M_{102}$
$M_{23} = 0.5 M_{101} + 0.707 M_{102}$

Fig. 90. S-2A A/SPP bending moments and strain-gage locations

Force inputs at the landing gears and the dynamic response of the A/SPP will be recorded by 43 channels of instrumentation (17 accelerometers, 23 strain measurements, and 3 leg deflection potentiometers) for each of the five drop conditions.

b. S-9 vehicle. The S-9 vehicle will be vibrated on the *Centaur–Surveyor* adapter with the vehicle being excited torsionally about the roll (z) axis. The program is comprised of three series of tests: (1) low-level sine sweeps, (2) qualification-level sine sweeps, and (3) torsional pulse tests. This test program is expected to be completed on October 25.

5. Flight Instrumentation

a. Accelerometer amplifier system. Assembly for SC-2 has been completed. Assembly for SP-1 will be completed by July 30, 1965. The accelerometer amplifiers were calibrated prior to, and monitored during the *Surveyor* SC-1 vibration test. These data are not yet available for analysis.

b. Strain-gage amplifier system. Assembly for SC-2 is completed. The schedule for SP-1 has not changed; units will be delivered by August 13, and assembly completed by September 1965. All qualification test data will be

UNCLASSIFIED [redacted]

compiled and submitted for type-approval-test review. Installation and calibration of strain gages on one SC-2, two SC-3, and three S-9 shock absorbers will be started on July 19 at the vendor's facilities.

c. Leg position potentiometers. Qualification data will be compiled and submitted for type-approval-test review.

Table 34. Lunar landing cases for reduced velocity study

Case number	Spacecraft orientation (single leg in plane of symmetry)	A/SPP angle, deg	θ_0 spacecraft orientation, deg	θ_0 slope of surface, deg	Touchdown, ft/sec	
					Vertical	Lateral
1	1	17.5	0	0	20	0
2	1	17.5	0	0	15	0
3	1	17.5	0	0	12	0
4	1	17.5	0	0	8	0
5	2	17.5	0	15	20	6
6	2	17.5	0	15	17	6
7	2	17.5	0	15	14	6
8	2	17.5	0	15	10	6
9	1	17.5	2.0	15	20	2
10	1	17.5	2.0	15	18	2
11	1	17.5	2.0	15	15	2
12	1	17.5	2.0	15	11	2

6. *Static Test of Vernier Engine Brackets*

To maintain satisfactory thrust vector control, *Surveyor* spacecraft system functional requirements specify that the vernier-engine bracket stiffness should be 0.45 ±0.05 deg of angular rotation with respect to the spacecraft roll axis per 100 lb of engine thrust. The SC-1 bracket design and analysis was based on this requirement.

A static load-deflection test was performed to verify stiffness characteristics of the vernier-engine mounting bracket assembly and supporting structure. Only those loads produced by the thrust of the fixed vernier engine were considered. Loading was accomplished by means of an upward axial force applied against a pin mounted in place of the vernier engine trunnion (Fig. 91). This simulated thrust force was reacted at the three retro-engine mount points of the spaceframe.

Deflections were determined by dial gages placed so as to be capable of isolating the effect on vernier engine alignment of the flexibility of the spaceframe from that of the vernier mounting bracket assembly. Thus, the arrangement of the dial gages indicated angular deflections of the vernier thrust-chamber centerline with respect to the spacecraft roll axis, and axial deflections of the

Table 35. Maximum moments for lunar landings under reduced velocity conditions

Bending moment	Case number											
	1	2	3	4	5	6	7	8	9	10	11	12
	Load, in.-lb											
M_4	−1,157.0	−556.0	−609.0	−250.0	4,682.0	3,395.0	2,326.0	950.0	−8,242.0	−6,590.0	5,769.0	4,511.0
M_5	−4,041.0	−4,794.0	−3,226.0	−1,059.0	−8,656.0	6,901.0	−4,610.0	−3,130.0	−3,190.0	−4,407.0	−5,023.0	−1,759.0
M_6	682.0	−474.0	475.0	191.0	3,631.0	2,635.0	1,777.0	859.0	−6,619.0	−5,097.0	4,233.0	4,368.0
M_{13}	−1,521.0	−1,057.0	−919.5	−343.8	6,684.0	5,072.0	3,398.0	1,404.0	−13,460.0	−10,280.0	−8,606.0	−6,008.0
M_{14}	2,725.0	2,213.0	−1,999.0	−250.4	−9,709.0	−6,757.0	−4,598.0	−3,889.0	−1,914.0	−1,707.0	−1,752.0	−1,267.0
M_{15}	1,296.0	933.6	877.8	359.8	−5,873.0	−4,076.0	2,345.0	1,392.0	11,160.0	9,209.0	−7,554.0	−7,003.0
M_{19}	−1,571.0	−1,129.0	−1,073.0	−377.0	6,735.0	5,296.0	3,603.0	1,396.0	−13,460.0	−10,150.0	−8,990.0	−6,623.0
M_{20}	3,851.0	3,978.0	−3,218.0	−224.9	17,270.0	−14,680.0	9,933.0	−6,161.0	2,920.0	2,988.0	−3,261.0	−2,315.0
M_{21}	2,039.0	1,280.0	1,360.0	−526.3	−9,707.0	−6,223.0	4,112.0	−2,844.0	−22,090.0	−16,200.0	−16,740.0	7,758.0
M_{22}	5,389.0	6,273.0	5,537.0	387.5	22,620.0	−25,130.0	14,900.0	−10,060.0	4,995.0	4,812.0	−5,013.0	−4,128.0
M_{23}	3,065.0	−2,173.0	2,051.0	−772.6	−13,550.0	8,300.0	−6,146.0	4,259.0	−33,510.0	−26,800.0	−24,480.0	−20,270.0

UNCLASSIFIED [redacted]

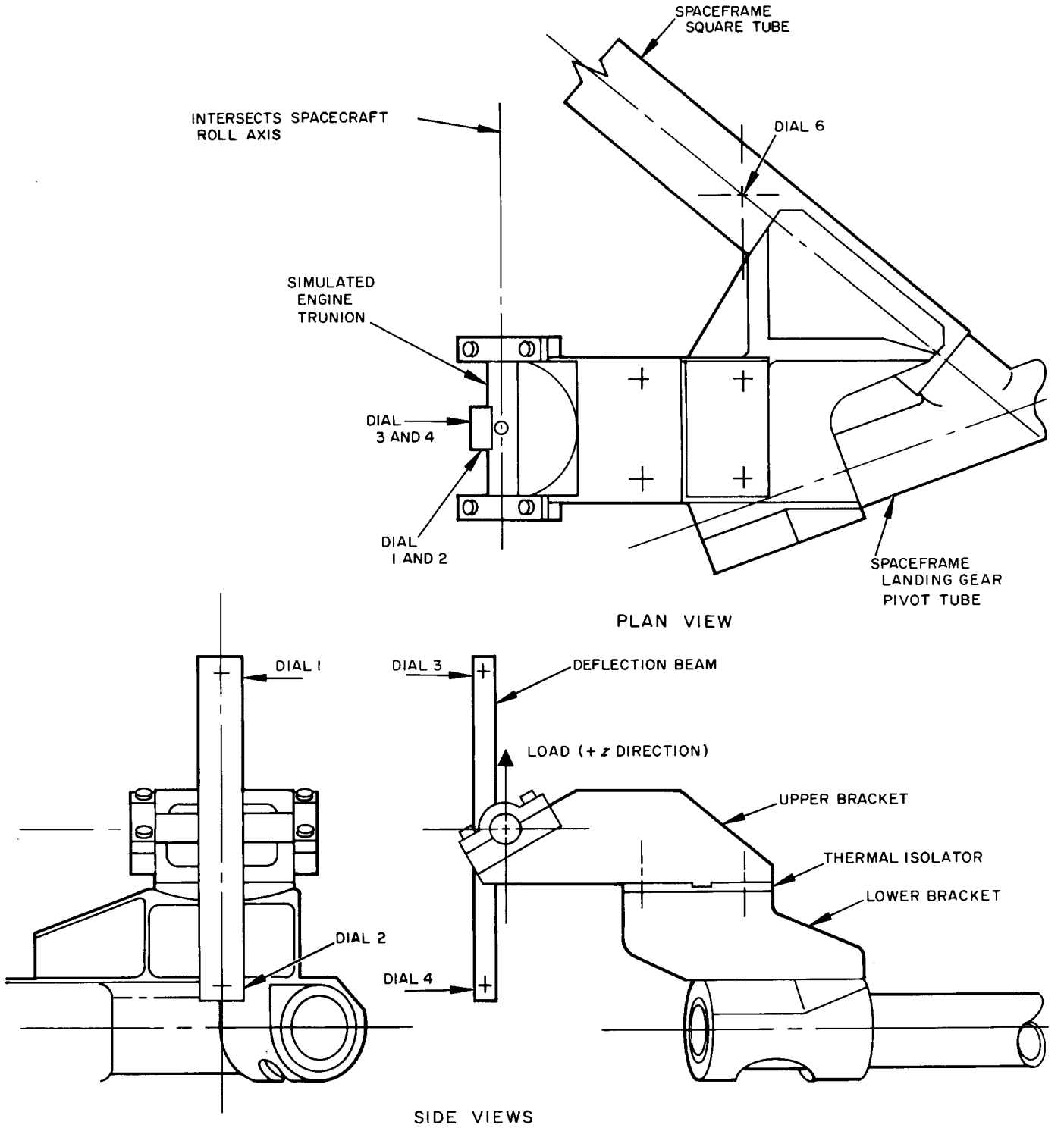

Fig. 91. Load application and instrumentation

vernier engine trunnion and of the spaceframe adjacent to the vernier-engine mounting bracket with respect to the retro-engine attach points. The loading schedule called for application of the load from 0 to 100 lb in 10-lb increments, and then for removal of the load in 20-lb decrements to zero. All dial gages were recorded at each step.

Fig. 92 presents a plot of angular deflection of the vernier engine in a plane perpendicular to a radial line to the spacecraft roll axis versus thrust load based on a typical test run. The maximum deflection of 0.485 deg at 100-lb thrust falls within the specified requirement mentioned above.

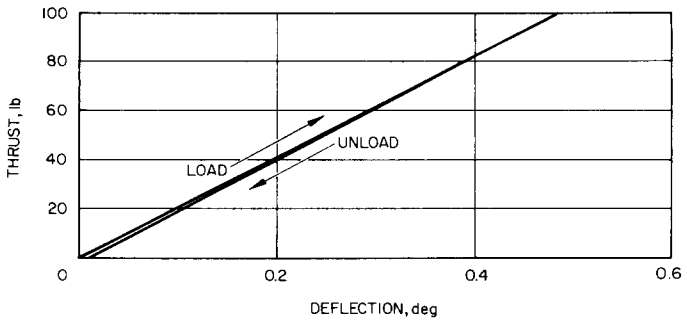

Fig. 92. Angular deflection of vernier engine in plane normal to theoretical radius arm to spacecraft roll axis vs simulated thrust force

Because of recent requirements for additional deflection information and minor structural changes in the bracket insulator design, a more comprehensive test plan is now in preparation. The new plan includes an investigation into the effects of lateral as well as axial loads during *Atlas–Centaur* boost, an evaluation of hysteresis effects on a permanent set relative to engine alignment, and a determination of alignment under zero-gravity conditions. The effects of various levels of retro-engine thrust will also be assessed. Thrust and inertia loads will be applied both simultaneously and separately in two loading cycles to measure repeatability and linearity of the system. Additional tests will also check the effects of local heating, especially in the area of the plastic washers, on the elastic action of the brackets.

The basic deflection tests will be performed on hard-mounted flight bracket assemblies prior to installation on flight spacecraft, and after installation will be repeated with strain-gage calibration runs to verify the rigidity of the spaceframe.

The test setup both for the hard-mounted and spaceframe-supported tests will be similar to the one used in the original test, but will also have provisions for the application of lateral loads in two orthogonal directions. Furthermore, longer deflection beams will be used to obtain greater dial gage accuracy. SC-2 and subsequent spacecraft (if deemed necessary) will be used for the tests discussed. The static test plan for Structural Test Model 62 will also include bracket tests according to this plan.

7. Static Test of Antenna/Solar Panel Positioner

A static test is currently in progress to evaluate structurally the SC-1 configuration of the A/SPP for the latest lunar-landing design loads. Because of failures that occurred in the region of the yoke plates during Drop Test 3 of the S-2A vehicle in February, the SC-1 A/SPP was strengthened in the region of the polar axis by substitution of heavier parts and the addition of bolted-on members. The static test specimen is indicated by the dark outline in Fig. 93. Because of the redundancy in load paths in the region of the elevation housing, gear and yoke plates, and the extreme effect of mechanical tolerance in this area, a static test of this nature was deemed necessary to substantiate the many assumptions used in the stress analysis. At present the test is approximately 60% completed.

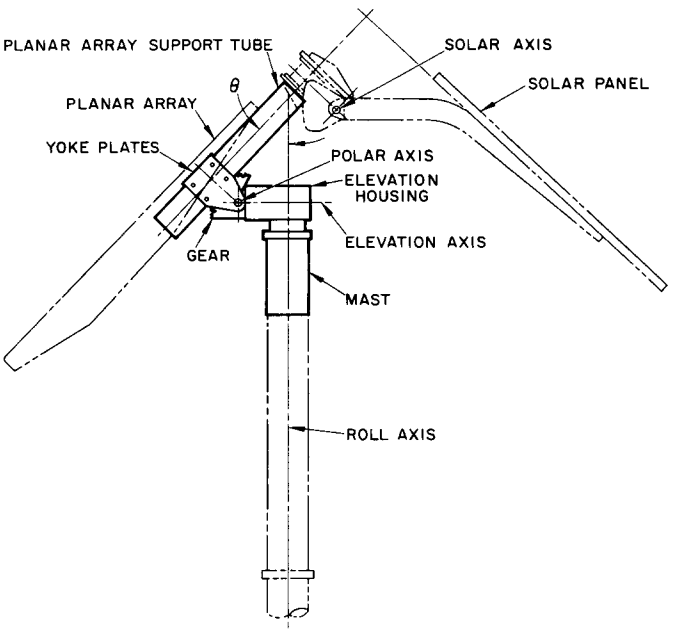

Fig. 93. Antenna/solar panel positioner test specimen

UNCLASSIFIED

Table 36. Test loads (100% × limit)[a]

Configuration		Applied load											
θ_0	Condition	S_4, lb	S_5, lb	S_6, lb	M_4, in.-lb	M_5, in.-lb	M_6, in.-lb	S_7, lb	S_8, lb	S_9, lb	M_7, in.-lb	M_8, in.-lb	M_9, in.-lb
87.0	1	14	174	−14	−2600	300	−3000	−13	118	16	−2000	−600	−7600
	2	106	−308	−213	5900	−1000	600	268	−682	−27	2200	−8000	−500
	3	472	−508	−296	8200	5800	2100	863	−1200	−98	1900	−4900	1600
70.5	1	56	465	−77	−4300	1000	−3900	16	667	56	300	−1300	−12200
	2	−359	−56	−302	600	−10500	2600	−388	−30	−429	1100	−13600	4100
45.0	1	−119	−197	86	7800	−2900	900	−115	−61	48	8900	−300	4200
	2	−372	−113	−107	1700	−10700	1100	−325	−178	−44	500	−11800	2900
	3	−146	305	−4	−2900	−3800	−4000	−175	401	−28	−700	−2400	−9700
36.5	1	−5	393	−8	−12200	400	−5000	50	409	−22	−11000	200	−9100
	2	−237	−218	−321	6600	−9200	3100	−122	−330	−140	5300	−16600	4000
	3	65	492	238	−8700	3800	−2400	−80	265	213	−7900	8700	−16300
0	1	0	486	13	−10700	0	−4800	24	623	−111	−7800	1000	−10500
	2	12	444	120	−8500	1100	−5600	111	306	245	−7500	1400	−17500
	3	−259	−224	−522	5900	−10000	2100	−463	−208	−179	4100	−16500	8600

[a] Fig. 94 shows the sign convention and legend.

The test loads are the latest landing inertia loads resulting from the dynamic analysis as described in *SPS 37-33*, Vol. I. In general, the loads tend to become more critical with decreasing planar array angle (Fig. 93). The actual test conditions being simulated are shown in Table 36 together with the resulting internal bending moments and shear forces in the planar-array support tube and at the polar axis. Fig. 94 gives the sign convention and legend for Table 36.

The test philosophy is to apply load conditions in the order of increasing severity, i.e., corresponding to decreasing planar-array angle at landing. Following the completion of testing at each angle θ, the operation of each motor axis is checked for changes in drive torque and the entire specimen is disassembled and inspected in detail for evidence of permanent damage. At completion of 87-, 70.5-, and 45-deg conditions, only insignificant changes occurred in operating torques.

The specimen is mounted as shown in Fig. 94, which also shows the location of strain gages on the planar-array tube. Figs. 95 and 96 show two views of the actual test setup. The strain gages are used to check the accuracy of the applied loading. The location of dial gages is as indicated in Fig. 97. Loads are applied to the specimen as couples and shear forces at the ends of the

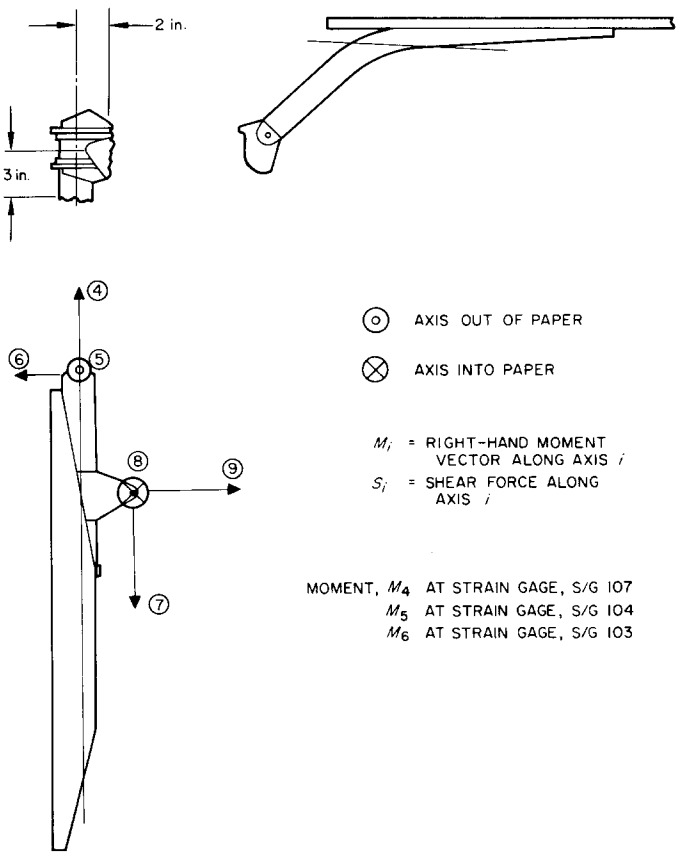

Fig. 94. Sign convention and legend for Table 36

cruciforms located at the top and bottom of the planar array tube (Fig. 94). Loads are applied in increments up to 100% during unloading so that the indications of the beginning of yielding and permanent set can be accurately measured.

To date, the tests have verified the stress analysis which predicted no damage at angles of 87 and 70.5 deg and a small amount of bearing deformation in the region of the roll axis and elevation-axis taper pinholes at 45 deg. The last condition that has been completed (Condition 1 at 36½ deg) resulted in larger amounts of bearing deformation at the two taper pinholes plus a small amount of permanent set at the gear retainer nut. At the completion of Condition 3 at $\theta = 0$ deg, the pin-puller squibs will be fired in a temperature environment of −180°F to determine the effect of large permanent deformations on pin retraction.

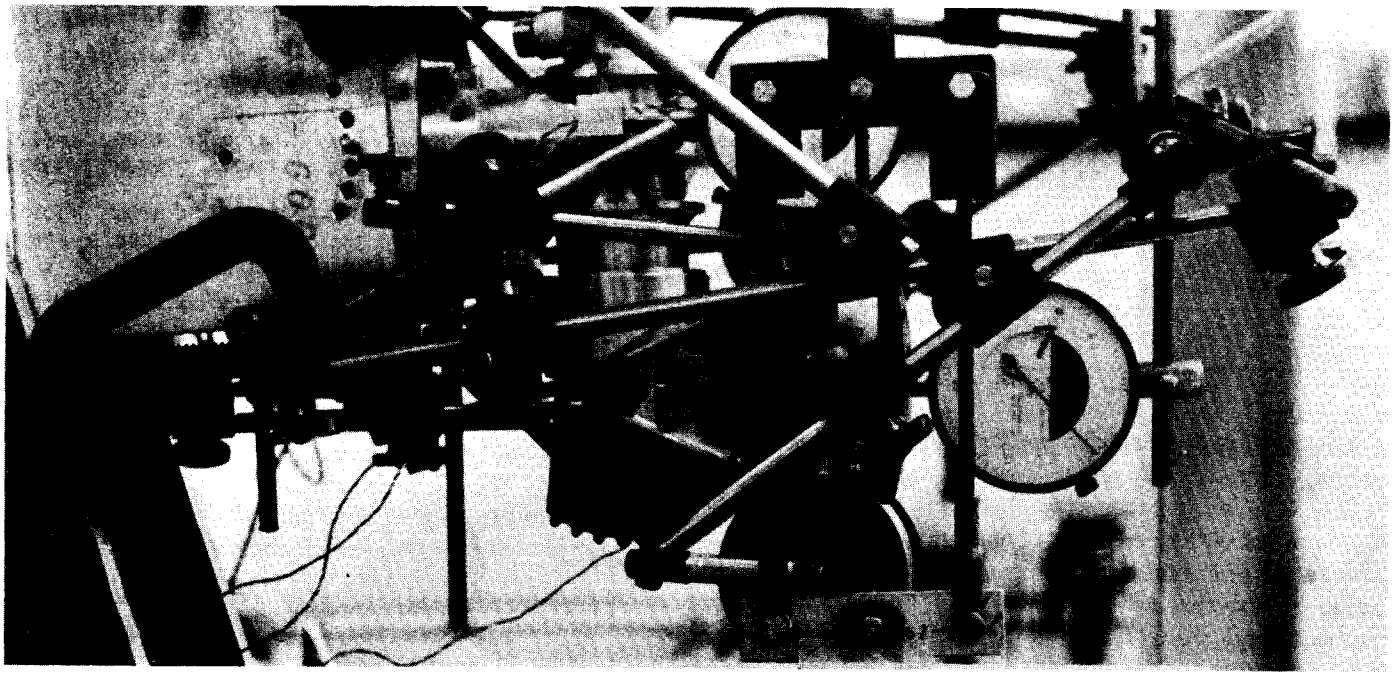

Fig. 95. A/SPP static test arrangement (side view)

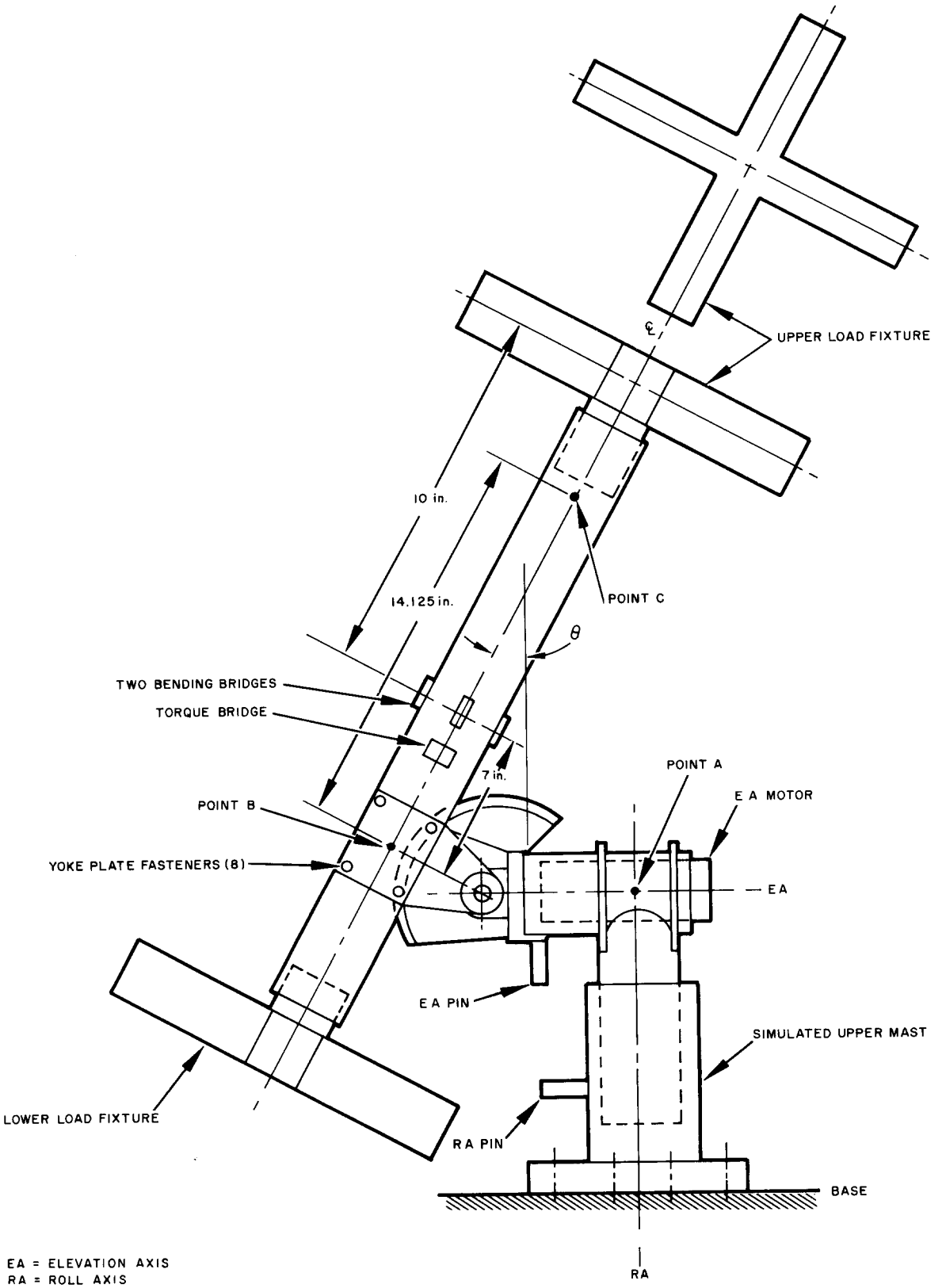

Fig. 96. A/SPP static test arrangement (configuration)

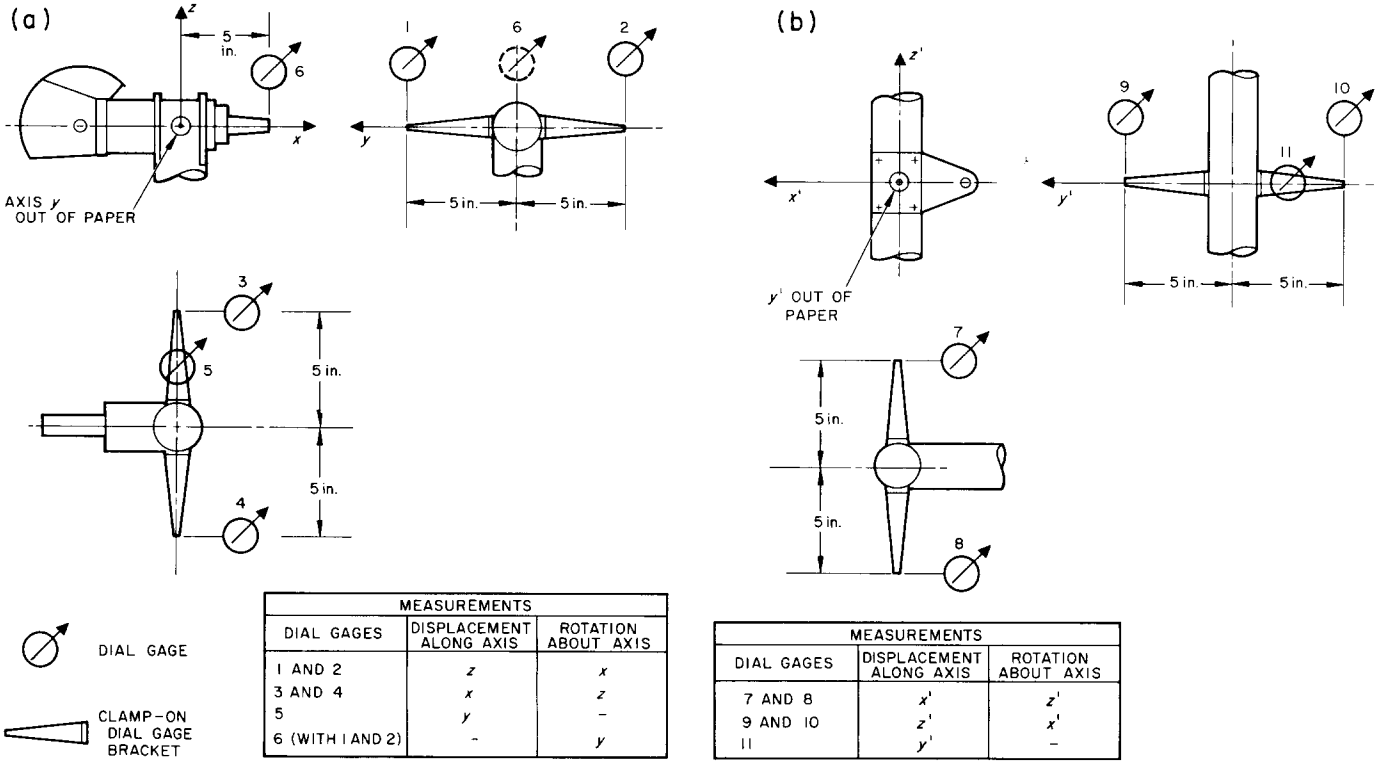

MEASUREMENTS		
DIAL GAGES	DISPLACEMENT ALONG AXIS	ROTATION ABOUT AXIS
1 AND 2	z	x
3 AND 4	x	z
5	y	–
6 (WITH 1 AND 2)	–	y

MEASUREMENTS		
DIAL GAGES	DISPLACEMENT ALONG AXIS	ROTATION ABOUT AXIS
7 AND 8	x'	z'
9 AND 10	z'	x'
11	y'	–

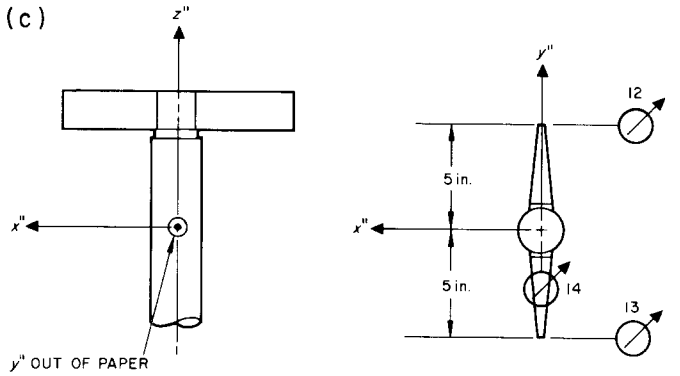

MEASUREMENTS		
DIAL GAGES	DISPLACEMENT ALONG AXIS	ROTATION ABOUT AXIS
12 AND 13	x''	z''
14	y''	–

Fig. 97. Dial gage locations: (a) Point A of Fig. 96; (b) Point B of Fig. 96; (c) Point C of Fig. 96

UNCLASSIFIED

References

1. *Surveyor Spacecraft Monthly Performance Assessment Report*, SSD 5357R, Hughes Aircraft Company, El Segundo, California, July 21, 1965.

2. Meisenholder, G. W., *Planet Illuminance*, Technical Report No. 32-361, Jet Propulsion Laboratory, Pasadena, California, November 10, 1962.

3. Courtney-Pratt, J. S., *Possibility of Photographing a Satellite Near the Moon*, Bell Telephone System Technical Publication, 1961.

4. *Engineering Planning Document No. 155*, Jet Propulsion Laboratory, Pasadena, California, May 13, 1963.

5. Kuiper and Middlehurst, *Planets and Satellites;* Harris, D. L., *Photometry and Colorimetry of Planets and Satellites*, p. 278.

6. *Decibel Allocation and Margin Summary for the Telecommunications Subsystem*, SSD 4021M, Hughes Aircraft Company, El Segundo, California, June 1965.

7. Piaggi, E. G., and Kirhofer, W. E., *Description of Approach Trajectory and Maneuver Model*, Technical Memorandum No. 312-463, Jet Propulsion Laboratory, Pasadena, California, July 24, 1964.

8. Davids, L. H., Meredith, C. M., and Ribarich, J. J., *Midcourse and Terminal Guidance Programs*, SSD 4051R, Hughes Aircraft Company, El Segundo, California, April 1964.

9. Silver, S., *Microwave Antenna Theory and Design*, Boston Technical Lithographers, Inc., Lexington, Mass., pp. 560–561, 1963.